IOWA STATE UNIVERSITY
Digital Repository

Retrospective Theses and Dissertations

Iowa State University Capstones, Theses and Dissertations

2008

NMR studies of complex carbon-containing materials: Maillard reaction products, soil, nanodiamond, and carbon modified TiO_2

Xiaowen Fang
Iowa State University

Follow this and additional works at: https://lib.dr.iastate.edu/rtd

 Part of the Analytical Chemistry Commons

Recommended Citation
Fang, Xiaowen, "NMR studies of complex carbon-containing materials: Maillard reaction products, soil, nanodiamond, and carbon modified TiO_2" (2008). *Retrospective Theses and Dissertations*. 15715.
https://lib.dr.iastate.edu/rtd/15715

This Dissertation is brought to you for free and open access by the Iowa State University Capstones, Theses and Dissertations at Iowa State University Digital Repository. It has been accepted for inclusion in Retrospective Theses and Dissertations by an authorized administrator of Iowa State University Digital Repository. For more information, please contact digirep@iastate.edu.

www.manaraa.com

NMR studies of complex carbon-containing materials: Maillard reaction products, soil, nanodiamond, and carbon modified TiO_2

by

Xiaowen Fang

A dissertation submitted to the graduate faculty

in partial fulfillment of the requirements for the degree of

DOCTOR OF PHILOSOPHY

Major: Analytical Chemistry

Program of Study Committee:
Klaus Schmidt-Rohr, Major Professor
Mei Hong
Victor Lin
Hans Stauffer
Michael Thompson

Iowa State University

Ames, Iowa

2008

Copyright © Xiaowen Fang, 2008. All rights reserved.

www.manaraa.com

UMI Number: 3316240

INFORMATION TO USERS

The quality of this reproduction is dependent upon the quality of the copy submitted. Broken or indistinct print, colored or poor quality illustrations and photographs, print bleed-through, substandard margins, and improper alignment can adversely affect reproduction.

In the unlikely event that the author did not send a complete manuscript and there are missing pages, these will be noted. Also, if unauthorized copyright material had to be removed, a note will indicate the deletion.

UMI Microform 3316240
Copyright 2008 by ProQuest LLC
All rights reserved. This microform edition is protected against unauthorized copying under Title 17, United States Code.

ProQuest LLC
789 East Eisenhower Parkway
P.O. Box 1346
Ann Arbor, MI 48106-1346

TABLE OF CONTENTS

www.manaraa.com

ABSTRACT

Advanced solid-state magic angle spinning NMR (SS-MAS NMR) techniques have been applied to study the structures of carbon-containing complex materials, including ^{13}C / ^{15}N labeled Maillard reaction products (melanoidins), soil and plant materials, detonation nanodiamond, and glucose-^{13}C modified TiO_2 photocatalyst.

Melanoidins, complex high molecular weight mixtures, are formed via the Maillard reactions between sugars and amino acids during heating. Due to their tremendous heterogeneity, the structure of melanoidins has remained poorly characterized. ^{13}C and ^{15}N labeling of the reactants has been combined with various solid-state NMR techniques to elucidate the structures of Maillard reaction products.

(i) The fate of glycine in the model Maillard reaction between $^{13}C/^{15}N$-labeled glycine ($^{13}C1$, $^{13}C2$, $^{13}C1,2$, $^{13}C2$-^{15}N, ^{15}N) and glucose in a 1:1 molar ratio in both dry and solution reaction conditions has been investigated. More than ~70% of glycine carbon remains in the products, and there is no detectable difference between C1 and C2 of glycine in terms of their individual mass loss. Most glycine C1-C2 and C2-N bonds stay unbroken indicating that the Strecker degradation of amino acids, where the C1 is split off as CO_2, is not a major reaction pathway. The C1 of glycine predominantly remains a COO moiety. More than 60% of C2-N bond remains connected while the remaining 40% glycine C2 forms new bonds to either carbon or oxygen of sugar. Novel ^{13}C-detected $^{15}N\{^1H\}$ dipolar dephasing experiments show that the majority of the nitrogen in the melanoidins is not protonated for both dry and solution reactions, implying in particular that nonprotonated N may be a characteristic marker of Maillard reaction products.

(ii) The major structural units of melanoidins have been explored in detail with the products made from glucose of distinct ^{13}C labeling site reacting with ^{15}N-glycine. Quantitative ^{13}C spectra show that alkyl units make up ~48% of carbon in melanoidins; meanwhile, the spectra also show striking differences between the structures formed by different carbons (C1 through C6) of glucose, strongly suggesting that specific structures are formed during Maillard reaction in dry-reaction condition. The reactivity of the glucose-C1 stands out: more than half of C1 forms additional C-C bonds, a much

www.manaraa.com

larger fraction than for the other sites. The C2 carbons are all bonded to heteroatoms and mostly not protonated, while the C3 is predominantly protonated and has a significant fraction of the sites not bonded to heteroatoms as in CCH_2 form. Only C4 and C5 remain significantly in alkyl OCH sites. C6 undergoes the least transformation, with most carbons in OCH_2; also, 1/5 of C6 is lost from the sample. C1 and C6 form the CH_3 end groups in similar quantities (2% of all C). All sites are characterized in more detail by spectral editing.

(iii) N of glycine is a very active site, and most of N form new N-C bonds with sugar molecules. Several complex nitrogen containing structures have been identified using two- and three-dimensional NMR techniques. A significant fraction of N is found in imidazolium, oxazolium and 4-pyridinyl rings. In addition, the N of glycine forms amides, mostly tertiary (nonprotonated), with C=O carbons from glucose, as well as some secondary and tertiary amines.

In another project, different aggregation fractions of four soil samples from two agriculturally managed fields in Iowa have been studied using quantitative ^{13}C direct polarization (DP)/ magic angle spin (MAS) and ^{13}C-^{1}H cross polarization (CP)/ total spinning sidebands suppression (TOSS) NMR techniques combined with elemental analysis results. The three fractions of each soil are unfractionated whole soil, particulate organic matter (POM), and the clay size fraction. HCl/HF treatments with or without heating have been applied to the whole soil and clay size fraction. In the untreated whole soil, esters are found to be a minor component. The only detectable effect of washing e.g. HCl/HF with or without heating is the protonation of COO^- to COOH. Heating does not produce significant structural changes. ^{13}C spectra were recorded to monitor the transformation of plant matter to POM and then to humic substances in whole soils and clay fractions. The crystalline cellulose in plants is lost and noncrystalline saccharides in POM and soil are formed. Meanwhile, the soil samples exhibit a pronounced signal of polymethylene chains. Oxidized char-coal components resonating around 130 ppm are major structural units in these grassland soils. The integrated intensities of quantitative ^{13}C NMR spectra correlated well with elemental analysis data, indicating that NMR measurements are representative even in the presence of

www.manaraa.com

some paramagnetic ions, especially for the whole soil samples, which have the shortest spin-lattice relaxation times. Quantitative analysis of different functional groups indicates that the main features are very similar for soils from different locations in central Iowa, within 5%. Nevertheless, with reduced drainage, the percentage of nonpolar aromatic component is increased measurably.

Further, we have characterized the structure of synthetic nanodiamond by NMR spectral editing combined with measurements of long range dipolar dephasing and relaxation times. The surface layer of these ~4.8-nm diameter carbon particles is mostly protonated or bonded to OH or NH_n groups, while sp^2-hybridized carbons make up less than 1% of the material. The surface protons surprisingly resonate at 3.8 ppm, but their bonding to carbons is proved by dipolar sidebands in ^{1}H-^{13}C HETCOR NMR. $^{13}C\{^{1}H\}$ HARDSHIP experiments, based on H-C dipolar dephasing by surface protons, show that seven carbon layers, in a shell of 0.63 nm thickness that contains ~60% of all carbons, predominantly resonate more than 6 ppm downfield from bulk diamond (i.e., within the 40 - 80 ppm range). The location of unpaired electrons (~40 unpaired electrons per particle) was studied in detail, based on their strongly distance-dependent effects on $T_{1,C}$ relaxation. The slower relaxation of the surface carbons, selected by spectral editing, showed that the unpaired electrons are not dangling bonds at the surface. This was confirmed by detailed simulations, which indicated that the unpaired electrons are mostly located in the disordered shell, at distances between 0.4 and 1 nm from the surface. On the basis of these results, a nonaromatic core-shell structural model of nanodiamond particles has been proposed.

Carbon-doping of TiO_2 photocatalyst has been reported to enhance the efficiency of photodegradation of small organic molecules under visible irradiation. Therefore, they are promising materials for environmental cleanup. Various advanced solid-state ^{13}C NMR techniques have been applied to characterize the carbon structures in glucose-$^{13}C_6$ modified TiO_2. In the gel formed before annealing, the sugar has been dramatically transformed, and chemical bonds with TiO_2 are identified based on their downfield chemical shifts. After washing and annealing at high temperature, a striking spectral feature is a sharp peak at 126-ppm overlapping with a broad aromatic band of coke. Based on its small chemical shift anisotropy and lack of bonding to other ^{13}C this peak is assigned to a CO_4 moiety. The

www.manaraa.com

$^{13}C\{^{1}H\}$ HARDSHIP decay indicates that the CO_4 is incorporated deep into the TiO_2 lattice with C substituting for Ti in the lattice, while the broad coke covers the surface. Quantitative NMR also enables the determination of the approximate carbon-weight fraction of the samples before and after annealing.

www.manaraa.com

CHAPTER 1. General introduction

1.1 Complex carbon containing materials

Carbon, as the fourth most abundant element in the universe by mass, participates in the formation of a huge variety of chemical compounds because it can have chemical bonds with both electronegative (i.e., O, S, N, F, Cl …) and electropositive (i.e., H) elements, and can also covalently bond with other carbon in single, double, or triple bonds. Complex carbon containing materials have attracted extensive interest because of their key roles in life, the environment, and materials science. For instance, they exist in all living organisms, are present in food and drugs, in soil and water such as humic substances, in coal, petroleum, and even in meteorites from outer space. Furthermore, carbon can form nano-materials, in which carbon is either the dominant element, i.e. carbon-carbon networks in detonation nanodiamond, graphite or fullerenes, or makes a nano-composite with another material, such as carbon modified TiO_2.

Many important complex materials either comprise hundreds or thousands of components and cannot be separated using current techniques, or form nanometer-scale structures, in which surface moieties play a dominant role for chemical properties and functionalities. Structural elucidation of these complex materials is essential for understanding their functionalities, and manipulating them for desirable applications. Although mass spectroscopy, solution NMR, HPLC, and CE etc are powerful analytical tools for structural determination, solid state NMR as a relatively new technique has been becoming an indispensable technology. In this thesis, we mainly focus on the applications of various advanced solid-state NMR techniques on the structural elucidation of complex materials, including melanoidins produced in the Maillard reaction, soil organic matter, detonation nanodiamond, and carbon modified TiO_2 photocatalyst.

1.1.1 Melanoidins

www.manaraa.com

Melanoidins are colored polymer products of the Maillard reaction with molecular weights within 1 kD ~ 200 kD. This reaction bears the name of the French scientist Louis-Camille Maillard who first reported it in 1912.[1] The reaction occurs between reducing sugars or polysaccharides and amino acids, polypeptides, or proteins during heat treatments such as frying, roasting or baking food. It also occurs *in vivo* to form advanced glycation end (AGE) products over a period of several months to years. This process is responsible for protein aging and complications of aging and diabetes, and is related to arteriosclerosis, nephropathy, neuropathy, retinopathy, and cataract.[2] The Maillard reaction is not a single reaction but a very complex network of reactions, in which various intermediates and multiple reaction steps are involved such as condensations, rearrangements, dehydrations, oxidations, Strecker degradation, and retroaldolizations.[3] Hodge first proposed an overall reaction scheme in 1953,[4] and his initial work started the research on the Maillard reaction. Because of the complexity of the Maillard reaction, current literature and textbooks only contain the overall reaction scheme and several initial reactions, while the middle and final polymerization stages are still not known. We tackle these issues by choosing glucose and glycine as reactants of our model reaction systems, combining various ^{13}C or ^{15}N labeling strategies, and performing multinuclear plus multidimensional advanced solid-state NMR techniques. It is the first time that not only standard cross polarization, but also various advanced solid-state NMR techniques are used to provide insights into the structures of melanoidins.

1.1.2 Soil organic matter

Air, water and minerals comprise more than 90 % of soil. The remaining less than 10 % is soil organic matter, which plays very important roles in the environment. It provides a nutrient source (e.g. N, S, P etc.) for growth of plants and soil biota. Soil organic matter retains a great deal of water, therefore it can exchange cations, help soil aggregation and prevent soil erosion. Soil organic matter is precursor of kerogens, peat, petroleum, coal etc., which are very important energy resources. Soil organic matter can also modify the toxicity of heavy metals, pesticides, and herbicides and affect water purification.[5] However, the characterization of humic substances, the majority of soil organic matter, is one of the most demanding challenges in modern analytical chemistry field. Many separation methods have

www.manaraa.com

been applied, but none of them has provided a definitive characterization [6]. In this dissertation, solid state NMR is used to extract valuable information about the structural features of soil organic matter for central Iowa.

1.1.3 Detonation nanodiamond

Nanometer scale diamonds have large and sometimes functionalized surfaces, which become more dominant with decreasing particle size. Nanodiamond is of interest not only for the basic understanding of carbon allotropes, but also for its potential applications in biomedicine, nanotechnology, surface chemistry, catalyst chemistry, and material science. The size of nanodiamond particles is often around ~ 5 nm with a very narrow size distribution.[7] It has been verified that nanodiamond with diameters of less than 5 nm is more stable than graphitic particles.[8, 9] The relative stability of diamond and graphite is dependent on the particle size due to the internal pressure caused by surface curvature and stress.[10]

The structure of detonation nanodiamond is still under debate. Several structural models have been proposed based on either experimental or theoretical investigations, e.g. the onion-shell model,[11] buckyball structural model,[12] hollow center structural model,[13] etc.. Furthermore, the distribution of paramagnetic centers and their origin are also interesting.[12] ^{13}C solid-state NMR is a suitable technique for studying detonation nanodiamond not only because of the presence of bulk carbon, but also the sensitivity of ^{13}C relaxation times to paramagnetic ions.

1.1.4 Sugar modified TiO_2 photocatalyst

TiO_2 has become an extremely promising photocatalyst for the following reasons: (1) it is relatively inexpensive; and (2) highly stable chemically; (3) the photogenerated holes are highly oxidizing; and (4) the photogenerated electrons are highly reductive to produce superoxide. Besides solar energy conversion, application of TiO_2 in environmental cleanup has been one of the most active areas of research. Air or water purification, sterilization of medical devices, food preparation surfaces, sanitaryware surfaces, self-cleaning paints and window panels, and cancer therapy[14] have been considered. All of these applications are

www.manaraa.com

based on the total destruction of organic compounds or bacteria via oxidation or reduction by the electrons or holes, after photo-excitation of TiO_2. However, due to its large band gap of 3.0-3.2 eV, the photocatalytic efficiency of TiO_2 under visible light is very low. Meanwhile, the recombination of electrons and holes retards its efficiency further. Therefore, modifications of TiO_2 to facilitate the photocatalytic degradation of organic compounds under sunlight have attracted extensive attentions.

Carbon modified TiO_2 has been found to be an active photocatalyst under visible light.[15-17] For example, sugar modified–n-TiO_2 gave a 13-fold increased initial rate of the photodegradation of 4-chlorophenol compared to those by regular n-TiO_2, whereas tetrabutylammonium hydroxide modified-n-TiO_2 increased 8-fold.[18] In order to understand how sugar carbon is incorporated into the TiO_2 nanocrystal, we have applied advanced solid-state NMR techniques to TiO_2 processed with $^{13}C_6$-glucose.

1.2 Solid state NMR in the studies of carbon containing materials

Because the nucleus can feel various local fields (i.e. chemical shifts, J-couplings, dipolar and quadrupolar interactions etc.), NMR has become a very important research tool in structure elucidation, monitoring of dynamics (e.g. conformation changes, binding dynamics), orientation and morphology studies.[19] In addition the weak interaction energy of radio-frequency pulses makes NMR a non-destructive analytical tool. NMR has been applied in biology, chemistry, materials, food, environmental science, medicine, and various industries. In our group, we focus on developing and extending the applications of solid state NMR techniques. This thesis mainly deals with spin 1/2 nuclei e.g. ^{13}C, ^{15}N and ^{1}H, at a magnetic field of 9.4 T.

In order to study carbon-containing complex organic matter, various advanced solid state magic angle spinning NMR experiments have been applied, including (1) ^{1}H-^{13}C / ^{15}N cross polarization,[20] which directly detects dilute nucleus with large chemical shift spread (~ 300 ppm), simultaneously borrows the polarization and fast relaxation rate from abundant nuclei ^{1}H which are favorable because of the large gyromagnetic ratio and strong homonuclear dipolar interaction; (2) ^{13}C direct polarization (DP) at high spinning speed, which gives

www.manaraa.com

quantitative intensity ratios without differential protonation bias. The necessary recycle delays are determined by running CP/T_1/TOSS experiments first.[21] (3) Spectral editing techniques such as CH [22] or CH_2 [23] selection; spectra of quaternary-C can be obtained by using gated decoupling before detection. In order to avoid phase distortion, a Hahn echo has to be used. Based on their different electronic symmetry, sp^2- and sp^3- hybridized C can be distinguished via chemical shift anisotropy dephasing experiments.[24] Different types of carbon, therefore, can be spectrally separated, which gives fundamental insights into structure. (4) Spin-lattice and spin-spin relaxation time as well as chemical shift anisotropy measurements[24] enable distance analysis in detonation diamond based on their strong dependence on the distance between carbon and the paramagnetic centers. The CSA measurement is also used in sugar modified TiO_2 study, where the CO_4 of C-TiO_2 is characterized experimentally in its first time. (5) Dipolar recoupling based on REDOR[25] is essential in various pulse programs. In our melanoidin study, ^{13}C-^{15}N REDOR has been extensively used for structure elucidation. HARDSHIP[26] is a novel H-X distance measurement technique developed in our group. It cleverly terminates the spin diffusion effect before it becomes significant, and thus can provide more accurate distance simulation results. We have applied it to detonation nanodiamond samples for estimating the thickness of disordered carbon layers. (6) The solid echo has been exploited for distinguishing ^{13}C-^{13}C spin pairs from isolated ^{13}C in our ^{13}C labeled samples, such as melanoidins and sugar modified TiO_2. (7) Multidimensional techniques, such as ^{1}H-^{13}C FSLG-HETCOR,[27] SUPER,[28] 2D exchange experiments, ^{13}C-$^{15}N\{^{1}H\}$ HSQC, and 3D experiments of ^{13}C-^{13}C exchange with ^{13}C-^{15}N HSQC have been performed for structural elucidation of melanoidins which are ^{13}C and ^{15}N labeled.

1.3 Outline of this thesis

Although the samples we studied are quite varied, carbon atoms are their common elements, and play a key role in their structures and functions. There are numerous open questions in their research and applications. Solid-state NMR techniques demonstrate their powerful capabilities on their structural elucidation.

Chapter 2 gives background on the various materials studied.

www.manaraa.com

Chapter 3 describes solid-state NMR techniques. First we start with the basic concepts; then the reasons for us to use solid-state NMR techniques are given, followed by the introduction of several local interactions, i.e. chemical shift and chemical shift anisotropy interactions, J-coupling, dipolar interaction; in the last section, frequently used solid-state NMR techniques and pulse sequences are discussed in some detail;

Chapter 4 focuses on the fate of glycine after the Maillard reaction;

Chapter 5 discusses the major units in the melanoidins formed by sugar;

Chapter 6 discusses complex N-containing structures in melanoidins, which form links between sugar and glycine in melanoidins;

Chapter 7 presents NMR results of soil organic matter, where spectral editing and direct polarization for quantitative measurements are the main techniques used;

Chapter 8 demonstrates solid-state NMR of detonation nanodiamond, and a structural model with paramagnetic centers is proposed;

Chapter 9 presents solid-state NMR characterization of ^{13}C-glucose modified TiO_2 photocatalyst;

Chapter 10 summarizes the structural and dynamics results for the various materials studied in this thesis.

References

1. Nursten, H., *The Maillard reaction: chemistry, biochemistry and implications*. 2005; p 5-30.
2. Nagaraj, R. H.; Shipanova, I. N.; Faust, F. M. *J. Biolog. Chem.* **1996,** *271,* 19338-19345.
3. Martins, S. I. F. S.; Jongen, W. M. F.; Boekel, V. M. A. J. S. *Tre. Food Sci. Technol.* **2001,** *11,* 364-373.
4. Hodge, J. E. *J. Agric. Food Chem.* **1953,** *1,* 926-943.

www.manaraa.com

5. Stevenson, F. J., *Humus chemistry genesis, composition, reactions*. John Wiley & Sons, INC.: New York, 1994.
6. MacCarthy, P., *Humic substances structures, models and functions*. The Royal Society of Chemistry Cambridge, 2001.
7. Kruger, A.; Kataoka, F.; Ozawa, M.; Fujino, T.; Suzuki, Y.; Aleksenskii, A. E.; Vul, A. Y.; Osawa, E. *Carbon* **2005,** *43,* 1722-1730.
8. Badziag, P.; Verwoerd, W. S.; Ellis, W. P.; Greiner, N. R. *Nature* **1990,** *343,* 244-245.
9. Wang, C.; Chen, J.; Yang, G.; Xu, N. *Angew. Chem. Int. Ed.* **2005,** *44,* 7414-7418.
10. Zhao, D.-S.; Zhao, M.; Jiang, Q. *Diamond Relat. Mater.* **2002,** *11,* 234.
11. Aleksenskii, A. E.; Baidakova, M. V.; Vul, A. Y.; Siklitskii, V. I. *Phys.Solid State* **1999,** *41,* 668-671.
12. Raty, J. Y.; Galli, G.; Bostedt, C.; Buuren, V. T. W.; Terminello, L. J. *Phys. Rew. Lett.* **2003,** *90* 037401, 037401-037404.
13. Vereshchagin, A. L.; Yur'ev, G. S. *Inorg. Mater.* **2003,** *39,* 247-253.
14. Linsebigler, A. L.; Lu, G.-Q.; Yates, J. T. *Chem. Rev.* **1995,** *95,* 735-758.
15. Sakthivel, S.; Kisch, H. *Angew. Chem. Int. Ed.* **2003,** *42,* 4908-4911.
16. Cheng, Y.-P.; Sun, H.-Q.; Jin, W.-Q.; Xu, N.-P. *Chem. Engin. J.* **2007,** *128,* 127-133.
17. Savoskin, M. V.; Yaroshenko, A. P.; Lazareva, N. I.; Mochalin, V. N.; Mysyk, R. D. *J. Phys. Chem. Solids* **2006,** *67,* 1205-1207.
18. Xu, C.-K.; Killmeyer, R.; Gray, M. L.; Khan, S. U. M. *Appl. Cataly. B: Envir.* **2006,** *64,* 312-317.
19. Watts, A. *Nature Rev. Drug Disc.* **2005,** *4,* 555-568.
20. Schmidt-Rohr, K.; Spiess, H. W., *Multidimensional solid-state NMR and polymers*. Academic Press, INC: San Diego, CA, 1999.
21. Torchia, D. A. *J. Magn. Reson.* **1978,** *30,* 613-616.
22. Schmidt-Rohr, K.; Clauss, J.; Spiess, H. W. *Macromole.* **1992,** *25,* 3273-3277.
23. Mao, J.-D.; Schmidt-Rohr, K. *J. Magn. Reson.* **2005,** *176,* 1-6.
24. Mao, J.-D., Schmidt-Rohr, K. *Solid State Nucl. Magn. Reson.* **2004,** *26,* 36-45.
25. Gullion, T.; Schaefer, J. *J. Magn. Reson.* **1989,** *81,* 196-200.

www.manaraa.com

26. Schmidt-Rohr, K., Rawal, A., Fang, X.W. *J. Chem. Phys.* **2007,** *126,* 054701-054701-054716.

27. VanRossum, B. J.; Forster, H.; DeGroot, H. J. M. *J. Magn. Reson.* **1997,** *124,* 516-519.

28. Liu, S. F.; Mao, J. D.; Schmidt-Rohr, K. *J. Magn. Reson.* **2002,** *155,* 15-28.

www.manaraa.com

CHAPTER 2. Introduction and background

This chapter gives background information on the complex carbon containing materials investigated in this thesis, which have been studied using various techniques including spectroscopy techniques, mass spectrometry, chromatography, crystallography, microscopy, thermal treatment (i.e. TGA, pyrolysis), hybrid techniques, i.e. GC-MS, HPLC-MS, GC-MS-pyrolysis, and chemical synthesis.

2.1 Melanoidins

2.1.1 Chemistry of the Maillard reaction

The Maillard reaction occurs often in our daily lives when we cook food. It also occurs *in vivo*, and forms advanced glycation end products, which are linked to protein aging and aging related diseases such as diabetes, and cataract. The Maillard reaction is not a single reaction, but a very complicated reaction network between reducing sugar and amine compounds. In 1953, Hodge proposed an overall reaction scheme [1] for this complicated reaction network as shown in Figure 2.1. This reaction network can be divided into three stages. The initial stages are the sugar-amine condensation (A) followed by the Amadori rearrangement (B) through various enolization steps. At the intermediate stage, the sugar is dehydrated (C), or loss amine compounds along with sugar fragmentation (D). The sugars are further cyclized into heterocyclic aromatic rings such as furan and pyrrole. Meanwhile the amino acids react with α-dicarbonyl sugar compounds, so-called reductones, and go through the Strecker degradation (E), where the amino acid are broken into three pieces: the carboxyl carbon turns to carbon dioxide, the α-carbon to an aldehyde functional group, and the nitrogen becomes part of ammonia. The heteroatom aromatic compounds formed by the cyclization of sugar with or without the participation of amino acids are reported as highly potential agents for further polycondensation via aldol condensation (F) and aldehyde-amine polymerization (G). Melanoidins of high molecular weight are formed, but are poorly characterized.

www.manaraa.com

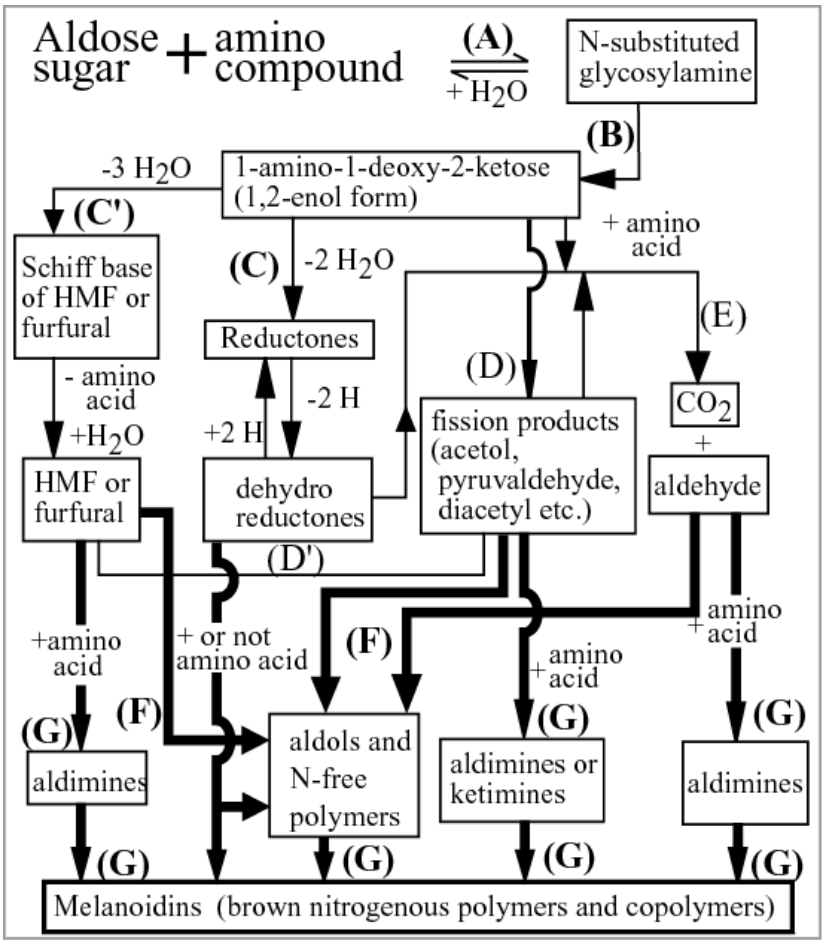

Figure 2.1. Hodge scheme of the Maillard reaction. The reactions occurring at the initial stage are (A) sugar-amine condensation and (B) Amadori rearrangement. The reactions are divided into intermediate stage as (C) Sugar dehydration, (D) sugar fragmentation and (E) the Strecker degradation of amino acid after reacting with the products of sugar dehydration. The final stage reactions are polycondensation steps including (F) Aldol condensation and (G) Aldehyde-amine polymerization. Melanoidins are there final products which involve multisteps and various reaction intermediates, and their structure is poorly characterized. (Figure adapted from [1])

The reactions at initial and intermediate stages are demonstrated in Figure 2.2 by using glucose as a representative reducing sugar. In these reactions, the N of the amine compounds, and the C1, C2 and C3 carbons of glucose show strong reactivity. For example, the N first attacks the glucose aldehyde C1 to form imines. Amadori rearrangement switches the double bond between C1-N to C2-O, followed by enolization, α-dicarbonyl compounds are formed. It can further switch the double bonds to C3-C4 or C4-C5 via subsequent enolization. Meanwhile, dehydration or de-amination occur simultaneously shown in (B) and (C). In (C),

www.manaraa.com

the 5,6-dihydroxy-2-oxohe-3-enal can go through 2,5-cyclization to form hydroxyl methyl furfural (HMF), where the glucose C1 and C6 still stay in their original aldehyde and methanol forms, respectively. In (E) when the N of the amine compound attacks C3 carbonyl groups in the 2,3-dicarbonyl sugar intermediate, the amine compound consequentially fragments into three pieces as $C1O_2$, -RHC2=O, and ammonia (Strecker degradation). And the C2 of the 2,3-dicarbonyl sugar intermediate is reduced to a hydroxyl group.

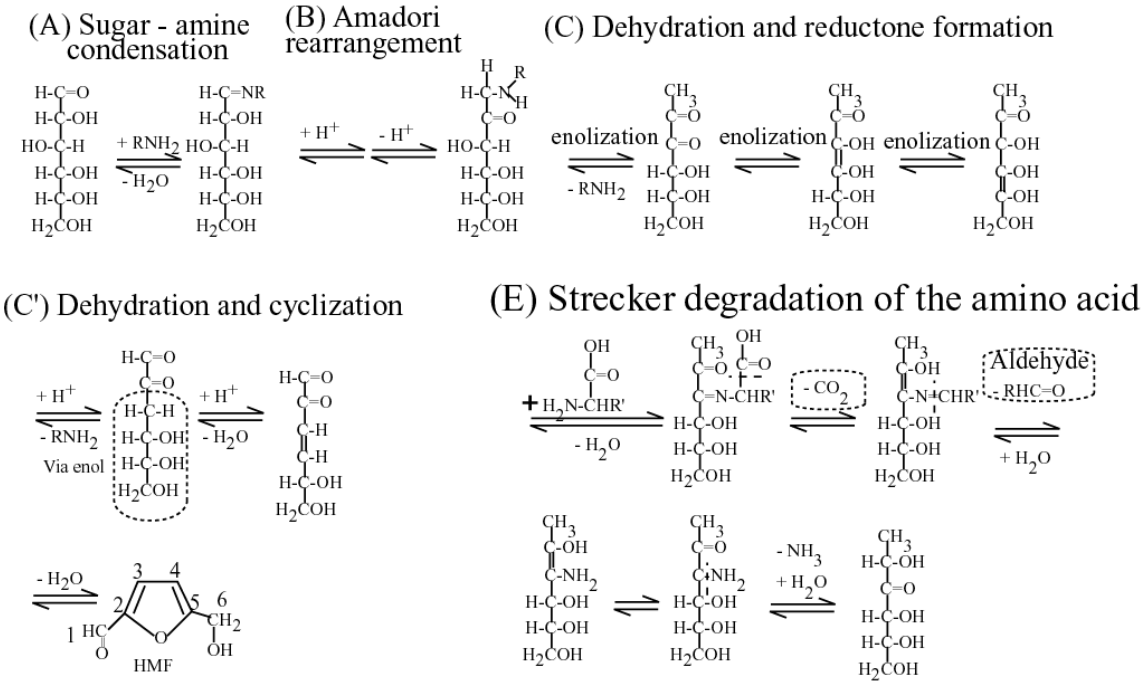

Figure 2.2. Some highly probable reactions at the initial and intermediate stages of the Maillard reaction network [2]. Glucose is used here as a representative sugar reactant.

The fragmentation of glucose, as shown in (D) in Hodge's scheme, with or without the participation of amino acids is shown in Figure 2.3 as proposed by Tressl in 1998. After catalysis by amine compounds, various sugar intermediates fragment through different mechanisms. For example, after the condensation between amine and hexoses, Amadori rearrangement, and sugar dehydration, the 3-deoxy-aldoketose intermediate (labeled as A) is formed and further undergoes C_1+C_5 fragmentation, the so-called α-dicarbonyl fragmentation labeled as (1) in Figure 2.3. Once intermediate A is formed, it could also consequently lose a second water molecule to form intermediate B named 3,4-dideoxy aldoketose, or enolize to

www.manaraa.com

β-dicarbonyl intermediate C. Therefore, various fragmentation intermediates can be formed. They fragment into either pentoses or tetroses by losing C1, C1+C2, or C6 carbons as $H_2C=O$. The fragmentation generated pentoses and tetroses further cyclize into 5-member heterocyclic aromatic rings (furans, pyrroles etc.) with various substituents as shown in Figure 2.3.

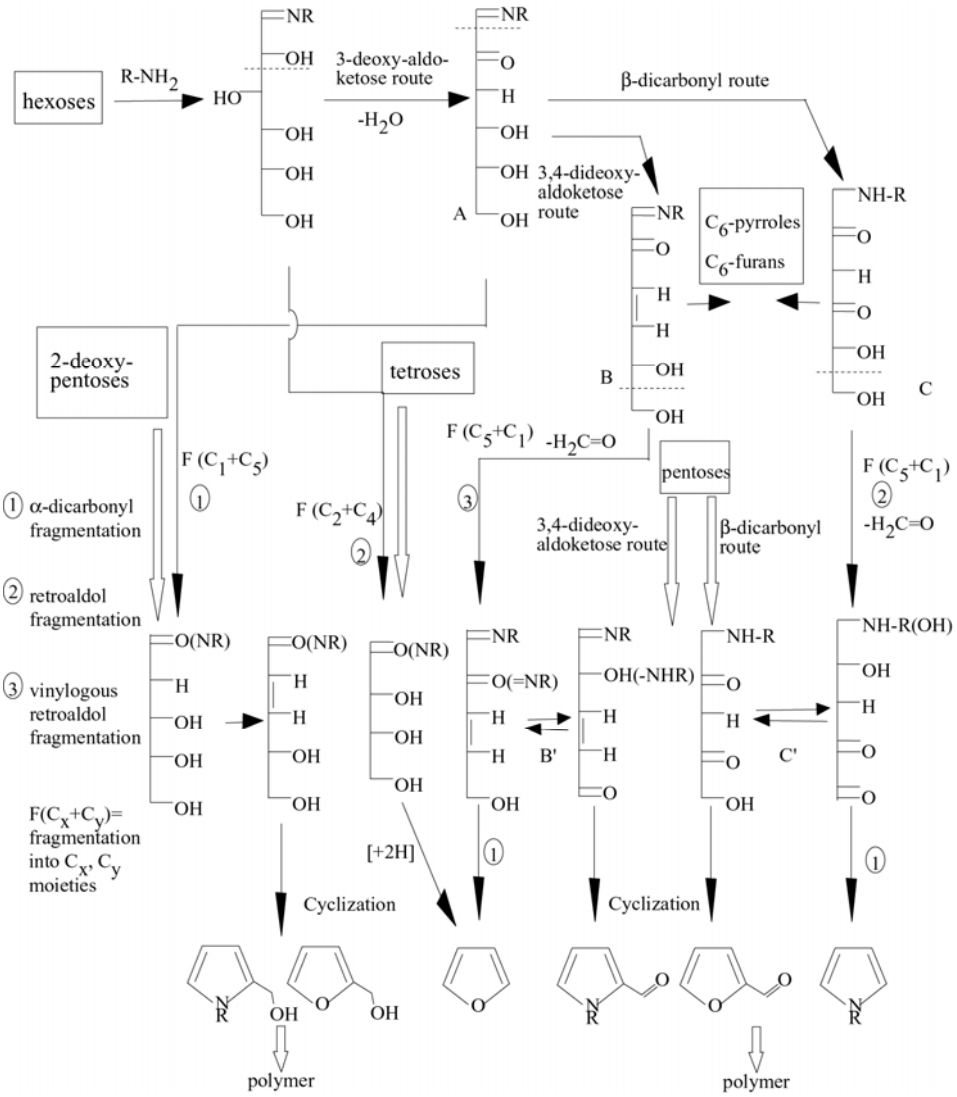

Figure 2.3. The various pathways of sugar fragmentation proposed by Tressl in 1998. Starting with hexose sugar, pentoses and tetroses are formed with the catalysis of amine compounds. The fragmentation could occur through α-dicarbonyl fragmentation (1), or retroaldol fragmentation (2) or vinylogous retroaldol fragmentation by involving different reaction intermediates. In most cases, C1 and C6 are detached from the hexoses. The fragmentation intermediates further cyclize into furan and pyrroles with different substituents (adapted from [3]).

www.manaraa.com

2.1.2 Mass percentages of different fractions from dry heating reaction

According the COST Action 919 (European cooperation in the field of scientific and technical research), the standard procedures of preparing melanoidins consist of six steps: (1) mix the reactants by dissolving them in distilled water and (2) freeze dry this mixture overnight. After (3) thermal treating the mixture for 2 h at 125 ^{o}C in a sealed oven, (4) dissolve the reaction products in distilled water and stir for 12 hours at 4 ^{o}C, then (5) filter the sample by using Whatman no. 4 filter paper; during this last step, the water-insoluble fraction is obtained. The remaining water-soluble fractions can be separated into high and low molecular weight fractions by (6) dialyzing them using dialysis tubing. In a study of the glucose-glycine reaction system following this standard procedure, the mass percentages of different fractions were measured by Hofmann et al. shown in Figure 2.4 [4].

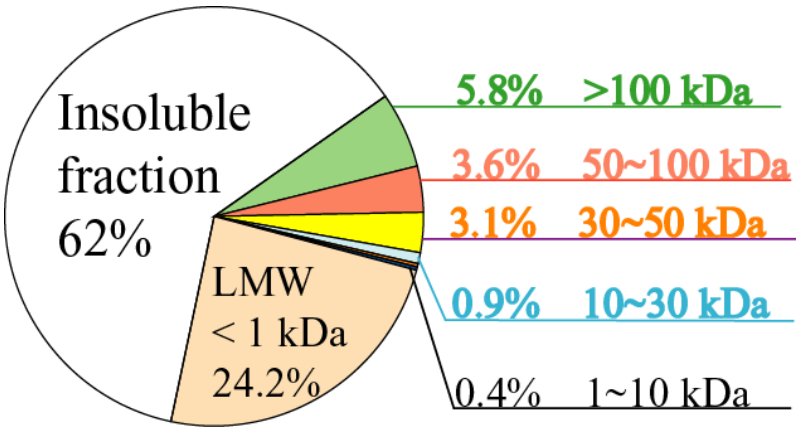

Figure 2.4. The mass percentages of different fraction products to the mass of reactants in the equal-molar glucose-glycine model system. The reaction was conducted following the COST action 919 standard procedure. 62% of reactants were converted to water-insoluble fraction (black pigment) with a molecular weight higher than 100 kDa. 24.2% are transformed into low molecular fraction with MWs of less than 1 kDa. The remaining 13.8% is the so-called higher molecular weight fraction. Among this fraction, only relatively small amount (~ 0.4 %) formed the molecules with MWs between 1 k Da to 10 kDa.

The water-insoluble fraction comprises the major black product accounting for about 62% of the products. The second most abundant products are low molecular weight compounds making up 24% of total mass. The mass percentage of the high molecular weight fraction with molecular weight greater than 1 kDa is around 13.8%. Among this HMW component, products with molecular weight between 1k and 30 kDa were found in

www.manaraa.com

comparatively low yields (about 1.3%). Although the volatiles are very interesting to study, they only account for less than 0.2% of total products.

In our glucose-glycine in 9 to 1 ratio model reaction system, the amount of water-insoluble fraction is much less than the amount in 1 to 1 ratio reaction sample. The HWM fraction has slightly increased amount.

2.1.3 Volatile Maillard reaction products

During the Maillard reaction, hundreds of volatile compounds (~ 0.2 % of total products by mass) are formed. The volatiles are relevant to the flavor and odor of foods, such as coffee, cocoa, malt and meat. GC-MS has become a workhorse in identifying these numerous volatile compounds. For example, half of the 950 volatile compounds known so far in coffee aroma are formed during the Maillard reaction. Furans, pyrroles, pyrazines, ketones, phenols, pyridines, oxazole derivatives, alkylthiazoles, alkyl-3-thiazolines have been identified with the substitutions of alkyl, alkenyl, acetyl, furanyl, or furfuryl groups [5]. Figure 2.5 shows the composition of roasted coffee flavors with the numbers of each identification.

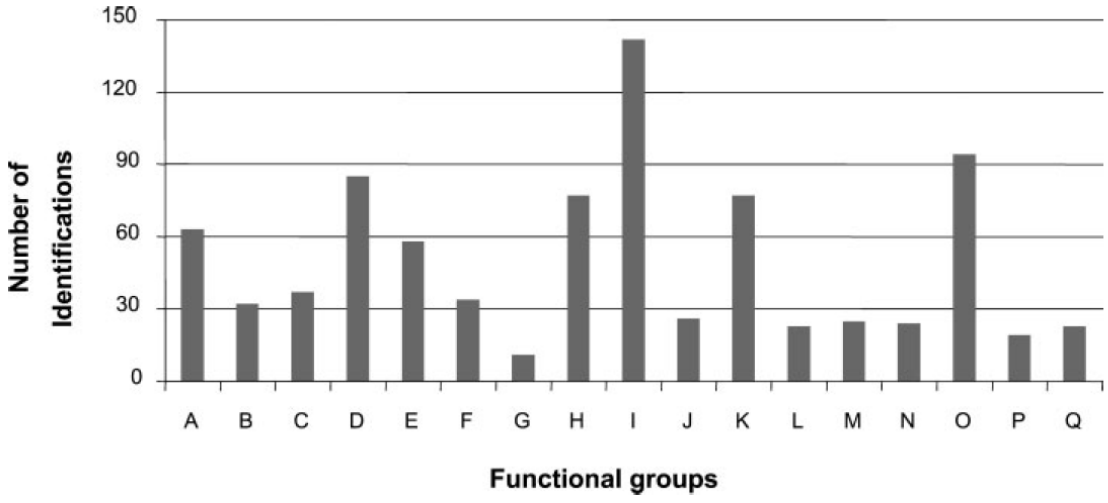

Figure 2.5. Composition of roasted coffee flavor sorted in different chemical categories. (A): Hydrocarbons, (B) alcohols, (C) aldehydes, (D) ketones, (E) acids, (F) esters, (G) lactones, (H) phenols, (I) furans-pyrans, (J) thiophenes, (K) pyrroles, (L) oxazoles, (M) thiazoles, (N) pyridines, (O) pyrazines, (P) miscellaneous N-containing compounds, (Q) misc S-containing compounds (adapted from [5]).

www.manaraa.com

2.1.4 Low molecular weight Maillard reaction products

The majority products in the Maillard reaction are colored nonvolatile compounds. The low molecular weight (LMW) products have molecular weights less than 1 kD. Chromatography, MS and solution NMR have been combined for the characterization of LMW products. Numerous structures, and their formation mechanism have been proposed. For instance, by combining NMR, LC/MS, UV and IR spectroscopy, many structures of chromophoric substances linked to brown color have been identified and their structures are shown in Figure 2.6. By taste dilution analysis, which uses the human tongue as a biosensor for flavor, several taste related compounds have also been identified, see Figure 2.6 (10) and (11).

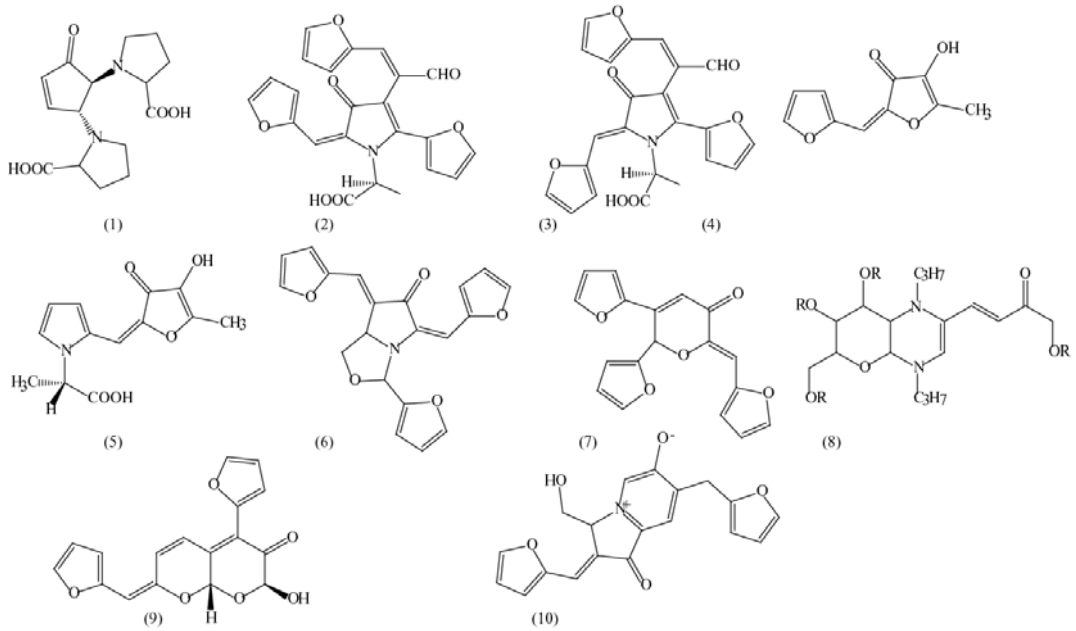

Figure 2.6. Examples of structures of several LMW substances formed during the Maillard reaction and identified by using various analytical methods, such as GC-MS, HPLC, UV, IR. (1) (*E*)-4,5-bis[(*S*)-2-carboxypyrrolidinyl]-2-cyclopenten-1-one;[6] (2) (*S*)-*N*-(1-carboxyethyl)-2(*E*)-(2-furyl- methylene)-4(*E*)-(1-formyl-2-furyl-1-ethenyl)-5-(2-furyl)-3(2*H*)-pyrrolinone; [6] (3) (*S*)-*N*-(1- carboxyethyl)-2(*Z*)-(2-furylmethylene)-4(*E*)-(1-formyl-2-furyl-1-ethenyl)-5-(2-furyl)-3(2*H*)-pyrrolinone; [6] (4) 2-[(2- furyl)-methylidene]-4-hydroxy-5-methyl-2*H*-furan-3-one;[6] (5) (*S*)-4-hydroxy-5-methyl- 2-[(*E*)-*N*-(1′- carboxyethyl)-pyrrolyl-2-methylidene]-2*H*-furan-3-one; [6] (6) (2*R*)-4-oxo-3,5-bis[(2-furyl) methylidene]-tetrahydropyrrolo[1,2-*c*]-5(*S*)-(2-furyl)oxazolidine and its 5(*R*)-(2-furyl)oxazolidine isomer;[6] (7) (*Z*)-2-[(2- furyl)-methylidene]-5,6-di(2-furyl)-6*H*-pyran-3-one[8]; (8) [(4a*S*,6*R*,7*S*,8*R*,8a*R*)-4,-4a,6,7,8,8a-hexahydro- 7,8-dihydroxy-6-hydroxymethyl-1,4-dipropyl-1*H*-pyrano[2,3-*b*]pyrazine-2-yl]-1-hydroxy-3-buten-2-one;[9] (9) bitter-tasting quinizolate; (10) capsaicin-like compound.[10]

www.manaraa.com

2.1.5 Structures of (HMW plus insoluble fractions) of melanoidins

Melanoidins are high molecular weight, brown colored products of the Maillard reaction. They are the predominant products, accounting for ~ 75 % of total products by mass.[4] Melanoidins remain interesting in various fields, e.g. food nutrition, toxicology, metabolism during ageing and diabetes. Although they are the predominant product of the Maillard reaction, their structures have remained unknown because of their high heterogeneity. The following three main structural models for melanoidins have been proposed:

(1) Melanoidins form via polycondensation reaction, the repeating unites are furans and/or pyrroles;

(2) Through crosslinks with larger molecules, e.g. crosslink free amine group of lysine in protein, LMW structures become large coloured melanoidins;

(3) The backbones of melanoidins is mainly built up from sugar degradation produces during the early stages of the Maillard reaction, linked by polymerization and amino compounds.[2]

In our model Maillard reaction studies, there are larger proteins or peptides present, so the second structure proposal can be excluded, although it is very possible in food or living organisms.

Due to the high polymerization potential of five-member heteroatom aromatic rings, such as furans, and pyrroles shown in Figure 2.3, Tressl et al proposed a structural model for melanoidins shown in Figure 2.7. In this model, the major structural units are furan and pyrrole rings with most nitrogen joining the pyrroles. The backbone of the amine compound remains intact. This model shows high aromaticity, and highly substituted short alkyl chains and olefin carbons. Pyrolysis followed by GC-MS indicates besides pyrrole and furan, there are also other types heterocyclic aromatic rings present, such as oxazoles, pyridines, pyrazines shown in Figure 2.8.

www.manaraa.com

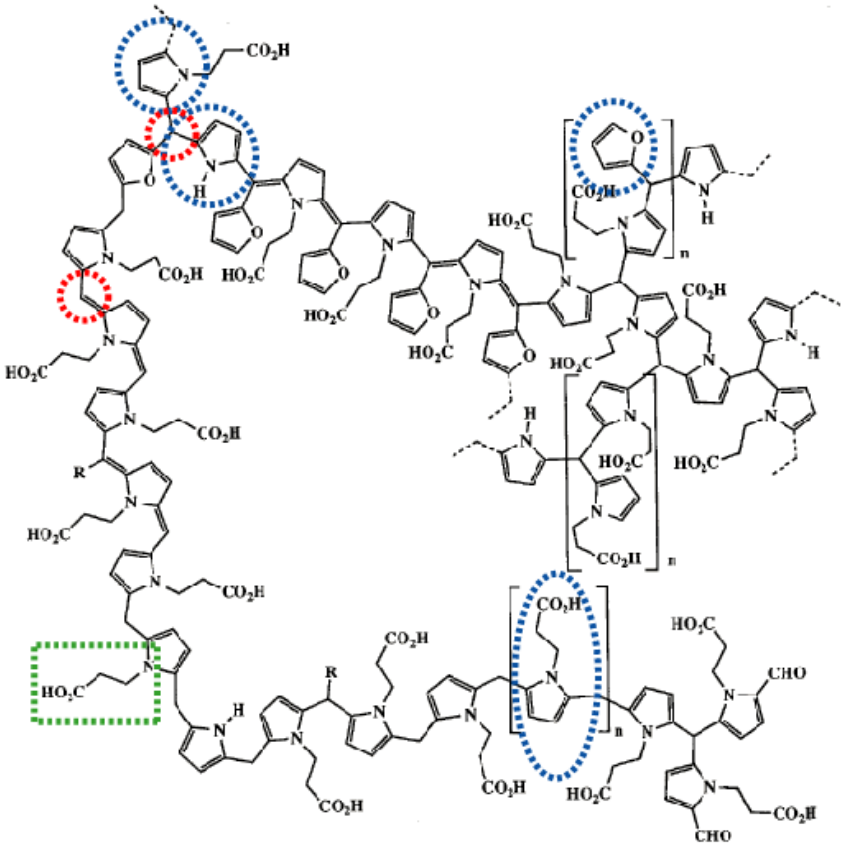

Figure 2.7. Structural model of melanoidins proposed by Tressl et al. in 1998.[3] In this model, pyrrole and furan are their major structural units connected through highly branched short alkyl chain or olefin chain. The backbone of amine compound remains intact, and the amine compounds are incorporated into the pyrrole rings via reactions between sugar carbons and the nitrogen of amine compounds. (adapted from [3])

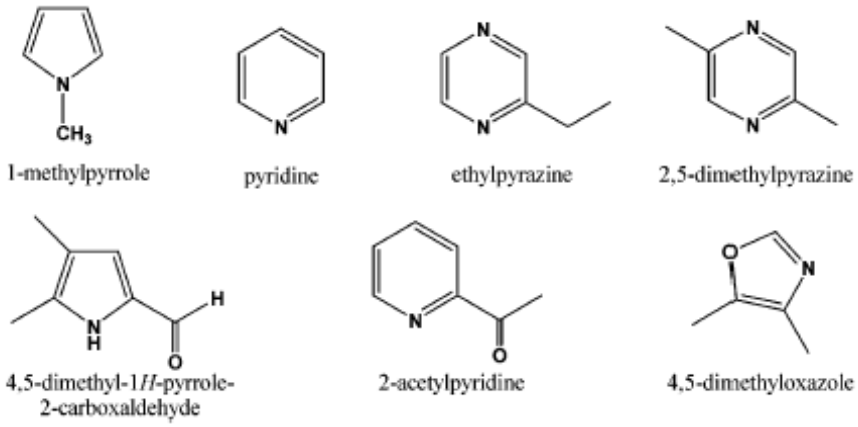

Figure 2.8. Some potential aromatic heterocycles from the pyrolysis of model melanoidins made from glucose-glycine reactants system in dry reaction condition. The structures are determined by GC-MS. (Adapted from [11])

www.manaraa.com

2.2 Soil organic matter

Air, water and inorganic mineral comprise more than 90% of soil. The remaining <10% is soil organic matter. Soil organic matter can further be divided into two categories: humic substances and nonhumic substances. The differences between them are whether they are chemically recognizable or not. If organic matter is chemically recognizable, it belongs to nonhumic substances, e.g. carbohydrates, amino acids, proteins, peptides, fats, waxes, resins, organic acids, organic alkanes, organic bases, lignin, etc in soil.

While nonhumic substances are chemically distinguishable, the humic substances are extremely complex and their characterization is one of the most demanding challenges in modern analytical chemistry. Many separation methods have been applied to its study, but none of them can provide a definitive characterization. In this dissertation, solid state NMR will be used to extract valuable information about their structural features.

Soil organic matter plays very important roles to the earth and environments. It provides nutrient source (e.g. N, S, P etc.) for plant growth. Soil biota feed on them. Soil organic matter retains a great deal of water, and it has a large cations exchange capacity, which helps soil aggregation and prevents soil erosion. Soil organic matter is a precursor of kerogens, peat, petroleum, coal etc., which are very important energy resources. Soil organic matter can also modify the toxicity of heavy metals, pesticides, and herbicides and can affect water purification.

Based on the solubilities of humic substances, humic substances can be divided into three fractions. They are: (1) fulvic acids, (2) humic acids, and (3) humin. Fulvic acids can dissolve in both acidic (e.g. HCl) and alkaline (e.g. NaOH) solutions. They contain both acidic and basic functional groups, and their molecular weight is less than that of humic acids. Humic acids can only dissolve in alkaline solutions. They contain acidic functional groups, e.g. carboxylic and phenolic groups. It is dark, amorphous organic matter. Humin is insoluble in both acidic and alkaline solutions. They are a black, high molecular weight fraction and contain the highest carbon content.

www.manaraa.com

2.3 Detonation Nanodiamond

In the preceding sections, we discussed the great structural diversity of carbon in organic compounds (melanoidins and soil organic matter), in which carbon forms covalent bonds with C, O, H, N. In this section, the allotropes of pure carbon will be reviewed briefly, followed by the introduction of detonation nanodiamond and its applications.

2.3.1 Allotropes of carbon

Allotropes of carbon have received intensive attention because of their inherited physical fascination and the associated applications of biomedicine, new materials, electronics, and energy research. Carbon atoms can arrange themselves into different hybridized chemical bonds and therefore can exhibit very different physical and chemical features, such as diamond and graphite. They are two well-known allotropes of carbon in nature, where carbons arrange themselves in sp^3 or sp^2 chemical bonds, respectively. Diamond has unmatched hardness; it is a good electronic insulator, but a good conductor of heat, and also chemically inert; while graphite is semiconductor and can be oxidized by oxidizers. With the development of new detection techniques and prediction theories, many other types of allotropes of carbons have been found or synthesized. Figure 2.9 gives their representative stick-ball structural models.

(a) Diamonds are transparent crystals with cubic lattice structure shown in Figure 2.9 (a). Since each atom bonds to four others tetrahedrally to form a 3-dimensional network under high pressure, the density of diamond ranges from 3.15 to 3.53 g/cm³ (depending on the purity), almost twice the density of graphite. At pressures above 60 kbar, diamond is the thermodynamically stable form of carbon [12, 13]. Diamond can be converted into graphite at low pressure, i.e. above 1500 ^{o}C under vacuum, where the graphite is a stable form of carbons. At ambient conditions, the conversion from diamond to graphite is undetectable. Due to the strong C-C bonds, diamond has a Mohs hardness of 10, harder than any other known substance. Lonsdaleite is also called hexagonal diamond due to the graphitic hexagonal crystal structure shown in Figure 2.9 (c). It is formed from graphite due to the strong impact forces during the short moment of meteorites hitting the earth.

www.manaraa.com

(b) Graphite is composed of sp^2 carbon forming an infinite planar layer ideally. Within a layer, each carbon atom is chemically bonded to three other carbons by using $2p_{x/y}$ hybridized orbital, and the un-hybridized $2p_z$ orbital of each carbon together forms delocalized π bonds and results in fused stable hexagonal rings formation; weak van der Waals forces keep layers stacked on each other at 3.354 Å distance, as shown in Figure 2.9 (b). At room temperature, graphite is more stable than diamond because of the presence of π clouds.

(c) Fullerenes have a similar hexagonal planar ring structure as graphite and pentagonal or sometimes heptagonal rings to bend these hexagonal rings into different shapes with positive or negative curvatures. Fullerenes have several varieties based on their shapes, such as buckyball in spherical shapes with hollow center; buckytubes with cylindrical symmetries; nanobuds combining features of both buckyball and buckytubes; and graphene with a planar fullerene sheet.

(d) Amorphous carbon is neither graphite nor diamond, although it is comprised of both sp^2 and sp^3 hybridized carbon without long-distance ordering. However, on the nanometer scale, they show polycrystalline or nanocrystalline features of graphite or diamond. They contain a high concentration of dangling bonds, which can result in a distribution of inter-atomic distances and bond angles.

(e) Glassy carbon only contains sp^2 hybridized carbons, made from polymer pyrolysis with the carbon retaining the original morphology. In contrast to the soft graphite, glassy carbon is hard and brittle with glassy-like appearance. It has two-dimensional structure without dangling bonds, which makes glassy carbon different from amorphous carbon. High temperature resistance, extreme resistance to chemical attack and impermeability to gases and liquids make glassy carbon widely useful as an electrode material in electrochemistry as well as crucibles.

There are also several exotic allotropes of carbon, such as aggregated diamond nanorods, carbon nanofoam and linear acetylenic carbon. These new materials contain advantageous

www.manaraa.com

features and have potentially useful applications in nanotechnology, electronics, optics and other fields of materials science.

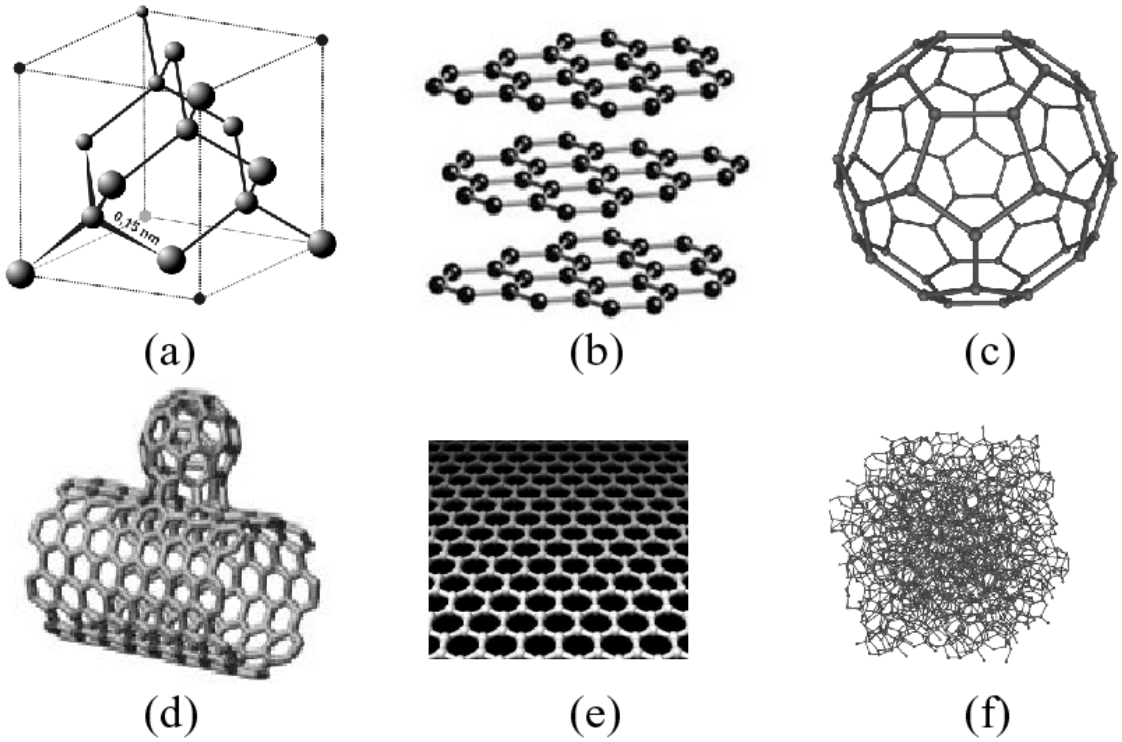

Figure 2.9. Some allotropes of carbon: (a) diamond; (b) graphite; (c) fullerenes C60; (d) buckybud (buckyball + buckytube); (e) graphene; (f) amorphous carbon.

2.3.2 Detonation method of producing nanodiamond

Nanometer scale diamonds have a large and sometimes functionalized surface area, which becomes more dominant with the decreasing of the size of particle. Combined with the unique lattice structure of diamond, nanodiamond is not only interesting for the basic understanding of the allotropes of carbon, but also for their potential applications in biomedicine, nanotechnology, surface chemistry, catalyst chemistry and new materials science.

Detonation is an effective method to produce large amount of nanodiamond. Detonation nanodiamond synthesis includes the following steps: charging organic explosive such as TNT into a sealed metal chamber; followed by depleting oxygen either by CO_2 or argon gas;

www.manaraa.com

and igniting the explosives electrically. The pressure and temperature suddenly increases to a regime shown in Figure 2.10 as a shadowed area, during the short moment of detonation of explosives (seconds). The incompletely combusted organic explosive delivers carbon atoms at high pressure and those carbon atom crystallize into diamond with size not beyond 10 nanometers due to the limited crystallization time at suitable conditions. After detonation, pressure drops quickly, while temperature decreases slowly unless coolants are provided. The incomplete combustion of the organic explosive also produces CO_2, CO, N, water and debris of metal from the chamber of reactor. In order to optimize the nanodiamond growth conditions, cooling rates around 3000–4000 K min^{-1} [14] are used to reduce the transition from sp^3-hybridized C in diamond to sp^2 –hybridized C in graphite.

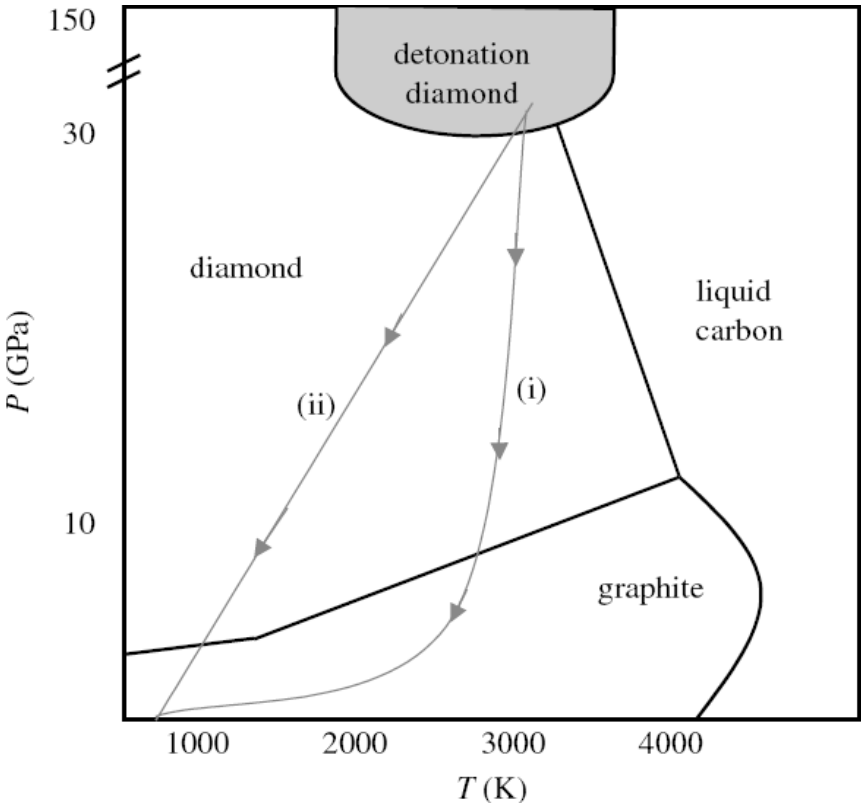

Figure 2.10. P-T phase diagram of carbon. The conditions for detonation diamond synthesis is the shadowed region at the top of this diagram. (i) Slow cooling of the detonation products and (ii) fast cooling P-T conditions, which can facilitate diamond formation instead of conversion to graphite in situation (i) (adapted from [14]).

www.manaraa.com

After detonation, nanodiamond is embedded in a matrix of amorphous carbon and graphite. Therefore, rigorous purification is needed to remove nondiamond materials, such as sp^2 carbon and metallic impurities. A schematic of the purification processes of detonation nanodiamonds is shown in Figure 2.11.

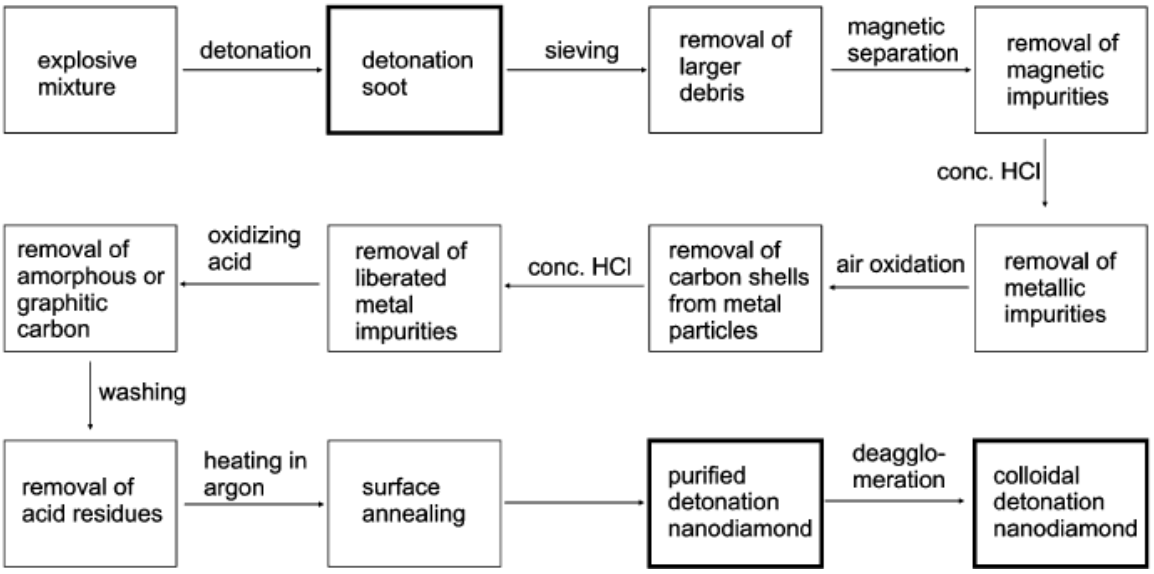

Figure 2.11. Standard procedures for purification of industrial detonation nanodiamond (adapted from [15]).

After detonation, the larger debris is removed via sieving. Magnetic separation is used to get rid of magnetic impurities. After the first two physical steps, concentrated HCl solution and air oxidation are used to remove some metallic impurities. Oxidizing acid, such as HNO_3, is often applied to dissolve away some amorphous or graphitic carbon components.

In order to obtain nearly purified detonation nanodiamond, a bead-milling technique was invented in Ōsawa's lab [16]. 30 μm zirconia balls are used to destroy amorphous structures inside agglutinate therefore disintegrate nanodiamond particles. During milling, generation of a graphitic layer may occur and can be removed by heating with concentrated NaOH solution. The schematic procedure is shown in Figure 2.12.

www.manaraa.com

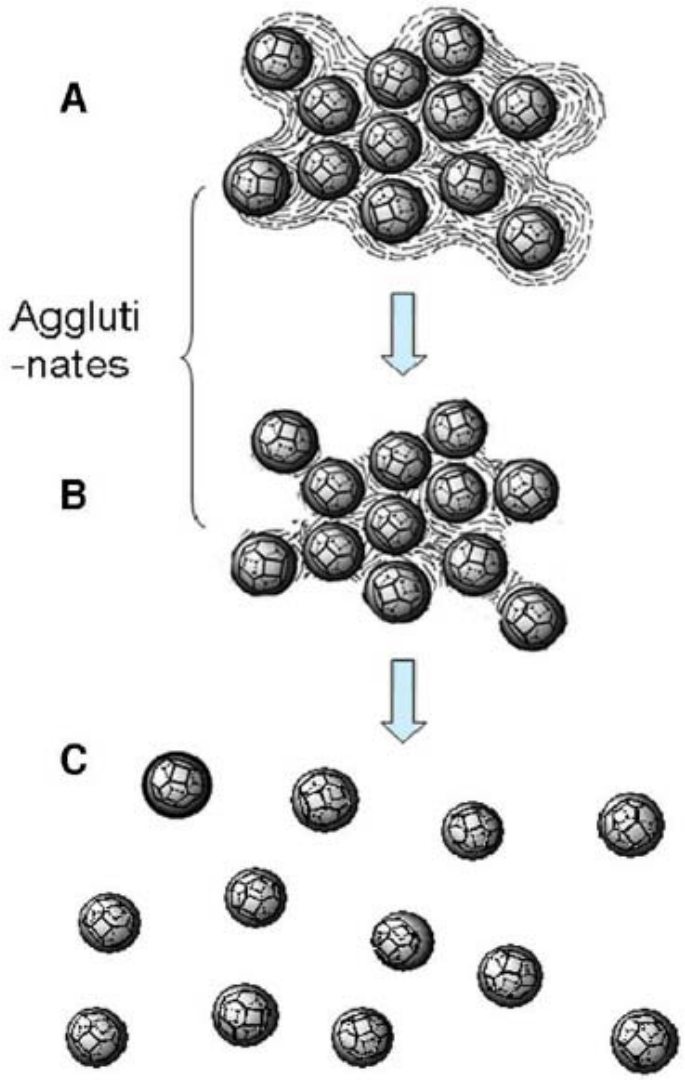

Figure 2.12. Tight agglutinate of detonation nanodiamond (A) was treated with hot-nitric acid and the graphitic carbons near the surface of the agglutination can be removed, however, the inside graphitic carbons remain as shown in (B). Milling between micro-beads can destroy amorphous structure via physical impaction, and disperse nanodiamond into individual particles.

2.3.3 Characterization of detonation nanodiamond

After purification of using oxidizing acids, XPS shows that nanodiamond mainly consists of carbon, but also contains 10-20% oxygen, 2-3% nitrogen [14], as well as some trace amount of metal contaminants. The small amount of nitrogen may originate from the explosives. The trace amount of metal is from the wall of the detonation reactor. The oxygen may be introduced during oxidizing acids treatments. Figure 2.13 (a) shows the transmission

www.manaraa.com

electron microscope (TEM) image of commercial 5 nm detonation nanodiamond powder. Chemical bond formation on the inter-particle surface may be the cause of the agglomeration of nanodiamond powder. Figure 2.13 (b) shows another structural model of the agglomerates of detonation nanodiamond, different from the one shown in Figure 2.12. The acidic functional groups on the surface in Figure 2.13 (b) may come from the modifications of surface carbon during oxidizing acid purification.

The diameter of nanodiamond particles is often around ~ 5 nm, and with a narrow size distribution.[17] The likely reason is the limited crystallization time in the suitable pressure and temperature region shown in Figure 2.10 during or after detonation of the explosives, in which the pressure is sufficient for the compact sp^3 network growth. In theoretical calculation,[18-20] it has been verified that nanodiamond with diameters of less than 5 nm is more stable than graphitic particles, and the stability is dependent on the size of the carbon cluster due to the internal pressure caused by surface stress and the curvature of nanoparticles.[21] Detonation nanodiamond particles commonly have a round shape, which is related to the isotropic growth of the particles and the more active reactivity at tips and steps.[15]

Several structural models for detonation nanodiamond have been proposed based on experimental results or theoretical calculations. For example, Figure 2.14 (a) shows a commonly accepted onion-shell model with a crystalline diamond core coated by a fractal structure formed from graphite-like platelets. Figure 2.14 (b) shows another structural model for 5-nm diameter detonation nanodiamond based on large-Q neutron diffraction, in which the core contains only sp^3 bonded diamond carbons. In order to gradually terminate the sp^3 bulk carbon network, several distorted or strained diamond carbon layers, which are surrounded by non-crystalline carbon with a mixture of sp^2 and sp^3 carbons, are proposed to be present, and with the surface oxygen-terminated surface. The compressibility experiments show a strong evidence of the presence of distortion of the diamond lattice in the surface shell of nanodiamond powder [22]. The outer shell of nano-size diamond has a much higher compressibility than bulk diamond while the grain core shows a lower compressibility.

www.manaraa.com

(a)

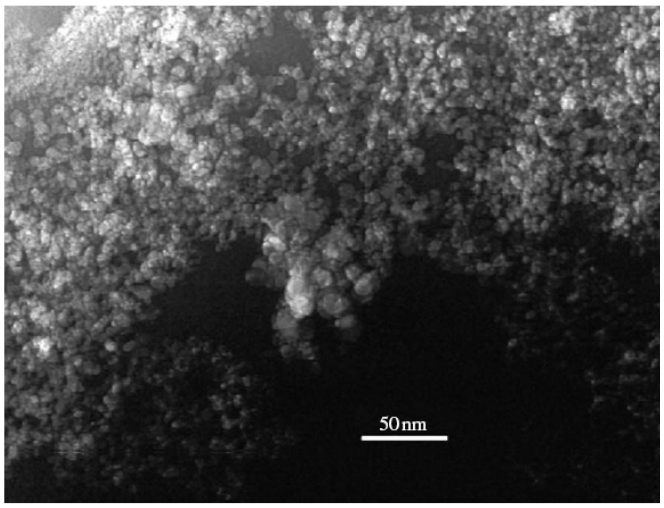

(b)

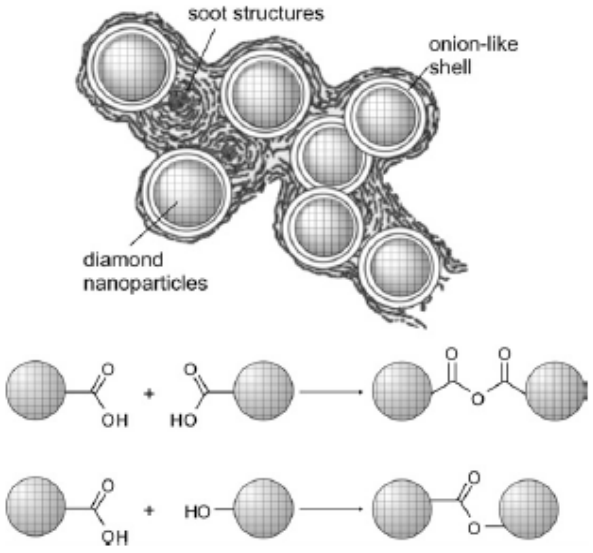

Figure 2.13. TEM image of commercial detonation nanodiamond, which shows that the particles aggregate up to several micrometers in dimension ((a) is adapted from [14]; and (b) is an aggregate model, in which the primary nanodiamond crystalline spheres embed in soot to form tight aggregates (adapted from [15]).

Raty et al. applied *ab initio* calculations using density functional theory (DFT) to reconstruct nanodiamond and led to a new family of carbon clusters: bucky diamonds shown in Figure 2.15 (b) [23]. The simulation results for this bucky diamond agree with pre-edge

www.manaraa.com

features observed in measured X-ray absorption spectra of detonation nanodiamonds shown in Figure 2.15 (a).

Detonation nanodiamonds have also been investigated by Shames via EPR, ^{13}C NMR and TEM [26]. The concentration of paramagnetic centers is around 10^{20} spin/gram, which was attributed to dangling bonds on the surface of the nanoparticles. NMR shows short spin-lattice relaxation times of ~ 150 ms due to the interaction of paramagnetic centers with the carbons. The line shapes of ^{13}C NMR also supports that the surface is different from bulk carbon core.

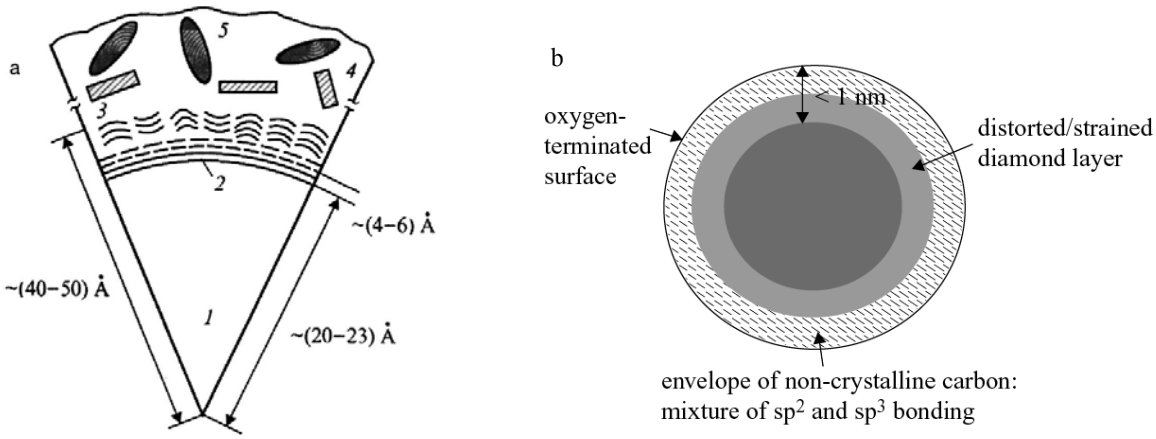

Figure 2.14. (a) Onion structure model of detonation nanodiamond after hot nitric acid oxidization [24]. In this model, 1-diamond core with perfect diamond lattice; 2- onion like sp^2 shell surround the diamond lattice core; 3-nanosized graphite platelets; 4-graphite particles; 5- metal-oxide inclusions. (b) Another very similar structural model of 5 nm detonation nanodiamond, the figure is not drawn to scale. In this model, nanodiamonds have a pure sp^3 hybridized diamond core and gradually distorted outer layers and some non-crystalline layers, and finally terminated with oxygen containing function groups [25]. This surface feature facilitates multiple applications based surface modifications.

2.3.4 Surface chemical modification of detonation nanodiamond

In order to increase the solubility of detonation nanodiamond in various solvents, preventing agglomeration, and introduce surface functionalities for applications in various fields, surface modifications of this material have become a focus in terms of the applications of detonation nanodiamond.

www.manaraa.com

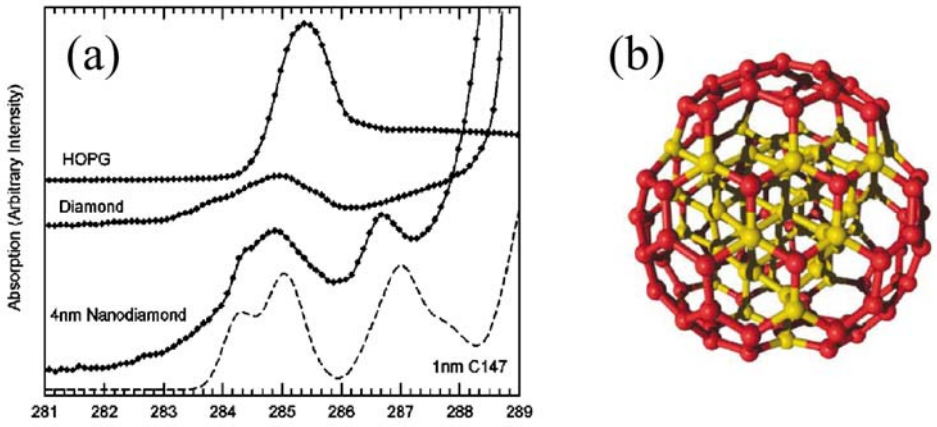

Figure 2.15. (a) The pre-edge of X-ray-absorption spectroscopy (XAS) spectra of graphite (HOPG), diamond, and 4 nm detonation nanodiamond. The 4 nm nanodiamond powder spectra differs significantly from those of both diamond and graphite. The computed density of unoccupied states (dashed line) of the 1 nm, fully reconstructed, C147 cluster is shown for comparison. The pre-edge peaks are the signature of a mixture of pentagons and hexagons on the reconstructed surface of the diamond core shown in (b). (adapted from [23])

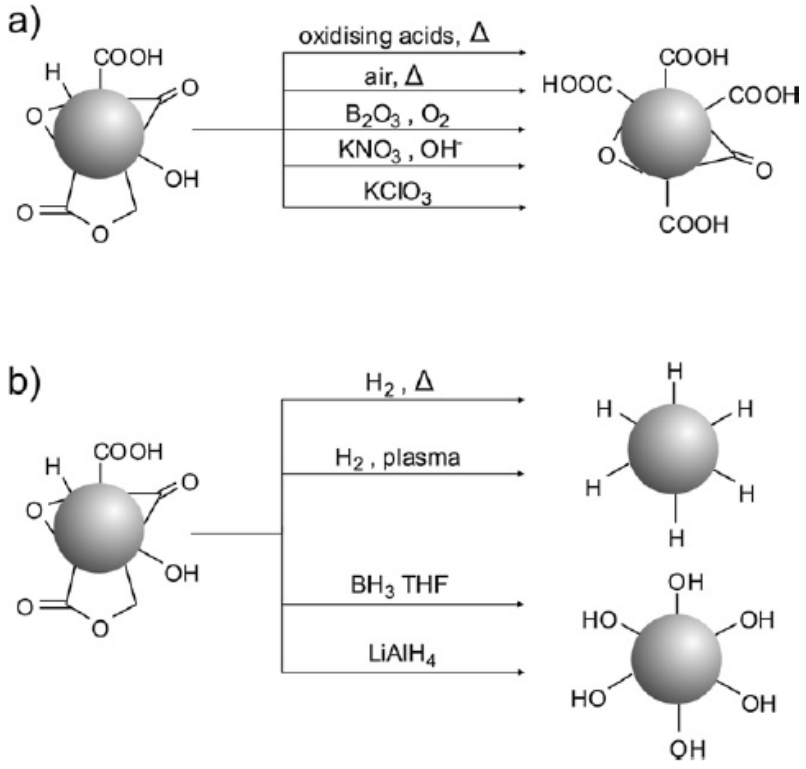

Figure 2.16. Homogenization of the surface of nanodiamond can be performed by using (a) oxidative or (b) reductive methods (adapted from [15]).

www.manaraa.com

Oxidizing acids or other compounds at elevated temperature (e.g. nitric acid or KNO_3, $KClO_3$), oxygen air with heating, or boric oxide in a oxygen atmosphere have been applied to homogenously oxidize the surface of detonation nanodiamond and result in, i.e. carboxyl, oxidized function groups, see Figure 2.16. By using reducing agents such as H_2, BH_3 in THF, $LiAlH_4$, hydrogenated or hydroxyl surface can be formed as shown in Figure 2.16 (b).

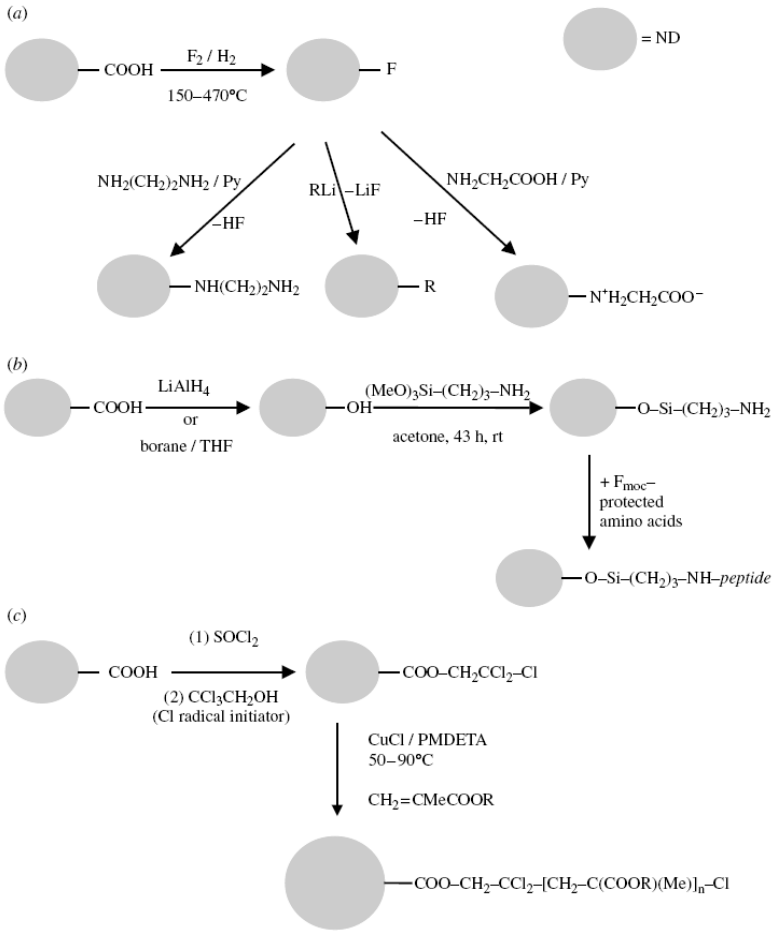

Figure 2.17. Chemical modification schemes of COOH-terminated nanodiamond surface. (a) fluorination of nanodiamond at elevated temperature and H2 atmoshpere, and then further steps to produce alkyl-, amino-, or amino acids terminated particles; (b) reduction of COOH moieties to OH and followed by silanation to produce amino termination, and then peptide synthesis on modified particles; (c) formation of methacrylate-based polymer brushes on nanodiamond using atom transfer radical polymerization methodology; R=i-Bu (adapted from [15]).

Figure 2.17 (a) shows the primary reaction with fluorine gas at 150 to 470 ^{o}C. Chlorine can also be used instead of fluorine. The secondary reactions can be performed with more

www.manaraa.com

complex moieties, such as the fluorinated or chlorinated nanodiamond can further react with ammonia, or lithium organic reagents to produce C-N or C-C chemical bonds. Or hydroxylated nanodiamond reacts with functional silanes as shown in Figure 2.17 (b), which is bioactive. This can be further covalently grafted with bioactive structures such as peptides or biotin or used for the immobilization of maleimide linkers, or initiators / monomers for polymerization [15]. Figure 2.17 (c) shows the reaction with radical reagents to produce polymer brushes on nanodiamonds.

The surface of detonation nanodiamond with hydrophilic oxygen-containing groups can easily adsorb various small or larger polar molecules via hydrogen bonds or adsorption interaction, so-called non-covenant modification. For example, water can form a thin layer on its surface; poly-L-lysine, protein lysozyme, cytochrome c and apoobelin etc. can be coated on the surface of nanodiamond.

2.3.5 Applications of detonation nanodiamond [16]

All applications of nanodiamonds are based on an understanding of their structures, or the capabilities of chemical or adsorption modifications of their surface. With the development of disintegration, purification and functionalization techniques, detonation nanodiamond has found diverse applications such as:

(1) Nanodiamond can be mixed with polymer [27] or metals [28] to form nano-composite materials to enhance mechanical properties, increase the mechanical resistance of coatings, and improve the adhesion with substrates;

(2) Due to the $(N\text{-}V)^-$ centers, one type of lattice defect, fluorescence can be observed in living cells when excited with ultraviolet light (< 400 nm) [29, 30]. This feature has enabled detonation nanodiamond to be developed as a biolabel without bleaching and blinking labeling systems [30-32]. It can also be used as a fluorescent marker for cell imaging.

(3) Because of the $(N\text{-}V)^-$ centres, nanodiamond is a photostable, single-photon source, thus could serve as a solid-state room temperature qubit. Therefore, nanodiamond could potentially be used in a quantum computer.

www.manaraa.com

(4) As stationary phase in HPLC columns, detonation nanodiamond has shown ion exchanging capability for separation technology [33]; Nanodiamond has also been used to separate recombinant proteins from *E. coli* [34], in which proteins can be directly analyzed by using MALDI-TOF-MS with separation from nanodiamonds [35].

(5) Nanodiamond can serve as a solid catalyst support; however, it has been found that nanodiamond can also directly catalyze the oxidation of CO to CO_2 [36]. The rate of methanol decomposition also shows a correlation with the amount of nanodiamond used in the catalyst. In this case, nanodiamond contributed to the formation of more effective catalytic centres.

(6) It can be used as seeds for the crystal growth of CVD diamond film.

2.4 Titanium dioxide and its modifications

Due to its large refractive index, bright stable white color, nontoxicity, low cost, TiO_2 is widely used as opacifier pigments in paints, coatings (including glazes and enamels), plastics, paper, inks, food and cosmetics. Since 1972 Fujishima and Honda discovered that TiO_2 is a photocatalyst, which can split water and generate O_2 and H_2 on an n-type TiO_2 electrode in a solar photovoltaic cell, in which the UV-VIS light was used instead of an external voltage [37], TiO_2 has become a promising photocatalyst. The reasons that make TiO_2 close to an ideal photocatalyst are: (1) it is relatively inexpensive; (2) highly stable chemically; (3) the photogenerated holes are highly oxidizing; and (4) the photogenerated electrons are highly reductive to produce superoxide. Besides the potential applications in energy generation and storage, environmental cleanup has been one of the most active research fields, such as air or water purification, sterilization of medical devices, food preparation surfaces, sanitaryware surfaces, self-cleaning paints and window panels, and cancer therapy. All of the applications are based on the total destruction of organic compounds or bacteria via oxidation or reduction reactions, which originate from the electrons or holes after photo-excitation. However, due to its large band gap of 3.0-3.2 eV, its photocatalytic efficiency under visible light is very low, meanwhile the recombination of electrons and holes retards its efficiency further. Therefore modifications of TiO_2 to facility

www.manaraa.com

the photocatalytic degradation reaction of organic compounds under sunlight have been researched extensively.

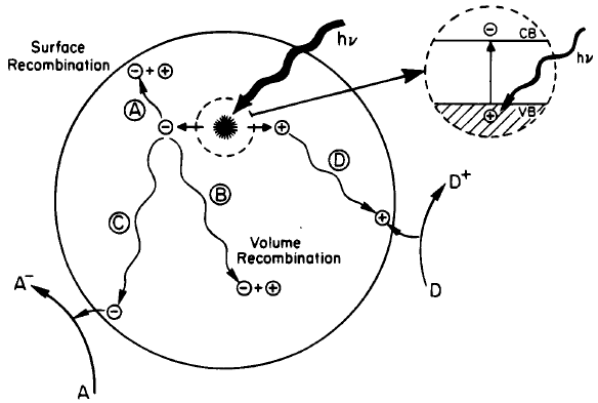

Figure 2.18. Schematic of semiconductor electronic excitation in TiO2 and the pathways of electrons or holes migrating towards the surface and playing roles in the reaction with pollutants near the surface (adapted from [38])

Figure 2.18 shows the semiconductor electronic excitation, and the several possible fates of the electron and hole during their migration towards the surface. The enlarge section shows the photoexcitation of electrons from the valence band (VB) to the conduction band (CB), and holes remain in the VB via absorbing energy from light. Path A indicates surface recombination; path B is volume recombination; path C indicates the electrons successfully reaching the surface and participating the reduction reaction with chemical agents; path D shows the holes successfully reaching the surface and joining the oxidization reaction.

The quality of photocatalysts is evaluated by several factors including the efficiency of reactant conversion, the range of wavelength response and the stability under illumination. The aims of semiconductor modifications lie in reducing the chances of surface or volume recombination and making the electrons or holes successfully participate reduction or oxidization reaction with pollutants or bacteria [38] and meanwhile lower the gap band to have the capacity of using natural sunlight to degrade organic contaminants [39-41]. There are several ways to realize these goals as follows:

(1) Metal semiconductor modification is schematically shown in Figure 2.19, where metal is deposited on the surface of TiO_2 semiconductor. Metal serves to trap the electron and leave the hole to freely migrate to the surface to produce oxidization reaction.

www.manaraa.com

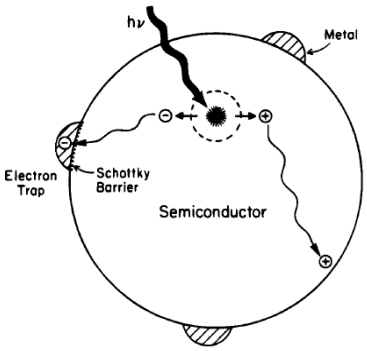

Figure 2.19. Schematic of a metal-modified semiconductor photocatalyst particle. The alignment of Fermi levels of the metal and semiconductor causes electrons to flow to the metal from the semiconductor. Instead of morphology or geometry, only the optimum metal content affects the distribution of electrons in the system (adapted from [38]).

(2) Composite semiconductors provide another way to extend the range of wavelength response and increase the separation of charges geometrically. Figure 2.20 shows coupled CdS and TiO_2 semiconductors. The relative positions of the energy levels are referenced to the vacuum level. The two semiconductors are in direct contact with multiple CdS particles on each TiO_2 particle. This coupled system exhibits a broad absorption wavelength range from 550 to 750 nm, and produces a more efficient photocatalyst via better charge separation.

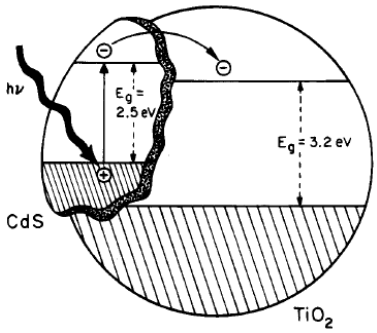

Figure 2.20. Schematically illustration of composite semiconductor-semiconductior photocatalyst. The light only can excite the semiconductor with smaller band-gap, the electrons subsequently transfer to the CB of TiO2 with larger band-gap, while the holes still stay in their original positions. In this case, electron can freely migrate towards the surface to have reduction reaction with the agents absorbed on the surface of TiO_2 particle.

(3) Surface sensitization is another modification method, whose principle is very similar to the composite semiconductors method. Dyes are chemically or physically absorbed on the surface of TiO_2 semiconductor particle, and they are relatively easily excited by light

www.manaraa.com

followed by electron transfer to TiO_2 conductor band if the oxidative energy level of the coupled system is favorable in terms of the excited state of the dye with respect to the energy level of the CB of TiO_2. Some common dyes used in this service include erythrosine B, thionine, and analogs of $Ru(bpy)_3^{2+}$.

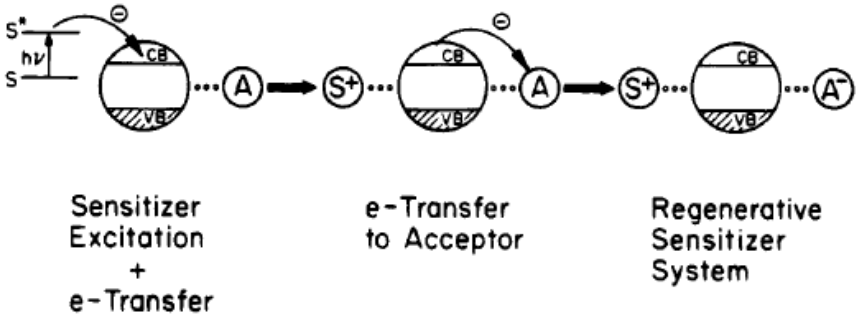

Figure 2.21. The steps of using dyes as molecular sensitizers in TiO_2 photocatalyst modification (adapted from [38]).

(4) Transition metal doping is another effective way to reduce the recombination of electrons and holes during illumination. To date, only certain transition metals such as Fe^{3+} and Cu^{2+} [42] have been found to be suitable for this purpose and the concentration has to be very small.

Carbon modified TiO_2 has been found to be an active photocatlyst under visible light [43-45], for example, sugar modified–n-TiO_2 gave 13-fold increase at the initial rate of the photodegradation of 4-chlorophenol compared to regular n-TiO_2, whereas tetrabutylammonium hydroxide modified n-TiO_2 increased only 8-fold [46]. In order to understand how sugar is incorporated and might affect the photocatalysis process, we have studied the fate of carbon by advanced solid-state NMR techniques. The results will be discussed in detail in Chapter 10.

References

1. Hodge, J. E. J. Agric. Food Chem. **1953,** 1, 926-943.
2. Nursten, H., The Maillard reaction: chemistry, biochemistry and implications. 2005; p 5-30.
3. Tressl, R.; Wondrak, G. T.; Garbe, L. A. J. Agric. Food Chem. **1998,** 46, 1765-1776.

www.manaraa.com

4. Hofmann, T.; Ames, J.; Krome, K.; Faist, V. Nahrung/Food **2001,** 45, 189-194.
5. Fay, L. B.; Brevard, H. Mass Spectrom. Rev. **2005,** 24, 487-507.
6. Hofmann, T. J. Agric. Food Chem. **1998,** 46, 932-940.
7. Hofmann, T. J. Agric. Food Chem. **1998,** 46, 3902-3911.
8. Frank, O.; Heuberger, S.; Hofmann, T. J. Agric. Food Chem. **2001,** 49, 1595-1600.
9. Knerr, T.; Lerche, H.; Pischetsrieder, M.; Severin, T. J. Agric. Food Chem. **2001,** 49, 1966-1970.
10. Hofmann, T. Ann. N.Y. Acad. Sci. **2005,** 1043, 20-29.
11. Adams, A.; Tehrani, K. A.; Kersÿieneú, M.; Venskutonis, R.; N.D., K. J. Agric. Food Chem. **2003,** 51, 4338-4343.
12. Mantell, C. L., Carbon and graphite handbook. Interscience Publishers: New York, 1968.
13. Falcao, E. H. L.; Wudl, F. Journal of Chemical Technology and Biotechnology **2007,** 82, 524-531.
14. Holt, K. B. Phil. Trans. R. Soc. A **2007,** 365, 2845-2861.
15. Krueger, A. J. Mater. Chem. **2008,** 18, 1485-1492.
16. Ōsawa, E. Diamond Relat. Mater. **2007,** 16, 2018-2022.
17. Kruger, A.; Kataoka, F.; Ozawa, M.; Fujino, T.; Suzuki, Y.; Aleksenskii, A. E.; Vul, A. Y.; Osawa, E. Carbon **2005,** 43, 1722-1730.
18. Badziag, P.; Verwoerd, W. S.; Ellis, W. P.; Greiner, N. R. Nature **1990,** 343, 244-245.
19. Raty, J. Y. G., G. Nat. mater. **2003,** 2, 792-795.
20. Wang, C.; Chen, J.; Yang, G.; Xu, N. Angew. Chem. Int. Ed. **2005,** 44, 7414-7418.
21. Zhao, D.-S.; Zhao, M.; Jiang, Q. Diamond Relat. Mater. **2002,** 11, 234.
22. Pantea, C.; Zhang, J.; Qian, J.; Zhao, Y.; Migliori, A.; Grzanka, E.; Palosz, B.; Wang, Y.; Zerda, T. W.; Liu, H.; Ding, Y.; Stephens, P. W.; Botez, C. E. In NSTI Nanotech, Boston, Massachusetts, 2006; Boston, Massachusetts, 2006.
23. Raty, J. Y.; Galli, G.; Bostedt, C.; Buuren, V. T. W.; Terminello, L. J. Phys. Rew. Lett. **2003,** 90 037401, 037401-037404.
24. Aleksenskii, A. E.; Baidakova, M. V.; Vul, A. Y.; Siklitskii, V. I. Phys.Solid State **1999,** 41, 668-671.

www.manaraa.com

25. Palosz, B.; Pantea, C.; Grzanka, E.; Stelmakh, S.; Proffen, T.; Zerda, T. W.; Palosz, W. Diamond Relat. Mater. **2006,** 15, 1813-1817.
26. Shames, A. I.; Panich, A. M.; Kempinski, W.; Alexenskii, A. E.; Baidakova, M. V.; Dideikin, A. T.; Osipov, V. Y.; Siklitski, V. I.; Osawa, E.; Ozawa, M.; Vul, A. Y. J. Phys. Chem. Solids **2002,** 63, 1993-2001.
27. Li, L.; Davidson, J. L.; Lukehart, C. M. Carbon **2006,** 44, 2308-2315.
28. Tsubota, T.; Tanii, S.; Ishida, T.; Nagata, M.; Matsumoto, Y. Diamond Relat. Mater. **2005,** 14, 608-612.
29. Aleksenskii, A. E.; Osipov, V. Y.; Vul, A. Y.; Ber, Y. B.; Smirnov, A. B.; Melekhin, V. G.; Adriaenssens, G. J.; Iakoubovskii, K. Phys. Sol. State **2001,** 43, 145-150.
30. Yu, S. J. K., M. W.; Chang, H. C.; Chen, K. M.; Yu, Y. C. J. Am. Chem. Soc. **2005,** 127, 17604–17605.
31. Fu, C.-C.; Lee, H.-Y.; Chen, K.; Lim, T.-S.; Wu, H.-Y.; Lin, P.-K.; Wei, P.-K.; Tsao, P.-H.; Chang, H.-C.; Fann, W. Proc. Natl. Acad. Sci. U.S.A. **2007,** 104, 727-732.
32. Neugart, F.; Zappe, A.; Jelezko, F.; Tietz, C.; Boudou, J. P.; A., K.; Wrachtrup, J. Nano Lett. **2007,** 7, 3588-3591.
33. Nesterenko, P. N.; Fedyanina, N.; Volgin, Y. V.; Jones, P. J. Chromatogr., A. **2007,** 1155, 2-7.
34. Bondar, V. S.; Pozdnyakova, I. O.; Puzyr, A. P. Phys. Sol. State **2004,** 46, 758–760.
35. Barnard, A. S.; Sternberg, M. J. Phys. Chem. B **2005** 17107-17112.
36. Bogatyreva, G. P.; Marinich, M. A.; Ishchenko, E. V.; Gvyazdovskaya, V. L.; Bazalii, G. A.; Oleinik, N. A. Phys. Sol. State **2004,** 46, 738-741.
37. Fujishima, A.; Honda, K. Nature **1972,** 238, 37-38.
38. Linsebigler, A. L.; Lu, G.-Q.; Yates, J. T. Chem. Rev. **1995,** 95, 735-758.
39. Ollis, D. F., Photocatalytic purification and treatment of water and air. Elsevier: Amsterdam, 1993.
40. Ollis, D. F. Enuiron. Sci. Technol. **1986,** 19, 480.
41. Matthews, R. W. J. Phys. Chem. B **1987,** 91, 3328-3333.
42. Butler, E. C.; Davis, A. P. J. Photochem. Photobiol., A: Chem. **1993,** 70, 273-283.
43. Sakthivel, S.; Kisch, H. Angew. Chem. Int. Ed. **2003,** 42, 4908-4911.

www.manaraa.com

44. Cheng, Y.-P.; Sun, H.-Q.; Jin, W.-Q.; Xu, N.-P. Chem. Engin. J. **2007,** 128, 127-133.

45. Savoskin, M. V.; Yaroshenko, A. P.; Lazareva, N. I.; Mochalin, V. N.; Mysyk, R. D. J. Phys. Chem. Solids **2006,** 67, 1205-1207.

46. Xu, C.-K.; Killmeyer, R.; Gray, M. L.; Khan, S. U. M. Appl. Cataly. B: Envir. **2006,** 64, 312-317.

www.manaraa.com

CHAPTER 3. Introduction of solid-state NMR techniques

Solid state NMR is an indispensable method for structure, morphology, dynamics and distance measurements of many areas in academia and industry, such as structural studies of natural organic products (e.g. soil, coal, plant materials, foods), dynamics of biological systems (e.g. dynamics of interface of bone, insertion of membrane protein into lipid), drug development (e.g. interactions between DNA & RNA and drug, domain size of drug pill, morphology structures), material science (Nafion film, nanocomposite polymers), and catalysts (e.g. C-TiO_2). Basic concepts of NMR such as the Larmor frequency and various types of secondary interactions such as chemical shift and chemical shift anisotropy, J coupling, homonuclear or heteronuclear dipolar interactions are introduced in the first part of this chapter. Several solid-state NMR techniques, which have been applied to the studies of this dissertation, are introduced in the second part. These solid state NMR techniques include Magic Angle Spinning (MAS), Cross Polarization (CP), Total spinning Sideband Suppression (TOSS), Chemical Shift Anisotropy (CSA) filter, CH_2, CH, selection, HeteronucleAr Recoupling with Dephasing by Strong Homonuclear Interactions of Protons (HARDSHIP), and multidimensional NMR techniques such as Separation of Undistorted chemical-shift anisotropy Powder pattERns (SUPER), Frequency Switch Lee-Goldburg (FS-LG) ^{1}H-^{13}C HETeronuclear CORrelation (HETCOR), ^{13}C-^{13}C exchanging, and ^{13}C-^{15}N Heteronuclear Single Quantum Correlation (HSQC).

3.1 General introduction of NMR

Nuclear Magnetic Resonance (NMR) is a powerful analytical tool and the theory is based on quantum mechanics. It is used to provide information about molecular structures (such as identification of compounds in mixtures, conformation information, binding sites) and dynamics (such as motions, chemical exchange, spin diffusion). Due to the weak interaction energy of RF pulse with molecules (< 0.2 J/mol), NMR is also a non-destructive analytical tool, which is desirable in many fields.

Subatomic particles (electrons, protons and neutrons) have spin, which is their intrinsic angular moment. Nuclei containing odd number of protons or neutrons have a

www.manaraa.com

nonzero overall spin angular moment, $\vec{L} = \hbar \vec{I}$. The overall spin angular moment and magnetic moment are directly proportional and the ratio is the gyromagnetic ratio γ: $\overrightarrow{M} = \gamma \vec{L}$. When an external magnetic field is applied to the spin system, the magnetic moment interacts with the external magnetic field. This Zeeman interaction is the predominant interactions in regular NMR. The Hamiltonian of the Zeeman interaction can be written as [1]:

$$\begin{aligned} \hat{H} &= -\overrightarrow{M} \cdot \overrightarrow{B_0} \\ &= -\gamma \vec{L} \cdot \overrightarrow{B_0} \\ &= -\gamma \cdot \hbar \vec{I} \cdot \overrightarrow{B_0} \end{aligned} \tag{2.1}$$

Since spin is quantized, the spin vector can have (2I+1) discrete projections along an arbitrary Z direction (where I is the spin quantum number). The magnetic quantum number (m) represents each projection and is the number from –I, -I+1 to I. For instance, the spin number of ^{13}C is 1/2, so the spin vector of ^{13}C has two different projections along Z direction, and its magnetic quantum number is –1/2 and 1/2. If no external magnetic field applied, their arbitrary Z directions are random directions and there is no energy difference between their different projections. Once an external magnetic field is applied, the projections along B_0 have lower energy than the ones opposite to B_0 direction (for $\gamma > 0$ nuclei). The energy difference between different projections is:

$$\Delta E = -\Delta m \hbar \gamma B_0. \tag{2.2}$$

By Planck's law ($E=h\upsilon$) and equation (2.2), the Larmor frequency can be calculated as

$$\omega_0 = -\gamma B_0 \tag{2.3}$$

At statistical equilibrium, the number of particles at different energy levels follows the Boltzmann distribution and more particles stay at the lower energy level. According to equation (2.4), the population difference between different energy level is $\propto (\Delta m \hbar \gamma B_0)/(2I+1)$. Only signals of $\Delta m=1$ can be observed directly. The gyromagnetic ratio

www.manaraa.com

reflects the sensitivities of NMR signals with respect to its corresponding nucleus. Increasing B_0 also increases the population difference [2].

$$\begin{aligned}\frac{N_m}{N} &= \frac{\exp\left(-\frac{E_m}{k_B T}\right)}{\sum_{m=-I}^{I} \exp\left(-\frac{E_m}{k_B T}\right)} \\ &= \frac{\exp\frac{m\hbar\gamma B_0}{k_B T}}{\sum_{m=-I}^{I} \exp\frac{m\hbar\gamma B_0}{k_B T}} \\ &\cong \frac{\left(1+\frac{m\hbar\gamma B_0}{k_B T}\right)}{\sum_{m=-I}^{I}\left(1+m\hbar\gamma B_0\right)} \\ &= \frac{\left(1+m\hbar\gamma B_0\right)}{(2I+1)}\end{aligned} \qquad (2.4)$$

In order to disturb the equilibrium state and detect the NMR signals, a short period (~ 4 μs) radio frequency pulse is applied in Fourier transfer (FT) NMR, and this RF pulse can excite a range of frequencies around 40 ~ 500 MHz. When an excitation energy matches the energy gap of m = 1 energy levels, the particles at lower energy level absorb RF energy and occupy a higher energy level. This resonance is called nuclear magnetic resonance. During RF pulse, the magnetization precesses around radio frequency B_1 field when on resonance. In experiments, the process is not directly measured. Instead a free-induction-decay (FID) of a non-zero magnetization component in the xy plane after RF pulses is measured, which is a time domain signal. After Fourier transformation, frequency domain signals can be obtained. In order to extract structure, dynamics, quantity and distance information from NMR experiments, different pulse programs, which combine different RF pulses and delays, need to be applied to achieve different goals.

3.2 Why do we mainly use solid state NMR instead of solution NMR in our research?

www.manaraa.com

NMR experiments can be performed in either liquid or solid states. Since the reorientation in solution is much faster than the evolution time of dipolar interactions, the anisotropic dipolar couplings are averaged out. This leads to sharper peaks and better resolution than the solid state NMR spectra. Magic angle spinning solid state NMR, however, can give high resolution for dilute nuclei species. Many unique interactions in solid state, which can be reintroduced through certain pulse sequences under MAS, provide more interesting information about orientation, distances, morphology, dynamics and structure. They are not available in solution NMR. Meanwhile, some samples are not suitable for using solvents or cannot be dissolved such as cross-linked polymers or soil organic matter. Even if a sample is easy to dissolve in common solvents, the concentration is diluted, and cannot meet the sensitivity requirement. With the increase of magnetic fields and MAS speed, solid state NMR appears to be more promising indeed.

3.3 Interactions of Solid-State NMR present in this dissertation [1]

(a) Chemical shift and chemical-shift anisotropy

Electrons surrounding a nucleus have their own magnetic moment. The interaction between the applied external magnetic field and electrons magnetic moment cause diamagnetic current in electron orbital. This diamagnetic current produces a local magnetic field, therefore, alter the magnetic field felt by the nucleus. This is called shielding. The strength of the local field depends on the electron density, and therefore on the electronegativity of its adjacent elements and is also orientation dependent. Usually the more the electron shells, the larger the alteration of local magnetic field is. Since the resonance frequency of nuclei is directly proportional to the net magnetic field $(1-\sigma)B_0$, the variation of resonance frequency encodes their corresponding molecular environments. The chemical shift Hamiltonian can be expressed as:

$$\hat{H}_{CS} = \gamma\hbar\hat{\vec{I}}\,\sigma\vec{B}_0 = \gamma\hbar\left(\hat{I}_x\sigma_{xz}^{LF} + \hat{I}_y\sigma_{yz}^{LF} + \hat{I}_z\sigma_{zz}^{LF}\right)B_0 \qquad (2.5)$$

www.manaraa.com

σ^{LF} is a shielding tensor (a 3 by 3 matrix) in the lab frame. The large Zeemann interaction truncates all non-zz terms (much weaker than Zeemann interaction) in (2.5), and only the last term remains since the σ_{zz}^{LF} commutes with I_z. The Hamiltonian of chemical shift can be simplified as equation (2.6). In experiments, the unit of chemical shift is part per million (ppm), which is defined in equation (2.7).

$$\hat{H}_{CS} = \gamma \hbar \hat{I}_z \sigma_{zz}^{LF} B_0 = -\omega_0 \hbar \hat{I}_z \sigma_{zz}^{LF} = \omega_{CS} \hbar \hat{I}_z \tag{2.6}$$

$$\delta_{CS}[ppm] = \frac{\left(\omega_{CS} - \omega_{CS,ref}\right) \cdot 10^6}{\omega_{CS,ref}} \tag{2.7}$$

If the electron cloud distribution around a nucleus is not spherical or of cubic symmetry, the chemical shift is dependent on the orientations of the electron cloud and thus the orientation of the molecule. This is called chemical shift anisotropy (CSA). For a non-sp^3-hybridized ^{13}C site, the anisotropy of chemical shift can be more than 100 ppm. The anisotropic frequency can be expressed as:

$$\omega(\theta,\phi) = \delta \tfrac{1}{2}(3\cos^2\theta - 1 - \eta \sin^2\theta \cos(2\phi)) \tag{2.8}$$

$$\begin{aligned} \delta &= \sigma_z \\ \eta &= \frac{\sigma_y^{PAS} - \sigma_x^{PAS}}{\sigma_z^{PAS}} \end{aligned} \tag{2.9}$$

$$\sigma_{iso} = \frac{\sigma_x^{PAS} + \sigma_y^{PAS} + \sigma_z^{PAS}}{3} \tag{2.10}$$

Where δ is the anisotropy parameter, η is the asymmetry parameter. θ and ϕ denote the polar angles of the B_0 field in the PAS (principle axes system), where the 3 by 3 matrix σ is diagonalized. The angles are defined in figure 3.1. Figure 3.2 displays chemical shift anisotropy powder patterns.

www.manaraa.com

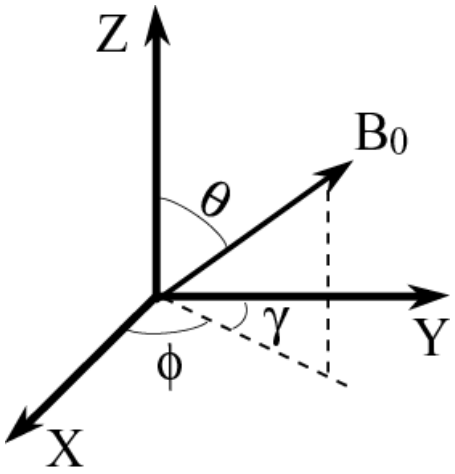

Figure 3.1. B_0 at the principle axes coordinator system. θ is the angle between B_0 and Z, ϕ, γ are the angles of the projection of B_0 on xy-plane to X or Y-axes.

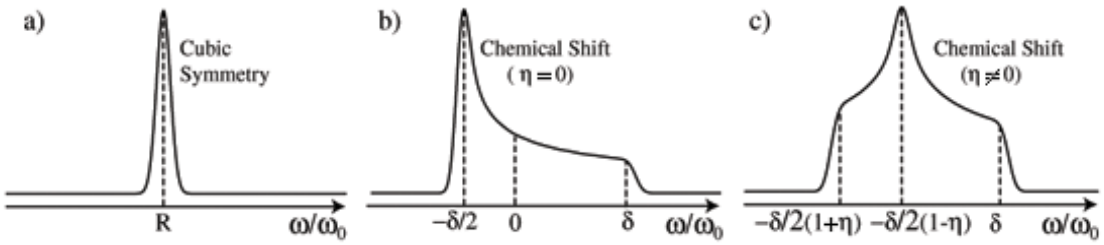

Figure 3.2. Calculated NMR spectra of polycrystalline or amorphous samples (powder patterns) corresponding to chemical shift under different symmetry conditions. (adapted from [3])

(b) J coupling

J coupling is also named as scalar coupling and plays a very important role in solution NMR due to the lack of other large internal interactions. J coupling is used rarely in solid state NMR. Nevertheless, J coupling can give us information about chemical bonds connections with higher resolution and accuracy because the polarization transfer via J-modulation is through chemical bonds and have small coupling values. In this dissertation, we will give examples for its uses in the structure elucidation of isotope labeled samples.

When two nuclei ($s \neq 0$) share their electrons, for instance forming covalent chemical bonds (within a distance of 1 to 4 bonds) or by hydrogen bonds, the magnetic moment of electrons (associated with nucleus A) is polarized by the applied external magnetic field. This

www.manaraa.com

polarization can be transferred to other electrons (associated with nucleus X) through chemical bonds or hydrogen bonds (H--H) [4], and finally affects the local field of nucleus X, and vice versa. The magnetization of nucleus A has different projections (2I+1) on the Z-direction and can cause the resonance frequency of nucleus X to split. The size of the split is the value of the J coupling constant in Hz. The more overlap of the electron clouds from the two nuclei, the larger the J coupling constant is. The Hamiltonian of J coupling can be expressed as [5]:

$$\hat{H} = 2\pi\hbar J_{IS} \hat{\vec{I}} \cdot \hat{\vec{S}} \tag{2.11}$$

$$J_{IS} = \left(\frac{\hbar}{2\pi}\right)\left(\frac{8\pi\mu_0}{3}\right)^2 \gamma_I \gamma_S \cdot \lambda^{-1} \Delta(r_N) \tag{2.12}$$

$$\text{with } \Delta(r_N) = \sum \Gamma_{IS} \langle \phi_I | \delta(r_N) | \phi_S \rangle$$

Where $\mathbf{J}_{IS}$ is the J-coupling tensor, a 3x3 real matrix and has molecular orientation dependence. At the weak coupling condition, where the J coupling is much smaller than the difference between the chemical shifts of two nuclei, the chemical shift Hamiltonian truncates the Hamiltonian of the J coupling and only z-direction Hamiltonian remains. Therefore, the Hamiltonian of the J coupling under weak coupling condition can be further expressed as:

$$H = 2\pi\hbar J I_z S_z \tag{2.13}$$

(c) Dipolar interactions

Dipolar interactions are the interactions between nuclear magnetic moments through space instead of through chemical bonds as J-coupling. For instance, two nuclei I and S, the magnetic moment of I produces a local field at the position of nucleus S. Therefore, S can feel nucleus I via its own local field change, and vice versa. The Hamiltonian of the dipolar interaction is:

www.manaraa.com

$$\hat{H} = -\frac{\mu_0}{4\pi}\hbar \sum_{j,k-pairs}\sum \gamma_j \gamma_k \frac{3\left(\frac{\vec{I^j}}{\vec{r_{jk}}}\right)\left(\frac{\vec{I^k}}{\vec{r_{jk}}}\right) - \vec{I^j}\,\vec{I^k}}{r_{jk}^3} \qquad (2.14)$$

The dipolar coupling (~ kHz) is much smaller than Zeeman interaction (~ MHz), hence the components which are perpendicular to B_0 direction will be truncated.

Because $\vec{I}\cdot\vec{S}$ does not commute with (I_Z+S_Z) in the heteronuclear dipolar interaction case, but for homonuclear dipolar interaction, the $\vec{I}\cdot\vec{I}$ commutes with ($I_{1,Z}$+$I_{2,Z}$), the Hamiltonians of heteronuclear and homonuclear dipolar interactions are different after truncation by an external magnetic field. They can be expressed as:

$$\hat{H}_D^{IS} = -\frac{\mu_0}{4\pi}\hbar\frac{\gamma^I\gamma^S}{r^3}\frac{1}{2}\left(3\cos^2\theta - 1\right)2\hat{I}_Z\hat{S}_Z \qquad (2.15)$$

$$\hat{H}_D^{II} = -\frac{\mu_0}{4\pi}\hbar\frac{\gamma_I^2}{r^3}\frac{1}{2}\left(3\cos^2\theta - 1\right)\left(3\hat{I}_{z,1}\hat{I}_{z,2} - \vec{I}_1\vec{I}_2\right) \qquad (2.16)$$

The dipolar coupling constant is directly proportional to the product of the gyromagnetic ratios of the two nuclei and inversely proportional to the cube of the internuclear distance.

$$\omega_d = -\frac{\mu_0}{4\pi}\hbar\frac{\gamma_1\gamma_2}{r_{1,2}^3} \qquad (2.17)$$

Therefore, the dipolar coupling is very sensitive to changes in distance. A typical dipolar coupling strength for ^{1}H-^{13}C pair at a distance of ~1.5 Å is around 30 kHz. But for the pair with a distance of ~ 10 Å, the dipolar coupling strength drops to 30 Hz.

3.4 Solid state NMR techniques used in our study

In this section, the theoretical derivations are from the book written by Klaus Schmidt-Rohr and Hans Wolfgang Spiess, [1], the notes from Dr. Mei Hong's class, and other literature as cited.

www.manaraa.com

(a) Magic angle spinning (MAS)

The fast molecular tumbling (on the ns time scale) in solution can average out all orientation-dependent terms and makes the absorptive peaks very sharp. The peak position represents the isotropic chemical shift frequency. Molecules in solid samples are relatively fixed and lack this fast averaging motion. In solid state NMR spectra, the spectral intensity $S(\omega)$ depends on the orientation distribution percentage function $P(\theta, \phi)$. Some typical powder patterns are shown in figure 3.1 in the preceding section. The frequency distribution contains molecular orientation information, however, in most situations it is considered as undesirable line broadening. In order to reduce the line broadening and obtain better resolved spectra of solid samples, magic angle spinning is a very popular technique, especially for spin 1/2 nuclei.

Under fast uniaxial rotation, the averaged precession frequency due to chemical shifts or spin-pair dipolar coupling can be written as:

$$\overline{\omega} = \omega_{iso} + \frac{1}{2}\left(3\cos^2\beta_p - 1 - \eta\sin^2\beta_p\cos 2\alpha_p\right)\delta\,\frac{1}{2}\left[3\cos^2\theta_r - 1\right] \qquad (2.18)$$

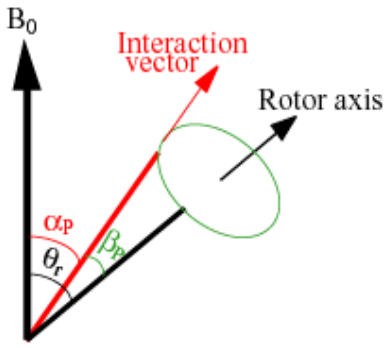

Figure 3.3. Interaction vectors of different orientations rotate along the rotor axis and behavior like one entity.

The angles in this equation are depicted in figure 3.3. When $\theta_r = \theta_m = 54.74^o$, the so-called magic angle, the second term is zero. MAS can split the anisotropic couplings into spinning sidebands at multiples of spinning frequency ω_r. Figure 3.4 depicts the rotational echoes signals in the time domain and its corresponding frequency domain signals after FT.

www.manaraa.com

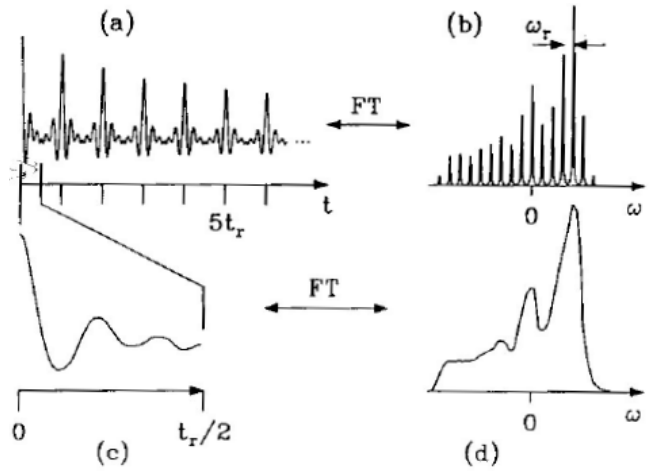

Figure 3.4. Time and frequency signals of magic angle spinning rotational echoes. In the time domain, the intensity is periodic. In the frequency domain, the side bands appear at $n\omega_r$. (adapted from [1])

In organic solids, the dipolar couplings (> 20 kHz) between ^{1}H and ^{1}H or ^{13}C are greater than conventional magic angle spinning speed (<20 kHz). MAS cannot eliminate the multispin homonuclear coupling. RF irradiation can be introduced to decouple homonuclear or heteronuclear dipolar interaction. In our studies, two main RF decoupling techniques have been used very often, they are (1) high-power continuous-wave (cw) decoupling and (2) two-pulse phase modulated decoupling (TPPM).

When the sample is rotating around the magic angle axis, the time dependent frequency can be obtained via transformation from the equation (2.18) in PAS coordinates to the MAS rotor-fixed frame. Figure 3.5 depicts the definitions of the Euler angles (α, β, γ).

$$\overline{\omega}^{RF} = \widetilde{R}\left(\alpha,\beta,\gamma\right)\overline{\omega}^{PAS}\,\widetilde{R}^{-1}\left(\alpha,\beta,\gamma\right) \tag{2.19}$$

$$\omega(t) = \omega_{iso} + C_1\cos(\gamma + \omega_r t) + C_2\cos\left(2\gamma + 2\omega_r t\right) + S_1\sin(\gamma + \omega_r t) + S_2\sin\left(2\gamma + 2\omega_r t\right)$$

$$\text{or}\quad \omega(t) = \omega_{iso} + \widetilde{C}_1\cos(\omega_r t) + \widetilde{C}_2\cos\left(2\omega_r t\right) + \widetilde{S}_1\sin(\omega_r t) + \widetilde{S}_2\sin\left(2\omega_r t\right) \tag{2.20}$$

The C and S coefficients are functions of δ, η, α and β [see table 3.1 in ref. [1]]. When

www.manaraa.com

η=0, e.g. the dipolar interaction of isolated spin pairs, $S_1=S_2=0$, $C_1(\beta) = -\delta \frac{\sqrt{2}}{2} \sin 2\beta$ and $C_2(\beta) = \delta \frac{1}{2} \sin^2 \beta$.

Based on equation (2.19), for a single segment, the intensity of the sideband at $N\omega_r$ can be expressed as:

$$I_N(\alpha,\beta,\gamma) = \frac{1}{2\pi} A(\alpha,\beta,\gamma) e^{-i\gamma N} \int_0^{2\pi} A^*(\alpha,\beta,\gamma) e^{-i\gamma N} \, d\gamma \qquad (2.21)$$

Where $A(\alpha, \beta, \gamma)$ is a frequency function related to orientation angles.

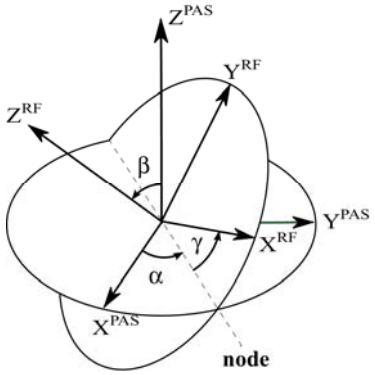

Figure 3.5. Definitions of the Euler angles (α, β, γ). The node line is perpendicular to both Z axes. α is the angles of X^{PAS} rotate to the node line around Z^{PAS}. β is the angle between two Z axes. γ is the angle between the node line and X^{RF}.

Although higher speed MAS is desirable, currently the rotors are made of nonconductive materials which do not permit MAS at supersonic speed. Otherwise the friction between air and the rotor could heat the sample too much and cause the rotor to explode. The cylindrical rotors are usually made from ceramics, e.g. zirconia, or silicon nitride, or from polymers. The end caps can be made from Kel-F, Vespel, zirconia, or boron nitride. The outside diameter of rotors can range from 1.6 to 15-mm [6]. A smaller rotor has a smaller outside diameter and thus the higher MAS speed can be achieved. But the smaller rotor can hold less sample, which reduces the signal.

(b) Total suppression of spinning sidebands (TOSS)

www.manaraa.com

Although spinning sidebands contain anisotropy information, in most cases, spinning sidebands are undesirable and overlap with the center bands of other chemical sites. The TOSS pulse sequence for sideband suppression was first introduced by [7]. The pulse sequence is depicted in figure 3. 6. TOSS is a useful tool to obtain sideband-free spectra. In the indirect dimension of a 2D experiment, TOSS-t_1-deTOSS as shown in figure 3.6 (B) can generate spectra equivalent to fast-spinning spectra. Before acquisition, four properly timed 180° pulses are introduced to randomize the phases of the spinning sidebands while preserving the phase of the center bands.

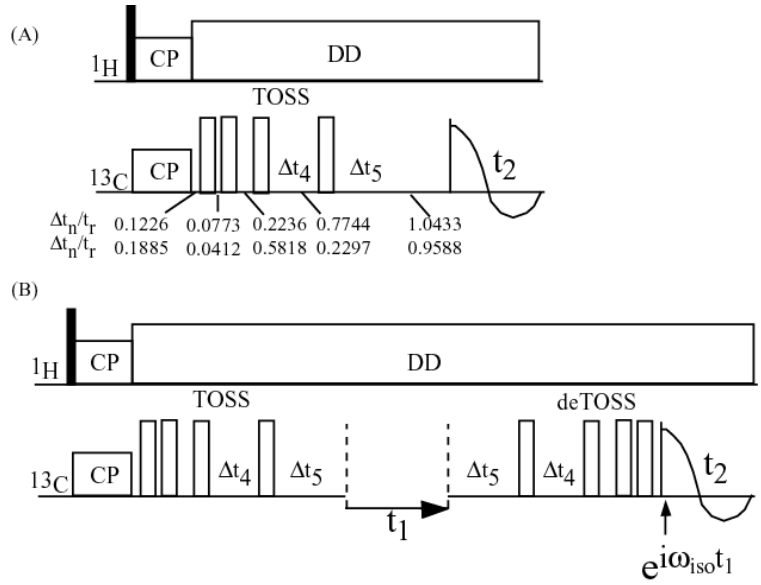

Figure. 3.6. Pulse sequences of (A) TOSS and (B) TOSS-deTOSS embedded in 2D experiments. (A) Four 180° pulses with accurate timing make the sum of all isochromates only precess with the isotropic chemical shift and no spinning sidebands appear. (B) After t_1 evolution, a mirror TOSS pulse named deTOSS is applied to make the magnetization evolve with the isotropic chemical shift before t_2 acquisition. Two timing schedule are listed and the unit is t_r (adapted from [1]).

(c) Cross Polarization (CP)

^{1}H is an abundant nucleus in organic compounds. Its natural abundance is ~ 99% and the other 1% nucleus is deuterium. ^{1}H has a large gyromagnetic ratio and fast spin-lattice relaxation rate. The large ^{1}H-^{1}H dipolar line broading and narrow chemical shift range (< 20 ppm), however, make multiple-pulse homonuclear decoupling or fast MAS necessary for obtaining any chemical shift resolution. ^{13}C and ^{15}N are dilute nuclei. The small

www.manaraa.com

gyromagnetic ratios and long T_1 relaxation time make their sensitivity low although they have larger chemical shift ranges. CP is the technique that can enhance the signals of dilute nuclei by a factor of γ_H/γ_X and greatly reduce the necessary recycle delays. The CP pulse sequence is shown in figure 3.7. The first 90° pulse on ^1H and the magnetization starts from ^1H and is proportional to its gyromagnetic ratio. RF irradiations are applied simultaneously on both channels after the first 90° pulse. The duration of this RF pulse is called contact time. If the two spins locked fields achieve Handmann Hahn match condition, both the toggling frames of ^1H and ^{13}C process synchronously and polarization transfer can occur between the two nuclear species. The average-Hamiltonian theory can be used here to elucidate the transfer process [1].

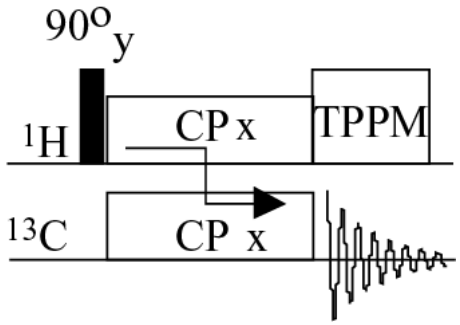

Figure. 3.7. The pulse sequence of ^1H-^{13}C CP. During spin locking, the two irradiation frequencies are Hartmann- Hahn matched ($\omega^1_H - \omega^{13}_C = n\,\omega_r$). The recycle delay is dependent on T_1 of ^1H

(1) The initial density operator after the 90^o_y pulse is:

$$\hat{\rho}(0) = \hat{I}_x \tag{2.22}$$

(2) During CP contact time with B_e along the x direction, the average heteronuclear dipolar Hamiltonian in the interaction frame is:

$$\begin{aligned}\overline{(\hat{H}^{IS})}_T &= \sum_{j,k} \omega_{IS}^{jk} 2\int_0^{n\cdot 2\pi} \frac{d(\omega t)}{n\cdot 2\pi}(\hat{I}_z^j \cos\omega t - \hat{I}_y^j \sin\omega t)(\hat{S}_z^k \cos\omega t - \hat{S}_y^k \sin\omega t) \\ &= \sum_{j,k} \omega_{IS}^{jk}(\hat{I}_z^j \hat{S}_z^k + \hat{I}_y^j \hat{S}_y^k)\end{aligned} \tag{2.23}$$

www.manaraa.com

$$\overline{(\hat{H}^{II}_{z,rot})_T} = -\frac{1}{2}\hat{H}^{II}_x \quad \text{(It commutes with } I_x \text{ and no effects on } I_x) \tag{2.24}$$

$$\overline{(\hat{H}^{I}_{cs})_T} = \overline{(\hat{H}^{S}_{cs})_T} = 0 \tag{2.25}$$

Where $\omega_{IS} = \frac{-\mu_0 \hbar \gamma^I \gamma^S}{4\pi} \frac{1}{r^3_{IS}} \frac{1}{2}\left[3\cos^2\left(\theta^{IS}\right) - 1\right]$

(3) The final density operator after CP is:

$$I_x \xrightarrow{I_z S_z + I_y S_y} I_x \frac{1}{2}(1+\cos\omega_{IS}t) + S_x \frac{1}{2}(1-\cos\omega_{IS}t) + (I_y S_z - I_z S_y)\sin\omega_{IS}t \tag{2.26}$$

After CP irradiation, the polarization of ^{1}H is transferred to ^{13}C with the coefficient $\frac{1}{2}(1-\cos\omega_{IS}t)$. The signal increases with the increasing of initial contact time and oscillates according to $(1-\cos\omega_{IS}t)$. If more spins are involved, the initial stage will give the similar trend as the two-spin situation. But the oscillation becomes more flat afterwards. The contact time is limited by $T_{1\rho}$, which decays signals by relaxing the magnetization to environment. Usually 1 ms contact time is used for normal CP experiment in our systems. But when only protonated ^{13}C is wanted, 50 μs contact time may be used at moderate MAS to exclude long distance magnetization transfer. During acquisition of ^{13}C signals, ^{1}H -^{13}C heteronuclear dipolar decoupling is applied on the ^{1}H channel. If there is a gate time (~ 40 μs) without heteronuclear decoupling pulse, the detected signals are from nonprotoned carbons.

Although CP is used widely in solid state NMR, it cannot provide accurate quantitative information due to its inherited bias on different protonated dilute nuclei. Direct polarization techniques can give more quantitative information for all carbons. The recycle delays of dilute nuclei for direct polarization measurements depend on the T_1, which can be measured by the experiment of CP/T_1/TOSS [8].

(d) Solid echo [1]

www.manaraa.com

For bilinear Hamiltonians such as homonuclear J-coupling, dipolar coupling or quadrupolar coupling, the 180° pulse cannot refocus their time evolution because it flips two spins simultaneously and causes no change at those Hamiltonians, e.g. after 180° Hahn echo, the homonuclear dipolar coupling Hamiltonian is unchanged and can be written as: $\left[3\left(-\hat{I}_z^a\right)\left(-\hat{I}_z^b\right)-\left(-\hat{\vec{I}}^a\right)\left(-\hat{\vec{I}}^b\right)\right]$. The pulse sequence of solid echo for bilinear homonuclear interactions is displayed in figure. 3.8.

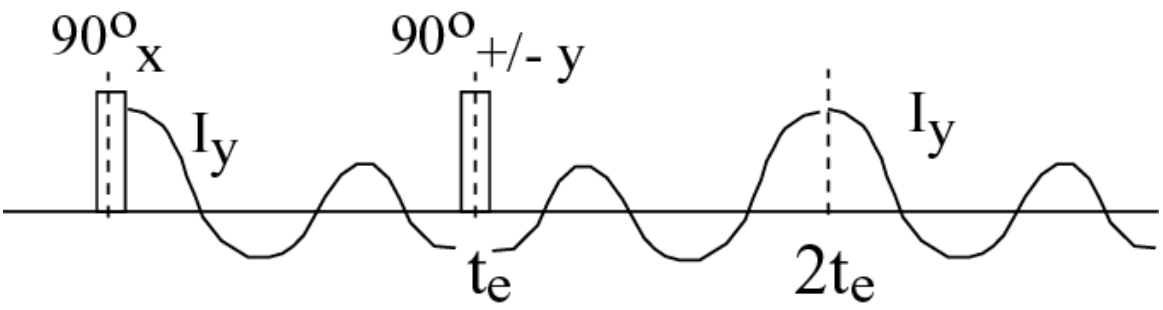

Figure 3.8. Solid echo pulse sequence. [1]

(1) The initial density operator after the 90°_x pulse is:

$$\hat{\rho}(0)=\hat{I}_y \tag{2.27}$$

(2) The propagator at a time $2t_e$ can be written and further simplified as:

$$\begin{aligned}\hat{U}\left(2t_e\right)&=e^{-i\omega_0\left(3\hat{I}_z^a\hat{I}_z^b-\hat{I}^a\hat{I}^a\right)t_e}\,e^{i\frac{1}{2}\pi\hat{I}_y}\,e^{-i\omega_0\left(3\hat{I}_z^a\hat{I}_z^b-\hat{I}^a\hat{I}^a\right)t_e}\\&=e^{-i\omega_0\left(3\hat{I}_z^a\hat{I}_z^b-\hat{I}^a\hat{I}^a\right)t_e}\,e^{i\frac{1}{2}\pi\hat{I}_y}\,e^{-i\omega_0\left(3\hat{I}_z^a\hat{I}_z^b-\hat{I}^a\hat{I}^a\right)t_e}\,e^{-i\frac{1}{2}\pi\hat{I}_y}\,e^{i\frac{1}{2}\pi\hat{I}_y}\\&=e^{-i\omega_0\left(3\hat{I}_z^a\hat{I}_z^b-\hat{I}^a\hat{I}^a\right)t_e}\,e^{-i\omega_0\left(3\hat{I}_x^a\hat{I}_x^b-\hat{I}^a\hat{I}^a\right)t_e}\,e^{i\frac{1}{2}\pi\hat{I}_y}\\&=e^{+i\omega_0\left(3\hat{I}_y^a\hat{I}_y^b-\hat{I}^a\hat{I}^a\right)t_e}\,e^{i\frac{1}{2}\pi\hat{I}_y}\end{aligned} \tag{2.28}$$

(3) The echo can be formed since $\hat{I}_y$ commutes with $\hat{U}\left(2t_e\right)$.

$$\hat{\rho}\left(2t_e\right)=\hat{U}\left(2t_e\right)\hat{I}_y\hat{U}^{-1}\left(2t_e\right)=\hat{I}_y \tag{2.29}$$

www.manaraa.com

Here dipolar interaction Hamiltonian is used as an example. The analogous proof is applicable to the J-coupling Hamiltonian. The phase cycle of the second 90° pulse can remove undesired spurious signals.

(e) CSA filter [9]

The chemical shifts of aromatic and alkyl carbons overlap in the chemical shift range of 90 – 120 ppm. For instance, ketal carbons resonate up to 117 ppm, and aromatic carbons two bonds from oxygen resonate around 100-120 ppm. The aromatic carbon in 1,3,5-trimethoxyl benzene resonates down to 86 ppm. Fortunately, sp, sp^2 and sp^3 hybridized carbons have very different CSA values: $\Delta\sigma_{sp3} < 70$ ppm, $\Delta\sigma_{sp2} = 120 - 230$ ppm, $\Delta\sigma_{sp} = 200 - 400$ ppm. Hence sp or sp^2 hybridized carbon signals can be dephased by reintroducing CSA coupling, and the sp^3 carbons can be observed selectively with an efficiency of > 60 % and with little differential dephasing. Figure 3.9 displays two types of CSA recoupling pulse sequences. The signal dephasing can be expressed as:

$$S/S_0 = \langle \cos [\Phi_{tot}(2t_{csa})] \rangle \qquad (2.30)$$

where the pointed brackets indicate the powder average and S_0 is the signal intensity without CSA filter.

For the 3-pulse sequence shown in figure 3.9 (a), $\Phi_{tot}(2t_{csa})$ can be expressed as: [10]

$$\begin{aligned}
\Phi_{tot}\left(2t_{CSA}\right) &= -\int_0^{t_{CSA}} \omega\,(t)\,dt + \int_{t_{CSA}}^{2t_{CSA}} \omega\,(t)\,dt \\
&= -\int_0^{t_{CSA}} \omega\,(t)\,dt + \int_0^{2t_{CSA}} \omega\,(t)\,dt - \int_0^{t_{CSA}} \omega\,(t)\,dt \\
&= \Phi\left(2t_{CSA}\right) - 2\Phi\left(t_{CSA}\right)
\end{aligned}$$

$$= \frac{\delta_{CSA}}{\omega_r}\left[\begin{array}{l}
\widetilde{S_1}\left\{2\cos\left(\omega_r\, t_{CSA}\right) - \cos\left(\omega_r\, 2t_{CSA}\right) - 1\right\} + 0.5\,\widetilde{S_2}\left\{2\cos\left(2\omega_r\, t_{CSA}\right) - \cos\left(4\omega_r\, t_{CSA}\right) - 1\right\} \\
+\widetilde{C_1}\left\{\sin\left(\omega_r\, 2t_{CSA}\right) - 2\sin\left(\omega_r\, t_{CSA}\right)\right\} + 0.5\,\widetilde{C_2}\left\{\sin\left(4\omega_r\, t_{CSA}\right) - 2\sin\left(2\omega_r\, t_{CSA}\right)\right\}
\end{array}\right]$$

www.manaraa.com

(2.31)

where, $\widetilde{S}_1$, $\widetilde{S}_2$, $\widetilde{C}_1$, $\widetilde{C}_2$, are dependent on η, γ, δ, α and β.[1]

For the 5-pulse sequence in figure 2.9 (b), $\Phi_{tot}(2t_{csa})$ can be expressed as:

$$\begin{aligned}
&\Phi_{tot}\left(2t_r, t_{CSA}\right) \\
&= -\Phi\left(t_{CSA}\right) + \left[\Phi\left(t_r\right) - \Phi\left(t_{CSA}\right)\right] - \Phi\left(2t_r - t_{CSA}\right) + \left[\Phi\left(2t_r\right) - \Phi\left(2t_r - t_{CSA}\right)\right] \\
&= -2\Phi\left(t_{CSA}\right) - 2\Phi\left(t_r - t_{CSA}\right) \\
&= \frac{4\delta_{CSA}}{\omega_r}\left[\widetilde{S}_1\left\{COS\left(\omega_r t_{CSA}\right) - 1\right\} + 0.5\,\widetilde{S}_2\left\{\cos\left(2\omega_r t_{CSA}\right) - 1\right\}\right]
\end{aligned} \tag{2.32}$$

According to the equations above, the dephasing is related to ω_r, t_{CSA} and their inherent δ_{CSA}.

(f) $^{13}C\{^1H\}$ REDOR (rotational echo double resonances)

The dipolar interaction is very sensitive to distance according to the coupling strength D $\propto \hbar\gamma_S\gamma_I/r^3$. MAS can spin out dipolar interactions and make spectra better resolved. REDOR is one of techniques to recouple heteronuclear dipolar coupling under intermediate MAS speed. This is achieved by a train of 180° pulses at every half rotational period. [11]

The figure 3.10 displays the two pulse sequences used in $X\{^1H\}$ REDOR. (a) is with a ^1H-^{13}C dipolar recoupling 180° pulse train, measuring the dephased signal S; (b) is a reference pulse sequence measuring the reference signal S_0. Taking the ratio S/S_0 compensates for T_2 relaxation. The middle 180° pulse on the ^{13}C channel is used also to refocus the isotropic chemical shift of ^{13}C. Usually the 180° pulse train is not on the detection channel.

Here we can use average Hamiltonian theory to analyze REDOR within one rotor periods. The results can be similarly extended to Nt_r.

www.manaraa.com

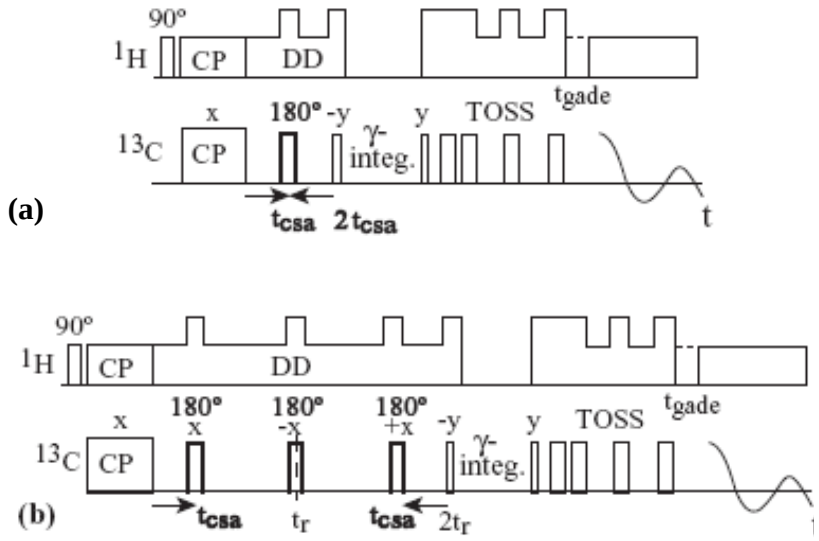

Figure 3.9. CSA recoupling pulse sequences. (a) 3-pulse sequence. The 180° pulse is used to refocuse the isotropic chemical shifts and recouple CSA. The two 90° pulses are used as z-filter to avoid phase-distorted signals and enable γ-averaging. (b) 5-pulse sequence. The three 180° with a fixed $2t_r$ time function similarly as (a). The t_{CSA} (< tr/2) can be tuned to get best suppressing results. Meanwhile the combination of three 180° pulses can alleviate the effects of pulse imperfections (adapted from [9]).

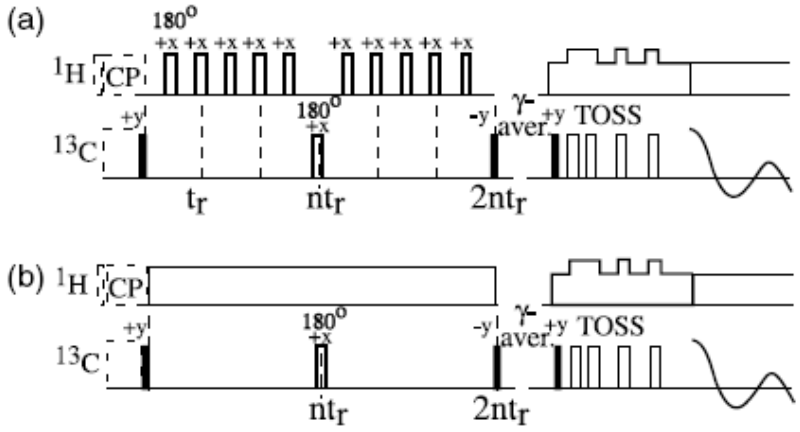

Figure 3.10. Rotational echo double resonance pulse sequence (a) and its reference (b). There is no 180° pulse train in (b) but it has same T_2 relaxation period as (a). Incrementationof the z-period in four steps of tr/4 (γ-average) before TOSS can suppress sidebands up to the fourth order. [12]

(1) After the 90° pulse on ^{13}C or through ^{1}H-^{13}C CP:

$$\rho(0) = S_x \qquad (2.33a)$$

www.manaraa.com

(2) At the end of t_r with central 180° pulse.

$$\begin{aligned}\rho_r(t_r) &= e^{i\Phi 2I_z S_z} e^{i\pi I_x} e^{-i\Phi 2I_z S_z} \rho(0) e^{i\Phi 2I_z S_z} e^{-i\pi I_x} e^{-i\Phi 2I_z S_z} \\ &= e^{i\Phi 2I_z S_z} e^{i\pi I_x} e^{i\Phi 2I_z S_z} \left[e^{-i\pi I_x} e^{i\pi I_x}\right] \rho(0) \left[e^{-i\pi I_x} e^{i\pi I_x}\right] e^{i\Phi 2I_z S_z} e^{-i\pi I_x} e^{-i\Phi 2I_z S_z} \\ &= e^{i\Phi 4I_z S_z} e^{i\pi I_x} S_x e^{-i\pi I_x} e^{-i\Phi 4I_z S_z} \\ &= S_x \cos\left[2\Phi\left(\frac{t_r}{2}\right)\frac{t_r}{2}\right] - 2S_y I_z \sin\left[2\Phi\left(\frac{t_r}{2}\right)\frac{t_r}{2}\right]\end{aligned} \tag{2.33b}$$

Here, $\Phi\left(\frac{t_r}{2}\right) = \int_0^{\frac{t_r}{2}} \omega_{IS}(t)\,dt \Rightarrow \overline{\omega}_{IS} = \frac{\Phi\left(\frac{t_r}{2}\right)}{\frac{t_r}{2}}$ and

$\omega_{ani}(t) = \widetilde{C_1}\cos\omega_r t + \widetilde{C_2}\cos 2\omega_r t + \widetilde{S_1}\sin\omega_r t + \widetilde{S_2}\sin 2\omega_r t$.

During $t_r/2$ periods, the integrals of the $2\omega_r t$ terms and cosine terms become zero and only $\widetilde{S_1}$ term remains.

Therefore $\Phi\left(\frac{t_r}{2}\right) = S_1\int_0^{\frac{t_r}{2}} \sin(\omega_r t)\,dt = \frac{\delta}{\pi}\cdot\sqrt{2}\sin(2\beta)\sin(\gamma)$

(3) Nt_r cycle.

$$\rho_r(Nt_r) = \pm S_x \cos\left[Nt_r \cdot 2\Phi\left(\frac{t_r}{2}\right)\right] \mp 2S_y I_z \sin\left[Nt_r \cdot 2\Phi\left(\frac{t_r}{2}\right)\right] \tag{2.33c}$$

$$\rho_r(Nt_r) = \pm S_x \cos\left(\overline{\omega_{IS}}\, Nt_r\right) \mp 2S_y I_z \sin\left(\overline{\omega_{IS}}\, Nt_r\right)$$

Only S_x is observable and the ratio can be expressed as

$$\frac{S}{S_0} = \sum_{\theta} \cos\left(Nt_r\,\overline{\omega_{IS}}\right)\sin(\theta) \tag{2.33d}$$

where when η=0, $\widetilde{S_1} = \frac{\delta}{2}\sqrt{2}\sin(2\beta)\sin(\gamma)$, $\overline{\omega_{IS}} = -\frac{\mu_0}{4\pi}\hbar\frac{\gamma^I\gamma^S}{r^3}\frac{1}{2}\left(3\cos^2\theta - 1\right)$ and $\sin(\theta)$ is geometry weight factor.

www.manaraa.com

The decay ratio is only related to the dipolar coupling. By measuring the amplitude ratio, distance and structure information can be extracted. The REDOR pulse sequence can also be embedded within other techniques to serve as dipolar coupling modulated magnetization evolution, e.g. in HSQC pulse sequences.

(g) CH selection

For any carbon-containing substances, spectral editing techniques can help to distinguish different protonated carbons such as C_q, CH, CH_2, and CH_3. This information can provide insights about their structure and assign cross peaks in multidimensional experiments.

In spectral editing, clean suppressions of the signals of other types of carbons are essential. In CH selection pulse sequence, CH_2 signals are eliminated during Multi-Quantum periods labeled in the diagram by the coupling of the carbon to the second ^1H. CH_3 is suppressed by using a T_1 filter. Meanwhile CH_3 and C_q remain in a corresponding spectrum with gated decoupling pulse sequence (leaving a short period of 40 μs without heteronuclear decoupling) before detection. The difference of the two spectra with or without gated decoupling gives the CH signals. The overall efficiency for CH selection is ~ 14 %. [13]

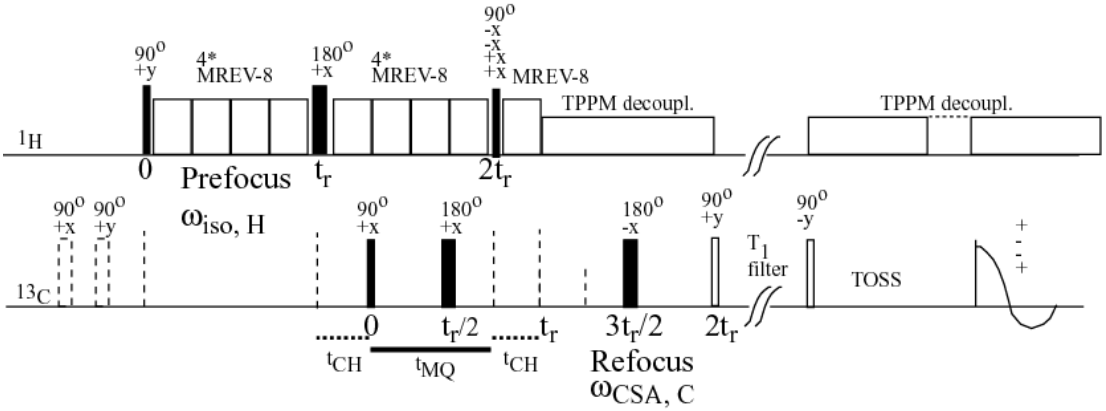

Figure 3.11. Block diagram of the CH-selection pulse sequence. MREV-8 is used for homonuclear decoupling between ^1H. Phase cycle is labeled on the diagram. 4-180° TOSS pulses are not plotted explicitly. [13]

The pulse sequence is shown in Figure 3.11. MREV-8 is used for homonuclear decoupling among ^1H.

www.manaraa.com

(1) ^{1}H is excited first by the first 90^{o} pulse on the ^{1}H channel.

(2) The chemical shift isotropy is refocused by the 180^{o} pulse in the middle of the first $2t_r$.

(3) During the first $t_{CH}(=t_r/4)$, ^{1}H magnetization is transferred to ^{13}C via heteronuclear dipolar coupling by generating MQ term $2I_yS_y\sin(\phi)$.

(4) During the MQ period as labeled in Figure 3.11, due to $[I_zS_z, I_yS_y] = 0$, heteronuclear dipolar coupling Hamiltonian $2I_zS_z$ is not effects on I_yS_y of CH. However, CH_2 have two protons. $I_z(A)S_z$ is not commuting with $I_y(B)S_y$, and vice versa. Therefore, during MQ period, heteronuclear coupling causes the CH_2 signals to decay quickly.

(5) During the second t_{CH}, only I_yS_y of CH is reconvert into SQ coherence as $[S_x\sin^2(\phi)]$.

(6) The second t_r period on the ^{13}C channel, a 180^{o} pulse at $3t_r/2$ is used to refocus the CSA, which is generated during the first t_r on the ^{1}H channel.

In this pulse sequence, the short dipolar transfer t_{CH} time $(t_r/4)$, the gated decoupling and T_1-filtering can reducing methyl signals and quaternary carbons.

(h) CH_2 selection [14]

The CH_2 selection pulse sequence is based on the factor that C (S spin) bonded to two H (I, J spins) can produce three spins coherence ($S_{x/y}I_ZJ_Z$), which cannot be produced by CH. Figure 3.12. (A) shows the essential part of the CH_2 pulse sequence. (B) is the pulse sequence used in experiments with chemical shift pre-refocusing, CSA refocusing, and a Z-filter. Homonuclear decoupling by MREV is used during only one t_r period. 0^{o} / 90^{o} pulses divide this t_r period into two parts: the first part is $t_r/4$ to generate the three spin coherence term. The second part $(3t_r/4)$ is used to reconvert the original three-spin coherence term into S_x for ^{13}C observation.

The density operator calculations are as follow based on Figure 3.12 (A).

www.manaraa.com

(1) After a short CP from ^{1}H to ^{13}C, the magnetization of ^{13}C is along x and can be written as:

$$\rho(0) = S_x \tag{2.34}$$

(2) During the τ period:

(i) The density operator for CH_I is:

$$\rho(\tau) = S_x \cos\Phi_{IS} + 2S_y I_z \sin\Phi_{IS} \tag{2.35}$$

Where $\Phi_{IS} = \int_0^\tau \omega_{IS}(t)dt$

(ii) The density operator for CH_2 is:

$$\begin{aligned}\rho(\tau) = {} & S_x \cos\Phi_{IS}\cos\Phi_{JS} + 2S_y I_z \sin\Phi_{IS}\cos\Phi_{JS} \\ & + 2S_y J_z \cos\Phi_{IS}\sin\Phi_{JS} - 4S_x I_z J_z \sin\Phi_{IS}\sin\Phi_{JS}\end{aligned} \tag{2.36}$$

Where $\Phi_{JS} = \int_0^\tau \omega_{JS}(t)dt$

(3) 90^o pulse on ^{13}C channel:

$$\begin{aligned}\rho(\tau) = {} & S_x \cos\Phi_{IS}\cos\Phi_{JS} + 2S_z I_z \sin\Phi_{IS}\cos\Phi_{JS} \\ & + 2S_z J_z \cos\Phi_{IS}\sin\Phi_{JS} - 4S_x I_z J_z \sin\Phi_{IS}\sin\Phi_{JS}\end{aligned} \tag{2.37}$$

(3) 0^o or 90^o pulse on ^{1}H channel (two 45^o pulses with x,-x or x,x phases in alternating scans):

$$\begin{aligned}\rho(\tau,0^o) = {} & S_x \cos\Phi_{IS}\cos\Phi_{JS} + 2S_z I_z \sin\Phi_{IS}\cos\Phi_{JS} \\ & + 2S_z J_z \cos\Phi_{IS}\sin\Phi_{JS} - 4S_x I_z J_z \sin\Phi_{IS}\sin\Phi_{JS}\end{aligned} \tag{2.38}$$

$$\begin{aligned}\rho(\tau,90_x^{\,o}) = {} & S_x \cos\Phi_{IS}\cos\Phi_{JS} - 2S_z I_y \sin\Phi_{IS}\cos\Phi_{JS} \\ & - 2S_z J_y \cos\Phi_{IS}\sin\Phi_{JS} - 4S_x I_y J_y \sin\Phi_{IS}\sin\Phi_{JS}\end{aligned} \tag{2.39}$$

www.manaraa.com

(4) By inverting the phase of the detector, the density operator of two subsequent scan is:

$$\begin{aligned}\rho(\tau,0_x^{\,o}) - \rho(\tau,90_x^{\,o}) &= 2(S_zI_z + S_zI_y)\sin\Phi_{IS}\cos\Phi_{JS} \\ &+ 2(S_zJ_z + S_zJ_y)\cos\Phi_{IS}\sin\Phi_{JS} \\ &- 4(\underline{S_xI_zJ_z} + S_xI_yJ_y)\sin\Phi_{IS}\sin\Phi_{JS}\end{aligned} \qquad (2.40)$$

(5) During the second part ($3t_r/4$) of the MREV-8 period, $[S_zI_z, I_zS_z] = 0$, $[S_zJ_z, J_zS_z] = 0$, $[S_xI_yJ_y, I_zS_z$ or $J_zS_z] = 0$. They will not evolve during this period and are also unobservable. The only term ($-4\, S_xI_zJ_z \sin\Phi_{IS} \sin\Phi_{IS}$) will be reconverted into magnetization S_x of ^{13}C.

The final density operator, per scan, can be written as:

$$\rho(4\tau) = -S_x\left\langle \sin^2\Phi_{IS}\sin^2\Phi_{JS}\right\rangle/2 \qquad (2.41)$$

As long as the τ ($= t_r/4$) value > 0.025 ms, the theoretical efficiency of CH_2 can reach 12.5 %.

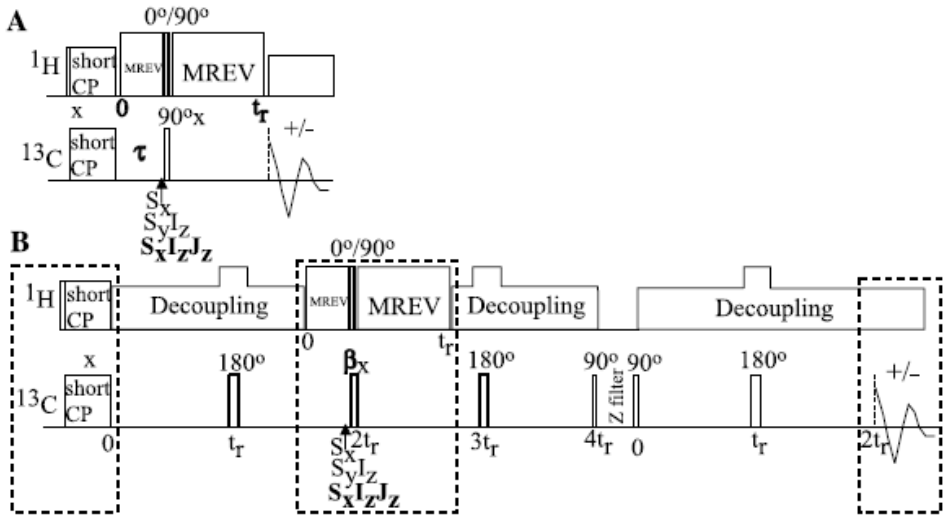

Figure 3.12. Pulse sequence for CH_2 spectral editing by three-spin coherence selection. (A) Simplified version, for explaining the method while neglecting chemical-shift and long-range coupling effects. (B) Actual version with prefocusing and refocusing of ^{13}C chemical-shift precession by 180° pulses, and with a $\beta > 90°$ pulse on ^{13}C to cancel signals from long-range couplings of CH groups. The basic phase cycle is indicated. The dipolar evolution time is $\tau = tr/4$, and the total homonuclear decoupling by MREV-8 is one rotation period in both sequences (adapted from [14]).

www.manaraa.com

Due to a combination of several factors: the short contact time on CP (~ 0.1 ms), short dipolar evolution time (~ 43 μs) and the Z-filtering, C_q and CH_3 can be further suppressed. In order to suppress the signal from long-distance coupling between C and H, the β pulse on ^{13}C is chosen as 101°.

(j) HARDSHIP

HARDSHIP stands for HeteronucleAr Recoupling with Dephasing by Strong Homonuclear Interactions of Protons. [15] Here are several key points listed for understanding the pulse sequence in figure 3.13.

(1) Sample should have distinguishable ^1H areas: (a) diluted ^1H domain and (b) surface or interface with abundant ^1H surrounding the dilute H domain such as nanodiamond with abundant H on surface and bulk C inside.

(2) The dephasing by the long T_2 ^1H is refocused by the end of every $2t_r$. ($\hat{H}_{(S-I)}$), therefore, long-T_2 ^1H do not contribute to total dephased intensity.

(3) The magnetization of short T_2 protons in the ^1H enriched domains decays completely before the magnetization dephasing can be refocused.

(4) Proton spin diffusion is slow and can be terminated by 90° pulse. Therefore, the distance simulation is more accurate than for regular REDOR, where spin diffusion must be considered for nucleus X coupling with multiple ^1H.

Figure 3.13 (a) shows the basic building block of the HARDSHIP pulse sequence, $t_c = Mt_r$ with $t_c << t_D$ (proton spin diffusion time). (i) In the first half, heteronuclear dipolar coupling is recoupled via regular REDOR with π pulse at every half t_r. The density operator of two-spin system can be written as:

$$\rho_{(S-I)}\left(Mt_r\right) = S_x \cos\left(2M\Phi\right) + 2S_y I_z \sin\left(2M\Phi\right) \qquad (2.42)$$

and the density operator of multispin symtem can be written as:

www.manaraa.com

$$\rho_{(S-I_n)}(Mt_r)$$
$$= S_x \Pi_n \cos(2M\Phi_n) + 2S_y \Sigma_n I_{z,n} \sin(2M\Phi_n) \Pi_{k\neq n} \cos(2M\Phi_k)$$
$$- 4S_x \Sigma_{n,m} I_{z,n} I_{z,m} \sin(2M\Phi_n) \sin(2M\Phi_m) \Pi_{k\neq n,m} \cos(2M\Phi_k)$$
$$- 8 S_y \Sigma_{n,m,j} I_{z,n} I_{z,m} I_{z,j} \sin(2M\Phi_n) \sin(2M\Phi_m) \sin(2M\Phi_j) \Pi_{k\neq n,m,j} \cos(2M\Phi_k) + \ldots$$

(2.43)

(ii) Two canceling π/2 pulses on the middle t_r period terminate the REDOR recoupling and make all $I_{z,n}$ term turn to the transverse plane. Since the S-I system has the long T_2, the change of the component is very small. However the short T_2 of S-I_n system make all transverse plane $I_{x/y,\,n}$ term decay due to T_2 relaxation. [16]

$$\rho_{(S-I)}(Mt_r + t_r) = S_x \cos(2M\Phi) + r2S_y I_z \sin(2M\Phi) \qquad (2.43)$$

(Here r is the remaining percentage after T_2 decay, r ≈1)

$$\rho_{S-I_n}(Mt_r + t_r) = S_x \Pi_n \cos(2M\Phi_n) \qquad (2.44)$$

(iii) At the end of the following REDOR period, since heteronuclear dipolar coupling Hamiltonian sign is changed into $-2I_zS_z$, the S-I coherence is refocused in an echo. For the strong homonuclear interaction S-I_n system, the detected S magnetization is partly dephased by the heteronuclear coupling. Equation (2.45) and (2.46) display only observed terms.

$$\rho_{(S-I)}(2Mt_r + t_r) = S_x\left\{\cos^2(2M\Phi) + r\sin^2(2M\Phi)\right\} \approx S_x \qquad (2.45)$$

$$\rho_{(S-I_n)}(2Mt_r + t_r) = \rho_{(S-I_n)}(Mt_r)\left\{\Pi_n \cos(2M\Phi_n)\right\}^2 \qquad (2.46)$$

(iv) After N cycles:

$$\rho_{(S-I)}\left\{N(2Mt_r + t_r)\right\} = S_x\left\{\cos^2(2M\Phi) + r\sin^2(2M\Phi)\right\}^N \approx S_x \qquad (2.47)$$

www.manaraa.com

$$\rho_{(S-I_n)}\left\{N\left(2Mt_r+t_r\right)\right\}=\rho_{(S-I_n)}\left(Mt_r\right)\left\{\Pi_n\cos\left(2M\Phi_n\right)\right\}^{2N}$$

$$\longrightarrow \frac{S}{S_0}=\left\{\Pi_n\cos\left(2M\Phi_n\right)\right\}^{2N}$$

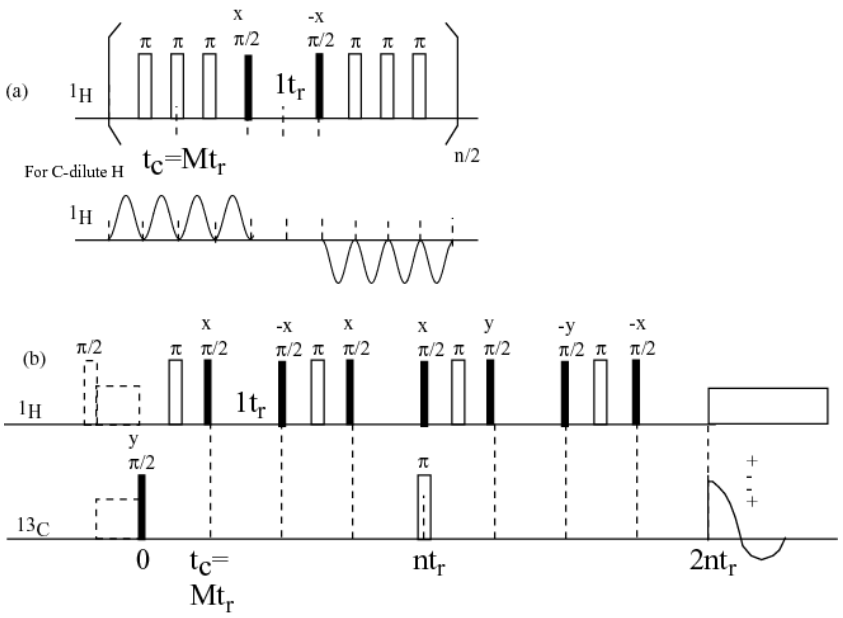

Fiugre. 3.13 (a) The basic cycle block of HARDSHIP pulse sequence. (b) the pulse sequence for intermediate spinning speeds (3.3-10 kHz) (adapted from [15])

(k) SUPER

SUPER stands for two-dimensional separation of undistorted chemical-shift anisotropy powder patterns in magic-angle-spinning. [17] The pulse sequence is shown in figure 3.14. The isotropic chemical shift in the ω_2 dimension correlates with the ω_1 dimension information of quasi-static chemical shift powder patterns. The two dimensional signal can be expressed as:

$$S\left(t_1,\omega_2\right)=\left\langle\exp\left(i\,\bar{\omega}\,t_1\right)\right\rangle\delta\left(\omega_2-\omega_{iso}\right) \qquad (2.48)$$

www.manaraa.com

In equation (2.48), the averaged precession frequency contains two scaled frequencies: chemical shift anisotropy: $\chi' \omega_{ani}$, and isotropic chemical shift: $\xi' \omega_{iso}$. Here, χ' and ξ' are their corresponding scaling factors.

$$\begin{aligned}\bar{\omega} &= \bar{\omega}_{ani} + \bar{\omega}_{iso} \\ &= \frac{1}{t_r}\int_0^{tr} p(t)\,\omega_{ani}(t)\,dt + \omega_{iso}\frac{1}{t_r}\int_0^{tr} p(t)(t)\,dt \\ &= \chi'\,\omega_{ani,stat.} + \xi'\,\omega_{iso}\end{aligned} \tag{2.49}$$

In equation (2.49), ω_{ani} can be explicited by calculated as:

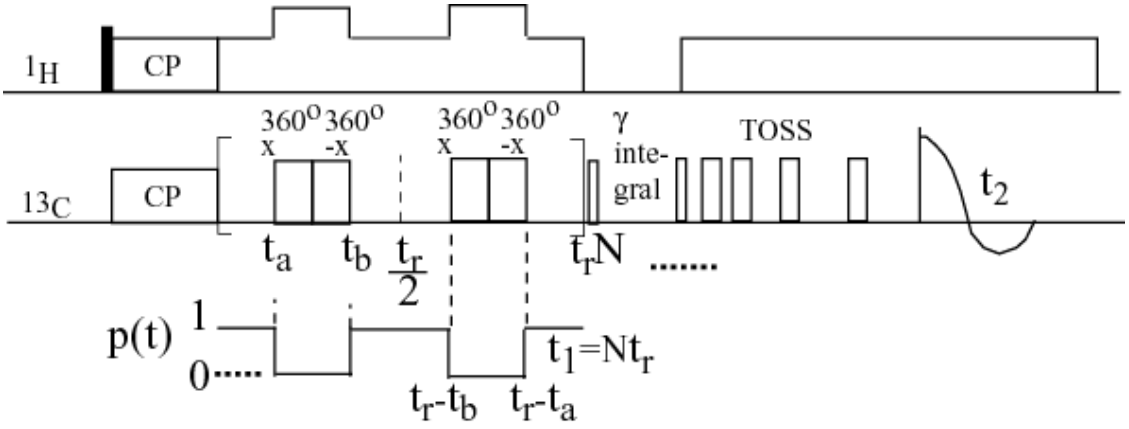

Figure. 3.14 Pulse sequence of two-dimensional SUPER. The ω_1 dimension contains quasi-static chemical shift powder patterns with frequency window as ω_r. the w2 dimension only contains chemical shift isotropy, therefore make the signal separation and easily access the function group features in terms chemical shift anisotropy (adapted from [17]).

$$\omega_{ani}(t) = \widetilde{C_1}\cos\omega_r t + \widetilde{C_2}\cos 2\omega_r t + \widetilde{S_1}\sin\omega_r t + \widetilde{S_2}\sin 2\omega_r t \tag{2.50}$$

When $\omega_r = 0$, this is static precession frequency.

$$\omega_{ani,stat.}(t) = C_1 + C_2 \tag{2.51}$$

www.manaraa.com

Only if χ' satisfy the following equation (2.52), the average chemical shift anisotropy can produce a static powder pattern with a scaling factor χ'.

$$\begin{aligned}\chi' &= \frac{1}{t_r}\int_0^{t_r} p(t)\cos(n\omega_r t)\,dt \\ &= \frac{1}{t_r}\int_0^{t_r}\cos(n\omega_r t)\,dt - \frac{2}{t_r}\int_{t_a}^{t_b}\cos(n\omega_r t)\,dt \\ &= -\frac{2}{t_r}\int_{t_a}^{t_b}\cos(n\omega_r t)\,dt \\ &= \frac{1}{\pi n}\left(\sin(n\omega_r t_a) - \sin\left(n\omega_r t_b\right)\right)\end{aligned} \tag{2.52}$$

According to the equation above, χ' is dependent on the timing of t_a, t_b and MAS speed.

The scaling factor ξ' of ω_{iso} is also dependent on timing of t_a, t_b and t_r.

$$\xi' = \frac{1}{t_r}\int_0^{t_r} p(t)\,dt = 1 - 2\left(\frac{t_b - t_a}{t_r}\right) \tag{2.53}$$

(l) ^{13}C-^{1}H FSLG-HETCOR

Multidimensional NMR experiments can separate signals into several spectral dimensions and construct correlations between different NMR features such as isotropic and/or anisotropic chemical shifts. HETCOR (Heteronuclear correlation) is a very popular two-dimensional NMR technique in solid state NMR. It directly detects dilute nuclei (e.g. ^{13}C) signals, and the signals of abundant nucleus (e.g. ^{1}H) are indirectly observed shown as Figure 3.7. (A). TPPM is used for heteronuclear decoupling during t_2 acquisition. Without decoupling the ^{1}H peaks on F1 dimension are very broad due to strong homonuclear dipolar coupling, unless fast motions are present. Homonuclear decoupling, for instance by frequency switched Lee Goldburg irradiation, is used to reduce the ^{1}H-^{1}H homonuclear dipolar coupling and thus increase the ^{1}H dimension resolution in 2D HETCOR.

www.manaraa.com

In order to explain the pulse sequence in Figure 3.15 (B), it can be divided into three periods: (1) θ_m pulse, (2) t_1, (3) Lee-Goldburg (LG)-CP for polarization transfer from ^1H to ^{13}C. The first two periods will be described in detail to explain how the proton spectra resolution is improved. Here two interactions need to be considered separately: (1) $\hat{H}_{cs,I}$ and (2) $\hat{H}_{II}$. The pulse sequences have three coordinate frames: (1) lab frame, (2) tiled frame created by θ_m pulses, (3) interaction frame created by spin lock field.

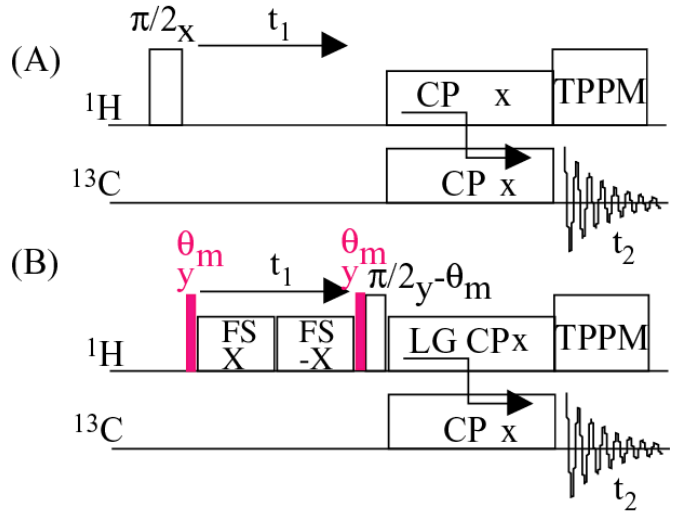

Figure. 3.15 (A) normal wide line separation 2D HETCOR. (B) During t_1 dimension frequency shift LG CP is used to increase ^1H dimension resolution (adapted from [18]).

Since t_1 dimension is for ^1H signal observation, two interactions, chemical shift and homonuclear dipolar coupling, are involved. The spin lock field frequencies are offset by $\Delta\omega$. The effective field relates irradiation strength $\omega_{1,I}$ and $\Delta\omega$: $\omega_{eff} = \sqrt{\Delta\omega^2 + \omega_{1,I}^2}$, and they fulfill the following relations: $\omega_{1,I} = \omega_{eff} \sin\theta_m$, $\Delta\omega = \omega_{eff} \cos\theta_m$

During the FS spin lock field, the RF Hamiltonian in the lab frame is:

$$\hat{H}^{L}_{RF,I} = \omega_{1I} \hat{I}_x + \Delta\omega \hat{I}_z \qquad (2.54)$$

It can be transformed into tilted frame by applying θ_m pulse

www.manaraa.com

$$\hat{H}'_{RF,I} = \omega_{1I}\left(\hat{I}_x \cos\theta_m - \hat{I}_z \sin\theta_m\right) + \Delta\omega\left(\hat{I}_z \cos\theta_m + \hat{I}_x \sin\theta_m\right)\cdot = \hat{I}_z\,\omega_{eff} \qquad (2.55)$$

(a) For chemical shift Hamiltonian in the lab frame and tilted frame:

$$\hat{H}^L_{cs,I} = \omega_{cs,I}\hat{I}_z \qquad (2.56)$$

$$\hat{H}'_{cs,I} = \omega_{cs,I}\left(\hat{I}_z \cos\theta_m + \hat{I}_x \sin\theta_m\right) \qquad (2.57)$$

The chemical shift Hamiltonian can be transformed into the interaction frame with the RF pulse.

$$\overline{\hat{H}^T_{cs,I}} = \frac{1}{t^p}\int_0^{t^p} \omega_{cs,I}\left[\hat{I}_z \cos\theta_m + \hat{I}_x \sin\theta_m \cos\left(\omega_{eff}\,t\right) + \hat{I}_y \sin\theta_m \sin\left(\omega_{eff}\,t\right)\right]dt \qquad (2.58)$$

When $t^p >> \frac{1}{\omega_{eff}}$, so that

$$\overline{\hat{H}^T_{cs,I}} = \omega_{cs,I}\hat{I}_z \cos\theta_m \qquad (2.59)$$

It is why the chemical shift of proton is linearly scaled by $\cos\theta_m$. For the chemical shift Hamiltonian, the second FS spin lock field gives the same result.

(b) For homonuclear interaction Hamiltonian in the lab frame and tilted frame:

$$\hat{H}^L_{II} = \omega_{II}\left(3\hat{I}^j_z\hat{I}^k_z - \hat{I}^j\hat{I}^k\right) \qquad (2.60)$$

$$\hat{H}'_{II} = \omega_{II}\left[3\left(\hat{I}^j_z \cos\theta_m + \hat{I}^j_x \sin\theta_m\right)\left(\hat{I}^k_z \cos\theta_m + \hat{I}^k_x \sin\theta_m\right) - \hat{I}^j\hat{I}^k\right] \qquad (2.61)$$

The $\hat{H}'_{II}$ can be transformed into interaction frame with the RF pulse.

www.manaraa.com

$$\overline{H_{II}^{T}} = \frac{\omega_{II}}{t^{p}} \int_{0}^{t^{p}} \left[\begin{array}{l} 3\left[\hat{I}_{z}^{j} \cos\theta_{m} + \hat{I}_{x}^{j} \sin\theta_{m} \cos\left(\omega_{eff}\, t\right) + \hat{I}_{y}^{j} \sin\theta_{m} \sin\left(\omega_{eff}\, t\right) \right] \\ \quad \times \left[\hat{I}_{z}^{k} \cos\theta_{m} + \hat{I}_{x}^{k} \sin\theta_{m} \cos\left(\omega_{eff}\, t\right) + \hat{I}_{y}^{k} \sin\theta_{m} \sin\left(\omega_{eff}\, t\right) \right] dt - \hat{I}^{j} \hat{I}^{k} \end{array} \right] \quad (2.62)$$

$$= \omega_{II} \left[3\hat{I}_{z}^{j} \hat{I}_{z}^{k} \cos^{2}\theta_{m} + \frac{3}{2} \hat{I}_{x}^{j} \hat{I}_{x}^{k} \sin^{2}\theta_{m} + \frac{3}{2} \hat{I}_{y}^{j} \hat{I}_{y}^{k} \sin^{2}\theta_{m} - \hat{I}^{j} \hat{I}^{k} \right]$$

$$= 0$$

Here, $t^{p} >> \frac{1}{\omega_{eff}}$, and $\sin^{2}\theta_{m} = \frac{2}{3}$, $\cos^{2}\theta_{m} = \frac{1}{3}$.

If the θ_m pulse is 90°, the homonuclear interaction Hamiltonian is scaled by 1/2 (see equation 3.24 in ref. [1]. Through the spin lock field frequency switch (from $\omega_{1,I}$ to $-\omega_{1,I}$), the sum of homonuclear interaction Hamiltonian at interaction frame will be zero.

In summary, the homonuclear dipolar interaction in ω_1 is averaged out and the chemical shift of proton is linearly scaled by $\cos\theta_m$.

(k) ^{13}C-^{13}C spin exchange

2D ^{13}C-^{13}C spin exchange experiments are very important for structural elucidation because they directly provide the C-C chemical bonds network and enable specific structure to be assigned.

The pulse sequence is shown in Figure 3.16. ^{1}H-^{13}C CP transfers polarization from ^{1}H to ^{13}C and ^{13}C chemical shifts of multiple sites develop separately at t_1 dimension with TOSS to suppress spinning sidebands. The first 90° pulse of carbon channel rotates the magnetizations of ^{13}C to the Z-direction otherwise the short T^{*}_{2} (~ 10 μs) in solid samples destroys the ^{13}C transverse signals quickly without spin diffusion building up. The dipolar interaction between ^{13}C-^{13}C within a distance of 0.15 nm is around 2 kHz. We usually chose a MAS frequency around 7 kHz in our 2D or 3D experiments. If no abundant protons exist as dipolar reservoir, MAS is sufficient to average out the ^{13}C-^{13}C dipolar coupling.

www.manaraa.com

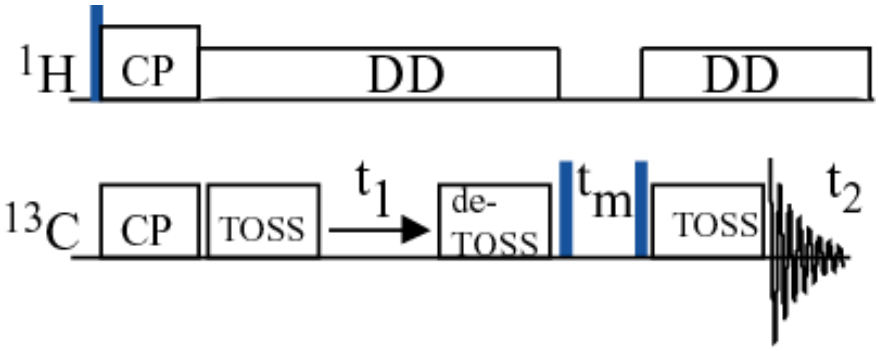

Figure. 3.16. 2D ^{13}C-^{13}C chemical shift correlation experiments via proton driven spin diffusion and combined with TOSS-deTOSS-TOSS pulses. t_m is mixing time for dipolar incoherence transfer from $^{13}C_a$ to $^{1}H_a$, coherence transfer from $^{1}H_a$ to $^{1}H_b$ and incoherence transfer back to $^{13}C_b$. This pulse sequence is suitable for ^{13}C enriched samples (adapted from [1]).

During t_m mixing time, the heteronuclear dipolar decoupling pulse on ^{1}H channel is off. Proton homonuclear dipolar interactions facilitate the polarization transfer to farther distance. Since the spin diffusion is dipolar coupling mediated polarization transferring, it is sensitive to distance. Two sites connected through direct single chemical bond have shortest distance and will give cross peak easily. Usually t_m of 50 ms is used in our studies.

(l) ^{13}C-^{15}N HSQC

The melanoidin samples are made from ^{13}C and ^{15}N labeled reactants (^{13}C-glucose and ^{13}C or ^{15}N-glycine), the isotope labeling enables us to use pulse sequences such as 2D ^{13}C-^{13}C spin exchange and ^{13}C-^{15}N HSQC quite easily and even combine these two pulse sequences for 3D experiments.

The ^{13}C-^{15}N HSQC pulse sequence, shown in figure 3.17, contains two INEPT (Insensitive Nuclei Enhanced by Polarization Transfer) sequences separated by a t_1 period. In the first step, ^{1}H is excited by a 90° pulse and then polarization is transferred to ^{13}C via cross polarization, $\rho(0) = S_x$. The first INEPT transfers ^{13}C polarization to ^{15}N via REDOR dipolar recoupling (instead of J-coupling, used in solution NMR) by applying two simultaneous π pulses on both ^{13}C and ^{15}N channels. The spin density operator at the end of the first INEPT block can be written as: [2]

www.manaraa.com

$$\rho\left(1^{st}, INEPT\right) = S_x \cos(2\Phi t) + \underline{2S_Z L_y \sin(2\Phi t)} \qquad (2.63)$$

During t_1 evolution, the second antiphase term can be detected under dipolar coupling during t_1 evolution. The density operator at the end of t_1 is:

$$\rho\left(t_1\right) = \ldots + 2S_Z L_y \sin(2\Phi t)\cos\left(2\Phi t_1\right) \underline{- L_x \sin(2\Phi t)\sin\left(2\Phi t_1\right)} \qquad (2.64)$$

Here the first term in equation (2.63) and their derivative terms are omitted since t_1 is for ^{15}N evolution. The reversed polarization transform (^{15}N to ^{13}C) occurs during the second INEPT and the density operator can be written as:

$$\begin{aligned}\rho\left(2^{nd}, INEPT\right) = \ldots & - L_x \sin(2\Phi t)\cos(2\Phi t)\sin\left(2\Phi t_1\right) \\ & \underline{+ 2S_y L_z \sin(2\Phi t)\sin(2\Phi t)\sin\left(2\Phi t_1\right)}\end{aligned} \qquad (2.65)$$

The density operator at the end of t_2 acquisition is:

$$\begin{aligned}\rho\left(t_2\right) = \ldots & \; 2S_y L_z \sin^2(2\Phi t)\sin\left(2\Phi t_1\right)\cos\left(2\Phi t_2\right) \\ & \underline{- S_x \sin^2(2\Phi t)\sin\left(2\Phi t_1\right)\sin\left(2\Phi t_2\right)}\end{aligned} \qquad (2.66)$$

Therefore the correlation is built via dipolar interaction between adjacent ^{13}C and ^{15}N.

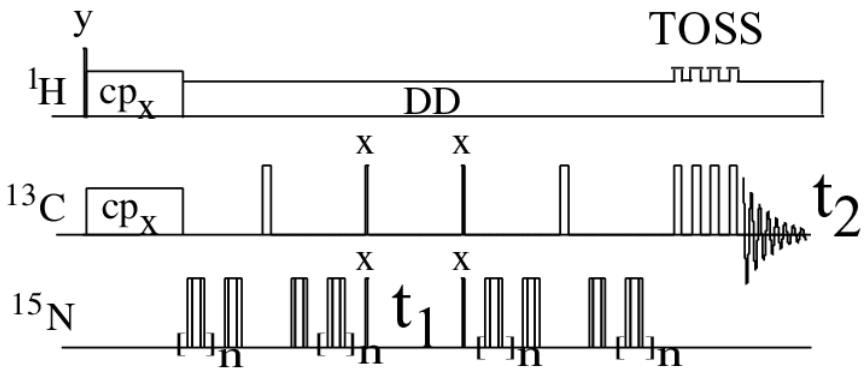

Figure. 3.17 The pulse sequence of ^{13}C-^{15}N HSQC. Usually at 7 kHz MAS, the dipolar recoupling period during each INEPT is 5 ms.

www.manaraa.com

Reference

1. Schmidt-Rohr, K.; Spiess, H. W., *Multidimensional solid-state NMR and polymers*. Academic Press, INC: San Diego, CA, 1999.
2. Cavanagh, J.; Faribrother, W. J.; Palmer III, A. G.; Skelton, N. J., *Protein NMR spectroscopy principles & practice. Academic press*. Academic press: 1996.
3. deAzevedo, E. R.; Bonagamba, T. J. *Brazilian Journal of Physics.* **2006,** *36,* 61-74.
4. Dingley, A. J.; Cordier, F.; Grzesiek, S. *Concepts in magentic resonance* **2001,** *13,* 103-127.
5. Wilkens, S. J.; Westler, W. M.; Markley, J. L.; Weinhold, F. *J. Am. Chem. Soc.* **2001,** *123,* 12026-12036.
6. Samoson, A. *Encycl. Nucl. Magn. Reson.* **2002,** *9,* 59-64.
7. Dixon, W. T. *J. Chem. Phys.* **1982,** *77,* 1800-1809.
8. Mao, J.-D.; Hu, W.-G.; Schmidt-Rohr, K.; Davies, G.; Ghabbour, E. A.; Xing, B. *Soil Sci. Soc. Am. J.* **2000,** *64,* 873-884.
9. Mao, J. D. S.-R., K.. *Solid state nuclear magnetic resonance* **2004,** *26,* 36-45.
10. Mao, J.-D., Schmidt-Rohr, K. *Solid State Nucl. Magn. Reson.* **2004,** *26,* 36-45.
11. Gullion, T. *Conc. magen. reson.* **1998,** *10,* 277-289.
12. deAzevedo, E. R.; Hu, W.-G.; Bonagamba, T. J.; Schmidt-Rohr, K. *J. Chem. Phys.* **2000,** *112,* 8988-9001.
13. Schmidt-Rohr, K. M., J.D. *J. AM. CHEM. SOC.* **2002,** *124,* 13938-13948.
14. Mao, J.-D.; Schmidt-Rohr, K. *J. Magn. Reson.* **2005,** *176,* 1-6.
15. Schmidt-Rohr, K., Rawal, A., Fang, X.W. *J. Chem. Phys.* **2007,** *126,* 054701-054701-054716.
16. Rawal, A. NMR investigations of biological and synthetic phosphate-based nanocomposites. Iowa State University, Ames, **2008**.
17. Liu, S. F.; Mao, J. D.; Schmidt-Rohr, K. *J. Magn. Res.* **2002,** *155,* 15-28.
18. VAN Rossum, B. J. F., H.; De Groot, H.J.M.. *Journal of magnetic resonance* **1997,** *124,* 516-519.

www.manaraa.com

CHAPTER 4. The fate of glycine in the Maillard reaction investigated by solid-state NMR

In the style of a paper to be submitted to The Journal of the American Chemical Society

Xiaowen Fang, Klaus Schmidt-Rohr*

Abstract

The fate of the amino acid in the Maillard reaction between glycine and glucose in a 1:1 molar ratio has been investigated by applying various ^{13}C and ^{15}N solid-state nuclear magnetic resonance (NMR) techniques to high molecular weight melanoidins formed in both dry and solution reactions. Quantitative ^{13}C NMR shows that ~18% of carbon in the final products is from glycine, which indicates that a quarter more moles of glycine than glucose are liberated during the Maillard reaction. Nevertheless, there is no significant difference between C1 and C2 of glycine in terms their individual mass loss under either reaction condition, indicating that loss of just C1 as CO_2 is not a major pathway of glycine loss. ^{13}C J-modulation experiments on melanoidins made from doubly ^{13}C-labeled glycine show that the C-C backbone of most (~73% for the dry and ~ 55% for the solution reaction) of the incorporated amino acids stays intact, and cannot have undergone Strecker degradation where the C1 carbon would have split off as CO_2. ^{13}C-^{13}C break-up occurs in the relatively rare instances when C2 is incorporated into NCH_3, $C\underline{C}H_n$, or aromatic units. The gycine-C1 carbon incorporated into the melanoidins predominantly (>90%) remains part of COO moieties, forming mostly COOH end groups, as well as some ester linkages. The C2-N bond remains intact for ~ 75% (in the dry reaction) and ~ 63% (in the solution reaction) of the incorporated glycine as proven by $^{13}C\{^{15}N\}$ and $^{15}N\{^{13}C\}$ REDOR. While ^{13}C spectra of glycine carbons in melanoidins are relatively simple, with dominant COO and NCH_2 resonances, the ^{15}N spectra of glycine nitrogen show many peaks, over a 200-ppm range. ^{15}N and ^{13}C-detected $^{15}N\{^{1}H\}$ dipolar dephasing experiments show that the majority (> 80 %) of the nitrogen in the melanoidins, in particular most pyrrolic N, is not protonated. Most of the features described are observed similarly for dry and solution reactions; in particular, the results indicate that nonprotonated nitrogen may be a characteristic marker of Maillard reaction products.

www.manaraa.com

Introduction

The Maillard or unenzymatic browning reaction of reducing sugars with amine compounds (e.g. amino acids) is of significant interest in a wide variety of fields, such as food science, medicine,[1] and soil science.[2, 3] The formation of caramel candy from sugar and milk protein, and the baking of cookies from sugar and egg protein are particularly pertinent examples of the Maillard reaction. In spite of their common occurrence, the structures of the final products of the Maillard reaction are poorly known due to their great complexities.

A complex network of Maillard reactions, including the Amadori rearrangement of sugar-amino acid condensation products *N*-substituted glycosylamine derivative of the amine component, de-amination, sugar dehydration and fragmentation, the Strecker degradation of amino acids,[4-6] has been proposed for the initial and intermediate steps of the Maillard reaction. In the Strecker degradation, the amino acid is broken into CO_2, an aldehyde, and nitrogen liberated as ammonia or reintegrated with sugar carbons to form a variety structures, see Scheme 1.

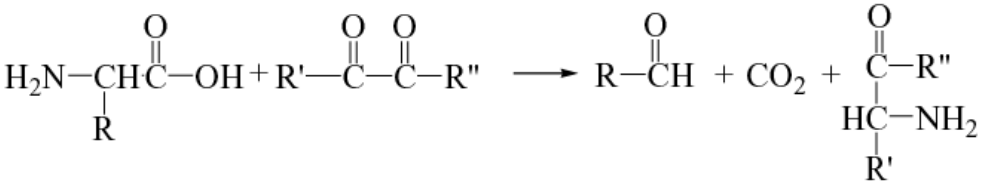

Scheme 1. Strecker degradation of an amino acid reacting with a reductone

In this paper, we will show that most glycine does not undergo the Strecker degradation in both dry and solution Maillard reactions.

Rather little is known about the later steps as well as the polymeric melanoidins formed in the end. The presence of aromatic five-membered heterocyclic rings such as furan and pyrroles has been established by NMR and mass spectrometry,[7-9] but not really explained for hexose sugar reactants. We have now tackled this issue by multidimensional and multinuclear NMR of ^{13}C- and ^{15}N-labeled melanoidins. Here we focus on the fate of the amino acid, which is relatively simple compared with the transformations of the sugar.

www.manaraa.com

Modern NMR of suitably ^{13}C- or ^{15}N-labeled compounds can elucidate the amount, type, and connectivity of carbons or of carbons and nitrogens introduced into the melanoidin from a specific site in a reactant. Quantitative ^{13}C NMR and a technique for selecting isolated ^{13}C spins in a melanoidin produced from doubly ^{13}C-labeled glycine enable us to assess the occurrence of fragmentation at the C-C bond of glycine, while fragmentation at the C-N bond was probed by ^{15}N-^{13}C experiments. In order to distinguish NH_n from tertiary N_t, we performed carbon detected $^{15}N\{^1H\}$ dipolar dephasing experiments, which can avoid the bias of ^1H-^{15}N CP experiments in favor of protonated nitrogen.

Experimental Section

Materials. D-glucose, anhydrous 99+% (MW 180.16) and glycine, 98% (FW 75.06) were purchased from Acros Organics (NJ USA). D-Glucose (U-$^{13}C_6$, 99%, CLM-1396-1) and three labeled glycines (1-^{13}C, 99 %, CLM-422-1; 2-^{13}C, 99%, CLM-136-1; and ^{15}N, 98%, NLM-202-1) were obtained from CIL Inc. (MA USA). Glycine-2-^{13}C-^{15}N (99 atom % ^{13}C, 98+ atom % ^{15}N) was obtained from Isotec (OH USA). If not otherwise mentioned, the following chemicals are A.C.S. grade and were purchased from Fisher scientific: $NaH_2PO_4 \cdot H_2O$ (FW=137.99), $Na_2HPO_4 \cdot 7H_2O$ (FW=268.07), Na_2CO_3 (FW=105.99). The dialysis tubing used was made of regenerated cellulose from Fisherbrand with nominal MWCO 6000 to 8000, vol/cm = 5.10 ml. Filter papers are 41 ashless from Whatman (England). Water is E-pure water (Barnstead).

Sample preparation

Melanoidin from dry reaction. Following reference,[6] an equimolar mixture of glucose and glycine (5.6 mmol each) was dissolved in 10 to 15 ml E-pure water in a scintillation vial, and was freeze-dried for one day using a lyophilizer (Labconco Freezon 4.5). The dried sample in the scintillation vial was heated in a closed preheated oven (VMR scientific products, Model 1430) for 2 hours at 125 ^oC. After heating for two hours, the color of the sample turned to dark brown and its volume increased. When cooled down to room temperature in a desiccator, the sample was dissolved into 100 ml of E-pure water, with magnetic stirring for one hour to dissolve as much sample as possible. Then the solution was filtered twice through filter paper, the filtrate was collected and transferred into 30-cm long dialysis tubing.

www.manaraa.com

The tubing was submerged in 2 L of E-pure water at 4 ^{o}C. Every 12 hours, the water surrounding the dialysis tubing was replaced with fresh water (2000 ml) for four times total. After 48 hours of dialysis, the solution in the tubing was collected and freeze-dried. This high molecular weight fraction melanoidin was analyzed in this study.

Melanoidin from solution reaction. Following reference,[10] a 500 ml flask containing 100 ml solution of D-Glucose and glycine (0.056 M each) dissolved in a pH=8 buffer solution was sealed and heated in a preheated oven at 100 ^{o}C for one week. After the first 48 hours, the color of the solution turned brown and the pH dropped to ~5. $Na_2HPO_4 \cdot 7H_2O$ was added to adjust the pH back to 8 at room temperature. Another five days of reaction caused the pH of the solution drop to less than 6. The remaining steps (filtering, dialysis, and freeze-drying) were same as for the dry-reaction products.

NMR parameters. Solid-state MAS NMR experiments were performed at room temperature using a Bruker DSX 400 spectrometer at 400 MHz for ^{1}H, 100 MHz for ^{13}C, and 40 MHz for ^{15}N. A Bruker 4-mm triple-resonance magic-angle spinning (MAS) probe head was used for ^{13}C and ^{15}N measurements of isotopically labeled samples at the various MAS speeds, while the unlabeled melanoidin samples were measured using a 7-mm Bruker double-resonance probe head at 6.5 kHz MAS. 4-mm and 7-mm diameter ZrO_2 rotors were used with 4 mm length glass inserts at the bottom to constrain the sample to within the radio frequency coil. ^{13}C and ^{1}H chemical shifts were referenced to TMS, using the COO^- resonance of α-glycine at 176.49 ppm as a secondary reference for ^{13}C, and the NIST hydroxyapatite proton peak at 0.18 ppm as a secondary reference for ^{1}H. The ^{15}N chemical shifts were referenced to liquid ammonia by setting the N-actyl valine peak to 122 ppm. The 90^{o} pulse length was 4 μs for both ^{13}C and ^{1}H. Two-Pulse Phase Modulation (TPPM) decoupling on the ^{1}H channel was applied during ^{13}C or ^{15}N signal detection.

CP/TOSS NMR. For routine analysis of unlabeled and labeled samples, ^{1}H-^{13}C CP combined with four-pulse TOtal Suppression of Spinning sidebands (TOSS)[11] spectra were acquired at 6.5 kHz MAS. The CP contact time was 1 ms, and the recycle delay was 3 s.

www.manaraa.com

High-speed quantitative ^{13}C DP/echo/MAS NMR. In order to quantify the percentages of glycine-C1 and C2 in the melanoidins, quantitative ^{13}C Direct Polarization (DP)/MAS NMR spectra were acquired for the samples produced from singly or doubly glycine-^{13}C labeling reactants at 14 kHz MAS. A Hahn echo requiring two rotation periods was used before detection to avoid baseline distortions. The recycle delays were estimated by measuring CP/T_1/TOSS spectra with two or three different T_1 filter time. The T_1 filter time that reduced all carbon signals to less than ~ 5% of the full intensity was chosen as the recycle delay of the quantitative DP/echo/MAS experiment, which ensures that all carbons are fully relaxed. More details are given in reference.[12]

Two-dimensional separation of undistorted chemical shift anisotropy powderpatterns (SUPER). The ^{13}C chemical-shift anisotropy powder pattern of COOC is different than those of COOH or COO^- because of their different electronic environments. By the 2D SUPER technique, the powder pattern can be measured for each isotropic chemical shift. During each t_1 rotation period, two 720° pulses (consisting of four 180° pulses) on the ^{13}C channel were applied symmetrically to recouple the chemical shift anisotropy. More details regarding the principle of SUPER pulse sequence and the powder patterns of different carbon functional groups can be found in reference.[13] SUPER was applied to the glycine-$^{13}C1$ labeled melanoidins to elucidate the chemical structure of the COO groups. A cross-polarization time of 1 ms was used, at a spinning frequency of 5 kHz. The increment of the evolution time t_1 was one rotation period (t_r = 200 μs).

CH_2 spectral editing. Spectral editing of CH_2 signals was achieved by selection of the three-spin coherence of CH_2 groups, using a ^{13}C 90° pulse and ^1H 0°/180° pulses applied after $t_r/4$ with MREV-8 decoupling.[14] The MAS frequency was 5.787 kHz.

Isolated ^{13}C vs. ^{13}C-^{13}C spin-pairs. After the Maillard reaction, the chemical bond connectivity of C1-C2 of glycine was determined using J_{C-C}-modulation solid echo pulse sequence, see Figure 1. In this pulse sequence, after a 90° excitation pulse for direct polarization of ^{13}C, heteronuclear TPPM decoupling is turned on. On the ^{13}C channel, two back-to-back 45° pulses divide a total period of ~ 10 ms (68 t_r at a MAS frequency of 7 kHz)

www.manaraa.com

into two parts before detection. [15, 16] Two 180° pulses were placed in the middle of each part to refocus isotropic chemical shift evolution. When the two 45° pulses are of the same phase, a solid echo is generated to refocus the evolution under the J-coupling, and this signal is recorded as a reference, S_0. The S_0 signal decays because of T_2 relaxation. If the two 45° pulses have +x and –x phases to cancel each other, the J-coupling effects continue to accumulate and dephase the magnetization of ^{13}C-^{13}C spin pairs. The J-dephased spectrum S contains only signals of ^{13}C not bonded to another ^{13}C. The difference between S_0 and S is the spectrum of ^{13}C-^{13}C spin pairs. The optimum duration of the J-modulation was determined on a model compound, ^{13}C1,2-leucine, see Figure 2. Since C1 and C2 are ^{13}C labeled, they show up in the S_0 spectrum (thin line) but are dephased by the C-C J-coupling in the S spectrum (thick line). The small peak at 27 ppm in both spectra is from the natural-abundance (isolated) methyl ^{13}C.

^{13}C chemical-shift-anisotropy filter. The ^{13}C chemical-shift-anisotropy (CSA) filter technique with five pulses [17, 18] was used to monitor the dephasing by the chemical shift anisotropies (CSA) with a filter time of 38 μs. During detection, two-pulse phase modulation (TPPM) decoupling was applied. The spinning frequency was 6.5 kHz. After CSA filtering, only aliphatic carbons with small CSA can be remained.

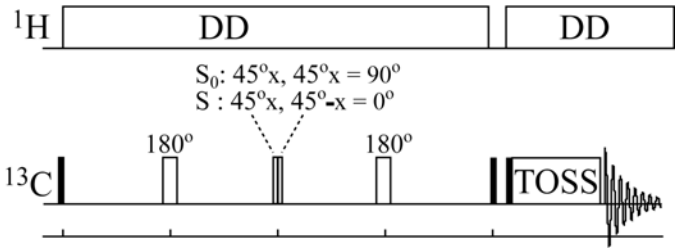

Figure 1. ^{13}C-^{13}C J-modulation pulse sequence used for separating signals of ^{13}C-^{13}C spin pairs from isolated ^{13}C due to their different J-coupling. Directly polarization of ^{13}C is used for quantitative determination of the fractions of isolated carbons and spin pairs. The central two 45° pulses can either form a 90° pulse or cancel each other, which yields S_0 and S spectra, respectively. In the measurement of S_0, the 90° pulse refocuses the J-modulation into a solid echo. In the measurement of S, the ~50-Hz homonuclear J-coupling dephases the ^{13}C-^{13}C spin pair signals. The two 180° pulses, before and after the two 45° pulses, are needed to refocus carbon chemical shift evolution.

www.manaraa.com

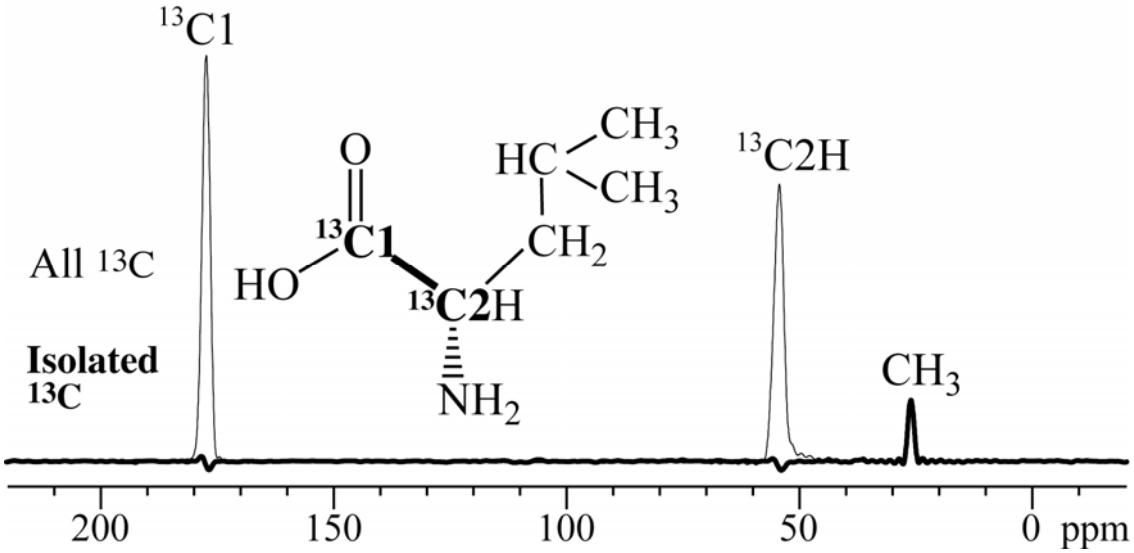

Figure 2. S_0 and S spectra of the ^{13}C-^{13}C J-modulation experiment applied to the model compound, ^{13}C1,2-leucine. Since C1 and C2 are ^{13}C labeled, they show up in the S_0 spectrum (thin line) but are dephased by the C-C J-coupling in the S spectrum (thick line). The small peak at 27 ppm in both spectra is from the natural-abundance (isolated) methyl ^{13}C.

^{1}H-^{15}N CP/MAS NMR. ^{1}H-^{15}N cross polarization spectra were acquired with or without gated decoupling for dipolar dephasing, with a CP time of 2 ms at an MAS frequency of 5 kHz. The Hartmann-Hahn condition for cross polarization was set carefully on the nonprotonated N of ^{15}N-t-BOC-proline. The 90^{o} pulse length on the ^{15}N channel was 6 μs, the recycle delay 3 s. TPPM decoupling was used during detection.

Selection of ^{15}N-bonded glycine-^{13}C2 and glycine-^{13}C2-bonded ^{15}N. In order to determine how many glycine C2 are bonded to ^{15}N, carbon detected ^{13}C{^{15}N} REDOR experiments were applied to the glycine-^{13}C2-^{15}N labeled melanoidins. The total REDOR time was N t_r = 2 ms, at 5-kHz MAS. If the REDOR 180^{o} pulses on the ^{15}N channel were turned off, the reference signal S_0 was obtained. With these REDOR 180^{o} pulses on, the carbon signals were dephased by their adjacent nitrogen, and only the "S" signals of carbons not bonded to nitrogen remain. The intensity difference $\Delta S = S_0 - S$ is the spectrum of the carbons directly bonded to ^{15}N.

In order to determine what fraction of nitrogen remains in N-C2 bonds, nitrogen detected ^{15}N{^{13}C} REDOR experiments were conducted at 5-kHz MAS. The pulse sequence

www.manaraa.com

and parameters are same as in the corresponding $^{13}C\{^{15}N\}$ REDOR experiments. The only difference is switching the observed nucleus to ^{15}N, and REDOR pulses were applied on the ^{13}C channel.

Two-dimensional ^{13}C-^{15}N HSQC. In order to see the connectivity of glycine $^{13}C2$ with its ^{15}N after the Maillard reaction, 2D ^{13}C-^{15}N HSQC experiments with REDOR recoupling were performed at 7 kHz MAS.

Selection of ^{13}C bonded to nonprotonated ^{15}N. A ^{13}C-^{15}N REDOR period of 1.14 ms duration was used in this 1D experiment to transfer coherence between ^{13}C and ^{15}N, see Figure 3. During the central period, the dipolar interactions between ^{15}N and ^{1}H can be recoupled for 2 t_r (0.29 ms) of ^{1}H-^{15}N "REDOR". The S_0 signal was recorded without ^{15}N-^{1}H recoupling by simply continually applying decoupling pulses on the ^{1}H channel. The dephased spectrum S is recorded with ^{15}N-^{1}H recoupling that dephases the coherence of protonated N. The CP contact time was 1 ms, the MAS frequency 7 kHz. Meanwhile, 40 μs gated decoupling between ^{13}C and ^{1}H before detection was also incorporated to selectively detect the signals of quaternary carbons. A short ^{1}H-^{13}C CP contact time of 50 μs with or without 40 μs of gated decoupling was applied to extract the protonated-carbon signals.

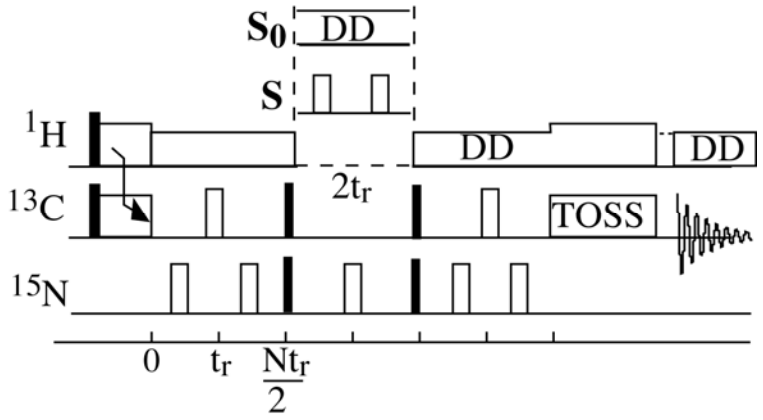

Figure 3. Pulse sequences for ^{13}C-detected ^{15}N-^{13}C REDOR with ^{15}N-^{1}H recoupled dipolar dephasing. The ^{13}C reference signal S_0 is acquired with regular ^{1}H decoupling of the transverse ^{15}N coherence during the central period of 2 t_r duration. The ^{13}C signal S is obtained with ^{15}N-^{1}H recoupled dipolar dephasing during the 2 t_r period.

www.manaraa.com

The pulse sequences were tested on two model compounds. The first model compound contains a nonprotonated N bonded to three carbons. Figure 4 shows that 75% of the reference signal in (a) remains after $2t_r = 0.28$ of $^{15}N\{^1H\}$ dephasing in (b). Therefore, a scaling factor of 1/0.75 was used for the dephased melanoidin spectra below. The second model compound contains a protonated N bonded to two carbons, of which one, a CH_2 carbon, is ^{13}C labeled. Since the nitrogen is protonated, only 8% of the reference signal in Figure 4 (c) remains in (d).

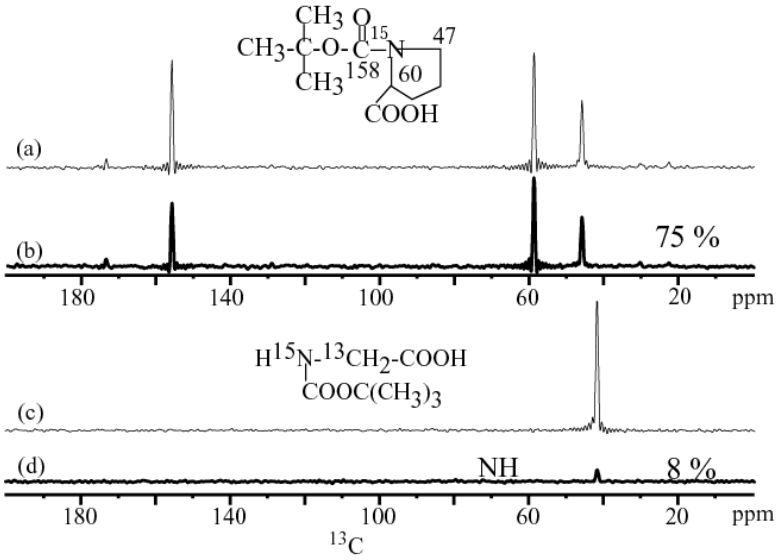

Figure 4. Carbon-detected 1D $^{13}C\{^{15}N\{^1H\}\}$-NMR spectra of two model compounds. The first model compounds with nonprotonated nitrogen nearby three carbons, as plotted in (a) for carbon bonded to all types N, (b) for carbon bonded to nonprotonated N, 75% of signal remains. For the second model compound with nitrogen bonded to one hydrogen and two carbons. The CH_2 is ^{13}C labeled. After $2t_r$ of $^{15}N\{^1H\}$ recoupling, only 8% of signal remains.

Results and Discussion

Tranformations of glucose and glycine. The complexity of glucose transformations in the Maillard reaction can be appreciated by looking at the CP/MAS ^{13}C NMR spectra of unlabeled melanoidins formed in the dry and solution conditions, shown in Figure 5 (a) and (b), respectively. Similarly complex spectra of melanoidins with signals ranging from 10 to 210 ppm have been reported by Ikan et al.[10] . Figure 5 (c), (d) also shows spectra selectively of the carbons originating from glucose (thick lines), which were obtained by measuring

www.manaraa.com

melanoidins prepared from glucose-$^{13}C_6$ (and glycine-^{15}N). The differences between these spectra are mostly due to the carbons of glycine, which are seen to contribute mostly the sharp COO peak near 173 ppm and N-$\underline{C}H_n$ signals near 50 ppm. Dramatic transformations of glucose, from the simple three-line spectrum of neat glucose shown in Figure 5 (e), have occurred during the Maillard reaction.

In contrast to glucose, glycine carbons do not undergo such dramatic changes, especially in the dry reaction. This is seen in quantitative ^{13}C NMR spectra of glycine carbons in melanoidins made from ^{13}C-labeled glycines, shown in Figure 6. The sharp peak of C1 at ~173 ppm is near its original position for neat glycine. The C2 carbon spectrum contains mostly bands in the alkyl region of the spectrum, with a dominant peak at ~ 50 ppm from untransformed NCH_2 moieties.

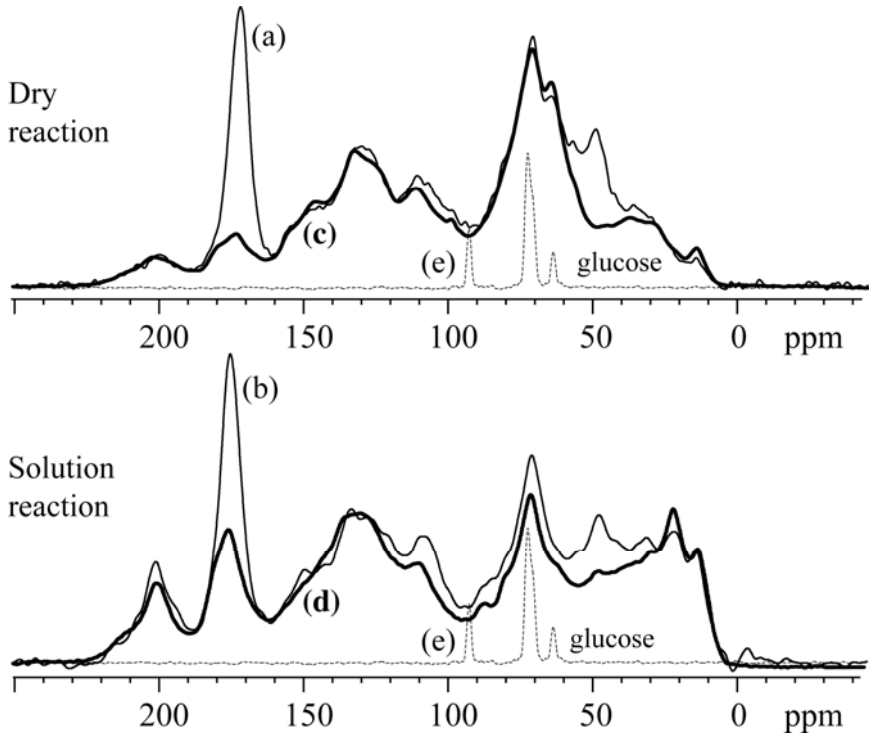

Figure 5. CP/TOSS ^{13}C NMR spectra of melanoidins made from glucose and glycine in a 1:1 molar ratio. (a), (b) ^{13}C in natural abundance (thin lines). (c), (d) Spectrum of glucose-$^{13}C_6$ reacted with glycine-^{15}N (thick lines). Top panel: dry reaction; bottom panel: solution reaction. (e) Spectrum of glucose for reference (dashed line), with the same line broadening as the other spectra.

www.manaraa.com

Extent of glycine loss. Differential degradation of reactants into volatile products during the Maillard reaction, as well as enrichment in low-molecular-weight fractions, can lead to loss of glycine relative to glucose in the high-molecular-weight melanoidins investigated here. This effect can be studied by quantifying the total ^{13}C NMR signals, see Figure 6, of glycine $^{13}C1,2$, $^{13}C1$, and $^{13}C2$ in the melanoidins for the two reaction conditions. For reference, quantitative ^{13}C spectra of melanoidin made from glucose-$^{13}C_6$ reacted with ^{15}N-glycine in both dry and solution reaction have also been measured and integrated. They provide a basis for the calculation of glycine-C percentages with respect to all carbons. The total carbon of melanoidin is the sum of the integral of the glucose-$^{13}C_6$ signal and the integral of the glycine-$^{13}C1,2$ signal, normalized for the number of scans, receiver gain, and sample mass in the rotor.

Given the 1:1 molar ratio of glucose and glycine reactants, the initial carbon percentage of glycine carbon is 25% of the total reactant carbon. After the reaction, the glycine carbons are found to contribute 17% of total carbon in the dry reaction products and 19% of total carbon in the solution reaction products.

In the both dry and solution reaction samples, 53% is from glycine C1 and 47% from glycine C2. Although more glycine carbons were lost compared to glucose, the majority of glycine (more than 68%) still remains in the products for both reaction conditions. The amounts of glycine C1 and C2 that remain are very similar, indicating that loss of just C1 as CO_2 is not a major pathway of losing glycine.

Fate of glycine C1. The quantitative ^{13}C spectra of the melanoidins prepared from glycine-$^{13}C1$ are particularly simple, see Figure 6 (b, e). The glycine-$^{13}C1$ melanoidin made in the dry reaction gives a single peak at 172 ppm, while the peak is at 174 ppm for the melanoidin made in solution. The signals at these chemical shifts could be due to esters (COOC, 165 ~ 175 ppm), carboxylic acids (COOH, 170 ~ 175 ppm), carboxylates (COO^-, 175 ~ 180 ppm), or amides (NC=O, 160 ~ 170 ppm). The difference between DP and DP gated decoupling in Figure 6 (b, e) arises from the ubiquitous two-bond ^{13}C-^{1}H dipolar couplings.

www.manaraa.com

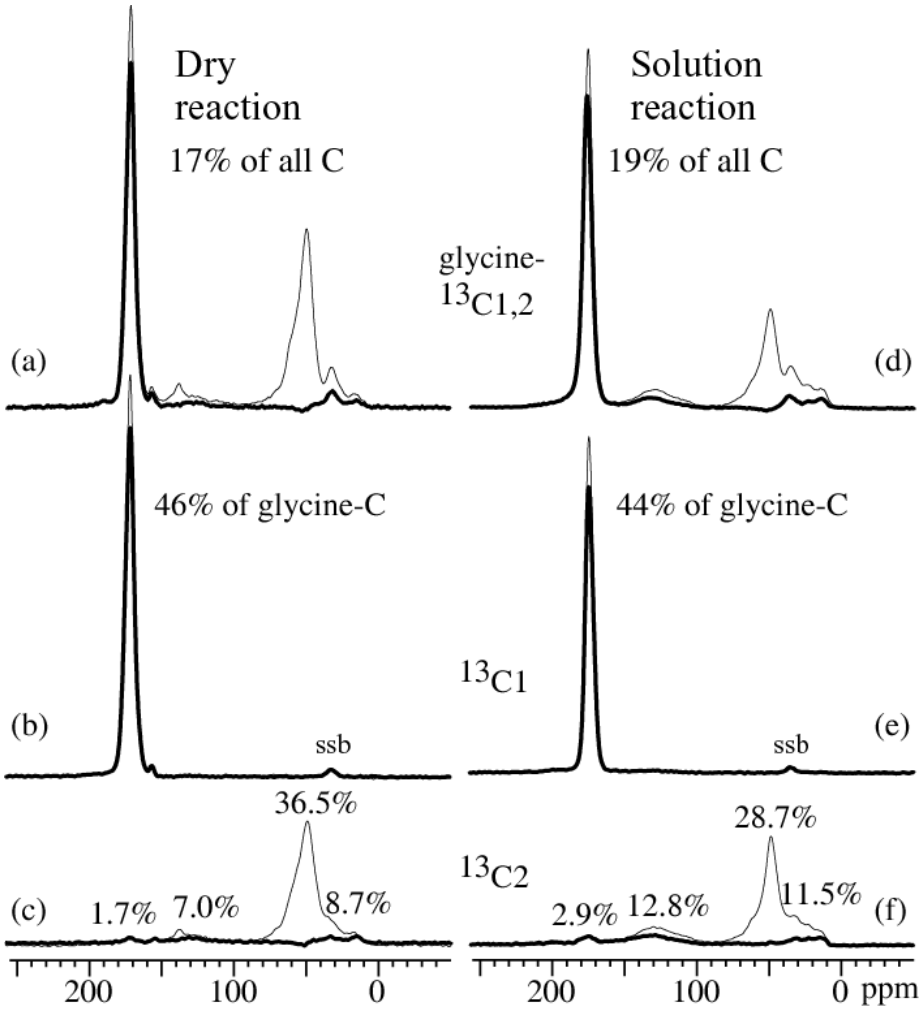

Figure 6. Quantitative direct-polarization ^{13}C NMR spectra of melanoidins made from glucose reacting with various ^{13}C-labeled glycines. Thin lines: full spectra; thick lines: corresponding selective spectra of quaternary carbons and methyl groups. (a-c): melanoidins from dry reaction; (d-f): melanoidins from solution reaction. The top two spectra are from $^{13}C1,2$-labeled glycine, accounting for 17% and 19%, respectively, of total carbons of the high-MW fraction. The middle row shows spectra of $^{13}C1$-labeled glycine samples, accounting for 53% of total glycine carbon. The bottom spectra are from $^{13}C2$-labeled glycine samples, accounting for 47% of total glycine carbon. Most glycine C2 remains in its original NCH_2 structure, while smaller fractions formed COO moieties, aromatic carbon, and other alkyl types of carbons, whose percentages of total glycine carbon are listed in the figure.

The chemical-shift anisotropy (CSA) powder pattern could help us to distinguish esters (COOC) from COOH or COO^-, since the highest peak in the CSA powder pattern of esters is distinctly upfield, while that of COO^- is distinctly downfield, and for COOH it is near the center of the spectrum. For the dry reaction sample, the isotropic chemical shift of the peak maximum is at 172 ppm. The cross sections shows the powder pattern of esters to a

www.manaraa.com

significant extent, see Figure 7 (c). For the solution reaction sample with the main peak at 174 ppm, most powder patterns resemble those of typical COOH groups.

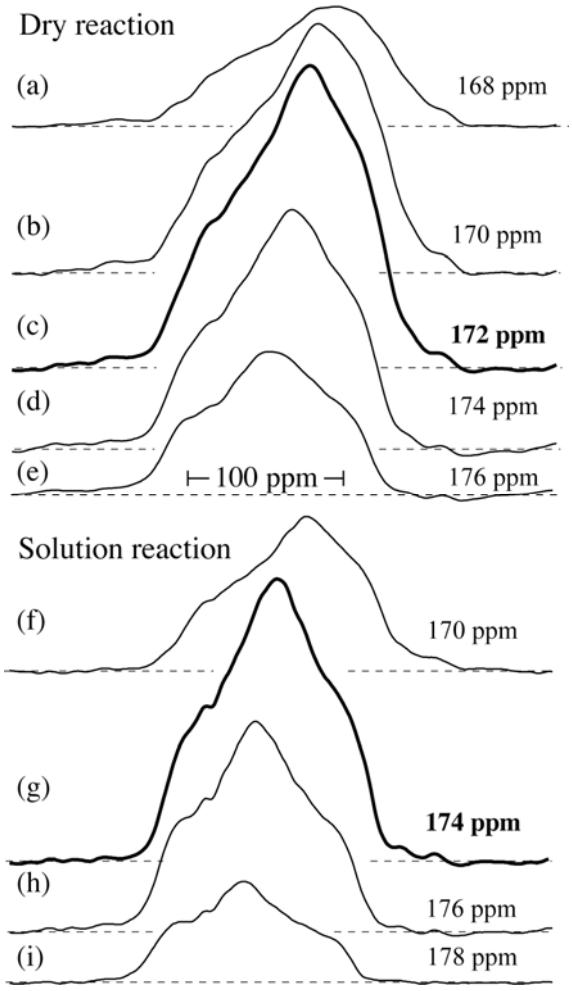

Figure 7. ^{13}COO powder patterns from two 2D SUPER spectra of glycine-^{13}C1 labeled melanoidins. Slices were taken at the isotropic-shift positions indicated on the right.

Fate of glycine C2. The fate of glycine-^{13}C2 can be assessed from the spectra in Figure 6 (c) and (f). After the Maillard reaction, the resonance near 50 ppm accounts for 36.5% of all glycine-C in the dry reaction melanoidins and 28.7% of all glycine-C in the solution reaction sample. Dipolar dephasing and spectral editing techniques, see Figure 8 (a) and (c), confirm that this is a CH_2 resonance; based on the chemical shift, it can be assigned to NCH_2 carbons.

www.manaraa.com

This assignment can be verified by carbon-detected $^{13}C\{^{15}N\}$ REDOR applied to melanodins prepared from doubly labeled glycine-$^{13}C2$-^{15}N shown below.

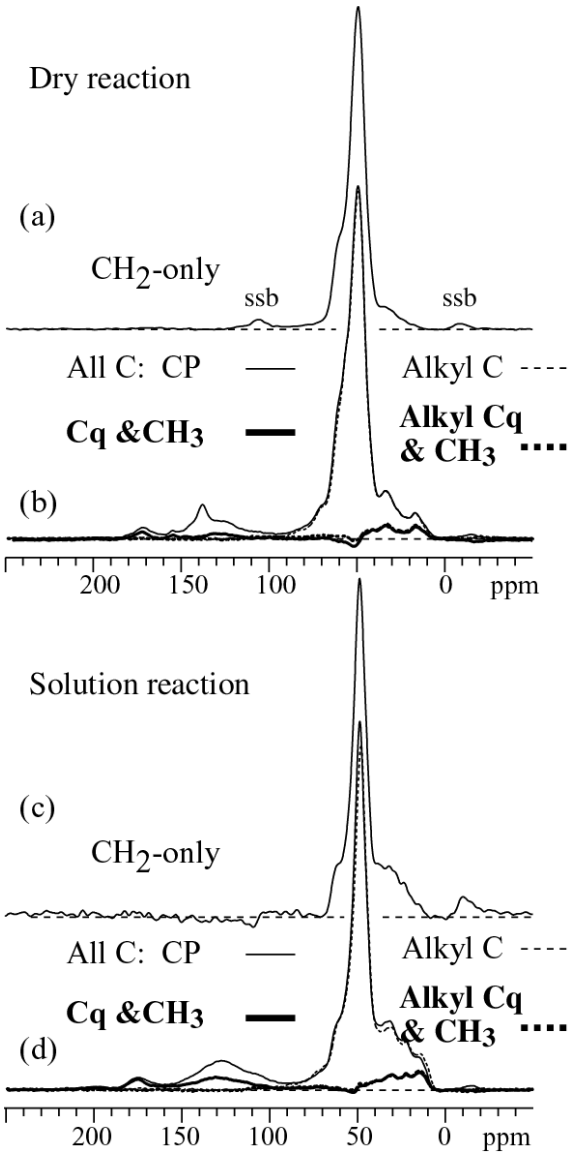

Figure 8. ^{13}C NMR spectra of glycine-$^{13}C2$ labeled melanoidins from (a,b) the dry reaction and (c, d) the solution reaction. (a, c): CH_2-only spectra, obtained with three-spin coherence selection. (b) and (d): Thick lines: full CP/TOSS spectra; thin lines: corresponding spectra of quaternary and methyl carbons, obtained after 40 μs of gated decoupling. Dashed lines: Corresponding selective spectra of all alkyl and of quaternary/CH_3 alkyl carbons.

www.manaraa.com

C1-C2 bonds of glycine. The aforementioned results showed that some glycine C2 changed into various structures, e.g. CCH_n, aromatic NCH, etc., while most of it remained in NCH_2 form. Are glycine C2 and C1 still chemically bonded with each other after these various reactions? The ^{13}C-^{13}C J- dephasing pulse sequence was applied to glycine-$^{13}C1,2$ melanoidins to determine the extent to which the glycine C1-C2 bond has been broken. Figure 9 (a) and (b) displays the results for the dry and solution reaction samples, respectively. With the solid echo, the homonuclear J-coupling evolution is refocused, and signals of spin pairs and isolated spins are observed (thin lines). Without the solid echo, the signals of carbon spin-pairs are dephased quickly via their strong J-coupling, and only the spectrum of isolated carbons remains (thick lines in Figure 9).

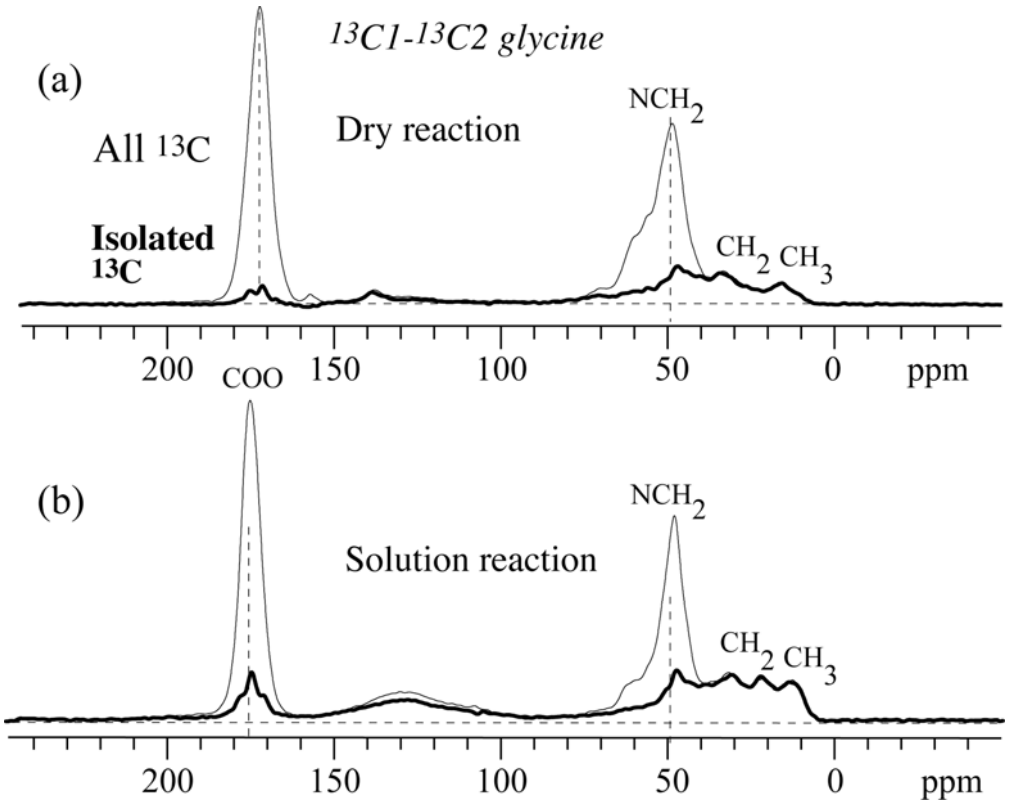

Figure 9. J-modulated spectra for glycine-$^{13}C1,2$ labeled samples made (a) in the dry reaction and (b) in solution. Thick lines: reference spectra; thin lines: isolated-^{13}C signals. The difference intensity is from the glycine C1-C2 spin pairs, which account for 73% of all glycine carbon in the dry-reaction sample and 56% in the solution-reaction sample. For signal noise issue, CP J-modulation spectra are shown here. Quantitative J-modulated spectra have also been acquired and used in quantitative interpretation.

www.manaraa.com

The J-modulation results indicate that the C-C bond of most glycine molecules remains intact in the melanoidin. In the dry reaction, 73% of all glycine carbons are still bonded to each other, and 56% in the solution reaction sample. The isolated glycine C2 formed various species, such as aromatic NCH, C-$\underline{C}H_2$-C $C\underline{C}H_3$, $N\underline{C}H_3$ and $\underline{C}OO$ moieties.

C-N bonds of glycine. The fraction of C-N bonds of glycine that remain intact can be determined from the intensities of $^{13}C\{^{15}N\}$ REDOR spectra shown in Figure 10. The spectra also confirm the assignments of glycine $^{13}C2$ resonances in melanoidins. When the C-N dipolar interaction is recoupled via REDOR of Nt_r = 2 ms duration, the signals of carbon bonded to ^{15}N are dephased, and only the signals of carbons not bonded to N are recorded in the spectrum S (dashed thin lines in Figure 10 (a) and (b)). Without the REDOR pulses, signals of all types of carbons are recorded in a reference spectrum S_0 (thin lines in Figure 10 (a) and (b)). Therefore, the difference $\Delta S = S_0 - S$ (thick lines) is the spectrum of the ^{13}C directly bonded to ^{15}N. The ΔS spectra in Figure 10 (a) and (b) show the highest peaks at 50 ppm for both samples, proving that these dominant peaks in Figure 6 (c) and (f) are NCH_2. In addition, there are signals of NCH_3 (at 35 ppm) and N-bonded aromatic carbon (around 135 ppm) in the ΔS spectrum, and CCH_n signals (from 40 to 10 ppm) in the S spectrum.

Taking the full integral of the ΔS spectrum relative to that of S_0 shows that ~ 82 % or 62% of glycine C2 in the dry or solution reaction samples, respectively, is bonded to N. In the dry reaction, more glycine C2 remains in $NC2H_2$ moieties.

By switching the detected nucleus to ^{15}N, we can probe the breaking of C-N bonds from a different perspective. In particular, we can determine whether glycine N gets incorporated into the melanoidin while the carbon is lost from the sample. $^{15}N\{^{13}C\}$ REDOR spectra measured for this purpose are plotted in Figure 11 (a) and (b) for glycine-$^{13}C2$-^{15}N labeled melanoidins made in the dry and solution reaction, respectively. Here, we focus on the effect of $^{13}C2$ on the ^{15}N intensities; the spectral features will be discussed below. The difference spectra (thick lines) between S_0 (thin lines) and S (dashed thin lines) represent the nitrogen directly bonded to glycine-$^{13}C2$. According to Figure 11, 75% and 63% of nitrogen is bonded to glycine-C2 made in dry and solution reactions, respectively.

www.manaraa.com

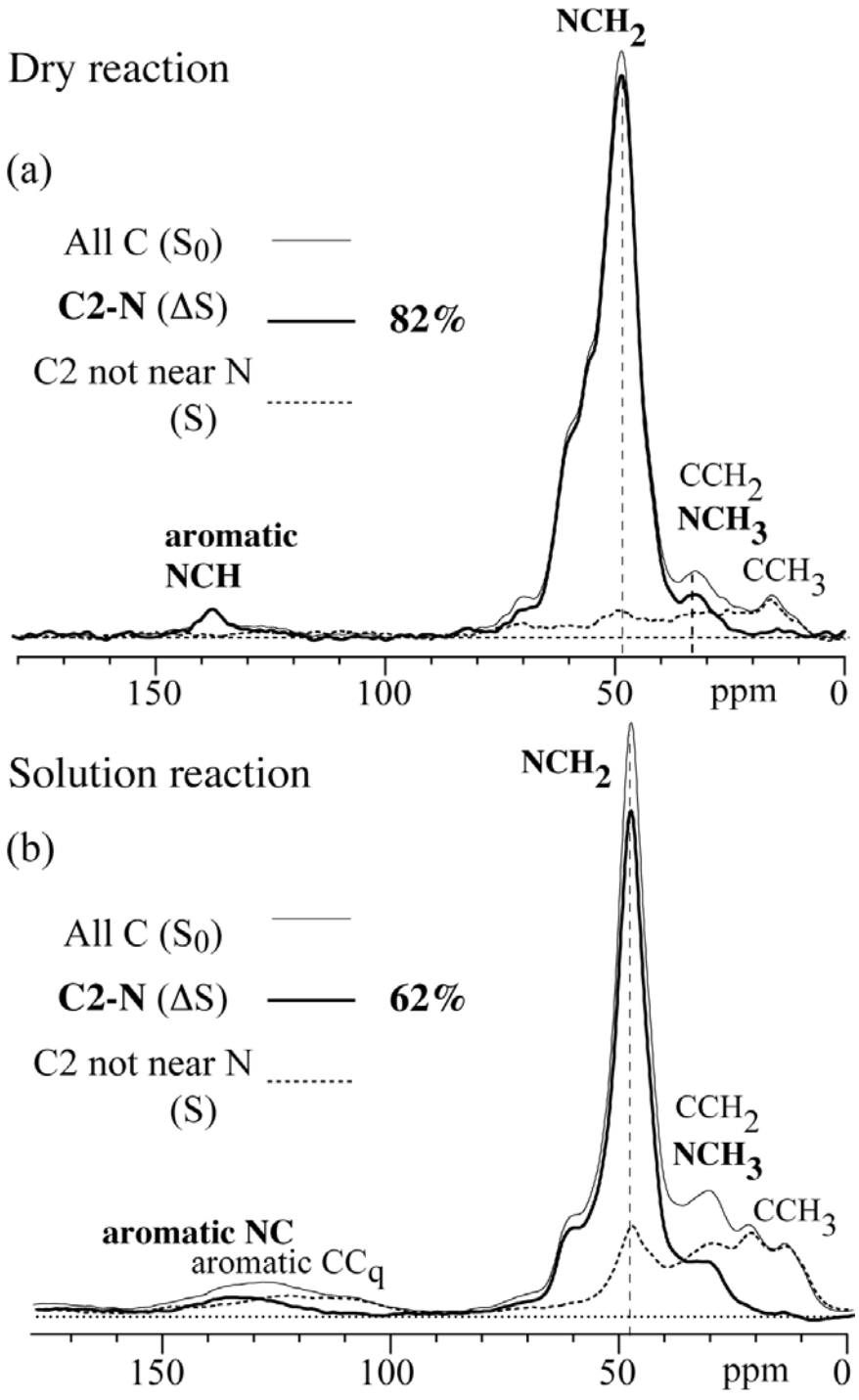

Figure 10. Carbon-detected $^{13}C\{^{15}N\}$ REDOR spectra for glycine-$^{13}C2$-^{15}N labeled melanoidins made in (a) dry and (b) solution reaction. Thin lines: Reference spectrum S_0 of all carbons; dashed lines: Signal S of carbons at least two bonds from nitrogen; thick lines: Difference spectrum $\Delta S = S_0 - S$ of carbons directly bonded to nitrogen. The total REDOR time was $Nt_r = 2$ ms at an MAS frequency of 5 kHz.

www.manaraa.com

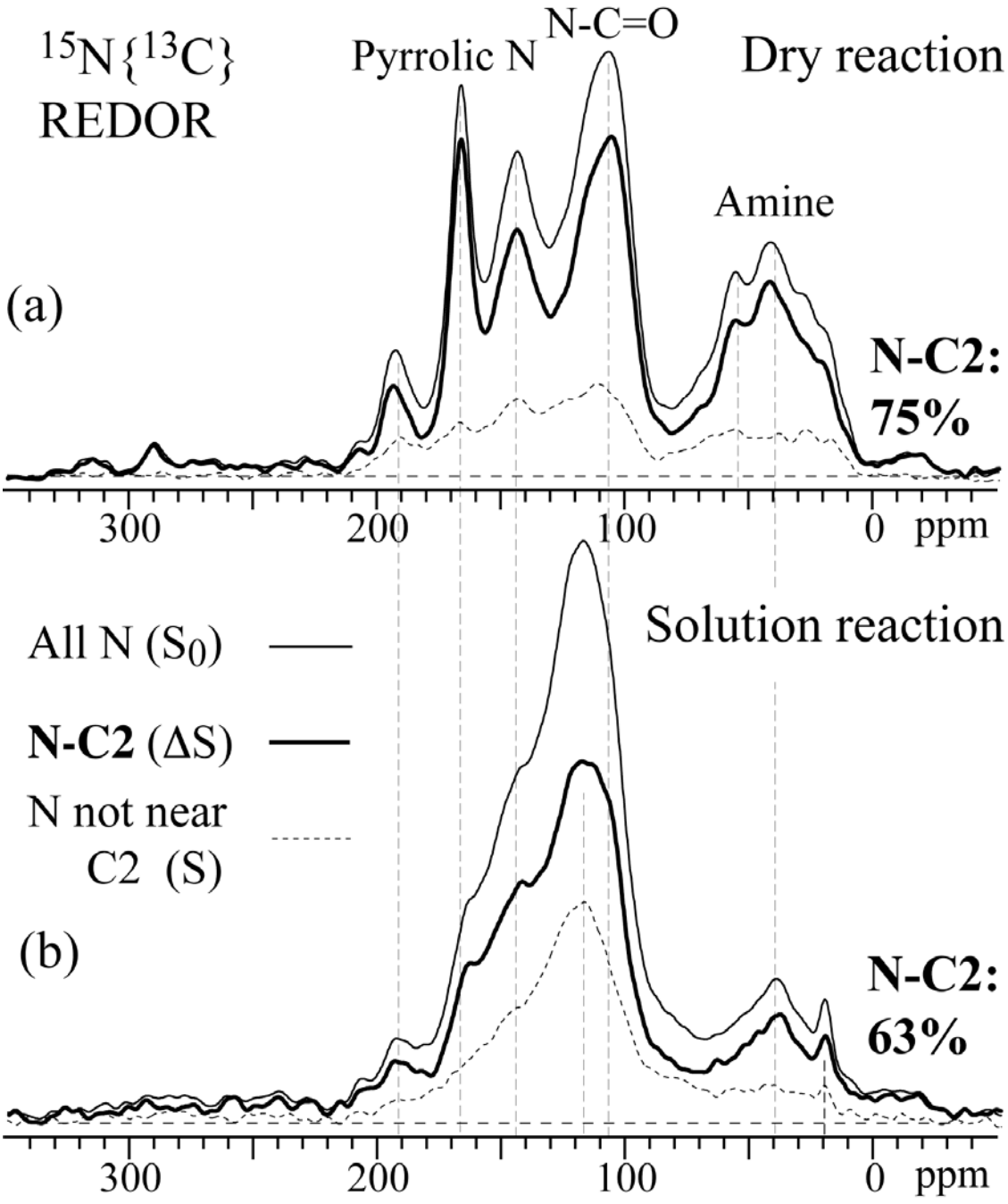

Figure 11. Nitrogen-15 detected $^{15}N\{^{13}C\}$ REDOR spectra for the glycine-$^{13}C2$-^{15}N labeled melanoidins from (a) dry and (b) solution reaction. The thin line spectra (S_0), used as references for T_2 correction, are without C-N recoupling. The dashed thin line spectra (S) represent nitrogen far from glycine-C2. Thick line: difference spectra $\Delta S = S_0 - S$, which represents nitrogen directly bonded to glycine-C2 (75% of nitrogen in dry reaction and 63% of nitrogen in solution reaction).

www.manaraa.com

Comparing the fractional intensities of the $^{13}C\{^{15}N\}$ and $^{15}N\{^{13}C\}$ ΔS REDOR spectra, there is no large percentage difference for the solution reaction sample: 62% of glycine-C2 are directly bonded to nitrogen, and 63% of nitrogen are directly bonded to glycine-C2. However, for the dry reaction sample, 82% of glycine C2 remain bonded to nitrogen, while slightly less, 75%, of nitrogen remains bonded to glycine C2. The difference, if significant, suggests that slightly more nitrogen remains in the system, or that two glycine-C2 simultaneously bond to the same nitrogen, which is possible for the aromatic C2H bonded to $NC2H_2$, since they show two cross peaks in Figure 12 (b) at the same imidazolium nitrogen chemical shift position around 180 ppm.

Fate of glycine N. The transformation of glycine nitrogen in the melanoidins can be assessed from the ^{15}N NMR spectra, such as the S_0 spectra shown in Figure 11. Unlike the simple ^{13}C spectra of glycine, the nitrogen spectra show many bands over a wide range of chemical shifts, comparable to glucose carbon. For ^{15}N-labeled melanoidins made by solution reaction, Benzing-Purdie et al.[19] observed spectra similar to that in Figure 11b, though significantly noisier. Two major ranges of ^{15}N resonances can be distinguished: sp^3-hybridized (amine) N between 80 and 0 ppm, and sp^2-N resonating from 80 to 215 ppm, including amide N resonating at ~120 ppm, pyrrole N (~150 ppm), imidazolium N (~170 ppm), and oxazolium N (~200 ppm). These assignments will be justified in future publications, based on ^{15}N-^{13}C-^{13}C NMR.[20]

The samples from dry and solution reactions show somewhat different ^{15}N spectral features. For the solution reaction, most nitrogen is in amides while the dry reaction distributes nitrogen more evenly among amine, amide, pyrrole, imidazolium, and oxazolium nitrogen. Both samples do not show strong intensity beyond 220 ppm, excluding a major contribution from pyridinic nitrogen.

www.manaraa.com

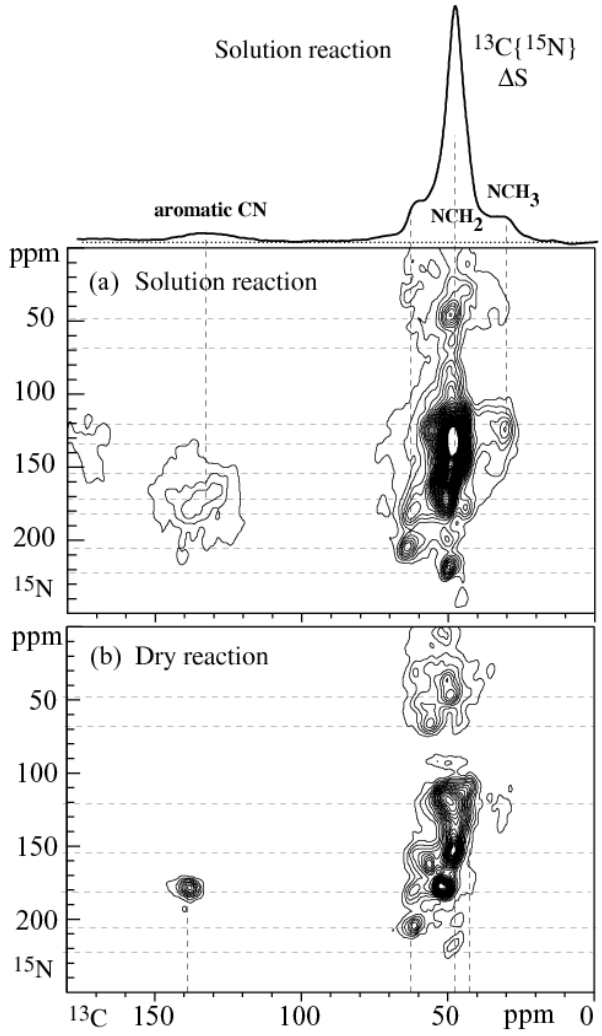

Figure 12. 2D ^{15}N-^{13}C HSQC spectra for glycine-$^{13}C2$-^{15}N labeled melanoidins made in (a) solution and (b) dry reaction, acquired at an MAS frequency of 7 kHz. The spectrum of C2 bonded to N for the solution reaction, obtained by $^{13}C\{^{15}N\}$ REDOR, is shown at the top of the figure.

While most intensity of the $^{13}C2\{^{15}N\}$REDOR ΔS spectra in Figure 10 resides in a single NCH_2 band, in the two-dimensional ^{13}C-^{15}N HSQC spectra displayed in Figure 12 this main peak is dispersed widely along the vertical ^{15}N dimension, for both reaction conditions. The 2D spectrum resolves a dozen or more bands, many more than observed in the 1D ^{15}N spectrum. All those different forms of nitrogens are bonded to CH_2 of glycine C2, which indicates that nitrogen is an active site for complicated reaction but usually without breaking the bond to glycine C2. According to the 2D HSQC spectrum, a relatively small fraction of aromatic C2H resonating at 132~138 ppm is bonded to imidazolium nitrogen for both

www.manaraa.com

reaction conditions. Also, some glycine C2 in NCH_3 groups, resonating at 30 ppm, is seen to be bonded to amide (N-C=O) nitrogen.

(Non)protonation of nitrogen. Unlike the carbons of glycine, its nitrogen has been transferred into a wide range of species. It has to form new chemical bonds with various glucose carbons. Whether nitrogen ends up being protonated or not can be assessed by ^{1}H-^{15}N dipolar dephasing experiments. CP/MAS ^{15}N NMR spectra with optimized cross polarization and with and without recoupled dipolar dephasing are shown in Figure 13 (a) and (b) for the dry- and solution-reaction melanoidins, respectively. The dipolar-dephased spectra (thick lines) in Figure 13 show that a large fraction (> 80%) of the nitrogen is not protonated. However, in nitrogen CP experiments, nonprotonated nitrogens are underrepresented. Due to the lower gyromagnetic ratio of nitrogen, transfer of polarization from protons to nonprotonated N takes 2.5 times longer than for nonprotonated carbons and is more susceptible to averaging by moderate-speed MAS. Within the typical cross-polarization times of 1 to 2 ms, the protonated nitrogen with their 10-kHz ^{1}H-^{15}N coupling will get more magnetization from protons.

In order to avoid the differential enhancement of protonated N, we have developed a carbon-detected $^{13}C\{^{15}N\{^{1}H\}}$-HSQC-REDOR method. In this pulse sequence as shown in Figure 3, ^{15}N-^{1}H "REDOR" is embedded within a ^{13}C-^{15}N-^{13}C coherence transfer sequence analogous to ^{15}N-^{13}C HSQC. During the central period with transverse ^{15}N and longitudinal ^{13}C coherence, ^{15}N-^{1}H recoupling is turned on for two rotation periods to dephase the nitrogen bonded to ^{1}H. The detected ^{13}C must be near nonprotonated ^{15}N (thick lines in Figure 14). Without ^{15}N-^{1}H recoupling, the detected ^{13}C is near all types of ^{15}N (thin lines in Figure 14). In addition, gated decoupling before ^{13}C detection and a short CP contact time were applied to spectrally edit nonprotonated and protonated ^{13}C.

www.manaraa.com

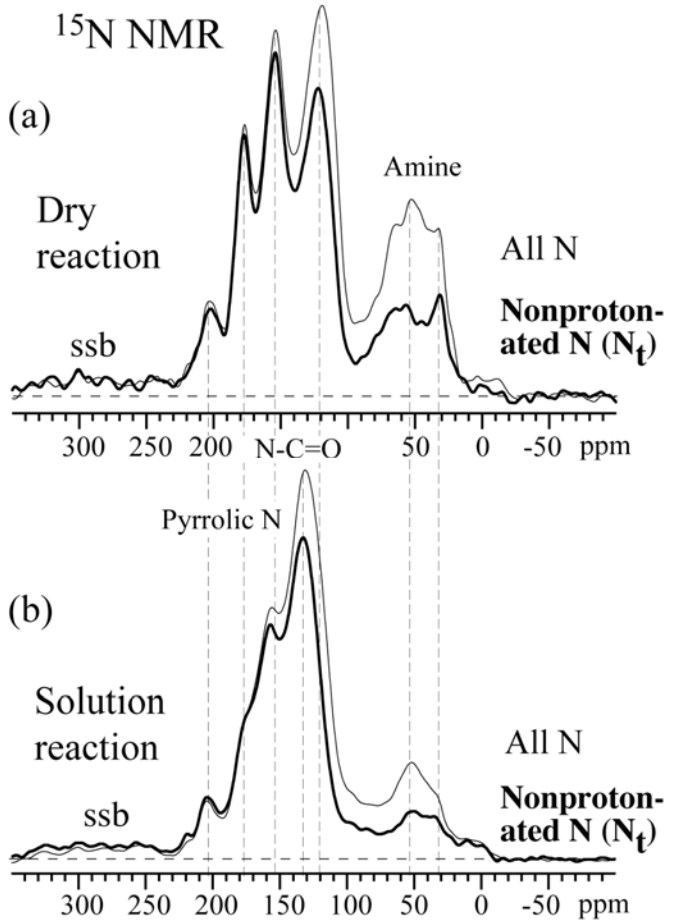

Figure 13. ^{1}H-^{15}N CP spectra of glycine-^{15}N labeled melanoidins from (a) dry reaction of glucose-$^{13}C1$ and glycine-^{15}N and (b) solution reaction of glucose-$^{13}C_6$ and glycine-^{15}N. The thin line spectra are for all nitrogen, and the thick line spectra are only for nonprotonated nitrogen detection by two rotation periods of recoupled ^{1}H-^{15}N dephasing before detection. Spinning frequency: 5 kHz, contact time: 2 ms. Spinning sidebands are marked by "ssb".

In Figure 14, (a-c) and (d-f) are for the glucose-$^{13}C6$ reacting with glycine-^{15}N in dry condition and solution condition, respectively. The thin-line spectra are for the carbons near all types of nitrogen, and the thick-line spectra for carbon near nonprotonated nitrogen, scaled by the factor of 1/0.75 determined in model compounds. Spectra shown in Figure 14, (a) and (d) are for all types of carbons, those in (b) and (e) for nonprotonated carbons, those in (c) and (f) for protonated carbons. The figure shows that nitrogen is predomainantly

www.manaraa.com

nonprotonated no matter whether the nearby carbon is protonated or not. In analyzing the intensities, it needs to be taken into account that a tertiary N is bonded to two glucose ^{13}C, while N-H is bonded to only one such ^{13}C. Spectral integrals taking these factors into account give N_t:NH ratios of 79:21 and 92:8, respectively, for the melanoidin from dry and solution reaction, respectively.

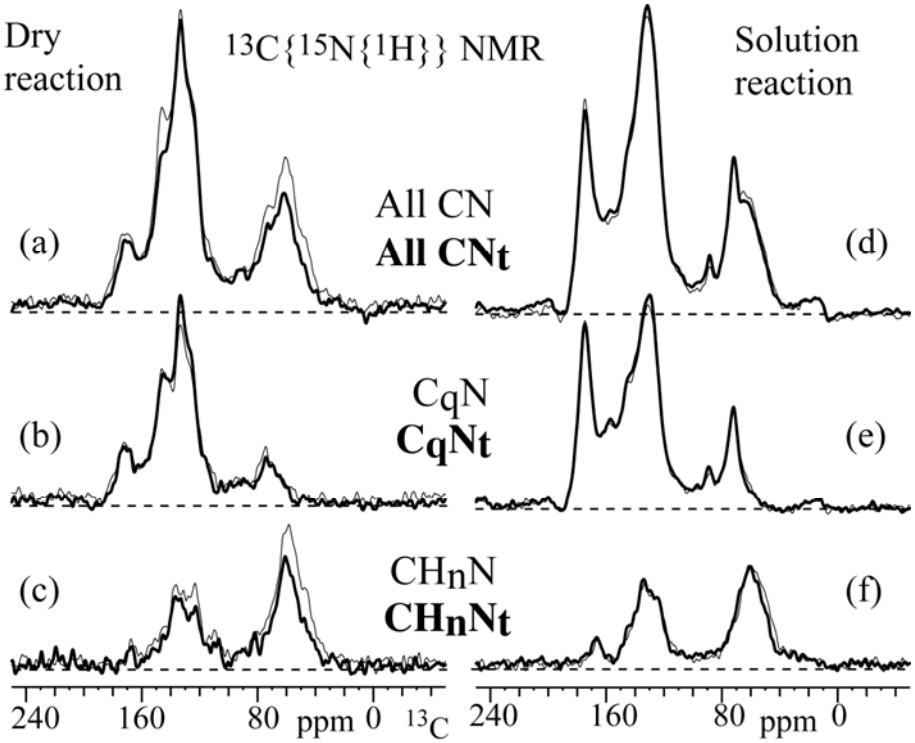

Figure 14. Carbon detected 1D $^{13}C\{^{15}N\{^{1}H\}\}$-HSQC-REDOR of melanoidins made in the dry and solution conditions with glucose-$^{13}C_6$ reacting with glycine-^{15}N. Left column: dry reaction; right column: solution reaction. Thin lines: Reference spectra of carbons bonded to both protonated and nonprotonated nitrogen. Thick lines: spectra of carbons bonded to nonprotonated nitrogen, scaled up by the factor of 1/0.75 determined in a model compound. (a) and (d) are spectra of all types of carbon near N, (b) and (e) are from nonprotonated carbons, and (c) and (f) from protonated carbons. The spectra show that nitrogen in melanoidins is predominantly nonprotonated.

For 1:1 glucose:glycine ^{15}N-labeled melanoidins made in solution, Benzing-Purdie et al.[19] observed spectra similar to that in Figure 13b, but they assigned the main peak to

www.manaraa.com

secondary (H-N-C=O) rather than tertiary amides; due to noise, they also failed to recognize the additional peaks downfield from the main band, which are more pronounced in the dry-reaction sample and can be assigned to imidazolium and oxazolium rings.[20]

Structural units and percentages of glycine in melanoidins. By applying various ^{13}C, ^{1}H, ^{15}N solid-state NMR techniques to melanoidins made from suitably ^{13}C- and ^{15}N-labeled glycine, several structural units can be proposed as listed in Table 1. In order to know the percentages of these structures, various spectra have been integrated. Some bands cannot be resolved in the quantitative ^{13}C spectra, as seen in Figures 6 (c) and (f). ^{13}C detected $^{13}C\{^{15}N\}$ REDOR experiments are useful to separate NCH_2, NCH_3, CCH_2, CCH_3, N-aromatic carbon and non-nitrogen aromatic carbon resonances. However, the carbon detected $^{13}C\{^{15}N\}$ REDOR experiments did not use direct polarization of ^{13}C; therefore, the relative peak intensities are not very quantitative percentages. Therefore, we first integrated the individual group region in the CN REDOR spectra as shown in Figure 10 (a, b), to obtain the internal ratios. The final percentages are compared with the data listed in Figure 6 (c) and (f).

Table 1. Structural units into which the glycine C2 and N have been transformed during the Maillard reaction, and their percentages of total glycine carbon or total glycine nitrogen.

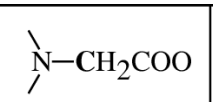		NCH_3	CCH_2	CCH_3	CCH(?)		NH
dry	33.6%	2.9%	3.5%	2.3%	2.9%	39% of N	21±2%
sol.	23.7%	2.4%	6.5%	2.6%	5.0%	31% of N	15±5%
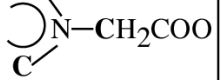				COO	Total **C2**	NC=O	N_t
dry	x_1	7.0%	3.8%-x_1	1.7%	54%	33% of N	79±2%
sol.	x_2	12.8%	5.5%-x_2	2.9%	56%	53% of N	85±5%

Around 50% of glycine remains intact with the nitrogen entering various glucose-derived chemical environments. Some of glycine C2 fragments into NCH_3, CCH_2, CCH_3 and aromatic NCH. The nitrogen has been transformed dramatically into pyrrolic, amide N, and amine N. The nitrogen is predominantly nonprotonated.

Conclusions

www.manaraa.com

The structural units of melanoidins formed from glycine and their percentages have been characterized by various ^{13}C, ^{15}N, and ^{13}C-^{15}N NMR experiments applied to melanoidins made from various isotopically labeled glycines reacted with glucose, in dry and solution reactions. About half of glycine stays intact. The C1 carbon remains mostly in a carboxyl group, while the nitrogen is incorporated into a wide range of amine, amide, and pyrrolic species. Nonprotonated N predominates (>80%) and may be a characteristic marker of Maillard reaction products, distinguishing them from proteinaceous materials and aminosugars, where almost all nitrogen is in NH groups.

Refrences

1. O'Brien, J.; Nursten, H. E.; Crabbe, M. J.; Ames, J. M., *The Maillard reaction in foods and medicine*. RSC Publishing: Cambridge, U.K., 1998.
2. Hodge, J. E. *J. Agric. Food Chem.* 1953, *1,* 926-943.
3. Hoering, R. C. *Carnegie Inst. Washington Yearbook* 1973, *72,* 682-690.
4. Hodge, J. E. *Adv. Carbonhydr. Res.* 1955, *10,* 169-205.
5. Ledl, F.; Schleicher, E. *Angew. Chem. Int. Engl. Ed.* 1990, *29,* 565-594.
6. Nursten, H., *The Maillard reaction: chemistry, biochemistry and implications*. 2005; p 5-30.
7. Hofmann, T. *J. Agric. Food Chem.* 1998, *46,* 941-945.
8. Hofmann, T. *J. Agric. Food Chem.* 1998, *46,* 3902-3911.
9. Tressl, R.; Wondrak, G. T.; Garbe, L. A. *J. Agric. Food Chem.* 1998, *46,* 1765-1776.
10. Ikan, R.; Ioselis, P.; Rubinsztain, Y.; Aizenshtat, Z.; Pugmire, R.; Anderson, L. L.; Woolfenden, W. R. *Org. Geochem.* 1986, *9,* 199-212.
11. Dixon, W. T. *J. Chem. Phys.* 1982, *77,* 1800-1809.
12. Mao, J.-D.; Hu, W.-G.; Schmidt-Rohr, K.; Davies, G.; Ghabbour, E. A.; Xing, B. *Soil Sci. Soc. Am. J.* 2000, *64,* 873-884.
13. Liu, S. F.; Mao, J. D.; Schmidt-Rohr, K. *J. Magn. Reson.* 2002, *155,* 15-28.
14. Mao, J.-D.; Schmidt-Rohr, K. *J. Magn. Reson.* 2005, *176,* 1-6.
15. Schmidt-Rohr, K.; Spiess, H. W., *Multidimensional solid-state NMR and polymers*. Academic Press, INC: San Diego, CA, 1999.

www.manaraa.com

16. Powles, J. G.; Strange, J. H. *Proc. Phys. Soc.* 1963, *82,* 6-15.

17. Mao, J.-D., Schmidt-Rohr, K. *Solid State Nucl. Magn. Reson.* 2004, *26,* 36-45.

18. Blano, F.J.; Tycko, R. *J. Magn. Reson.* 2001, *149,* 131-138.

19. Benzing-Purdie, L.; Ripmeester, J. A.; Preston, C. M. *J. Agric. Food Chem.* 1983, *31,* 913-915.

20. Fang, X.-W.; Schmidt-Rohr, K., Complex N-containing Structures Formed in the Model Maillard Reactions. In preparation.

www.manaraa.com

CHAPTER 5. Alkyl and other major structures formed in model Maillard reactions studied by solid-state NMR

In the style of a paper to be submitted to The Journal of the American Chemical Society

Xiaowen Fang, Klaus Schmidt-Rohr*

Abstract

Melanoidins formed in the Maillard reaction between glycine and glucose have been characterized using advanced solid-state NMR techniques on isotopically labeled samples. Spectral analysis of samples made in repeat reactions shows that the reproducibility is good. We have focused on glucose: glycine in 1:1 molar ratio, heated as a dry coprecipitated mixed powder at 125 ^{o}C for 2 hours, according to a standard procedure. Quantitative ^{13}C spectra show that alkyl and C=O units make up ~ 60 % of carbon in the melanoidins, disproving structural models with predominantly aromatic structures. The spectra of samples made from specifically labeled (C1, C2, C3, and C6) glucose are strikingly different, proving that specific structures are formed. More than half of the glucose-C1 carbons form new C-C bonds, while most schemes of the Maillard reaction emphasize C-O and C-N bond formation. The C2 carbons are indeed almost all bonded to heteroatoms and mostly (~ 72%) not protonated, while C3 carbons mostly (~69%) remain protonated and have a significant fraction of sites not bonded to heteroatoms such as methylenes in C-CH_2-C moieties. Only C4 and C5 remain significantly in alkyl OCH sites. C6 undergoes the least transformation, with most (52%) carbons in OCH_2 and some transforming to C-CH_2-C groups; also, 1/5 of C6 is lost from the sample. C1 and C6 form CH_3 end groups in similar quantities (a total of 2% of all C). All sites have been characterized in detail by Cq, CH, CH_2, alkyl, and C-N spectral editing. Based on connectivities measured by two-dimensional ^{13}C-^{13}C and ^{15}N-^{13}C NMR in samples made from uniformly and ^{13}C1-^{13}C2 labeled glucose reacted with glycine-^{15}N, several common structural fragments have been identified.

Introduction

The Maillard reaction between reducing sugars and N-containing compounds is of importance in food, health, and environmental sciences, among others. Its products are responsible for food aroma, browning color, and mutagenic properties. They are also related

www.manaraa.com

with aging diseases such as diabetes or cataract.[1,2] As a potential pathway of forming soil organic matter, the Maillard reaction may also play a role in the environment.[3] The Maillard reaction is not a single chemical reaction but a complex reaction network.[4-7] Due to the heterogeneity especially of the high-molecular-weight products, determination of their structures is one of the most demanding challenges in modern analytical chemistry. Various analytical methods, e.g. HPLC, MS, NMR, CE, SPME, thermal pyrolysis etc. have been used. Most studies, however, have mainly focused on the early stage products of the Maillard reaction or dealt with small molecules (less than 1 kDa),[8-10] which account for less than 25 % of the Maillard products.[11] Very little is known about the high molecular weight and the insoluble fraction, which account for most of the Maillard reaction products.

It has been shown that model Maillard reaction systems can be used to simulate the reactions occurring in food and in the human body.[5] A general scheme proposed by Hodge in 1953,[4] and elaborated by many scientists [5-7] has been widely accepted. At the initial stage of the model reactions, amines, as nucleophiles, condense with the carbonyl group of the sugar to form an N-substituted glycosylamine, which is not stable and isomerizes into the aminoketose via the aminoenol. For ketose sugars, aminoaldoses can be formed via imines as intermediates. The aminoketose or aminoaldoses are referred to as Amadori compounds. They rearrange themselves via 1,2-enolization or 2,3-enolization and further dehydrate and deaminate to form dicarbonyl compounds, which can further dehydrate into 3,4-dideoxy aldoketose,[6] and cyclize into 5-hydroxymethyl-furfural,[5] which may be suppressed if amino acids are overdosed. Amines can facilitate the migration of the carbonyl in the sugar, e.g., aldoses are converted into ketoses (such as fructose) and vice versa, or an imine becomes an aminoketose or aminoaldose. At the intermediate stage, those Amadori rearrangement products may undergo α-dicarbonyl, retroaldol, or vinylogous retroaldol fragmentation with acceleration by amines,[6] resulting in various fragmentation patterns (C_1+C_5, C_2+C_4, and C_5+C_1).[6] It has been proposed that in the presence of α-dicarbonyl compounds, the amino acids undergo Strecker degradation, which liberates the carbonyl carbon of the amino acid as carbon dioxide. The final stage of the reaction according to the scheme proposed by Hodge et al [4] may involve aldol condensation and aldehyde-amine condensation to form high-molecular-weight heterocyclic compounds.

www.manaraa.com

So far no isolated homogeneous melanoidins have been reported, and their structure is still unknown. Cämmerer and Kroh reported that the elemental composition of melanoidins is negligibly influenced by the molar ratio of the reactants, and proposed a structure [12] with a bond between C1 and the N of the otherwise unmodified amino acid, an olefin bond between C2-C3, and C4, C5, C6 unchanged, see Scheme 1.[12] A very different model of melanoidins has been proposed by Tressl et al., containing mostly aromatic rings made from the polycondensation between N-substituted pyrroles, 2-furaldehyde, and N-substituted 2-formylprroles.[6]

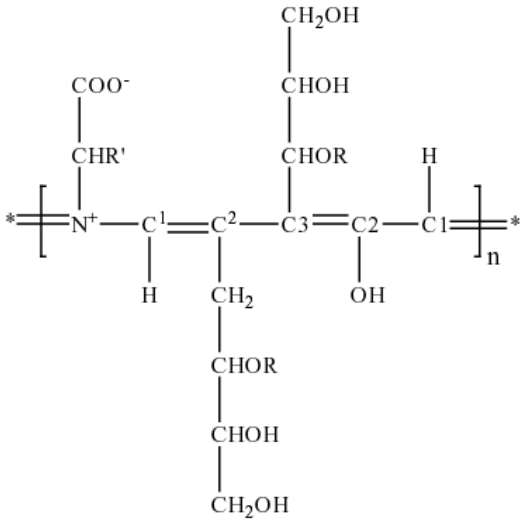

Scheme 1. Repeat unit of the structure proposed by Cämmerer and Kroh.[12]

Solid state NMR, as a nonintrusive and powerful atomic level technique, has been used successfully in studies of complex organic matter.[13,14] In the present work, solid-state NMR was applied to the high molecular weight products of the reaction, in dry conditions, between coprecipitated specifically ^{13}C-glucose and ^{15}N-labeled glycine. Samples have been prepared according to COST Action 919 (European COoperation in the field of Scientific and Technical research), and the reproducibility of this model reaction system has been tested using unlabeled reactants and NMR analysis. The specific ^{13}C labeling of glucose enables us to trace the origins of carbons in the final products. Two-dimensional ^{15}N-^{13}C and ^{13}C-^{13}C experiments provide N-C and C-C connectivities that enable identification of several common structural fragments.

www.manaraa.com

Experimental Section

Materials. D-glucose, anhydrous 99+% (MW 180.16) and glycine, 98% (FW 75.06) were purchased from Acros Organics (NJ USA). D-glucose with different ^{13}C-labeled sites: -$^{13}C_6$, -1-^{13}C, -2-^{13}C, -3-^{13}C, -6-^{13}C (all 99%), and glycine (-^{15}N, 98%) were selected based on availability and price, and obtained from CIL Inc. (MA USA). D-glucose (-1,2-$^{13}C_2$, 99%) was obtained from Isotec (OH, USA). Dialysis tubing made from regenerated cellulose was purchased from Fisherbrand with nominal MWCO 6000 to 8000, volume/length = 5.10 ml/cm. Filter papers are 41 ashless from Whatman (England). Water is E-pure water (Barnstead).

Sample preparation in the dry reaction condition. Following reference [7], a mixture of equal molar glucose and glycine was heated for 2 hours at 125 ^{o}C. After dialysis, high molecular weight fraction melanoidin was collected and used in this study. More details are given in ref. [15].

NMR Parameters. The NMR experiments were performed using a Bruker DSX400 spectrometer at 400 MHz for ^{1}H, 100 MHz for ^{13}C and 40 MHz for ^{15}N. A Bruker 4-mm triple-resonance MAS probe head was used for measurements of ^{13}C and ^{15}N labeled samples at various MAS speeds, while the natural abundance melanoidin samples were measured using a 7-mm Bruker double-resonance probe head at 6.5 kHz MAS. ^{13}C and ^{1}H chemical shifts were referenced to TMS, using the COO resonance of glycine at 176.49 ppm and the proton resonance of hydroxyapatite at 0.18 ppm as secondary references. ^{15}N chemical shifts were indirectly referenced to liquid ammonia by setting the signal of N-acetyl-D valine to 122 ppm. The 90^{o} pulse lengths were 4 μs for both ^{13}C and ^{1}H, and 6 μs for ^{15}N.

NMR Experiments

CP/TOSS experiments. For routine ^{13}C NMR characterization of various unlabeled and ^{13}C-labeled melanoidins, ^{13}C-^{1}H Cross Polarization (CP) combined with four-pulse TOtal Suppression of Sidebands (TOSS) [16] spectra were performed at 6.5 kHz MAS. CP contact time was 1-ms, recycle delay was 3 s, and Two-Pulse Phase Modulation (TPPM) decoupling was applied during detection.

www.manaraa.com

High-speed quantitative ^{13}C DP/Echo/MAS NMR. In order to quantitatively account for the contributions of the various, C1 through C6, glucose carbons to the melanoidins, quantitative ^{13}C DP (Direct Polarization) / Hahn echo / MAS NMR spectra were acquired for the samples made by reacting glucose-$^{13}C_6$, -$^{13}C1$, -$^{13}C2$, -$^{13}C3$, or -$^{13}C6$ with glycine-^{15}N, at 14 kHz MAS. The Hahn echo was used to avoid baseline distortion and TPPM decoupling was applied during detection. The recycle delays were estimated by measuring CP/T_1/TOSS spectra with two or three $T_{1,C}$-filter times. The $T_{1,C}$-filter time for which the residual carbon signals were less than 5% was set as the recycle delay of the corresponding quantitative DP/MAS experiments, which ensures that all carbon sites are fully relaxed. More details are given in reference [17].

CH and CH_2 spectral editing. CH (methine) signals can be selectively observed in dipolar DEPT experiments based on CH-group multiple-quantum coherence not being dephased by the spin-pair CH dipolar coupling, while CH_2 group coherence is dephased by the dipolar coupling of the carbon to the second proton.[18] Residual quaternary and CH_3 carbon signals can be subtracted out by acquiring a second spectrum under the same conditions but additionally applying 40 μs of gated decoupling before detection. The spinning speed was 5.787 kHz.

Spectral editing of CH_2 signals was achieved by selection of the three-spin coherence of CH_2 groups, using a ^{13}C 90° pulse and ^{1}H 0°/180° pulses applied after a quarter rotation period of MREV-8 decoupling [19]. The spinning speed was 5.787 kHz.

^{13}C chemical-shift-anisotropy filter. Selective spectra of alkyl (sp^3-hybridized) carbons were obtained by the ^{13}C chemical-shift-anisotropy (CSA) filter technique[20,21] with three 180° pulses (plus two 90° pulses) and a filter time of 38 μs, which dephases the signals of sp^2- (and sp-) hybridized carbons by the recoupled CSA.[20] During detection, TPPM decoupling was applied. The spinning speed was 6.5 kHz.

Selection of carbons near ^{15}N. In order to observe the glucose carbons directly bonded to N (denoted as C-N) or two-bond bonds from N (C- -N), a novel $^{13}C\{^{15}N\}$ MEdium and Long DIstance (MELODI)[22] technique has been implemented. The pulse sequence shown in Figure

www.manaraa.com

1a provides the signal S_0 of carbons within a one- or two-bond distance from N ("C-C-N"), while the sequence of Figure 1b retains only the signal S of the carbons at a two-bond distance to the N ("C- -N"). The difference $\Delta S = S_0 - S$ is the spectrum of carbons directly bonded to N ("C-N").

In the S_0 measurement, the 180° pulses on the ^{15}N channel were on and off in subsequent scans and the phase of receiver alternated every other scan. This is a REDOR-difference or heteronuclear-coherence pulse sequence that generates signals of carbons with dipolar couplings to ^{15}N. The longer the REDOR period, the longer the internuclear distances involved. Here we used 38 rotation periods (t_r) at the MAS frequency of 7 kHz to recouple one- and two-bond C-N interactions. In the S measurement, a second shorter REDOR period of 14 t_r duration was added, see Figure 1b, which selectively dephases the magnetization of N-bonded carbons ("C-N") due to their stronger dipolar coupling. Therefore, only the signals of carbons two bonds from N ("C- -N") remain.

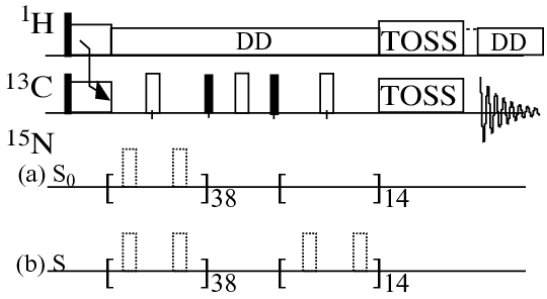

Figure 1. Pulse sequences for selectively observing the carbons of one or two bonds from their adjacent ^{15}N. (a) Reference pulse sequence used to obtain the signals S_0 of carbons within two bonds from ^{15}N (C-C-N). The 180° pulses on the ^{15}N channel are switched on and off and the phase of the receiver is correspondingly alternated to subtract out the carbons beyond ~ two bond distance to ^{15}N. (b) Pulse sequence used to obtain the signals S of carbons two bonds from ^{15}N by adding an additional short $^{13}C\{^{15}N\}$ REDOR that dephases the signals of C directly bonded to N. The spectrum of those C-N carbons can be obtained by taking the difference between the two spectra.

^{13}C-^{13}C spin pair selection. In order to investigate if the two ^{13}C in a doubly-labeled reactant such as glucose-$^{13}C1,2$ are still chemically bonded in the melanoidin, dephasing by the homonuclear J-coupling was measured.[15,23] A reference signal S_0 of all spin pairs and isolated ^{13}C spins was generated by a Hahn-solid-Hahn echo[15,23] that refocuses the J

www.manaraa.com

coupling. The difference between S_0 and S after J-dephasing shows the signals from ^{13}C-^{13}C spin pairs. The MAS frequency was 7 kHz.

Two-dimensional ^{15}N-^{13}C HSQC NMR. In order to detect the connectivities between glucose-^{13}C and glycine-^{15}N in the Maillard reaction products, the 2D ^{15}N-^{13}C heteronuclear single quantum (HSQC) pulse sequence with REDOR recoupling was applied.[24] The MAS frequency was 7 kHz.

Two-dimensional ^{13}C-^{13}C spin exchange. The ^{13}C-^{13}C connectivities in the glucose-$^{13}C_6$ and glucose-1,2-^{13}C reaction samples were traced by 2D ^{13}C spin exchange experiments, with mixing times of 50 or 10 ms to detect mostly cross peaks between directly bonded carbons. TOSS de-TOSS has been introduced before and after t_1 evolution time, and a third TOSS sequence was used before detection. A cross-polarization time of 1 ms and a MAS frequency of 7 kHz were used.

Results

CP/TOSS ^{13}C NMR spectra of melanoidins made from glucose and glycine in 1:1 or in 9:1 molar ratios are shown in Figure 2 (a) and (b). Figure 2 (c) is the CP spectrum for the sample made from neat glucose under the same reaction conditions. For comparison, the CP ^{13}C spectrum of glucose is also plotted in Figure 2 (dashed thin lines). Before the reaction, glucose gives three sharp peaks at 93, 70, and 60 ppm, assigned to the anomeric (half acetyl) O-CH-O (C1) carbon, the four CH-OH groups, and the CH_2-OH (C6) moiety, respectively.

Quantitative DP/Hahn echo/MAS ^{13}C NMR spectra of the melanoidin samples prepared from specifically ^{13}C-labeled glucose reacted with ^{15}N labeled glycine are plotted in Figure 3. From top to bottom, the samples are glucose-$^{13}C_6$, -$^{13}C1$, -$^{13}C2$, -$^{13}C3$, and -$^{13}C6$. The intensity of each spectrum has been normalized per scan and mass of sample in the rotor. The spectrum of $^{13}C4$ plus $^{13}C5$ was obtained by subtracting the sum of the spectra of glucose-$^{13}C1$, -$^{13}C2$, -$^{13}C3$ and -$^{13}C6$ from the spectrum of glucose-$^{13}C_6$. The thin lines are the spectra of all types of carbons, while the thick lines trace the corresponding selective spectra of quaternary and CH_3 carbons.

www.manaraa.com

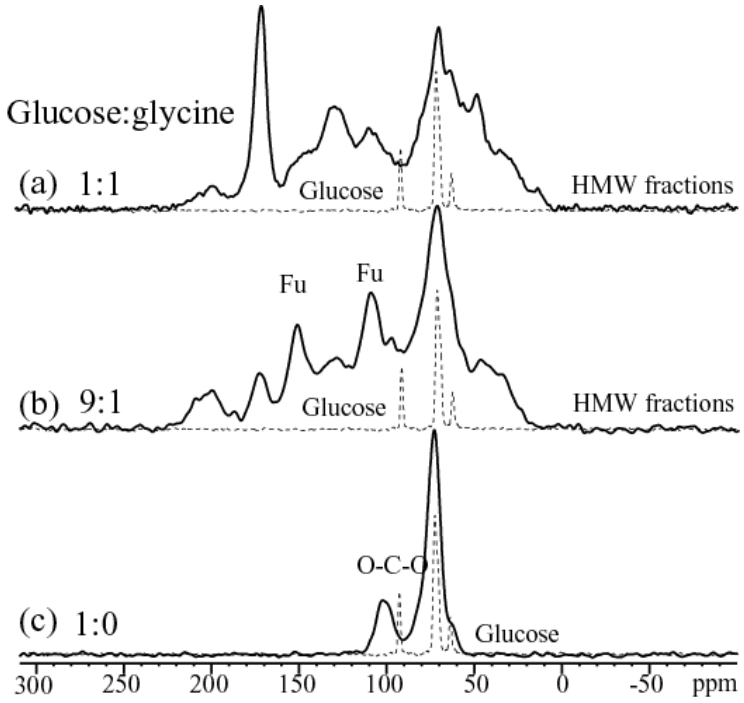

Figure 2. ^{13}C-^{1}H CP NMR spectra of melanoidins prepared from (a) glucose and glycine in 1:1 ratio or (b) 9 to 1 ratio. (c) Neat glucose subjected to the same heating cycle as the reactants in (a) and (b), but not fractionated by molecular weight. Dashed thin lines; Signal of neat glucose, with three sharp peaks.

Figure 4 shows spectral editing results for two specifically labeled samples, made by reacting glycine-^{15}N with glucose-$^{13}C1$ (a-d) or glucose-$^{13}C6$ (e-h). Figure 4 (a) and (e) shows quantitative ^{13}C spectra (thin lines), and their corresponding quaternary $^{13}C_q$ spectra (thick lines). Figure 4 (b) and (f) are selective spectra of the alkyl carbons, obtained by CSA-filtered spectra with or without gated decoupling (thin or thick lines, respectively). Figure 4 (c) and (g) are the CH-only (thin line) and CH_2-only (thick line) spectra. Figure 4 (d) and (h) show spectra of ^{13}C near ^{15}N, within one or two bonds from nitrogen (C-C-N, thin lines), directly bonded to nitrogen (C-N, thick lines), and two bonds from nitrogen (C- -N, dashed lines). Figures 5 and 6 show spectra of samples made from glucose-$^{13}C2$, -$^{13}C3$, and $^{13}C_6$, in the same sequence as Figure 4.

www.manaraa.com

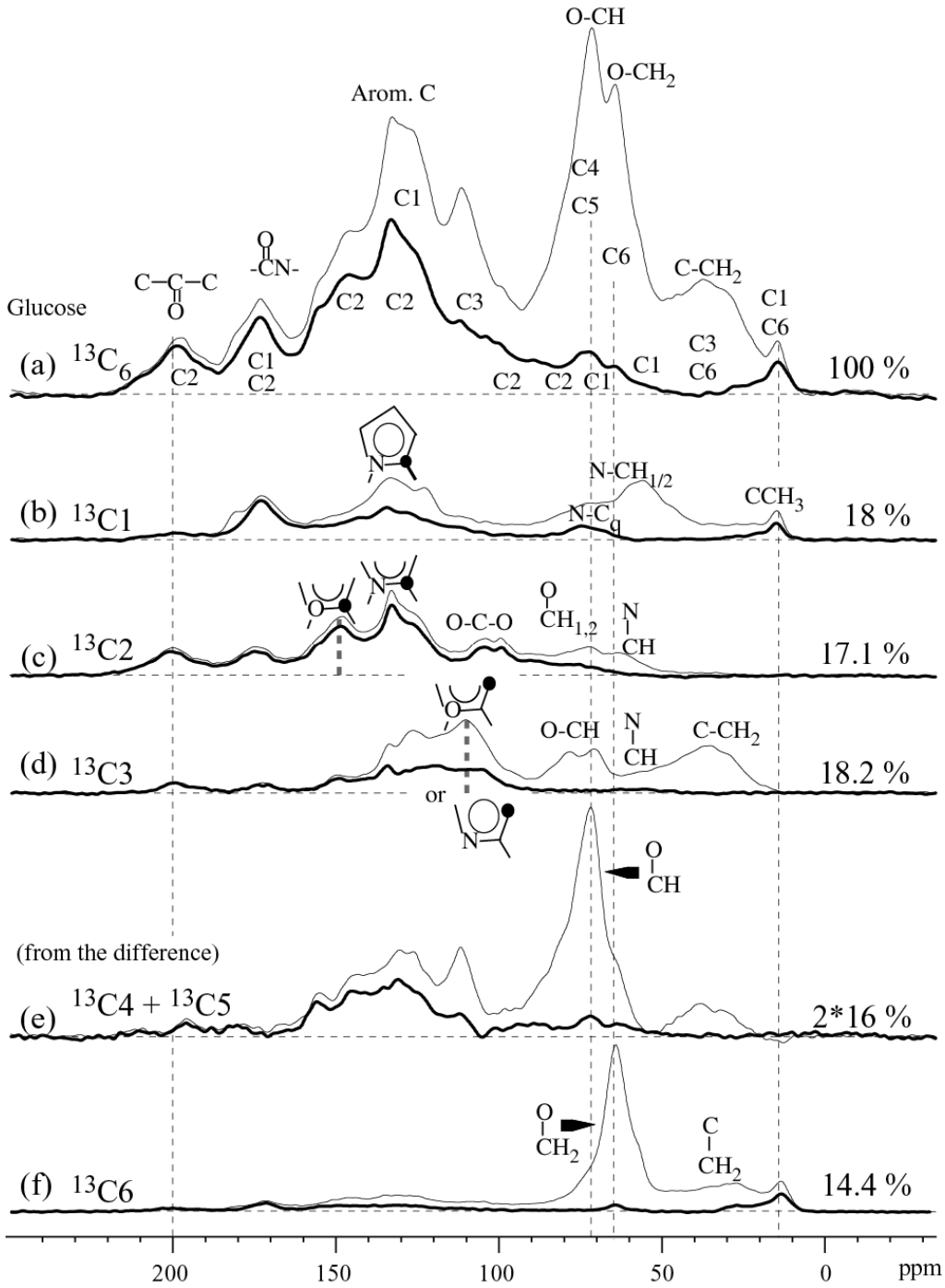

Figure 3. Quantitative ^{13}C spectra (thin lines) of melanoidins formed by reacting different ^{13}C labeled ($^{13}C1$ through $^{13}C6$) glucose with ^{15}N-labeled glycine in 1:1 ratio. "Glucose-$^{13}C4,5$" is obtained by taking the difference between the glucose-$^{13}C_6$ spectrum and the sum spectrum of glucose-$^{13}C1$, -$^{13}C2$, -$^{13}C3$, and -$^{13}C6$. Thick lines: corresponding spectra of quaternary and methyl carbons selected by adding 68 μs of gated decoupling before detection.

www.manaraa.com

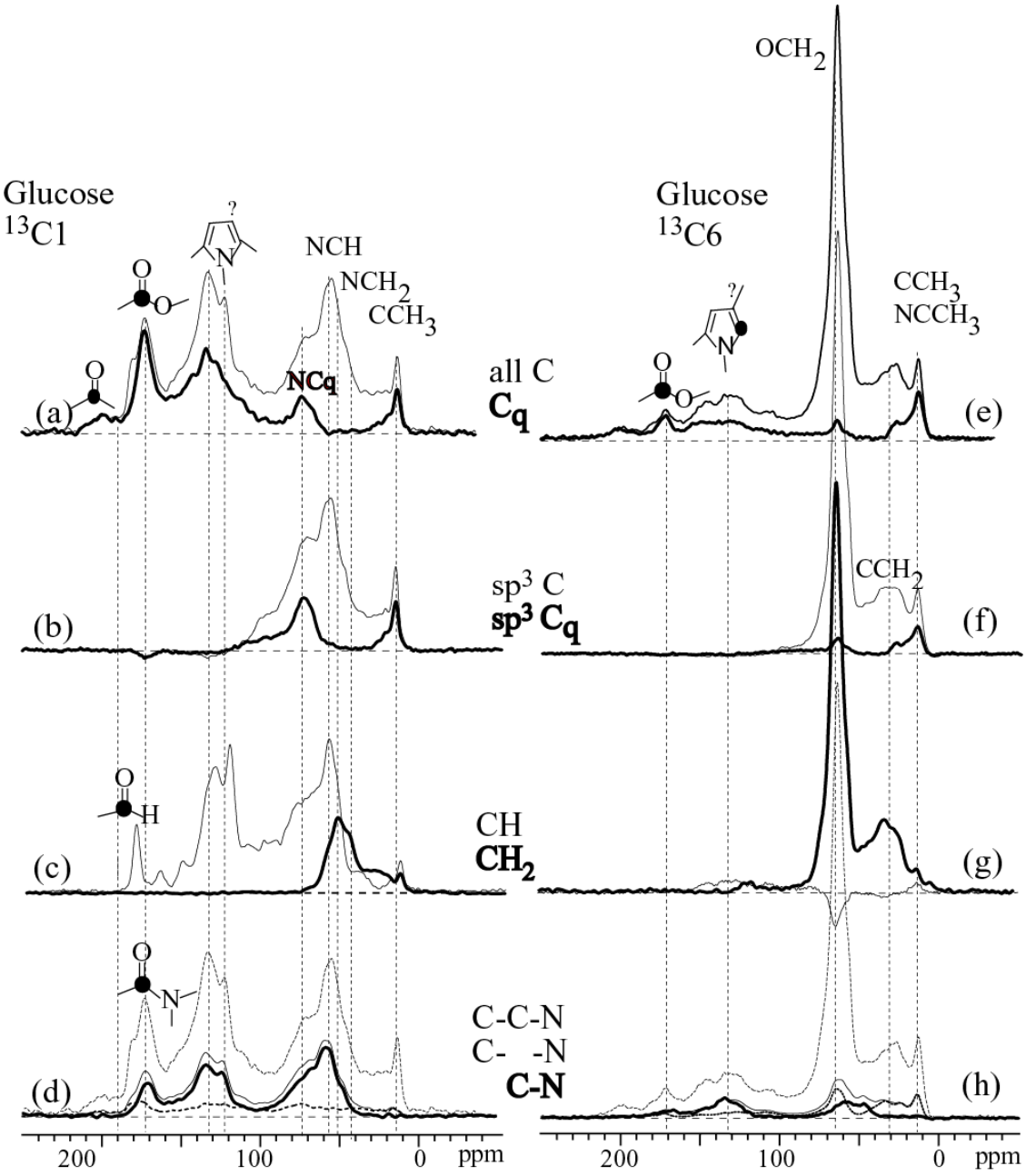

Figure 4. Spectral editing results of melanoidins made from glucose-^{13}C1 or glucose-^{13}C6 reacted with glycine-^{15}N were plotted in (a-d) and (e-h), respectively. (a) and (e): Thin lines: All signals of glucose-C1 or glucose-C6 in the products. Thick lines: Corresponding spectra of quaternary and methyl carbons obtained with 68 μs of gated decoupling at 14-kHz MAS; (b) and (f): Thin lines: CSA-filtered spectra with 38 μs CSA filter time. Thick lines: Quaternary and methyl sp^3-hybridized ^{13}C, selected by adding 40 μs of gated decoupling at 6.5 kHz MAS. Thin lines in (c) and (g): CH-only spectra, thick lines: CH_2-only, both with some CH_3 contributions. Solid thin lines in (d) and (h): Signals of carbons within two bonds from nitrogen; thick lines: carbons directly bonded to nitrogen; dashed lines: signal of carbon at least two bonds from nitrogen. Dashed thin lines: same quantitative spectra shown in (a) and (e).

www.manaraa.com

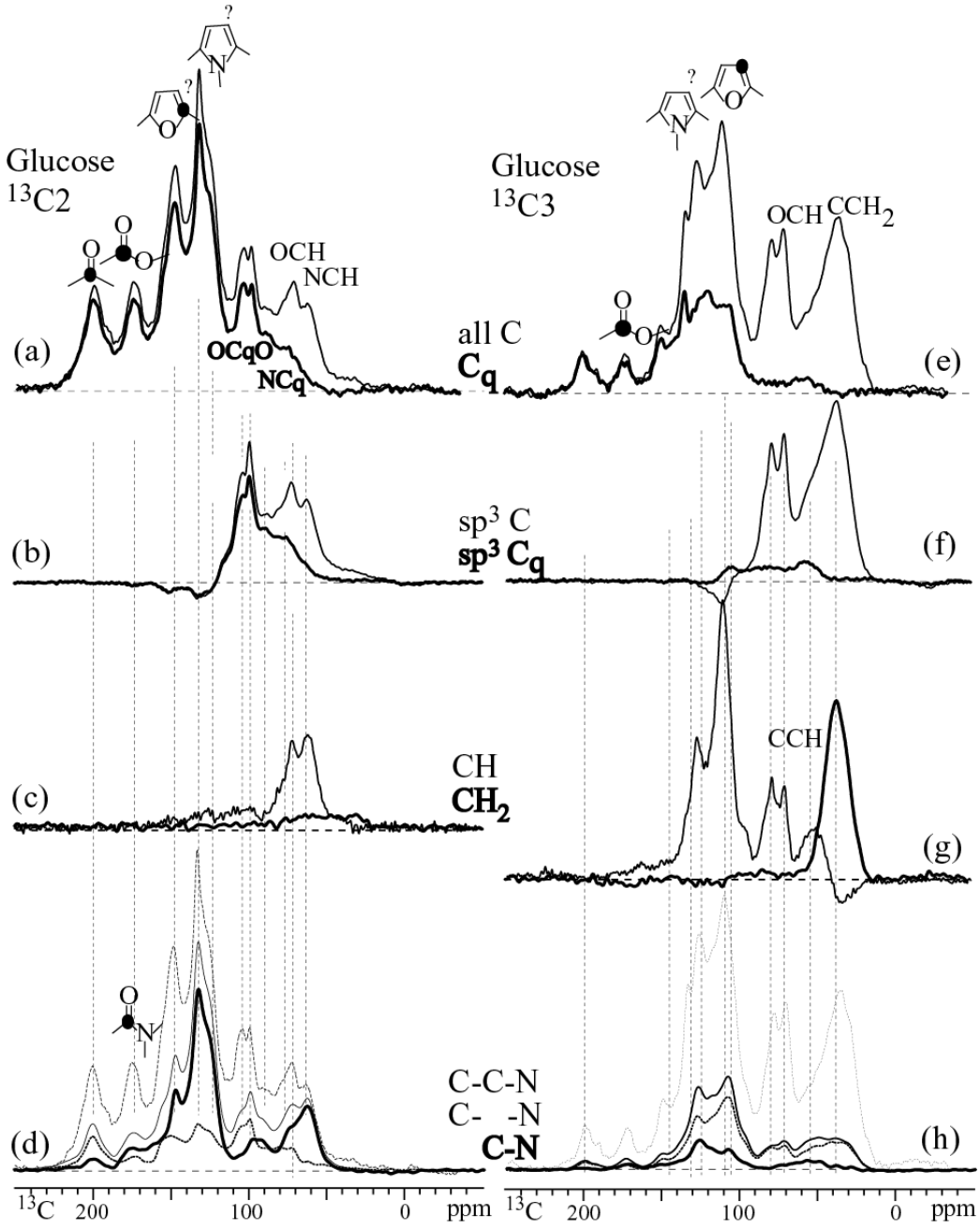

Figure 5. Spectral editing results of melanoidins made from glucose-^{13}C2 or glucose-^{13}C3 reacted with glycine-^{15}N were plotted in (a-d) or (e-h), respectively. (a) and (e): Thin lines: All signals of glucose-C2 or glucose-C3 in the products. Thick lines: Corresponding spectra of quaternary and methyl carbons obtained with 68 μs of gated decoupling at 14-kHz MAS; (b) and (f): Thin lines: CSA-filtered spectra with 38 μs CSA filter time. Thick lines: Quaternary and methyl sp^3-hybridized ^{13}C, selected by adding 40 μs of gated decoupling at 6.5 kHz MAS. Thin lines in (c) and (g): CH-only spectra, thick lines: CH_2-only, both with some CH_3 contributions. Solid thin lines in (d) and (h): Signals of carbons within two bonds from nitrogen; thick lines: carbons directly bonded to nitrogen; dashed lines: signal of carbon at least two bonds from nitrogen. Dashed thin lines: same quantitative spectra shown in (a) and (e).

www.manaraa.com

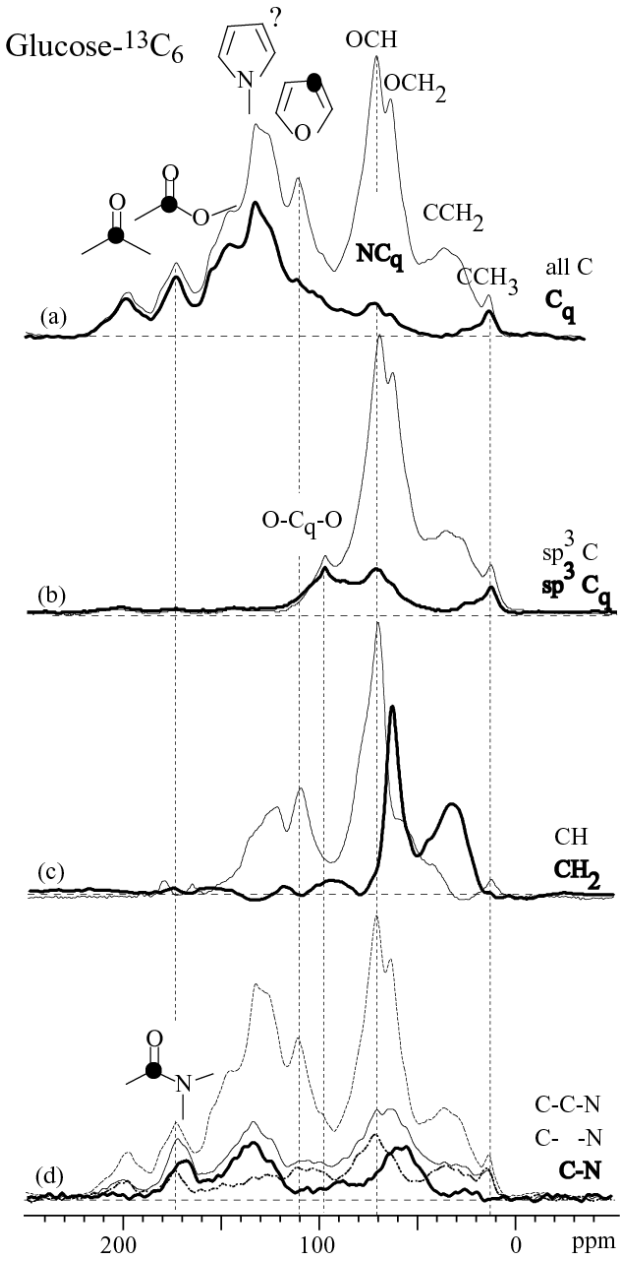

Figure 6. Spectral editing results of melanoidins made from glucose-$^{13}C_6$ reacted with glycine-^{15}N were plotted in (a-d). (a) Thin line: full spectrum; thick line: signals of quaternary carbons; (b) Thin lines: CSA-filtered spectrum with 38 μs CSA filter time. Thick lines: Quaternary and methyl sp^3-hybridized ^{13}C, selected by adding 40 μs of gated decoupling at 6.5 kHz MAS. Thin line in (c): CH-only spectrum, thick lines: CH_2-only, both with some CH_3 contributions. (d) Solid thin line: Signals of carbons within two bonds from nitrogen; thick line: carbons directly bonded to nitrogen; dashed line: signal of carbon at least two bonds from nitrogen. Dashed thin line: same quantitative spectrum shown in (a).

Figure 7 shows J-modulated spectra for the melanoidins made from glucose-$^{13}C1,2$ reacted with glycine-^{15}N. The reference spectrum S_0 (thick line) shows signals of spin pairs

www.manaraa.com

and isolated ^{13}C spins, while the J-modulated spectrum S (thin line) is only from the isolated ^{13}C spins. The difference $\Delta S = S_0 - S$ represents the signals of the ^{13}C-^{13}C spin pairs.

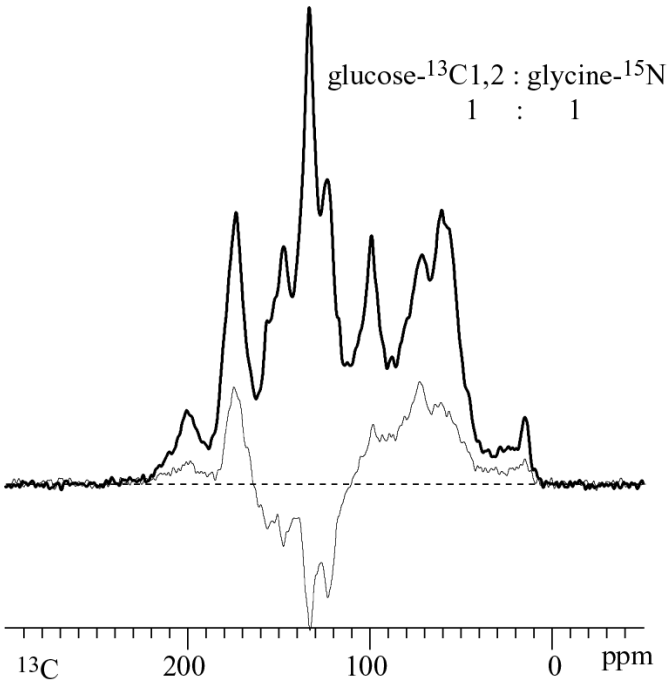

Figure 7. J-modulation spectra of melanoidins made from glucose-$^{13}C1,2$ with glycine-^{15}N in 1:1 ratio in dry reaction conditions. Thick line (S_0): Signals from ^{13}C-^{13}C spin pairs and isolated ^{13}C, thin line (S): signals of isolated ^{13}C spins. The negative bands in the aromatic carbon region indicate the larger J-coupling strength between ^{13}C-^{13}C spin pairs in aromatic rings.

The ^{13}C and ^{15}N labeled melanoidins enable us to apply 2D ^{15}N-^{13}C correlation spectroscopy to observe the carbon-nitrogen connectivity. Figure 8 shows the 2D HSQC spectra of melanoidins made from different selectively ^{13}C-labeled glucoses reacted with ^{15}N labeled glycine. From top to bottom, the melanoidins were prepared from glucose-$^{13}C_6$, glucose-$^{13}C1$, and -$^{13}C2$. The spectra of (d) to (f) are their corresponding HSQC spectra of quaternary and methyl carbons only. The spectra indicate that the signals with ^{13}C chemical shifts between 140 to 110 ppm are mainly from C1 and C2 of glucose. Amine-type nitrogens are not bonded to these aromatic or alkene carbons.

www.manaraa.com

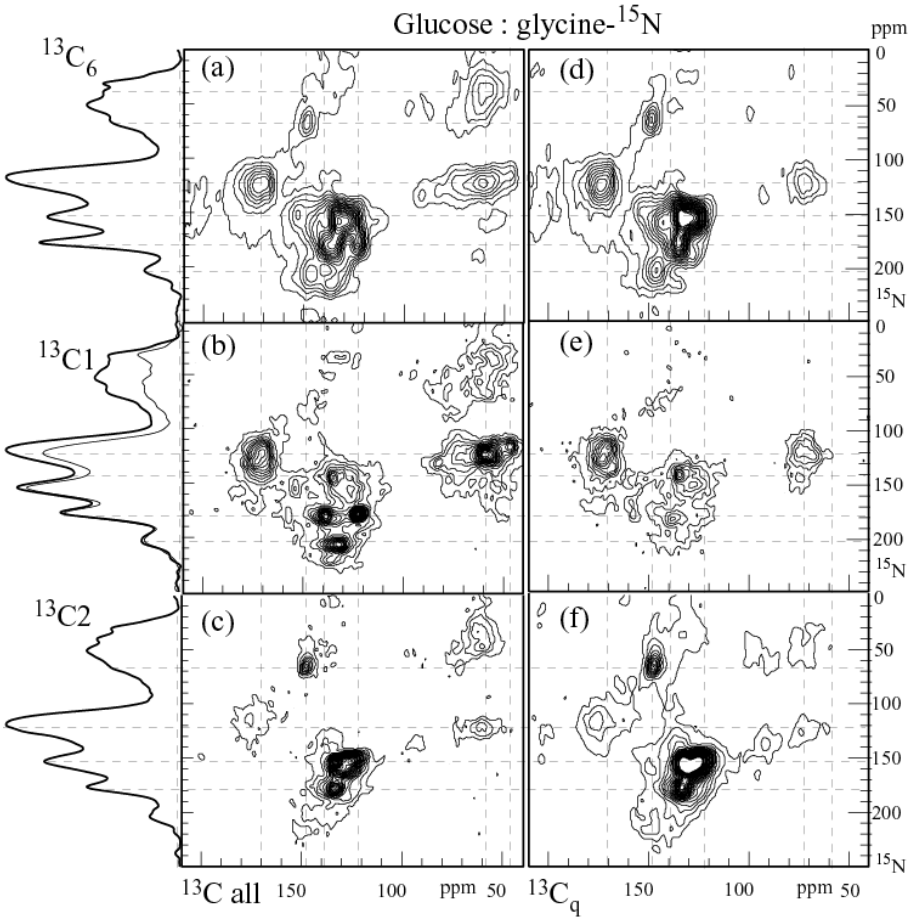

Figure 8. 2D ^{15}N-^{13}C HSQC of melanoidins made from selectively ^{13}C labeled glucose reacted with ^{15}N labeled glycine. From top to bottom, the sites of ^{13}C labeled glucose are (a, d) -$^{13}C_6$, (b, e) -^{13}C1, and (c, f) -^{13}C2. The spectra on the right, (d-f), were obtained after dipolar dephasing and show only signals of quaternary and methyl carbons. ^{15}N CP/MAS spectra of the three samples are shown on the right.

Two-dimensional ^{13}C spin exchange spectra for tracing ^{13}C-^{13}C connectivities via cross peaks are shown in Figure 9. Parts (a) and (b) are spectra of melanoidin made from $^{13}C_6$-labeled glucose, while those in (c) and (d) are from 50% diluted ^{13}C1,2-labeled glucose. In (c) and (d), the signals of quaternary and methyl carbons were selected in the ω_2 dimension by 40 μs of gated decoupling.

Discussion

Overall spectra. The Maillard reaction between glucose and glycine dramatically transforms the glucose structure, as seen in Figure 2 and also previously observed. [25] When the

www.manaraa.com

concentration of glucose is higher than that of glycine, i.e. in the 9 : 1 samples, there are more ketones (signal between 220 and 185 ppm), and more furans with characteristic peaks at 150 and 110 ppm, but less nitrogen-containing heterocyclic aromatic compounds such as pyrrole (around 140 to 110 ppm). More CHOH structures remains, as witnessed by the peak near 75 ppm in Figure 2 (b).

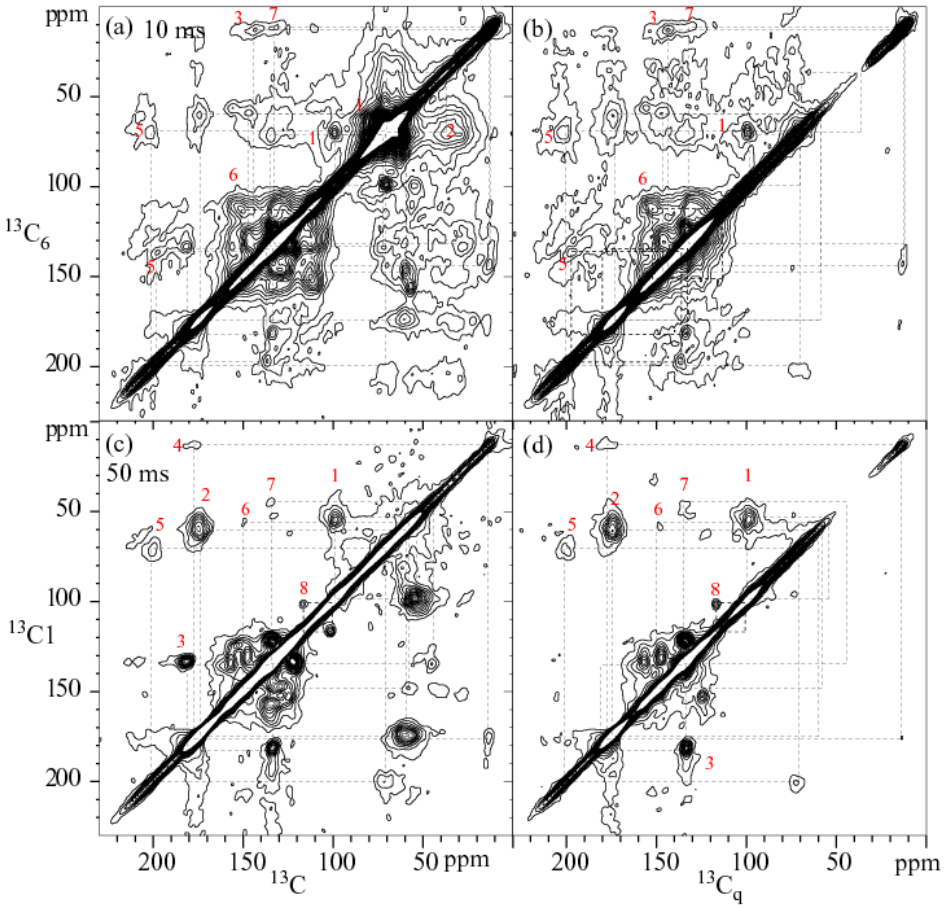

Figure 9. ^{13}C-^{13}C spin exchange spectra at 7 kHz MAS. (a) and (b) are for the samples made from glucose-$^{13}C_6$ reacted with glycine-^{15}N. 10 ms-spin diffusion time was used to obtain direct bonding information. (c) and (d) are for the samples made from 50% diluted glucose-$^{13}C1,2$ reacted with glycine-^{15}N. 50 ms-spin diffusion time was used. The spectra (b) and (d) show only quaternary and methyl carbon signals in the ω_2 dimension, selected by 40 μs of gated decoupling.

Without glycine, dry heating of glucose at 125 ^{o}C for 2 hours does not lead to major structural changes, as shown by its basically unchanged spectrum in Figure 2 (c), retaining the original three peaks, only broadened. The sugar has became amorphous or underwent

www.manaraa.com

oligomerization, without significant changes in the structure of the basic sugar ring. This demonstrates that in the dry reaction condition, amine compounds play a crucial role in the transformation of sugar into more complex compounds.

Percentage of each glucose carbon in the melanoidin. The quantitative ^{13}C and $^{13}C_q$ (quaternary carbon) NMR spectra in Figure 3 show striking differences between the structures formed by different glucose carbons (C1 through C6), proving that specific compounds are generated during the Maillard reaction under dry conditions. Taking the percentage of all glucose carbons in the HMW fraction products as 100%, C1 contributes 18 %, C2 17.1%, C3 18.2 %, C4+C5 32%, and C6 14.4 %. The percentage of the sixth C (C6) is significantly below the average value of 17%. C6 accounts for 1/6 = 16.5 % of all carbon in glucose, hence 1/7 of C6 was released from the HMW fraction sample. It could be lost during the reaction as gas or enriched in other fractions of melanoidins, e.g. low-MW or insoluble fractions. The lower percentage of C6 indicates C_5+C_1 fragmentation.

The spectrum of each glucose carbon in Figure 3 can be generally divided into to four relatively distinct spectral ranges: ketones from 220-185 ppm, amide and COO carbons from 185-160 ppm, aromatic and other C=C carbons from 160-100 ppm, and alkyl carbons resonating from 115-0 ppm. The overlap between alkyl and aromatic carbons between 115 and 100 ppm can be resolved by chemical-shift-anisotropy filtering. Setting the area of the full spectrum of each carbon to 100%, the percentages of these four subgroups are shown in Figure 10.

According to Figure 10, each carbon site of glucose produces significant amounts of both alkyl and aromatic carbons in the melanoidin. The remaining 6 to 18 % are contributed by C=O carbons of various types. The data indicate that about 40% of all carbons are in aromatic rings, and that C6 alkyl carbons must be attached to many of those aromatic rings, while the fate of glucose-C1 is more complicated.

Alkyl carbons in melanoidins. According to the CSA-filtered spectra in Figure 6(b), the alkyl (sp^3-hybridized) carbons resonate between 115 to 0 ppm. The overlap with the signals of sp^2-carbons in the region of 115 to 100 ppm can be resolved based on the chemical-shift

www.manaraa.com

filtered spectra, which retain the alkyl bands selectively. By integrating the quantitative ^{13}C spectrum in Figure 6 (a) from 115 to 0 ppm and correcting for overlapping aromatic signals, we found that the sp^3-hybridized carbons account for ~ 50% of total sugar carbons in melanoidins, and more than 80% of them are protonated. In the literature, for most volatile compounds, low molecular weight compounds, or even structural models of melanoidins [6], furan and/or pyrrole are often considered as their primary constituent units. Alkyl carbons have rarely been reported as the major units in melanoidins; Cämmerer's model[12] is the only example known to us, but while C3-C6 are in agreement with our experimental results, that structure contains no alkyl C2 or C1 and therefore cannot be the main alkyl structure in the melanoidin studied here.

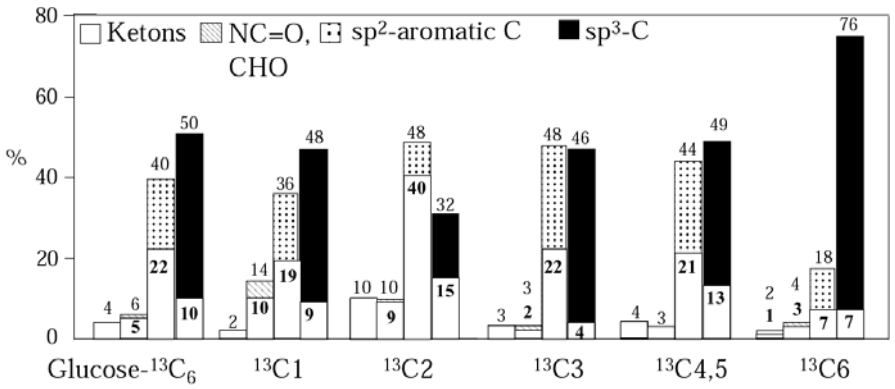

Figure 10. Percentages of various functional groups of each glucose carbon. The functional groups for each glucose carbon from left to right are: ketons, amide or aldehyl, aromatic carbons and sp^3 hybridized carbons. The white bars are their corresponding quaternary carbon percentages.

Alkyl carbons of melanoidins comprise 48% of C1, 32% of C2, 46% of C3, 49% of "C4+C5", and 76% of C6 (black bars in Figure 10). The alkyl carbon percentages in C1, C3 and C4,5 are very similar. Three quarters of C6 are alkyl carbons indicating C6 goes through the least transformation. Many of the alkyl $C6H_2$ and $C6H_3$ groups must be bonded to aromatic rings. The main features of alkyl carbons are as follows:

(i) O-alkyl carbons are present in significant amounts (~30% of all C). Two relatively sharp peaks, at 71 and 64 ppm, are mainly from C4+C5 as OCH (see Figure 3 (e), and from C6 as OCH_2 (see Figure 3 (f)), respectively. Many of these two types of carbons are bonded to each other, according to the strong cross peaks near the diagonal in

www.manaraa.com

Figure 9a. Figure 4h shows that only a small fraction of OCH_2 carbons are two bonds from N, while Figure 6d shows that OCH carbons are two bonds from N, as they would be if bonded to a pyrrole ring.

(ii) Ketose (O-C-O) carbons resonating at 105 and 99 ppm mostly belong to C2. They are bonded to OCH and themselves as O-C_q-O, according to the cross peaks in Figure 9, and they are two bonds from N according to Figure 5d.

(iii) Nonpolar methylenes, C-$\underline{C}H_2$-C, resonating between 50 to 20 ppm, are mainly from C3, with contributions from C4, C5, and C6. They are bonded to various types of C=O moieties, to aromatic rings, as well as to OCH and OCH_2 groups, according to Figure 9a.

(iv) $C\underline{C}H_3$ (2 % of all carbon) is mainly from C1 and C6, see Figure 3 at 14 ppm. The $C6H_3$ carbons are two bonds from N (Figure 4h), and bonded to pyrrole rings (Figure 9 a,b). In contrast, the $C1H_3$ groups are not close to nitrogen (see Figure 4d); some are bonded to C2OO groups, as part of acetyl residues, according to Figure 9c.

The following list compiles some characteristics of the alkyl carbons in melanoidins formed from each carbon of glycine:

(v) C1: 50% of sp^3-C1 is bonded to N, as $N\underline{C}H$ at 59 ppm, $N\underline{C}H_2$ at ~50 ppm, $N\underline{C}_q$ at 74 ppm, according to Figures 3 (b) and 4. In addition, $C\underline{C}H_{1\text{ or }2}$ from 50 to 20 ppm, and $C\underline{C}H_3$ at 10 to 25 ppm are also present. OCH_2 signals are negligible, and OCH bands broad and featureless. The majority of C1 of glucose ends up in sites with two bonds to carbon, which means that they must have formed new C-C chemical bonds, given that C1 in glucose has only one C-C bond, with C2 (see details below); exceptions among the alkyl sites are $N\underline{C}H_2$ and $C\underline{C}H_3$ groups.

(vi) C2: Almost all alkyl C2 carbons are bonded to O or N, as reflected in most chemical shifts being greater than 50 ppm. There are two sharp peaks of $O\underline{C}_qO$ at 105 and 99 ppm, OC_q at ~85 ppm, $N\underline{C}_q$ at ~ 75 ppm, $O\underline{C}H$ at 70 ppm, $N\underline{C}H$ at 61 ppm, according to Figures 3 (c) and 5. All types of CH_2 signals are quite negligible.

www.manaraa.com

(iii) C3: Almost all alkyl C3 carbons are protonated, see Figure 5f. C-$\underline{C}H_2$-C at 39 ppm is the major sp^3-C3 component, then O$\underline{C}$H at 80 and 70 ppm, and C$\underline{C}$H at 52 ppm, based on Figures 3 (d) and 5.

(iv) C4+C5: Most C4 and C5 carbons remain protonated, residing in OCH, some OCH_2, and C-CH_n-C sites, as shown in Figure 3 (e). NCH and CH_3 signals are absent. In Figure 6d, OCH peak resonating around 70 ppm are two bonds from N. They must be from C4 or C5.

(v) C6: Almost all C6 carbons remain multiply protonated, and most remain in HO-CH_2 sites resonating at 64 ppm; a shoulder at 73 ppm can be assigned to $\underline{C}H_2$-O-C ethers. Signals of C-$\underline{C}H_2$-C at 38 ppm, C-$\underline{C}H_3$ at 14 ppm, and NCH_2 at ~50 ppm are also observed in Figures 3 (f) and 4. CH signals are undetectable.

While the C4, C5, and C6 carbons have undergone only limited structural changes, the C1, C2, and C3 carbons have been dramatically transformed even in the alkyl-carbon region.

sp^2 hybridized carbons in melanoidin. In most studies of the early stages of the Maillard reaction and of the small molecules produced (volatiles and low-MW fraction) in the literature [6,26,27], researchers usually put emphases on aromatic rings and other sp^2-hybridized carbons, probably because these compounds are more chemically reactive and related to food color, aroma etc. Therefore, the unsaturated carbon structures have received most attention. As a result, even the structural models of melanoidins, i.e. the high-molecular-weight component, tend to emphasize aromatic structures.[6,28]

From Figure 3 (a) and Figure 10, sp^2 hybridized carbons account for 50% of total sugar carbons. Among them, ~10% formed carbonyl carbons in ketones resonating around 200 ppm, mainly from C2, with contributions from C3, 4, and 5, or in amides or carboxylates resonating around 175 ppm, mainly from C1, but also C2. The 2D correlation experiments can tell us how the carbonyl groups link to the remainder of the melanoidins, see below. Small amounts of C1 formed aldehyde type of carbon resonating at 180 ppm, see Figure 4

www.manaraa.com

(a). For signals at 200 ppm, C2 and C3 could be simultaneously double bonded to oxygen to form 2,3-α-dicarbonyl compounds, which were found in Amadori compounds. It is interesting to note that when C2 forms amide (~9%), it can remain bonded to only one carbon, and thus either the C1-C2 or the C2-C3 bond must be broken, indicating C_1+C_5 or C_2+C_4 fragmentation.[6]

Aromatic and alkene carbons resonate between 160 and 100 ppm, Various heteroaromatic rings are formed in the melanoidin studied here, such as furan, pyrrole, imidazolium and oxazolium specific information on the nitrogen-containing rings can be obtained from 2D ^{15}N-^{13}C HSQC and 3D ^{15}N-^{13}C-^{13}C spectra. The details will be discussed in a future publication.

(A) Furans. The band from 160 to 140 ppm in Figure 3 (a) must be assigned to aromatic C bonded to O. Most of them are associated with oxygen-containing aromatic rings, such as furans, in which the two carbons directly linked to oxygen resonate at ~150 ppm, while the carbons two bonds from the oxygen resonate at ~110 ppm. The corresponding cross peak is clearly seen in the 2D spectrum of Figure 9a. C2 and C4+C5 contain comparable quaternary carbons resonating at the 150±10 ppm, see Figure 3 (c) and (e), while C4+C5 and C3 have protonated carbons resonating at 110±5 ppm; however, some of the latter are also in pyrrole rings, being two bonds from N, see Figure 5h. In the Hodge scheme, 5-methylhydroxyl-furaldehyde has been proposed as an important intermediate with C1 forming an aldehyde and C6 staying intact. This kind of furan structure is consistent with our observation and explains why C2 and C5 are nonprotonated while C3 and C4 are protonated. Note, however, that no aldehyde bonded to a furan ring is observed in our sample (while an aldehyde bonded to a pyrrole is clearly detected in Figure 9). Thus, the C1 and C6 carbons of 5-methylhydroxyl-furaldehyde would have to undergo further reactions. From the intensities of the 150-ppm bands of C4+C5 and C2 in Figure 3, it is estimated that furan accounts for less than 15% of total sugar carbons

(B) Pyrroles. The pyrrole ring is one of major structure units of melanoidins considered in the literature. It would typically show resonances around 130 ppm for the C bonded to N,

www.manaraa.com

and around 110 ppm for the C two bonds from N. In Figure 3 (a), carbon intensities between 140 to 115 ppm are contributed by almost all glucose carbons in similar amounts, except for C6. Around 40% of C1, 70% of C2, and 25% of C3 are directly bonded to nitrogen in this chemical shift region, according to Figure 4 (d) and Figure 5 (d). Very little C6 is directly bonded to nitrogen; in the dominant OCH_2 form it is not even close to nitrogen within two bonds, but as CH_3 and C-CH_2-C, it is bonded to pyrrole rings. According to Figure 6 (d), ~ 35 % of carbons in the 140 to 115 ppm range could be assigned to nitrogen containing heteroaromatic compounds, such as pyrrole, imidazolium, or oxazolium rings. Since the glucose is uniformly ^{13}C labeled, the homonuclear J-coupling may cause the intensity to decay during the C-N recoupling periods of REDOR experiments. Therefore, it is likely that more than 35% of glucose carbons are associated with nitrogen in this spectral region. The remaining carbons resonating in this region could be olefinic, or in six-membered rings.

However, analysis of ^{15}N-^{13}C-^{13}C spectra, detailed in a forthcoming publication, shows that most C1 and some of the other carbons are involved not in simple pyrrole, but in more complex N-containing rings, such as oxazolium and imidazolium. This is also the origin of complexity in the ^{15}N spectrum of melanoidins，[15,29,30] see the ^{15}N signals downfield from 160 ppm in the HSQC spectra of Figure 8. Nevertheless, the ^{15}N signal of C2 at 150 ppm in Figure 8c and f, and protonated C3 carbons two bonds from N and resonating at 110±5 ppm in Figure 5h, are good indicators of a significant fraction of regular pyrrole rings. Except for the aldehyde (H-C1=O) resonating at 181 ppm, no strong cross peaks from pyrrole N-C2 to C1 outside the ring are observed. This suggests C_1+C_5 fragmentation, consistent with one of the reactions proposed by Tressl et al..[6]

(C) Alkenes. According to the Figure 6 (d), not all carbons in the chemical shift region of 140-110 ppm are in nitrogen-containing heterocyclic rings, and most furans do not contribute intensity in this spectral range. The remaining carbons resonating in this region may have formed alkenes, especially for C3 and probably C4, or may part of six-membered rings.

Additional C-C bond formation. In the original glucose molecules, C1 is bonded to one C (i.e. C2). After the Maillard reaction, according to Figure 3 (b) and Figure 4 (a) to (d),

www.manaraa.com

quaternary C1 between 150 to 20 ppm accounts for 28% of total C1, and alkyl-CH, mostly in NCH and OCH forms, accounts for 20% of total C1. Thus, about half of the C1 carbons of glucose must have formed new C-C chemical bonds if without chemical bond breaking. At least some of these are likely linkages that help form high-molecular-weight melanoidins. C6, as an end-group carbon, is also prone to form new C-C bonds in C-CH_2-*C* units (16%), but to a lesser extent than C1.

C2 and C3 have two C-C bonds in the starting material. Although most C2 carbons are not bonded to H, C2 usually forms new chemical bonds with nitrogen or oxygen. Thus, more than 95% of C2 does not appear to form additional C-C bonds. Alkyl-C3 exists as CCH_2, OCH, or NCH, and ~ 26% of C3 are protonated in the sp^2-C chemical shift range from 160 to 100 ppm. All of these carbons can have only two C-C bonds. Among the remaining ~22% of C3 from 160 to 100 ppm, half of them formed C3-N bonds, see Fgiure 5h. It is possible for less than 16% of C3 in 160 to 0 ppm region to form new C-C bonds.

13% of alkyl-"C4+C5" are quaternary carbons, see Figure 10. About half of them resonating around 90 ppm, which are attributed to O-C-O. Thus ~ 7% of C4+C5 are possible to form additional C-C bond in alky carbon region. For sp^2-hybridized "C4+C5", 22% of C4+C5 remain protonated. Some of quaternary sp^2-hybridized C4+C5 have formed new bonds with oxygen or nitrogen. Therefore, ~20% of C4 or C5 are possible to form additional new C-C bonds.

In summary, C1 stands out from the other carbons of glucose in its propensity for new C-C bond formation in the melanoidin with non-C1 carbons.

New C-N bond formation. From our previous results,[15] it is clear that nitrogen of glycine is very reactive. After the Maillard reaction, the nitrogen has changed into various compounds with new chemical bonds with sugar carbons, see Figure 8. According to Figure 4 (d, h) and 5 (d, h), the amide nitrogen is bonded to C1, C2; nitrogen is also bonded to alkyl carbons as NC_q, NCH, and NCH_2, again mostly with C1 and C2; Some nitrogen formed heterocyclic aromatic rings bonding to C1, C2, but less C3 and C6. As a symmetric counterpart, C4, C5

www.manaraa.com

may be also form C-N bond in those aromatic rings, but most C4+C5 have big fraction as OCH.

C-O bond cleavage and formation. Condensation and dehydration make most C1, C2, C3 and some C4, C5, and C6 carbons lose hydroxyl groups, to form CCH_n, NCH_n, NC_q, and CCH_3, as well as some alkene carbons or nitrogen-containing aromatic rings. In addition to C-O bond cleavage, some new C-O bond formation also occurs during the Maillard reaction, for instance when two furan carbons share one oxygen atom. For C2, it also contains two different types of OCO peaks near 100 ppm, where one carbon is bonded to two oxygen atoms.

C-C connectivities from 2D experiments. In Figure 9 (a), there are two main cross-peak domains, namely aromatic carbon domain (160-100 ppm) and polar alkyl carbon domain (80 to 50 ppm) with strong intensities. The significant cross peak intensity within the polar alkyl domain as well as their cross peaks with other alkyl carbons indicates the existence of the alkyl chain. Multiple linkages between the two domains have been found, which suggests that the connection of the various aromatic rings could be through the alkyl carbons, probably through alkyl carbons chains also. Meanwhile the cross peaks between aromatic carbons and ketone provide some other probabilities for aromatic ring connection.

Comparing with Figure 9 (a), several peaks are absent in Figure 9 (c), such as some cross peaks between aromatic carbons with polar or methyl, which indicates that they are from neither C1 nor C2.

Except for the aldehyde carbon cross peak with aromatic carbons, there are no obvious cross peaks found between carboxyl C or ketone carbon and aromatic carbons in the glucose-^{13}C1,2 labeled melanoidin as shown in Figure 9 (c).

Although the cross peaks between the nonpolar and polar alkyl carbons are remarkable, no cross peaks between methyl carbons (resonating around 10 to 20 ppm) and the nonpolar alkyl carbons have been found.

www.manaraa.com

Specific structural fragments. In the following, several specific structures are proposed and listed in Table 1, in which the numbers from (1) to (7) match the labels of the circled cross peaks in Figure 9 (a) and (c).

(1) The ketose (O-Cq-O) carbons resonating at ~100 ppm are mainly from glucose C2 according to Figure 3 (c). A cross peak between this ketose carbon signal and the polar carbon (OC3H) at 70 ppm in Figure 9 (a) can be clearly identified, telling us that the ketose C2 is bonded to C3 in an OCH group. Meanwhile, in Figure 9 (c) the ketose C2 carbons also show a clear cross peak with the protonated C1 carbons resonating at 54 ppm, assigned to NCH. The N in this structure is in an amide moiety (i.e., bonded to a C=O group), according to the HSQC spectrum of Figure 8b. Since the polar alkyl carbons have prominent cross peaks among themselves, as shown in Figure 9 (a), structure (1) in Table 1 can be proposed, where C3 connects with the rest of the untransformed polar alkyl chain. It seems likely that this structure is cyclized into a saturated carbon ring, as shown below the linear version. The C=O carbon of the amide, which is likely the C1 carbon of another alkyl fragment as discussed in structure (2), is shown bonded to an alkyl carbon, since the HSQC spectrum shows no significant amide-aromatic linkages.

(2) The amide C1 carbon resonating at 175 ppm, see Figure 4d, is bonded to a protonated polar alkyl C2 resonating at 60 ppm, according to one of the strongest cross peaks in Figure 9 (c). From Figure 5 (d), we can see that most C2 resonating at 60 ppm is bonded to nitrogen as NC2H. Since the next carbon, C3, shows a strong resonance at 38 ppm of CH_2 two bonds from N, see Figure 5g/h, the strong cross peak intensity at (60 ppm, 38 ppm) in Figure 9a can be assigned to a NC2H-C3H_2 linkage. The additional strong cross peak intensity at (70 ppm, 38 ppm) could be due to a linkage between C3H_2 and the commonly occurring C4H-O segment. On that basis, structure (2) can be proposed.

(3) According to Figure 9 (c), the aldehyde (H-C=O) C1 carbon resonating at 181 ppm is bonded to a nonprotonated aromatic C2 resonating at 132 ppm. The C1 carbon is two bonds from N, as seen in Figure 4d, and C2 is directly bonded to N, as seen in Figure 5d, confirming that the aromatic ring is a pyrrole. Therefore the structure (3) can be

www.manaraa.com

proposed. The C6 could be CH_3 or OCH_2 (even though these are rarely two bonds from N) since both candidates are supported by cross peaks in Figure 9 (a).

(4) Amide or ester carbons resonating at 178 ppm also show a cross peak with methyl resonances at 14 ppm in Figure 9 (c), where the methyl carbon is from C1 and the amide or ester carbon from C2. Since $C1H_3$ is more than two bonds from N, see Figure 4d, the C2 carbon must be an ester, see structure (3) in table 1. These acetyl groups must have been formed by C_2+C_4 fragmentation.[6]

Table 1. Alkyl and other major structures in melanoidins made from glucose reacted with glycine in a molar 1:1 ratio in a dry reaction.

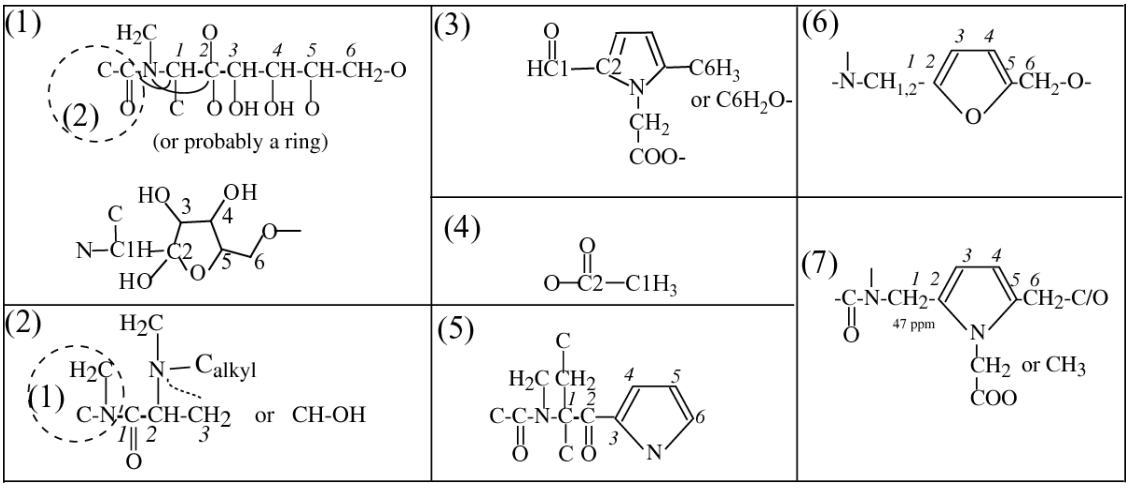

(5) Ketone C2 resonating at 201 ppm has a cross peak with the quaternary C1 at 70 ppm in Figure 9a, whose chemical shift and pronounced peak in the HSQC spectrum of Figure 8 proves an NCq structure. According to Figure 8(e), this quaternary alkyl C1 is bonded to amide nitrogen resonating at a ^{15}N chemical shift of 122 ppm. In Figure 9(a), ketone carbons have cross peaks with aromatic carbon at 138 ppm, which are absent in Figure 9(c). Therefore, structure (5) can be proposed, where ketone is bonded to C3, and C3-6 form a pyrrole ring.

(6) In Figure 9 (a), we can clearly see the cross peak near (150, 112 ppm) between the two pairs of furan carbons, with the protonated carbon two bonds from oxygen. In Figure 9 (c), the furan C2 resonating at 150 ppm has a cross peak with protonated polar alkyl

www.manaraa.com

carbons around 58 ppm. According to Figure 4 (c) and (d), this is $NC1H_{1, or\ 2}$. Therefore, structure (6) can be proposed. Based on Figure 8(b), the nitrogen is most likely an amide.

(7) In Figure 9 (c), there are cross peak between pyrrole carbon at 132 ppm and the alkyl carbon at 47 ppm. From Figure 8 (b), we also found this alkyl carbon is bonded to amide nitrogen. Based on Figure 4 (c), we know that this is most likely from NCH_2. Therefore, the structure (7) can be proposed.

Conclusions

Various solid-state NMR techniques, including spectral editing of CH, CH_2, and alkyl carbon signals, ^{15}N-^{13}C MELODI selection, 2D ^{15}N-^{13}C correlation, and 2D ^{13}C-^{13}C spin exchange, have been performed and yielded many insights about melanoidin structures. Quantitative ^{13}C spectra show that alkyl units make up ~ 48 % of carbon in melanoidins. The spectra show striking differences between the structures formed by different carbons (C1 through C6) of glucose, proving that specific structural units are formed during the Maillard reaction. The reactivity of the glucose-C1 carbon stands out: more than half of C1 carbons form additional C-C bonds, a much larger fraction than for the other sites. C2 carbons are all bonded to heteroatoms and mostly not protonated, while C3 is predominantly protonated and has a significant fraction of sites not bonded to heteroatoms. Only C4 and C5 remain significantly (~ 40%) in alkyl OCH sites. C6 undergoes the least transformation, mostly remaining in the OCH_2 form; in addition, it forms some C-CH_2-C units and ~1/5 is lost from the sample. C1 and C6 form CH_3 end groups in similar quantities (together, 6% of all C). C2-C5 are involved in formation of furan, which accounts for less than 15% of total sugar carbons, while nitrogen-containing five-membered aromatic rings are formed from all carbons. Based on the experimental data, specific structural fragments have been identified. Beside new bond formation, we also find specific evidence of sugar fragmentation, specifically C_5+C_1, C_1+C_5, and C_2+C_4, generally consistent with Tressl's proposal.[6]

www.manaraa.com

References

1. Monnier, V. M.; Cerami, A. *Sci.* **1981**, *211*, 491-493.
2. Hayase, F.; Usui, T.; Watanabe, H. *Mol. Nutr. Food Res.* **2006**, *50*, 1171-1179.
3. Ikan, R. *The Maillard Reaction: Consequences for the chemical and life sciences.*; John Wiley & Sons Ltd, 1996.
4. Hodge, J. E. *J. Agric. Food Chem.* **1953**, *1*, 926-943.
5. Ledl, F.; Schleicher, E. *Angew. Chem. Int. Engl. Ed.* **1990**, *29*, 565-594.
6. Tressl, R.; Wondrak, G. T.; Garbe, L. A. *J. Agric. Food Chem.* **1998**, *46*, 1765-1776.
7. Nursten, H. *The Maillard reaction: chemistry, biochemistry and implications*, 2005.
8. Ames, J. M.; Bailey, R. G.; Mann, J. *J. Agric. Food Chem.* **1999**, *47*, 438-443.
9. Hofmann, T. *J. Agric. Food Chem.* **1998**, *46*, 932-940.
10. Amrani-Hemaimi, M.; Cerny, C.; Fay, L. B. *J. Agric. Food Chem.* **1995**, *43*, 2818-2822.
11. Hofmann, T.; Ames, J.; Krome, K.; Faist, V. *Nahrung/Food* **2001**, *45*, 189-194.
12. Cammerer, B.; Kroh, L. W. *Food Chem.* **1995**, *53*, 55-59.
13. Benzing-Purdie, L. M.; Cheshire, M. V.; Williams, B. L.; Sparling, G. P.; Ratcliffe, C. I.; J.A., R. *J. Agric. Food Chem.* **1986**, *34*, 170-176.
14. Mao, J.-D.; Cory, R. M.; McKnight, D. M.; Schmidt-Rohr, K. *Org. Geochem.* **2007**, *38*, 1277-1292.
15. Fang, X.-W.; Schmidt-Rohr, K. In preparation.
16. Dixon, W. T. *J. Chem. Phys.* **1982**, *77*, 1800-1809.
17. Mao, J.-D.; Hu, W.-G.; Schmidt-Rohr, K.; Davies, G.; Ghabbour, E. A.; Xing, B. *Soil Sci. Soc. Am. J.* **2000**, *64*, 873-884.
18. Liu, S. F.; Mao, J. D.; Schmidt-Rohr, K. *J. Magn. Reson.* **2002**, *155*, 15-28.
19. Mao, J.-D.; Schmidt-Rohr, K. *J. Magn. Reson.* **2005**, *176*, 1-6.
20. Mao, J.-D. S.-R., K. *Solid State Nucl. Magn. Reson.* **2004**, *26*, 36-45.
21. Blano, F.J.; Tycko, R. *J. Magn. Reson.* 2001, *149,* 131-138.
22. Yao, X.-L.; Schmidt-Rohr, K.; Hong, M. *J. Magn. Reson.* **2001**, *149*, 139-143.
23. Powles, J. G.; Strange, J. H. *Proc. Phys. Soc.* **1963**, *82*, 6-15.
24. Bodenhausen, G.; Ruben, D. J. *Chem. Phys. Lett.* **1980**, *69*, 185-189.

www.manaraa.com

25. Ikan, R.; Ioselis, P.; Rubinsztain, Y.; Aizenshtat, Z.; Pugmire, R.; Anderson, L. L.; Woolfenden, W. R. *Org. Geochem.* **1986**, *9*, 199-212.
26. Tressl, R.; Helak, B.; Kersten, E.; Rewicki, D. *J. Agric. Food Chem.* **1993**, *41*, 547-553.
27. Kato, H.; Tsuchida, H. *Prog. Fd. Nutr. Sci.* **1981**, *5*, 147-156.
28. Adams, A.; Tehrani, K. A.; Kersÿieneú, M.; Venskutonis, R.; N.D., K. *J. Agric. Food Chem.* **2003**, *51*, 4338-4343.
29. Benzing-Purdie, L.; Ripmeester, J. A.; Preston, C. M. *J. Agric. Food Chem.* **1983**, *31*, 913-915.
30. Hayase, F.; Kim, S. B.; Kato, H. *Agric. Biol. Chem.,* **1986**, *50*, 1951-1957.

www.manaraa.com

CHAPTER 6. Complex N-containing structures formed in the model Maillard reactions

In the style of a paper to be submitted to The Journal of the American Chemical Society

Xiaowen Fang, Klaus Schmidt-Rohr*

Abstract

In the Maillard reaction of sugar with amine compounds, nitrogen plays a crucial role for structural transformations of glucose, especially under dry reaction conditions. Two-dimensional ^{15}N-^{13}C and ^{13}C-^{13}C spin exchange as well as three-dimensional ^{15}N-^{13}C-^{13}C solid state NMR techniques have been applied to ^{15}N- and ^{13}C-labeled melanoidins made in a dry reaction of glucose with glycine in a 1:1 molar ratio. The carbons associated with a downfield nitrogen band at 203 ppm indicate the presence of oxazolium mesoions. Based on the cross peak patterns in 3D cross sections of nitrogen resonating at 203 and 60 ppm, specific oxazolium structures have been proposed. Nitrogen resonating at 180 ppm is bonded to one nonprotonated C2 and two protonated C1 carbons of glucose, with C1 and C2 bonded to each other. Furthermore, one-dimensional CN_2 spectra prove that the downfield protonated C1H is bonded to two aromatic nitrogen atoms. On that basis, an imidazolium structure is proposed. For nitrogen resonating near 153 ppm, a clear cross peak pattern of a downfield protonated carbon bonded to a high-field quaternary carbon is observed and 4-oxopyridinyl is proposed as a tentative structure to match those constraints. Our multidimensional NMR experiments also show that CH_3 (mostly from C6) and HC=O (from C1) is bonded to specific pyrrole structures instead of furan. A specific amide structure with nitrogen chemical shift at ~120 ppm, proposed in our previous work, has also been confirmed. Although pyridines and pyrazines are often reported as Maillard reaction products in low molecular weight or volatile products, multinuclear solid state NMR results suggest that their amounts are insignificant compared to imidazolium and oxazolium.

Introduction

www.manaraa.com

The Maillard reaction is a very complicated reaction network between reducing sugar and amine compounds.[1-3] The structures of their products are still unknown.[4-6] In our previous work on the model Maillard reaction between glucose and glycine, the two glycine carbons remain mostly preserved as COO and NCH_2 moieties.[7] Unlike glycine carbons, glycine nitrogen plays a very important role during the whole period of the Maillard reaction. According to Hodge's scheme,[1] at the initial stage, sugar and amine condense to form N-substituted glycosylamine, which launches the Amadori rearrangements of sugar molecules,[8] further dehydration, fragmentation[3] or the amino acids undergo Strecker degradation. During the intermediate stage, the sugar derivatives either de-aminate and thereafter form final products without the participation of amine compounds, or condense with amine nitrogen to form various nitrogen-containing final structures. Multiple steps and a great variety of intermediates are involved in the Maillard reaction and in a wide mass distribution range. The formed structures are complicated, and the final stage reactions are still unknown.[2, 9]

The structural elucidation of final high molecular weight products may help chemists to trace back the final stage reaction paths. Pyrolysis of model melanoidins [10] from glucose reacted with glycine in the same preparation condition [2] as used here suggests that the melanoidins mostly contain heterocyclic aromatic structures such as furan, pyrroles, pyridines, pyrazines, oxazoles, where furan and carbonyl are predominant compounds and account for more 90% of products mass. Polycondensation has been considered as the main driving force of final polymer formation with molecular weights of more than 10 kDa. N-substituted pyrroles, 2-furaldehyde, and N-substituted 2-formylpyrroles have been reported as the components of extraordinary polycondensation activity based on their MS and NMR studies.[3] Great varieties of low molecular weight structures have been reported in the literature and they might be considered as precursors of the final polymer.[3, 5, 9, 11-27] Two- and three-dimensional NMR techniques[28] have been widely applied in biomolecular structural elucidation.[29] In this present work, various advanced solid state NMR techniques were applied for the first time to elucidate the melanoidin structures, and new major nitrogen containing structures have been identified.

www.manaraa.com

Experimental Section

Materials. D-glucose, anhydrous 99+% (MW 180.16) and glycine, 98% (FW 75.06) were purchased from Acros Organics (NJ USA). D-glucose (U-$^{13}C_6$, 99%), D-glucose (1-^{13}C, 99%), D-glucose (2-^{13}C, 99%), D-glucose (3-^{13}C, 99%), D-glucose (6-^{13}C, 99%) and glycine (^{15}N, 98%) were obtained from CIL Inc. (MA USA). D-glucose (1,2-$^{13}C_2$, 99%, hygroscopic) was obtained from ISOTEC (OH, USA). Dialysis tubing made of regenerated cellulose was purchased from Fisherbrand with nominal MWCO 6000 to 8000, vol/cm = 5.10 ml. Filter papers are 41 ashless from Whatman (England). Water is E-pure water (Barnstead).

Sample preparation in the dry reaction condition. Following the reference [2], a mixture of equal molar glucose and glycine was heated for 2 hours at 125 ^{o}C. After dialysis, high molecular weight fraction melanoidin was collected and studied here. More details were described in reference [7].

NMR Parameters. The NMR experiments were performed using a Bruker DSX400 spectrometer at 400 MHz for ^{1}H, 100 MHz for ^{13}C and 40 MHz for ^{15}N. A Bruker 4-mm triple-resonance MAS probe head was used for ^{13}C and ^{15}N labeled samples measurements at 7 kHz MAS speed. ^{13}C and ^{1}H chemical shifts were referenced to TMS, using the COO of glycine at 176.49 ppm as a secondary reference, hydroxyapatite proton at 0.18 ppm as proton's secondary reference, ^{15}N chemical shifts were referenced to NH_4NO_3, N-acetyl-D Valine at 122 ppm was uased as secondary reference. 90^{o} pulses were 4 μs for both ^{13}C and ^{1}H, and 6 μs for ^{15}N.

NMR Experiments

(1) Two dimensional ^{13}C-^{15}N HSQC and ^{13}C-^{13}C spin exchange

2D ^{13}C-^{15}N HSQC experiments have been performed to obtain the chemical bond connectivity between ^{15}N and ^{13}C with a total dipolar coupling modulation time of 1.1 ms. A 40 μs gated decoupling was chosen for quaternary carbon observation.

www.manaraa.com

In order to see the C-C connectivity of all glucose carbons, and glucose C1-C2 in melanoidins, 2D ^{13}C-^{13}C spin exchange experiments have been conducted to glucose-uniform-^{13}C and glucose-$^{13}C1,2$ labeled samples. 50 ms spin exchange time was used to produce the dipolar coupling transformation between two adjacent carbons. TOSS de-TOSS has been introduced before and after t_1 evolution time, which help remove sideband interferences on the first dimension. The third TOSS pulse was also used before detection to remove spinning sideband on the observation dimension. Meanwhile, a 40 μs gated decoupling was chosen for quaternary carbon detection.

(2) Three dimensional ^{15}N-^{13}C-^{13}C HSQC-spin exchange

Combining 2D ^{15}N-^{13}C HSQC and 2D ^{13}C-^{13}C spin exchange, a 3D ^{15}N-^{13}C-^{13}C HSQC-spin exchange pulse sequence as shown in Figure 1 (a) has been applied to the samples made from glucose-$^{13}C_6$ and glucose-$^{13}C1,2$ reacted with glycine-^{15}N, respectively. It provides the connectivity between ^{15}N and two ^{13}C. The experimental parameters were kept same as in their individual 2D experiments. 40 μs gated decoupling time was chosen for quaternary carbon observation.

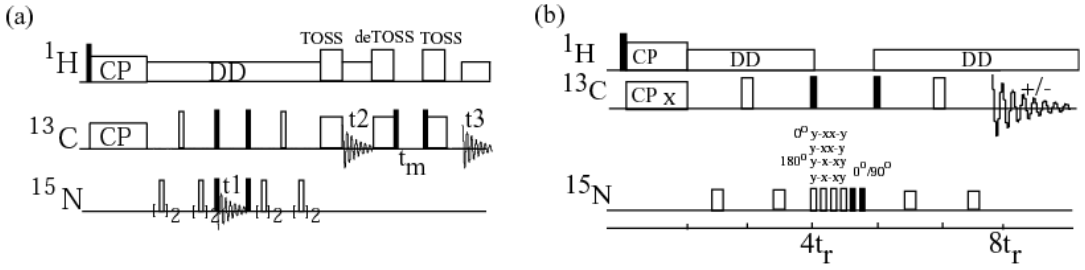

Figure 1. (a) The pulse sequence of 3D ^{15}N-^{13}C-^{13}C HSQC-spin exchange with or without 40 μs gated decoupling time. The first two dimensions provide the information about the ^{15}N and its adjacent ^{13}C, the second and third dimensions provide the chemical bond information about the ^{13}C with other ^{13}C. Therefore, at least three spin partners can be built. (b) The CN_2 selection pulse sequence similar as our often used CH_2 selection pulse sequence. The 90° pulse on ^{13}C and the 0°/90° pulses on ^{15}N channel are used to distinguish the single spin and three spin terms along with the 180° phase inversion of receiver to subtract the single spin terms in two subsequent scans. The two spin terms are removed by the 0°/180° and z-filter time.

(3) 1D CN_2 spectral editing

www.manaraa.com

Spectral editing of CN_2 signals was obtained by selection of the three-spin coherence of CN_2 groups, using a ^{13}C 90° pulse and ^{15}N 0°/90° pulses applied with MREV-8 decoupling to selectively keep the three spin term while subtracting out the single spin term. The 0°/180° pulses on ^{15}N channel combining with the z-filter time were used to get ride of the transverse plan two spin terms. The principle of CN_2 selection is very similar as the CH_2 selection technique.[30] The spinning speed was 5.787 kHz.

Results and Discussion

2D ^{13}C-^{15}N HSQC and 2D ^{13}C-^{13}C spin-exchange experiments have been carried out and the spectra of different glucose-^{13}C labeled melanoidins are shown in Figure 2 and 3. The samples in Figure 2, from top to bottom, are the melanodins made of glucose-$^{13}C_6$, glucose-$^{13}C1$, glucose-$^{13}C2$, glucose-$^{13}C1,2$ reacted with glycine-^{15}N in 1:1 ratio under dry reaction condition. In each 2D HSQC plot, there are five horizontal lines labeled as (a) to (e) indicating the nitrogen chemical shifts at 203, 180, 153, 120, and 60 ppm, respectively. These ^{15}N chemical shifts also correspond to the nitrogen positions where various informative cross planes were extracted from the 3D spectra.

Figure 3 (a, b) and (c, d) are for the glucose-$^{13}C1,2$ and glucose-$^{13}C_6$ labeled melanoidins, respectively. (a), (c) are for all types of carbon observation, and (b), (d) are only for quaternary carbon observation on the detection nuclei dimension. The aromatic region is our focus in the present work while the other crosspeaks have been discussed in our previous paper.[31]

In order to know how the peaks in Figure 2 and 3 are related to each other, 3D ^{15}N-^{13}C-^{13}C HSQC spin-exchange experiments were applied to the melanoidins made of glucose-$^{13}C_6$ or glucose-$^{13}C1$ reacted with glycine-^{15}N, respectively. In our 3D experiments, the first dimension is ^{15}N chemical shift evolution, the second dimension is the ^{13}C chemical shift evolution associated with the first dimension of nitrogen, and the third dimension is the ^{13}C that is bonded to the carbon of the second dimension. The pulse sequence is shown in Figure 1 (a). The second and third dimension C-C correlation spectra were obtained by taking the cross planes at certain nitrogen chemical shifts as shown in Figures 4, 5, 6 and 7. In the third

www.manaraa.com

dimension, the quaternary carbon can be selected by applying 40 μs gated decoupling before detection. Diagonal peaks in the 2D cross planes of Figure 4 to 7 are for the carbons directly bonded to their correspond nitrogen. Drawing horizontal lines cross both off-diagonal and diagonal peaks, the off-diagonal peaks represent the carbons bonded to their correspond diagonal carbons rather than the nitrogen.

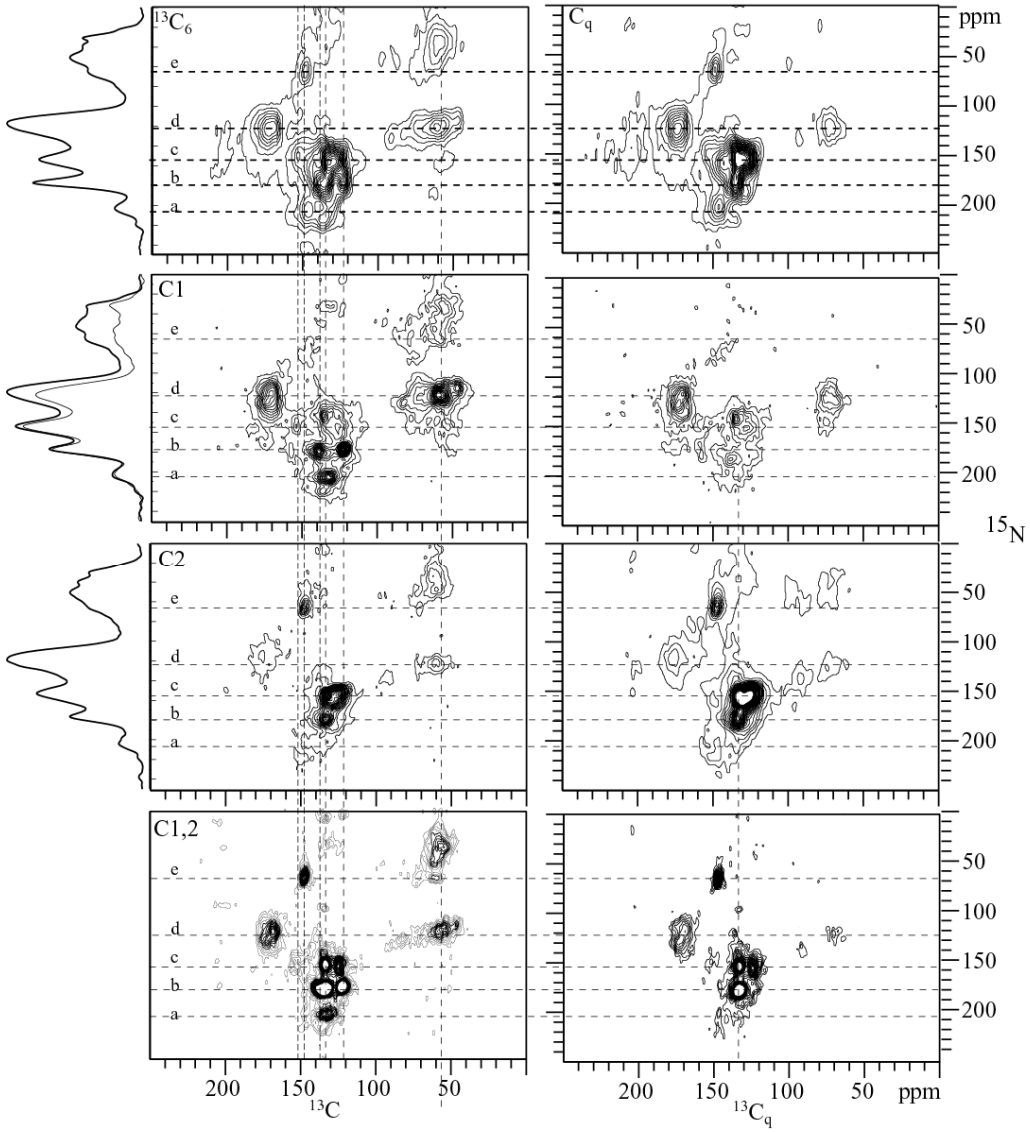

Figure 2. 2D ^{15}N-^{13}C HSQC of melanoidin made of glucose-$^{13}C_6$, glucose-$^{13}C1$, glucose-$^{13}C2$, glucose-$^{13}C1,2$ reacted with glycine-^{15}N, respectively, in 1 : 1 ratio and dry reaction condition. The horizontal dashed lines (a-e) indicate the nitrogen chemical shifts at 203, 180, 153, 122, and 60 ppm, respectively, which correspond to the cross planes taken from the 3D ^{15}N-^{13}C-^{13}C HSQC spin-exchange experiments.

www.manaraa.com

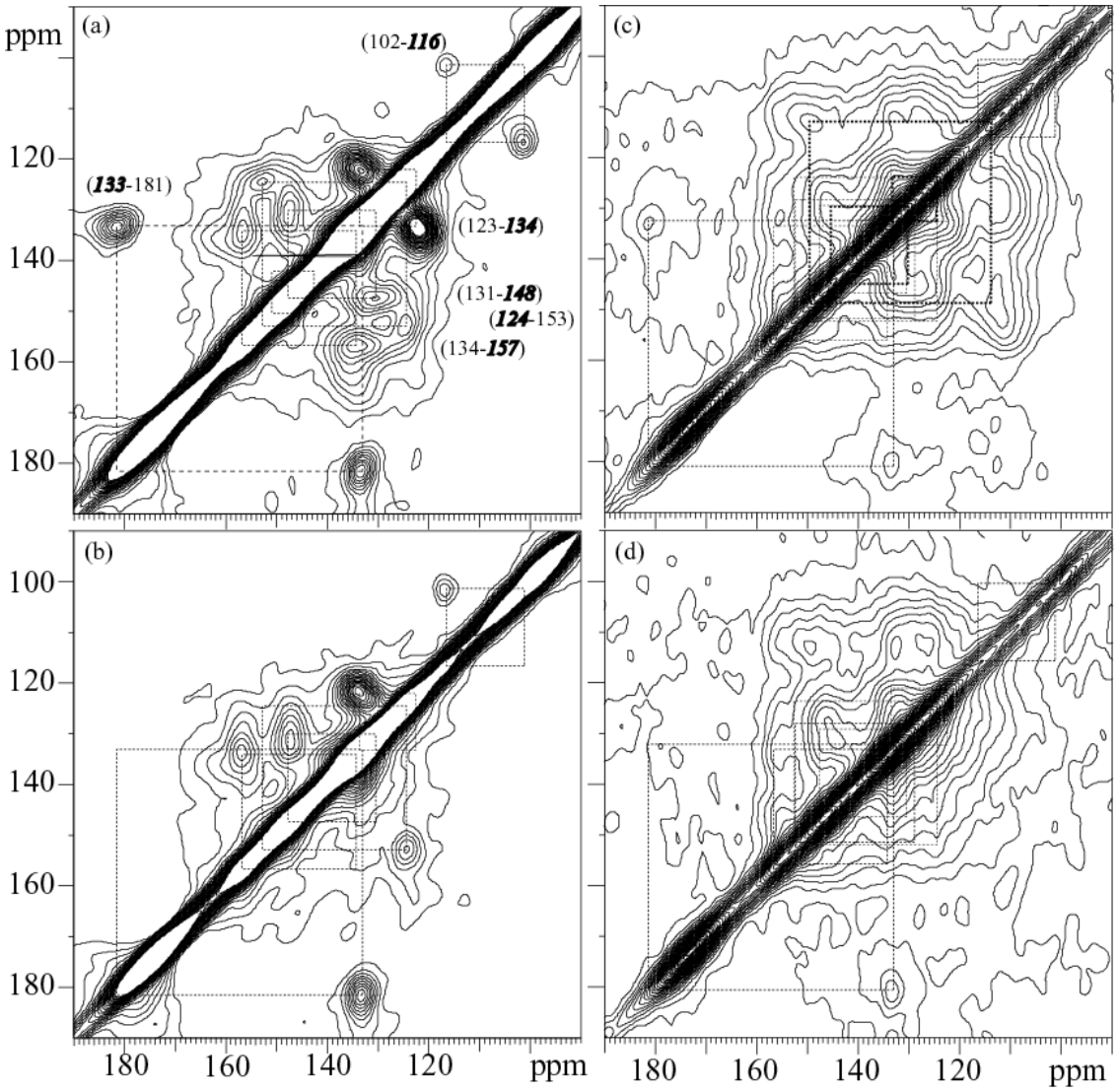

Figure 3. 2D ^{13}C-^{13}C spin exchange spectra of glucose-$^{13}C1,2$ labeled (a, b) and glucose-$^{13}C_6$ labeled (c, d) melanoidins. (b) and (d) are quaternary carbon 2D spectra by adding a 40 μs dipolar dephasing before the second dimension chemistry shift evolution, while the first dimension still contains protonated carbon signals. Only the aromatic region is shown here. For the glucose-$^{13}C1,2$ labeled melanoidin spectrum in (a), the chemical shifts of these cross peaks are listed. The aromatic spin pairs are alternatingly protonated incompatible with a fused-ring structure.

Based on these multidimensional NMR experiments, various structures have been proposed and their experimental ^{13}C chemical shifts agree with the prediction of ^{13}C chemical shift from the ACD software, within ± 10 ppm.

Oxazolium. According to Figure 2, there is a cross peak between nitrogen resonating at 203 ppm (line a) and protonated C1 carbon resonating at ~ 132 ppm. In Figure 3 (c), two ^{13}C-^{13}C

www.manaraa.com

pairs were found, one pair with ^{13}C of 134 ppm bonded to the ^{13}C at 157 ppm, another pair with ^{13}C of 131 ppm bonded to ^{13}C at 148 ppm. Both carbons at 131 ppm and 134 ppm carbon are protonated, while carbons at 148 and 157 ppm are quaternary carbons. Meanwhile in Figure 2, the lines (e) indicate a nonprotonated aromatic C2 at 148 ppm bonded to amine type nitrogen resonating around 60 ppm.

The 2D ^{13}C-^{13}C cross planes of 3D experiments with the nitrogen resonating at 203 ppm are shown in Figure 4 (a-c). 2D cross planes with the nitrogen resonating at 60 ppm are shown in Figure 4 (d-e). (a) and (d) are from the sample made of glucose-$^{13}C1,2$ reacted with glycine-^{15}N. Figure 4 (b) (c) and (e) (f) are for glucose-$^{13}C_6$ and glycine-^{15}N labeled melanoidin. (c) and (f) are spectra with only quaternary carbon detection on the third dimension.

In Figure 4 (b), two diagonal peaks are observed, one around 132 ppm, another around 146 ppm. Only the one at 132 ppm shows a strong diagonal peak in (a), indicating that the diagonal peak around 146 ppm in (b) and (c) are not from glucose-C1 or -C2. Meanwhile the quaternary carbon at 146 ppm has connection with a polar alkyl carbon resonating around 60 ppm. The appearance of a second cross peaks between the two signals at 132 ppm and 146 ppm in (b) is attributed to two-bond spin diffusion since aromatic bond length and angle draw close the two carbons.

According to Figure 4 (a), the protonated carbon (absent in (b)) at ~132 ppm has two different quaternary bonding partners, one around 148 ppm, another around 157 ppm, indicating different substitutions. Their correlation cross peaks also appear in Figure 3 (a). While the regular nitrogen in oxazole resonates around 250-260 ppm,[32] the mesoionic form move the chemical shifts towards higher field due to the changes of torsion angle and resonance of conjugation by adding an additional chemical bond.[33, 34] Therefore the structure (1) can be proposed and the ACD ^{13}C chemical shift prediction values are listed near their correspond carbons. Different substitutions would affect their ^{13}C chemical shifts.

Figure 4 (d-f) shows 2D cross planes taken at nitrogen 60 ppm. The amine type nitrogen is bonded to the quaternary carbon of 148 ppm, which is also found in the glucose-$^{13}C2$

www.manaraa.com

HSQC spectrum as indicated by lines (e) in Figure 2. Furthermore, in Figure 4 (d), the 148 ppm peak is from a carbon bonded to a protonated carbon resonating around 131 ppm. Therefore the amine type of nitrogen can be proposed to link with the oxazolium ring. On the other side, the amine nitrogen is bonded to the carbon showing a diagonal peak around 60 ppm in Figure 4 (d), a protonated carbon. This carbon is connected with an OC_qO (ketal) C2 carbon resonating around 100 ppm as also discussed in discussed in our previous paper.[31] Therefore, structure (2) can be proposed.

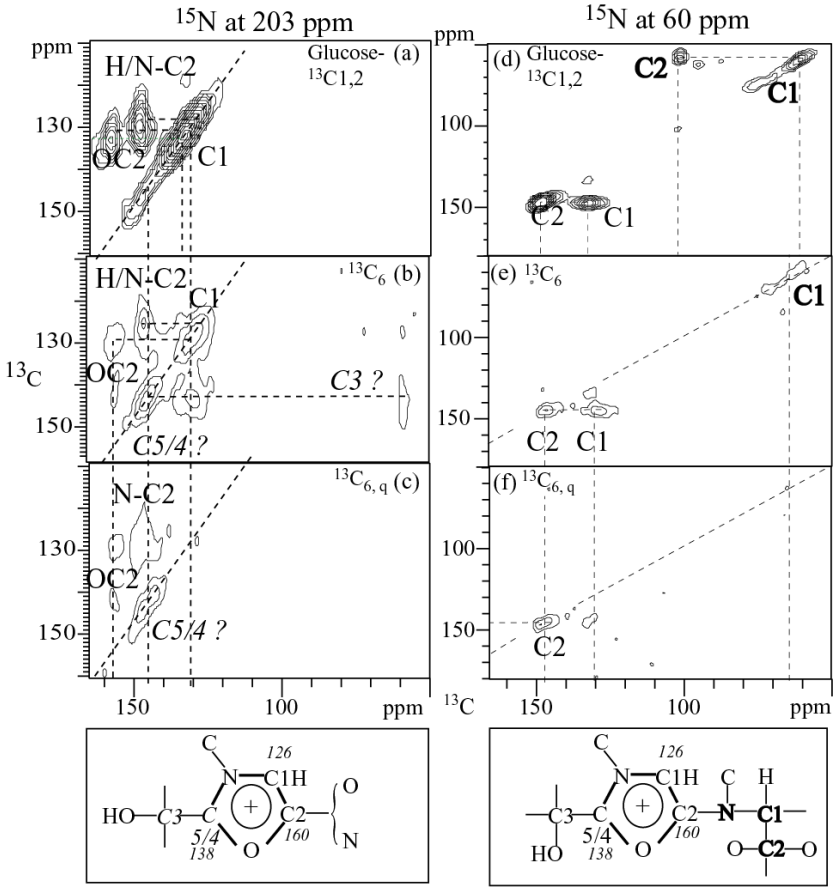

Figure 4. Experimental results supporting the existence of an oxazolium structure associated with the signal on lines "a" in Figure 2. (a-c) and (d-f): 2D ^{13}C-^{13}C plots taken from the 3D experiments with the nitrogen resonating at 203 ppm and 60 ppm, respectively. (a) and (d): of the sample made of glucose-$^{13}C1,2$ reacted with glycine-^{15}N in 1:1 ratio; (b,c) and (e, f): of the sample made of glucose-$^{13}C6$ reacted with glycine-^{15}N. (c) and (f): with 40 μs gated decoupling before the detection. Therefore the projection signals to the f3 dimension (the horizontal axis) are from quaternary carbons. The proposed structure (2) and (3) are also listed in this figure.

Imidazolium. The dashed lines (b) in Figure 2 indicate nitrogen resonating at 180 ppm. It is bonded to two protonated carbons in the $^{13}C1$ labeled sample with chemical shifts of 137 and

www.manaraa.com

123 ppm. Meanwhile in the C2 labeled sample, the 180 ppm nitrogen is also bonded to a quaternary C2 carbon resonating at 134 ppm. All three cross peaks also appear prominently in the ^{13}C1,2 labeled melanoidin HSQC spectra. Figure 3 shows that the quaternary C2 at 134 ppm is bonded to the protonated C1 at 123 ppm.

Figure 5 shows two 2D cross sections from of 3D ^{15}N-^{13}C-^{13}C HSQC-spin exchange spectra taken at the 180 ppm nitrogen position. In Figure 5 (a), there are the three diagonal peaks of 123 ppm, 134 ppm, 137 ppm, expected from the HSQC spectra of Figure 2. The 134 ppm peak is from a nonprotonated carbon, see Figure 5 (b), again as expected. Meanwhile, the cross peaks in Figure 5 (a) indicate that the two carbons at 123 and 134 ppm are bonded to each other, which agrees with the observation in Figure 3. A pyrrole N can be bonded to only two aromatic C in the same ring, and with three of the carbons directly bonded, there must be a second N in the ring, supported by downfield shift compared to compare to pyrrole N. The N must have a very similar chemical shift, so the structure must be quite symmetric with respect to two N. Based on these results, the imidazolium structure shown in Figure 5 can be proposed. The predicted carbon chemical shifts are listed next to the carbon, which support the existence of imidazolium as well. In this proposal, a mesoionic resonant structure between the sp^3 and sp^2 hybridized nitrogen are formed in that the two nitrogen show similar chemical shift position around 180 ppm.[34]

In the imidazolium structure, the 137 ppm C1 is simultaneously bonded to two resonant nitrogen. The CN_2 selection technique has been developed to further prove the existence of this type of glucose-C1.

(1) 4-oxopyridinyl

The dashed lines c in Figure 2 mark the nitrogen resonating around 153 ppm. It bonds with two quaternary carbons in the ^{13}C2 labeled sample at 133 and 124 ppm. If look at the two cross peaks more closely, we found that the centers of two cross peaks are slightly off, one nitrogen is around 155 ppm bonded to the carbon at 133 ppm, another nitrogen is around 150 ppm and bonded to the carbon at 124 ppm. In the 2D ^{13}C-^{13}C spin exchange spectra as shown in Figure 3 (a) and (b), the 124 ppm quaternary carbon is connected with a protonated

www.manaraa.com

C1 at 153 ppm, and the 132 ppm quaternary carbon is bonded to aldehyde carbon resonating around 181 ppm.

In Figure 6 (a), three diagonal peaks are at 124, 133, 155 ppm, in which the 124 ppm carbon and 155 ppm carbon show symmetric cross peak, while the 133 ppm carbon is bonded to the carbon resonating at 181 ppm. In Figure 6 (b) and (c), the diagonal peak at the 130 ppm area is relatively strong in the glucose-$^{13}C_6$ labeled sample, indicating that the intensity is also contributed from some other carbons besides C1 or C2 at 133 ppm. Meanwhile the 130 ppm digonal peak has connection with a protonated carbon resonating around 110 ppm, or some alkyl carbons from 80 to 10 ppm.

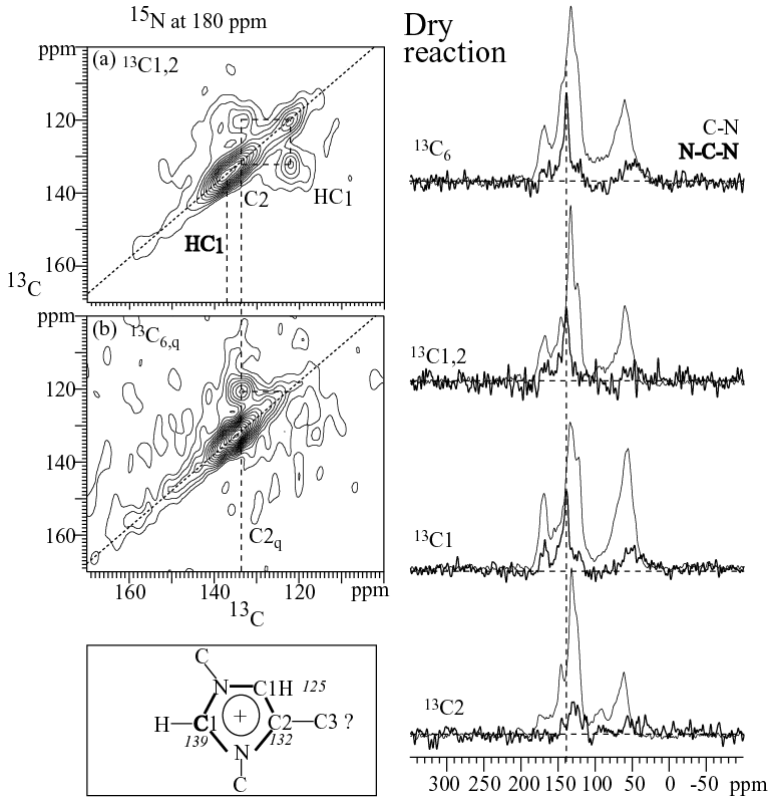

Figure 5. Experimental results supporting the existence of imidazolium structure associated with the signals on the line "b" in Figure 2. The left 2D plots were taken from the 3D experiments with the nitrogen resonating at 180 ppm. The bottom one is with 40 μs gated decoupling before the detection. Therefore the projection signals to the f3 dimension (the horizontal axis) are from quaternary carbons. The 1D spectra are the CN_2 selection spectra for the sample made in dry reaction with different glucose carbon labeling reacted with glycine-^{15}N in 1:1 ratio. Only the dry reaction sample, containing glucose-C1 labeling, shows a sharp peak at 137 ppm. Based on the results, the imidazolium structure has been proposed as shown in structure (3) of this figure.

www.manaraa.com

By taking al these constraints into consideration, such as the protonated C1 at 155 ppm bonded to quaternary C2 at 124 ppm, quaternary C2 at 133 ppm bonded to 181 ppm aldehyde carbon C1, non-C1,2 carbon bonded to protonated non-C1,2 carbon at 110 ppm, and four carbons all associated with the nitrogen resonating around 153 ppm, a 4-oxopyridinyl structure can be proposed as shown in Figure 6 with their simulation ^{13}C chemical shift listed next to each carbon. Due to the unequal diagonal intensities around 130 ppm area in Figure 6 (b) and (c) comparing with Figure 6 (a), the exceeding intensities may arise from a single pyrrole ring, with the nitrogen also bonded to an alkyl carbon.

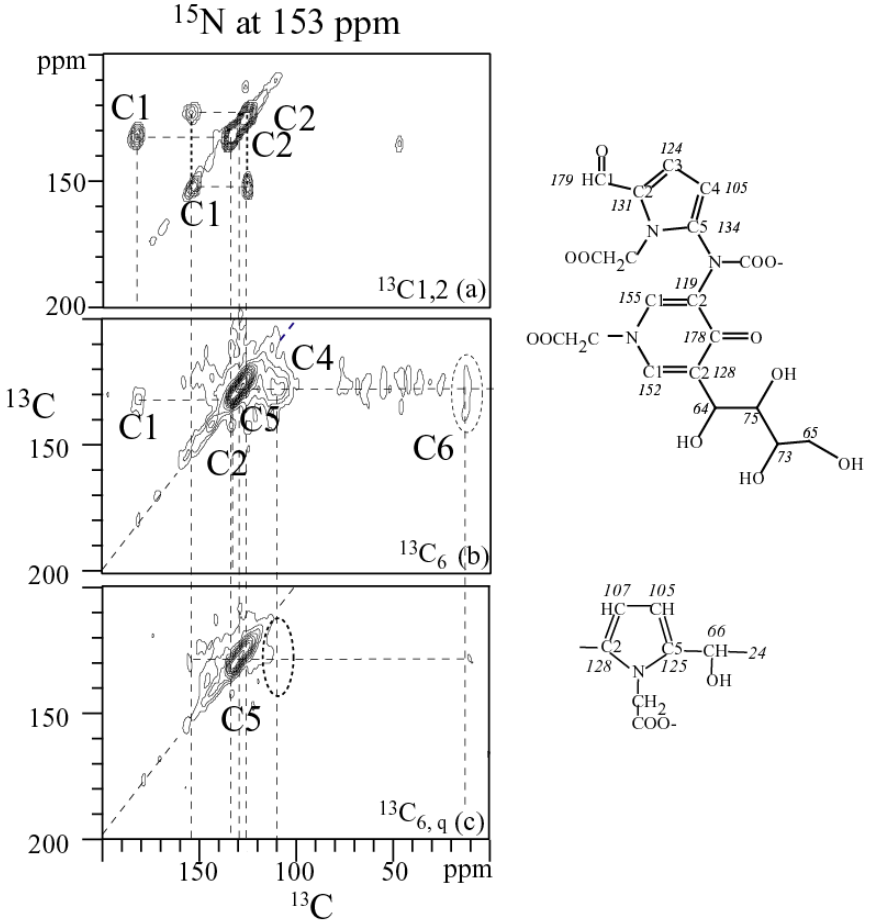

Figure 6. 3D NMR experimental results supporting the existence of a 4-oxopyridinyl structure. The left 2D plots were taken from the 3D experiments with the nitrogen resonating at 153 ppm. (a) for glucose-$^{13}C1,2$ labeled sample; (b) and (c) for glucose- $^{13}C_6$ labeled sample; (c) is with 40 μs gated decoupling before the detection. The 4-oxopyridinyl structure as shown on the right hand side can be proposed. Their prediction ^{13}C chemical shifts using ACD software are consistent with out experiments results. The dashed ellipse highlights the resonance position of a CH carbon, probably C4H.

www.manaraa.com

Amide. The dashed lines d in Figure 2 indicate the nitrogen resonating around 120 ppm. It bonds with amide C1 at 170, alkyl C1 at 58 and alkyl C2 at 62 ppm. Comparing with C2 labeled sample, according to Figure 2, we found that more C1 carbon are associated with the amide nitrogen. Meanwhile, most alkyl carbons are protonated based on C1 labeled sample in Figure 2.

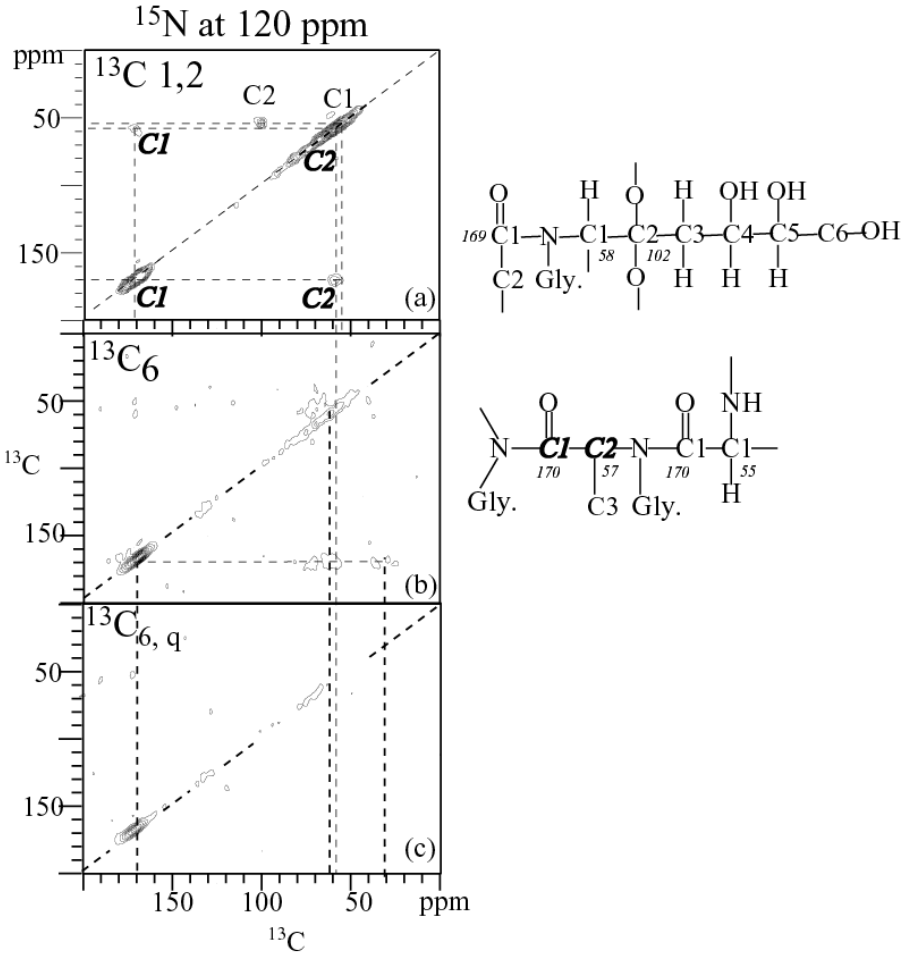

Figure 7. 3D experimental results taken at 120 ppm of ^{15}N chemical shift supporting the existence of a specific amide structure, in which some C1 formed new carbon-carbon bonds with C1self. (a) for glucose-$^{13}C1,2$ labeled sample; (b) and (c) for glucose-$^{13}C_6$ labeled sample; (c) is with 40 μs gated decoupling before the detection. Two different amide structures can be proposed with their ACD software prediction ^{13}C chemical shifts, which are consistent with our experiments results well.

www.manaraa.com

In Figure 7 (a), diagonal peaks are broad, indicating a great variety of substitutions. Three off-diagonal peaks can be found: 100 ppm ketal carbon bonded to 54 ppm amine carbon, 58 ppm amine carbon bonded to 170 ppm amide carbon. Furthermore, in our previous paper,[31] we discussed that the reactivity of C1 stands out and ~50% of C1 formed new C-C bond, C2 formed two types of ketal carbons resonating around 100 ppm, one is associated with aromatic carbon, another one is associated with polar alkyl carbon. Based on these observation, an alkyl structure can been proposed and shown in Figure 7.

Conclusion

Various specific nitrogen containing structures have been identified in melanoidin based on multidimensional solid state NMR experiments. They include oxazolium, imidazolium, specific pyrrole structures, and connections between alkyl chain. A CN_2 spectral editing technique, similar to CH_2 selection, has been developed to directly demonstrate that glucose-C1 is simultaneously bonded to two N at 137 ppm, while other glucose carbons do not show any sharp CN_2 peaks. The sharp $C1N_2$ peak position agrees well with our 3D experimental data, confirming the existence of imidazolium. The powerful capabilities of isotope labeling, multidimensional solid state NMR, and ^{13}C chemical shift prediction in elucidating the structure of complex organic matter have been demonstrated.

References

1. Hodge, J. E. *J. Agric. Food Chem.* **1953,** *1,* 926-943.
2. Nursten, H., *The Maillard reaction: chemistry, biochemistry and implications*. 2005; p 5-30.
3. Tressl, R.; Wondrak, G. T.; Garbe, L. A. *J. Agric. Food Chem.* **1998,** *46,* 1765-1776.
4. Kato, H.; Tsuchida, H. *Prog. Fd. Nutr. Sci.* **1981,** *5,* 147-156.
5. Kato, H.; Hayase, F. *International Congress Series* **2002,** *1245* 3 – 7.
6. Ikan, R., *The Maillard Reaction Consequences for the chemical and life sciences.* John Wiley & Sons Ltd: 1996.
7. Fang, X.-W.; Schmidt-Rohr, K., The fate of glycine in the Maillard reaction investigated by solid-state NMR. In.
8. Hodge, J. E. *Adv. Carbonhydr. Res.* **1955,** *10,* 169-205.

www.manaraa.com

9. Fay, L. B.; Brevard, H. *Mass Spectrometry Reviews* **2005,** *24,* 487-507.
10. Adams, A.; Tehrani, K. A.; Kersÿieneú, M.; Venskutonis, R.; N.D., K. *J. Agric. Food Chem.* **2003,** *51,* 4338-4343.
11. Ames, J. M.; Bailey, R. G.; Mann, J. *J. Agric. Food Chem.* **1999,** *47,* 438-443.
12. Amrani-Hemaimi, M.; Cerny, C.; Fay, L. B. *J. Agric. Food Chem.* **1995,** *43,* 2818-2822.
13. Arnoldi, A.; Corain, E. A.; Scaglioni, L.; Ames, J. M. *J. Agric. Food Chem.* **1997,** *45,* 650-655.
14. Bailey, R. G.; Ames, J. M.; Mann, J. *J. Agric. Food Chem.* **2000,** *48,* 6240-6246.
15. Frank, O.; Heuberger, S.; Hofmann, T. *J. Agric. Food Chem.* **2001,** *49,* 1595-1600.
16. Hofmann, T. *J. Agric. Food Chem.* **1998,** *46,* 932-940.
17. Hofmann, T. *J. Agric. Food Chem.* **1998,** *46,* 3896-3901.
18. Hofmann, T. *J. Agric. Food Chem.* **1998,** *46,* 3902-3911.
19. Hofmann, T. *J. Agric. Food Chem.* **1998,** *46,* 3918-3928.
20. Hofmann, T. *Carbohydr. Res.* **1998,** *313,* 215-224.
21. Hofmann, T. *Carbohydr. Res.* **1998,** *313,* 203-213.
22. Hofmann, T. *Ann. N.Y. Acad. Sci.* **2005,** *1043,* 20-29.
23. Knerr, T.; Lerche, H.; Pischetsrieder, M.; Severin, T. *J. Agric. Food Chem.* **2001,** *49,* 1966-1970.
24. Tressl, R., Nittka, C., Kersten, E. *J. Agric. Food Chem.* **1995,** *43,* 1163-1169.
25. Tressl, R.; Helak, B.; Kersten, E.; Rewicki, D. *J. Agric. Food Chem.* **1993,** *41,* 547-553.
26. Tressl, R.; Kersten, E.; Rewicki, D. *J. Agric. Food Chem.* **1993,** *41,* 2125-2130.
27. Yaylayan, V. A.; Kaminsky, E. *Food Chem.* **1998,** *63,* 25-31.
28. Ramamoorthy, A.; Wu, C.-H.; Opella, S. J. *J. Magn. Res.* **1999,** *140,* 131-140.
29. Ishii, Y.; Tycko, R. *J. Am. Chem. Soc.* **2000,** *122,* 1443-1455.
30. Mao, J.-D.; Schmidt-Rohr, K. *J. Magn. Reson.* **2005,** *176,* 1-6.
31. Fang, X.-W.; Schmidt-Rohr, K., Alkyl Structures Formed in the Model Maillard Reaction Studied by Solid-State NMR. In.

www.manaraa.com

32. Thorn, K. A.; Arterburn, J. B.; Mikita, M. A. *Environ. Sci. Technol.* **1992,** *26,* 107-116.

33. Przychodzen, W.; Doszczak, L.; Rachon, J. *Magn. Reson. Chem.* **2005,** *43,* 27-30.

34. Jazwinski, J.; Kamienski, B.; Staszewska-Krajewska, O. S.; Webb, G. A. *J. Molec. Str.* **2003,** *646,* 1-9.

www.manaraa.com

CHAPTER 7. NMR spectroscopic assessment of soil organic matter composition in Iowa mollisols

In the style of a paper to be submitted to Organic Geochemistry

Xiaowen Fang[1], Terisita Chua[2], Klaus Schmidt-Rohr*[1], Michael Thompson*[2]

Abstract

Different aggregation size of four soil samples from two fields in Iowa have been studied using quantitative ^{13}C DP/MAS and ^{13}C-^{1}H CP/TOSS NMR techniques combining with elemental analysis results. The three fraction of each soil are whole soil, POM, and clay size. HCl/HF with or without heating treatments have been conducted to whole soil and clay size fraction. By study the untreated whole soil, ester is found to be a minor component in soil, the acidification of HCl/HF with or without heating only makes COO^- become COOH. ^{13}C-^{1}H spectra displays the transformation from plant to POM and then to humic substances in whole and clay fraction soils by losing the crystalline cellulose in plants to form noncrystalline saccharides in POM and soil, while selectively preserving oxidized char-coal components resonating around 130 ppm. Meanwhile, the soil samples contain a pronounced signal of polymethylene chain. ^{13}C integration intensity of quantitative NMR data correlated very well with elemental analysis data, indicating that NMR measurements are representative with the presences of paramagnetic ions, especially for the whole soil samples, which have shortest spin-lattice relaxation time. Based on this argument, quantitative integral of different function group regions has been carried out, and the results indicates that the main feature of humic substances are very similar for soil obtained from different landscape within 5% variation range. With the decreasing of drainage, the percentage of nonpolar aromatic component is increasing.

Introduction

Long-term stabilization of organic matter in soils has been attributed to (1) the intrinsic recalcitrance of components of plant tissues, (2) protection of plant residues from enzymatic attack by storage in micropores of natural aggregates, (3) sorption of organic compounds to solid surfaces so that cleavage points are sterically unavailable to enzymes,

www.manaraa.com

and (4) transformation of plant residues to black C by fire [1-3]. Understanding which mechanisms are important in different kinds of soils – with different mineralogies, types of diagnostic horizons, and management practices – is critical to improving the predictive power of models of terrestrial C dynamics.

To further that understanding, many investigators have studied variations in soil organic matter components as a function of vegetation, cropping systems, tillage, depth, and size of aggregates. In Iowa, both the molecular-scale composition of humic substances isolated from aggregate size fractions and the occurrence of black C in prairie derived soils have been examined [4, 5]. Both the concentration and the stock of soil organic carbon vary predictably across the landscape in Iowa. The greater concentrations of SOM in poorly drained soils compared with well drained soils may be attributed to (1) slow oxidation of C by anaerobic microorganisms under long periods of low redox conditions, (2) accumulation of eroded, organic-matter-rich sediments at the base of slopes, and (3) sorption of SOM to clay minerals that also accumulate in low-lying landscape positions [6-8].

But, in addition to the total amount of C, does the distribution of SOM components also vary with landscape position and (therefore drainage regime)? It would be useful to know if this were the case. Dynamic models of soil carbon typically differentiate among three subtypes of SOM: active, slow, and passive, terms that refer to the rate of turnover or ease of microbial decomposition of the organic matter [9]. There is considerable interest in identifying and measuring the SOM constituents of that comprise these conceptual categories, because their integration into models such as CENTURY will improve long-term predictions of soil carbon management. Such knowledge could lead to improved modeling of the landscape-scale distribution and fate of soil carbon.

There are several reasons that the components of SOM might vary with drainage regime: (1) Both the composition of vegetative species and primary productivity differ with soil water regime, at least in uncultivated landscapes. Since plant species differ in the abundance of the primary tissue components (e.g., cellulose, hemicellulose, lignin, tannins, and lipids) and since the rates of decomposition of these components also differ, over long periods those components might be expected to differentially accumulate in soil organic

www.manaraa.com

matter. (2) Decomposition of lignin requires the presence of certain species of fungi and may be inhibited in poorly drained soils where O_2 levels in the soil solution are limited, thus enriching SOM in lignin residues [10, 11]. (3) The potential for lipids to be associated with clay fractions in soils has been noted by a number of authors [4, 12, 13]. Trapped in clay quasicrystals, they may be physically protected from enzymatic degradation. Or they may be chemically protected as their more hydrophilic moieties interact with the aqueous environment outside the quasicrystal, as suggested by Kleber et al. [14].

On the other hand, the distribution of SOM components might not vary with landscape position, especially in cultivated soils. The installation of drainage tile in cultivated soils may have equalized soil water regimes sufficiently to erase the signature of differential accumulations of plant polymers that would otherwise resist decay in low-redox conditions. And agricultural management across landscape positions (fertilization, tillage, and monoculture of hybridized crop cultivars) may have homogenized the annual inputs of above- and below-ground biomass so that present-day SOM reflects primarily these most recent additions, instead of older remnants from pre-cultivation periods.

In the present paper, we consider the hypothesis that the plant-derived components of soil organic matter in the surface horizons of Iowa Mollisols might vary as a function of landscape position. We have tested this hypothesis by investigating soils that occur in well and poorly drained catenary positions but that differ from one another primarily in parent material, that is, Wisconsinan till and Wisconsinan loess.

Experimental Section

Materials and separation methods

Soil. The soils for this study were selected from a larger investigation of the spatial variability of soil organic matter at the landscape scale. Two agriculturally managed fields in Iowa were chosen, one in Greene County, Iowa, in which the soils were developed in Wisconsinan till, and the other, in Black Hawk County, Iowa, in which the soils were developed in Wisconsinan loess. Both fields were managed in alternate-year corn –soybean (*Zea mays*, *Glycine max*) rotations over many years before sampling. At the Greene County

www.manaraa.com

field, 121 sites were sampled on a nested grid pattern over an area of ~17 ha by using a hydraulic probe (~9 cm in diameter) to a depth of 30 cm. At the Black Hawk County site, 141 sites were sampled by hydraulic probe on a regular grid over an area of ~14 ha, also to a depth of 30 cm. The samples were divided into depth increments of 0 – 5 cm, 5 – 15 cm, and 15 – 30 cm, air dried, and ground to pass a 2-mm sieve. Total C and N were determined for all samples by dry combustion of <100-mesh, finely ground subsamples [15], and bulk density was determined by the hydraulic-probe core method [16]. From this suite of data, four specific sampling sites were selected for this study. These sites were chose to have calculated C stocks (0 – 30 cm) at or very close to the median of all points that occurred in the well drained and poorly drained mapping units of each field, as indicated by the second-order soil surveys of those counties [17, 18]. For the purposes of this study, we selected the 0 – 5-cm samples to extract particulate organic matter because POM was most concentrated at the soil surface and the larger sample would be more representative for inter-site comparisons. We chose the 5 – 15 cm samples for the detailed characterization of SOM for the same reasons. The classification, landscape properties, particle size distribution, and pH of soil samples from 5-15 cm depths have been listed in Table 1.

Table 1. Classification, landscape properties, particle size distribution, and pH of the soil samples from the 5 – 15 cm depths.

Soil	Classification	Drainage Class	Landscape Position, Slope	5 – 15 cm depth			
				Clay	Sand	Silt	pH
Greene County				---------g kg^{-1}------			
Clarion (138B)	**Fine-loamy, mixed, mesic Typic Hapludoll**	**Well**	**Summit, ~5%**	**250**	**400**	**350**	**4.8**
Webster (107)	**Fine-loamy, mixed, mesic Typic Endoaquoll**	**Poor**	**Plane, 0%**	**280**	**340**	**380**	**4.9**
Black Hawk County							
Dinsdale (377C)	**Fine-silty, mixed, mesic Typic Hapludalf**	**Well**	**Side slope, ~6%**	**330**	**100**	**570**	**5.4**
Maxfield (382)	**Fine-silty, mixed, mesic Typic Endoaquoll**	**Poor**	**Concave, ~1%**	**360**	**90**	**550**	**6.2**

Particulate Organic Matter and Clay Fractionation. Fifty grams air-dried soil (≤ 2.0 mm) was gently dispersed in 250 mL of distilled water at 22 J/mL [19] using a 1.2 cm-diameter probe sonifier (Sonicator 3000, Misonix Inc., Farmingdale, NY). When dispersed, the suspension was passed through a 53-µm sieve and the filtrate was collected in a tall 1-L beaker for further separation. The residue (sand plus POM) on the sieve was transferred

www.manaraa.com

quantitatively to a previously weighed 100-mL beaker and then dried at 50°C. The dried residue was stirred and soaked in 50 mL of sodium polytungstate (adjusted to a density of 1.85 g mL^{-1} with water; Geoliquids Inc., Prospect Heights, IL) overnight. This allowed the light-weight POM to separate from the sand. The POM was siphoned into a tared beaker and then washed three times with distilled water. The beaker was dried at 50°C for 72 h and then weighed.

The filtrate, on the other hand, was adjusted to a final volume of approximately 500 mL before it was dispersed at 450 J mL^{-1}. The clay fraction was collected by exhaustive sedimentation and decantation, coagulated with 0.5 *M* $MgCl_2$, and then dialyzed against water that was replaced until a minimal amount of chloride was present in the dialyzate. The clay fraction was freeze-dried and then weighed to determine yield for each fraction.

HF Treatment. Six grams of the unfractionated soil (ground to pass a 100-mesh sieve) or the clay fraction were placed in 50-mL polyethylene centrifuge tube and treated with 15 mL of 0.1 *M* HCl to remove possible carbonate minerals and Ca. The sample was shaken end-to-end for 30 min and centrifuged at 1949 *g* for 10 min. The wash was discarded and the HCl treatment was repeated. The residue after the HCl washes was treated with 15 mL of 5 *M* HF and shaken for 30 min before centrifugation at 1949 *g* for 10 min. The HF treatment was performed four times, with the wash being discarded each time. The residue was washed with distilled water four times to remove excess acid and then freeze-dried.

For the HF plus heat-treatment, the samples in tubes (as above) were immersed in a 60°C water bath for 30 min during each HF treatment. The tubes were stirred while heated, and the excess acid was removed as described above before freeze drying.

Table 2 listed the carbon and nitrogen contents for unfractionated samples, clay fraction samples and particular organic matter. The first two fraction samples have been treated with HCl and HF with or without heating.

NMR parameters. The solid-state MAS NMR experiments were performed at room temperature using a Bruker DSX400 spectrometer at 400 MHz for ^{1}H and 100 MHz for ^{13}C.

www.manaraa.com

A Bruker 4-mm double-resonance magic-angle spinning (MAS) probe head was used in this study. ZrO_2 rotors of 4-mm diameter were used with 5-mm long glass inserts at the bottom to keep the sample within the radio frequency coil. The mass of each sample was recorded during packing. ^{13}C and ^{1}H chemical shifts were referenced to TMS, using the COO^- resonance of glycine at 176.49 ppm as a secondary reference for ^{13}C and the hydroxyapatite proton peak at 0.18 ppm as a secondary reference for ^{1}H. 90° pulses of both ^{13}C and ^{1}H were calibrated by using a $^{13}C1$-labeled glycine sample. The 90° pulse length for both nuclei was 4 μs. Two-pulse phase modulation (TPPM) decoupling on the ^{1}H channel was turned on during detection.

CP/TOSS experiments. ^{1}H-^{13}C cross polarization (CP) combined with four-pulse total suppression of sidebands (TOSS)[20] spectra were recorded at 6.5 kHz MAS. The CP contact time was 1 ms, with a 3-s recycle delay. The longitudinal relaxation time of ^{13}C ($T_{1,C}$) of each sample was estimated by using CP/T_1/TOSS pulse sequence. The $T_{1,C}$ filtering time, where the remaining signal is less than 5% of the full intensity, was set as the recycle delay of the quantitative DP/MAS experiments, in order to ensure that all carbon sites are fully relaxed[21].

High-speed quantitative ^{13}C DP/Echo/MAS NMR. In order to quantitatively detect carbon of soil organic samples, quantitative ^{13}C DP/Hahn echo/MAS (direct polarization) NMR spectra were acquired at 14 kHz MAS. A Hahn echo of two rotational periods was used before detection to avoid baseline distortions. The recycle delays were less than 10 s for whole soils and their clay fractions, 12 s to 55 s for HF-treated samples, 40 s to 60 s for particulate organic matter, and 120 s to 150 s for plant materials.

Results and Discussion

(1) Effects of HCl / HF treatment

Figure 1 shows direct-polarization ^{13}C NMR spectra of 107 whole soil without and with HCl/HF treatments, and the clay fraction of the same soil. Corresponding spectra of the nonprotonated C or C in mobile segments such as CH_3 groups are shown by thin lines. All the spectra are dominated by the band of aromatic C near 130 ppm, and a band of COO

www.manaraa.com

carbons near 172 ppm. Given the large fraction of nonprotonated aromatic carbons resonating near 130 ppm, the aromatic fraction can be identified predominantly as oxidized char-coal residues. Similar features had been detected in the spectra of mollisol humic acids;[4] now we have shown that these are also characteristic of the whole soil and not an artifact of selective extraction in the humic acid.

Table 2. C and N contents of samples before and after HF treatment to concentrate organic matter

	Before acid treatments			**HF, no heat treatment**			**HF, heat treatment**			
Soil	**C**	**N**	**C/N**	**C**	**N**	**C/N**	**C**	**N**	**C/N**	**Remaining Mass Fraction**
	----g kg^{-1}--			----g kg^{-1}----			----g kg^{-1}----			
Whole soil (5-15 cm depth)										
Clarion	**18.6**	1.8	10.6	**22.7**	1.6	13.8	**22.6**	1.7	12.9	0.32
Webster	**24.3**	1.9	12.8	**46.4**	3.1	15.1	**62.0**	4.2	14.7	0.30
Dinsdale	**17.9**	1.6	10.9	**38.7**	2.8	13.9	**42.6**	3.5	12.3	0.24
Maxfield	**24.0**	1.9	12.4	**65.5**	4.1	15.8	**83.6**	5.7	14.6	0.22
Clay fraction (< 2 µm) (5-15cm depth)										
Clarion	**40.5**	4.4	9.3	**232.0**	20.7	11.2	**256.7**	22.1	11.6	0.10
Webster	**51.4**	4.6	11.3	**318.0**	23.2	13.7	**286.2**	21.0	13.7	0.15
Dinsdale	**39.9**	4.3	9.4	**158.0**	14.1	11.2	**226.8**	20.0	11.3	0.11
Maxfield	**48.8**	4.1	11.8	**171.4**	12.5	13.8	**232.8**	18.0	12.9	0.17
Particlar organic matter (0-5cm depth)										
Clarion	**241**	14	17	No sample available						
Webster	**244**	13	19							
Dinsdale	**320**	15	21							
Maxfield	**296**	17	17							

The alkyl region of the spectra appears to exhibit resonances of O-CH groups at ~72 ppm, of nonpolar methylenes, C-CH_2-C, at 30 ppm, and of NCH or CCH groups at ~55 ppm. The similarity of the spectra of a given soil material with or without HCl/HF treatments proves that the treatment does not result in significant alterations of the component moieties.

The spectra in Figure 1 do show one significant difference between untreated and HF-treated samples: The COO resonance has shifted from 174 ppm in the untreated sample to 171 ppm after acid treatment. Such a shift is indicative of protonation of COO^- to COOH groups due to acidification.

www.manaraa.com

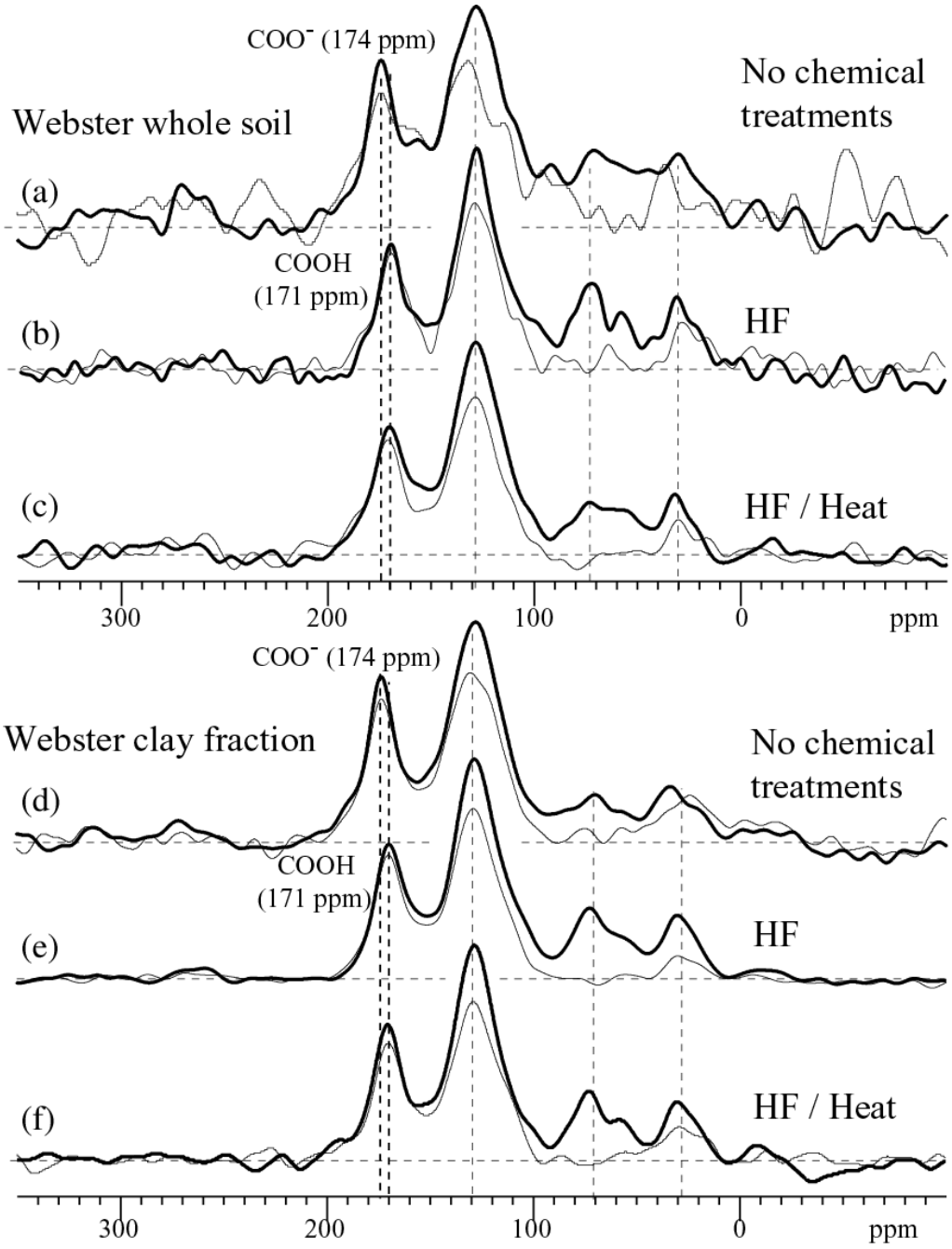

Figure 1. Quantitative ^{13}C NMR spectra of: (a-c) 107 whole soil and (d-f) 107 clay fraction, treated in three different ways: (a, d) no chemical treatments, (b, e) HCl + HF treatment, (c, f) heating at 60 ^{o}C during HCl + HF treatment plotted in each group. Thick lines are from all types of carbons, thin lines are from all quaternary carbons and CH_3 group. A 3-ppm chemical shift difference is observed between the COO/COOH resonances of untreated and HCl + HF treated samples, for both soil materials.

www.manaraa.com

(2) Esters as a minor fraction in whole mollisols

The 174-ppm position of the COO resonance in the untreated samples contains structural information not previously obtained. It excludes a dominant contribution from esters, COOC, which would resonate around 169 ppm. In this analysis, the absence of chemical treatment is crucial: Acid catalyzes the hydrolysis of esters into carboxyl- and hydroxyl-bearing fragments, and therefore studies on HF extracts or humic acids cannot reliably determine the abundance of esters in soil organic matter.

(3) Effects of heating during HF treatment

The data in Table 2 show that heating during HF treatment can significantly increase the enrichment in organic carbon. The comparison of ^{13}C NMR spectra without and with heating during HF treatment in Figures 2 and 3 for whole and clay-fractions, respectively, of three further locations demonstrates that no significant structural changes occur as a result of heating during HF treatment. This is also reflected in the area fractions compiled in Table 3.

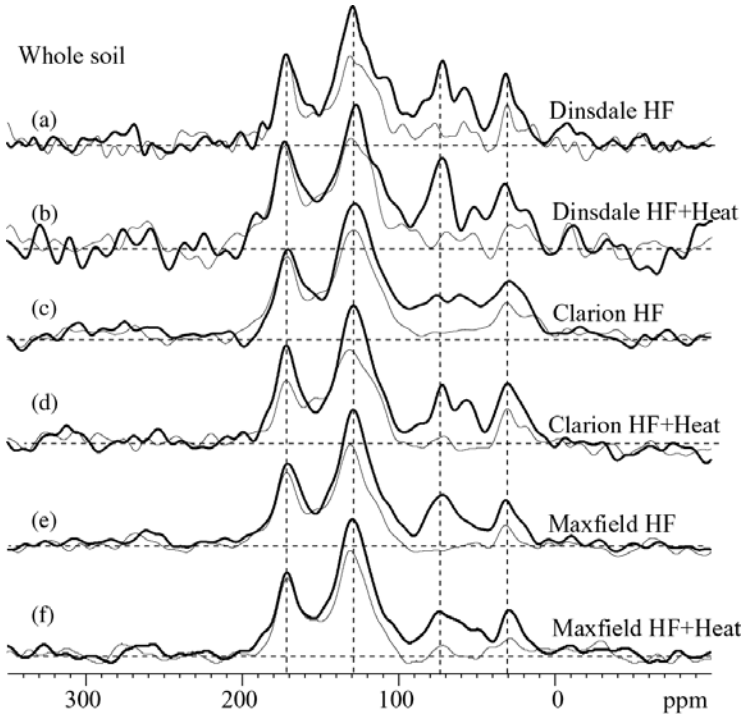

Figure 2. Quantitative ^{13}C NMR spectra of whole soil samples from different locations. For each sample, the full spectrum (thick line) and quaternary carbon plus CH_3 spectrum (thin line) with regular HCl and HF treatments is plotted first, followed by the corresponding spectra obtained after HCl + HF treatment at 60 ^{o}C.

www.manaraa.com

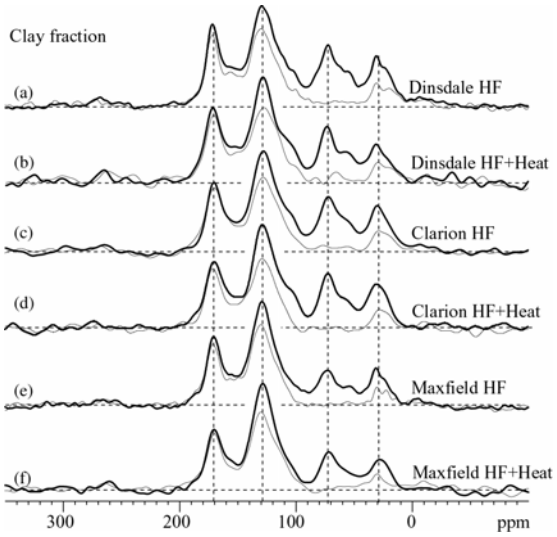

Figure 3. Quantitative ^{13}C NMR spectra of clay fraction from different locations. For each sample, the full spectrum (thick line) and quaternary carbon plus CH_3 spectrum (thin line) with regular HCl and HF treatments is plotted first, followed by the corresponding spectra obtained after HCl + HF treatment at 60 ^{o}C.

Table 3. Quantitative ^{13}C NMR percentages of C in chemical functional groups for organic matter in three different types of soil materials: particulate organic matter (POM), unfractionated soil samples, and clay fractions.[22]

Soil	Ketone	COO	polar aromatic C	nonpolar aromatic C	polar aromatic C_q	nonpolar aromatic C_q	O-alkyl	NCH	O-CH_3	non polar alkyl	Alkyl / O-alkyl	Aroma-ticity index
	205-185	185-160	160-145	145-100	160-145	145-100	115-60	60-49	60-50	49-0		
	----------				*ppm*		----------					
Particulate organic matter ----------					*%*		----------					
Clarion	2	12	8	22	*7*	*11*	34	4	2	15	0.43	0.39
Webster	1	12	9	25	*8*	*13*	30	4	3	16	0.51	0.43
Dinsdale	2	11	8	23	*7*	*12*	38	3	4	12	0.30	0.38
Maxfield	3	13	9	25	*8*	*14*	32	3	2	12	0.38	0.43
Unfractionated sample												
Clarion	0	15	7	41	*7*	*33*	16	2	2	16	0.99	0.60
Webster	0	15	6	43	*5*	*35*	19	3	1	13	0.65	0.61
Dinsdale	1	14	6	37	*5*	*25*	23	3	1	14	0.64	0.54
Maxfield	3	17	7	44	*7*	*33*	16	2	1	11	0.65	0.65
Clay (< 2 µm)												
Clarion	1	15	7	38	*6*	*29*	20	3	1	15	0.73	0.56
Webster	1	17	8	45	*7*	*36*	15	2	1	11	0.73	0.67
Dinsdale	1	15	8	36	*7*	*28*	21	3	1	15	0.71	0.55
Maxfield	2	16	8	42	*7*	*34*	16	2	1	13	0.78	0.64
Plant												
Leave	0	7	3	21	*3*	*4*	53	5	2	9	0.16	0.27
Cornstalk	0	5	5	22	*5*	*5*	54	4	3	8	0.14	0.29

www.manaraa.com

Detection efficiency in direct-polarization ^{13}C NMR. Do the spectra of Figures 1 – 3 exhibit signals of most of the organic carbon in the samples, or could they be distorted due to differential loss of signal from organic matter near unpaired electrons of iron, copper, or manganese oxides? The data shown in Figure 4 prove that in the samples studied here, most carbon is detected faithfully. The plot correlates the total (integrated) ^{13}C NMR signal, normalized per mg and per scan, with the atomic percentage of organic carbon from elemental analysis. The methyl resonance of alanine and the total spectral areas of polystyrene and Amherst humic acid[24] were used to obtain the slope of the calibration line.

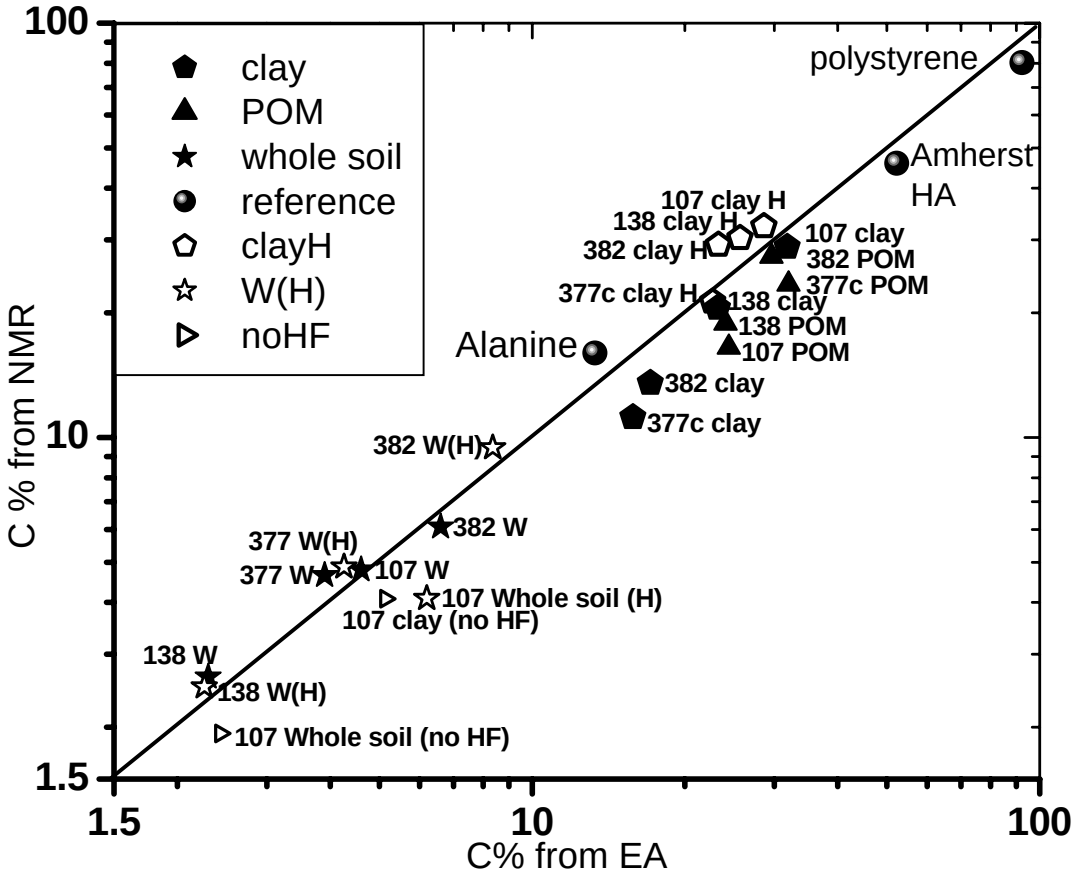

Figure 4. Correlation plot of carbon percentages from NMR measurements and from elemental analysis. The samples include clay fractions (pentagons), particulate organic matter (triangles), and whole soils (stars). They are from four different spots as indicated by the number. Filled pentagons and stars represent samples treated with regular HCl and HF. Open pentagons and stars represent samples heated during HCl and HF treatment. Open triangles are for the clay fractions and whole soils without any chemical treatment. The NMR measurement data are calibrated by measuring reference compounds (polystyrene, Amherst HA, and alanine) plotted as "spheres".

www.manaraa.com

Most samples give points near the calibration line, showing that > 80% of organic C is detected. Most surprisingly, even for whole soils with their low organic carbon fractions or equivalently overwhelming mineral fractions, most of the organic carbon is detectable. In fact, the clay and POM samples show more signal loss than the whole soil. The majority of HF+heat-treated samples (open stars and pentagons) show no signal loss, while the samples from site 107 show more than average signal loss, probably due to more para- (or ferri)magnetic minerals. Note that even for a point below the calibration line, the spectra could be undistorted if the signal loss is the same for all types of functional groups.

Structural changes with fraction and location. Figure 5 shows ^{13}C NMR spectra of HF-treated whole soil from 377C and its clay and particular organic matter fractions. For reference, a quantitative spectrum of leaves is also shown at the top. Stalks, corn kernels, and soy residue give rather similar spectra as the leaves, with strong, sharp cellulose signals at 74 and 103 ppm, broad and low aromatic-carbon bands of lignin[23], and NC=O and alkyl resonances mostly due to proteins. Compared to leaves, POM shows a reduced OCH signal apparently due to preferential degradation of cellulose. The aromaticity is still higher in the whole soil and its clay fraction. Spectral differences between the whole soil and two fractions from four different locations are evident in Figure 6.

Alkyl components. Some of the alkyl components in the samples studied here can be characterized with better sensitivity and resolution using non-quantitative cross polarization from ^{1}H to ^{13}C. The spectra in Figure 7 show that sharp signals of crystalline cellulose in plant material in the top row convert to noncrystalline saccharides in soil. Whole soil and even more prominently its clay fraction show a pronounced signal of polymethylene resonating near 30 ppm, which is partially mobile as proven by signal remaining after dipolar dephasing. This soft nonpolar alkyl fraction has been correlated with the capacity of the material for sorption of nonpolar aromatic contaminants. [24]

www.manaraa.com

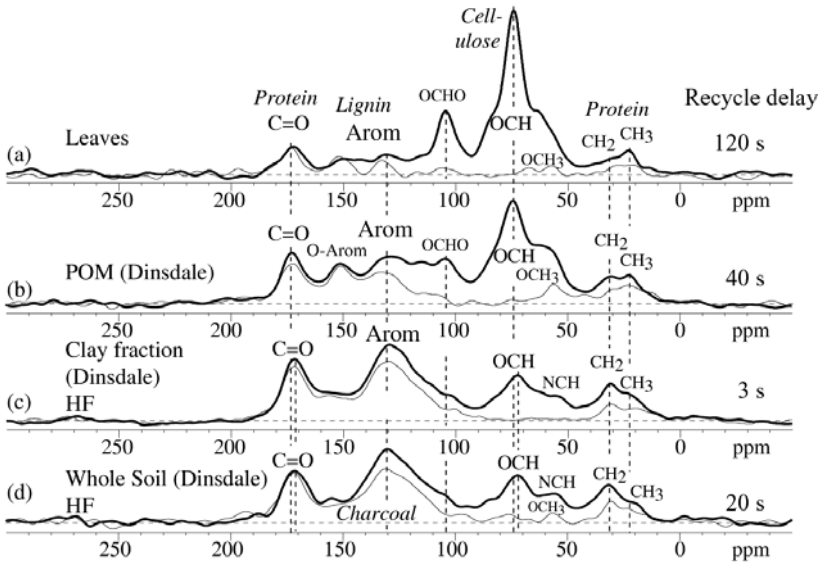

Figure 5. Quantitative ^{13}C NMR spectra of (a) leaves, pure plant material rich in cellulose and lignin. (b) Particulate organic matter (POM), which can be viewed as partially degraded plant materials and which show lower intensities of OCH, and OCHO peaks compared to leaves. (c) Clay fraction and (d) whole soil, which have higher aromatic carbons and polymethylene carbon intensities and lower cellulose carbon intensities. The corresponding spectra of their quaternary carbons and CH_3 groups are plotted with thin lines. The recycle delays used are listed on the right hand side.

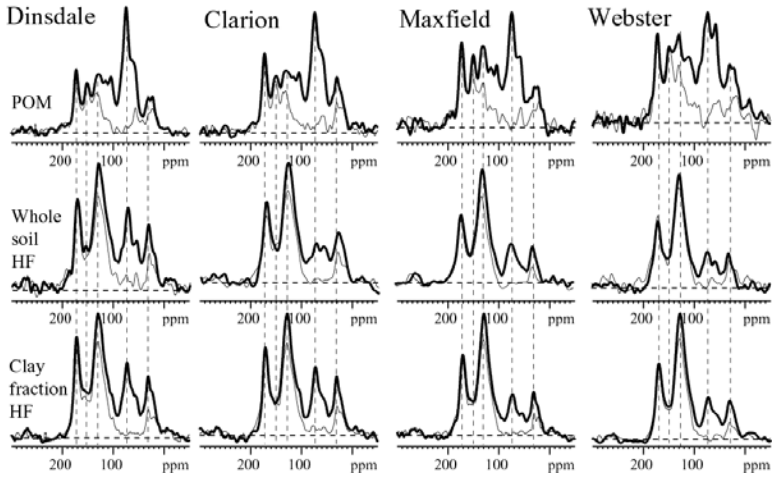

Figure 6. Quantitative ^{13}C NMR spectra for samples from four different locations (left to right: 377, 138, 107, 382) and three different fractions (top to bottom: particulate organic matter (POM), clay fraction, and whole soil. Thick lines are full spectra and thin lines are corresponding spectra of quaternary carbons and CH_3 groups.

www.manaraa.com

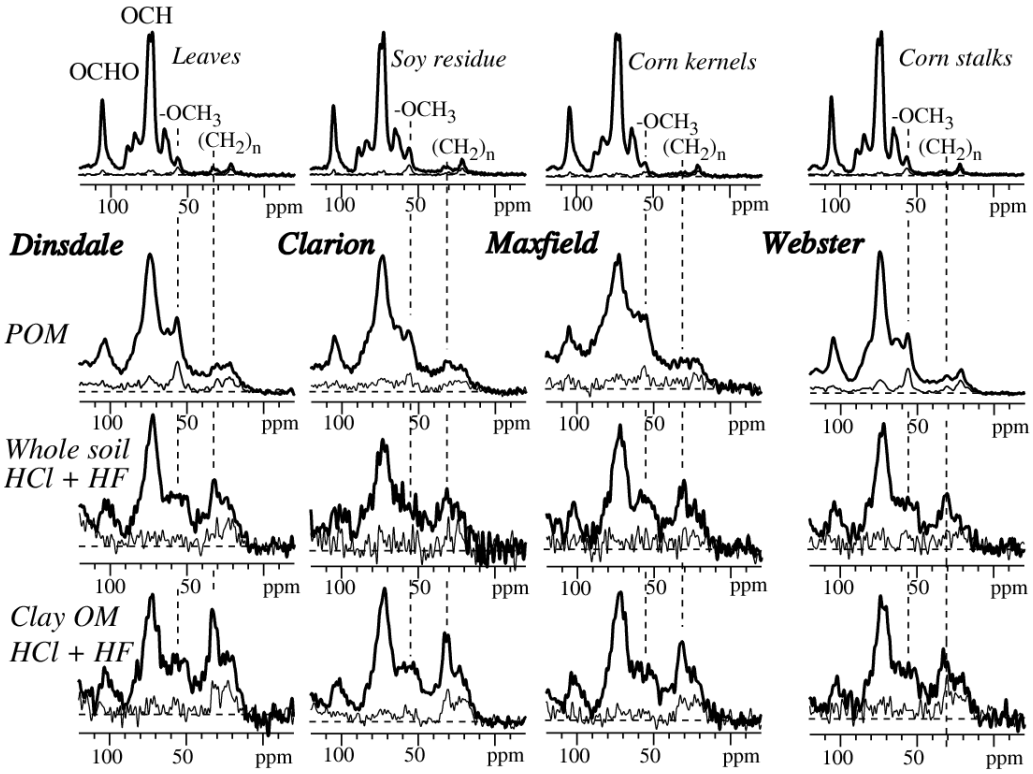

Figure 7. ^{1}H-^{13}C cross polarization ^{13}C NMR spectra at 8 kHz MAS. The spectra in the first row are all from plant materials: leaves, soy residue, corn stalks, corn kernels (from left to right). From the second to the bottom row, the samples are particulate organic mater, whole soil and clay fraction. They are obtained from 377, 138, 107 and 382, arranged from well drained to poorly drained. The thick lines are for all types of carbons obtained by applying CP/TOSS pulses sequence, the thin lines are their corresponding quaternary carbon and CH_3 signals after 40 μs of gated decoupling.

Conclusions

The capability of NMR to characterize the composition of the soil organic matter (SOM) after miniral sample treatment has been demonstrated in a study of three different aggregation size of four soil samples from two fields in Iowa. The quantitative ^{13}C DP/MAS NMR analyses allowed us to conclude (1) that the HF treatment had little impact on the organic carbon functional groups in the samples, the acidification of HCl/HF with or without heating only converts COO^- to COOH; (2) that organic carbon was detectable even in untreated soil materials, which contain paramagnetic ions; (3) that esters are only a minor fraction of SOM in these Mollisols; (4) that the aromatic components of SOM were enriched in the clay fractions (compared with the whole soils) and in the poorly drained soils (compared with the well-drained soils); (5) that nonpolar, non-protonated aromatic C,

www.manaraa.com

interpreted as a proxy for charcoal C, composed 28 – 36 % of total organic C in the unfractionated soil and clay-fraction samples and dominated the aromatic C in all soil samples. ^{13}C CP/TOSS spectra display the transformation from plant to particulate organic matter (POM) and then to humic substances in whole and clay-fraction soils with loss of the crystalline cellulose in plants to form noncrystalline saccharides in POM and soil, while selectively preserving oxidized char-coal components.

Reference

1. Sollins, P.; Homann, P.; Caldwell, B. A. *Geoderma* **1996,** *74,* 65-105.
2. Krull, E. S.; Baldock, J. A.; Skjemstad, J. O. *Functional Plant Biology* **2003,** *30,* 207-222.
3. von Lutzow, M.; Kogel-Knabner, I.; Ekschmitt, K.; Flessa, H.; Guggenberger, G.; Matzner, E.; Marschner, B. *Soil Biology and Biochemistry* **2007,** *39,* 2183-2207.
4. Mao, J. D.; Fang, X. W.; Schmidt-Rohr, K.; Carmo, A. M.; Hundal, L. S.; Thompson, M. L. *Geoderma* **2007,** *140,* 17-29.
5. Laird, D. A.; Chappell, M. A.; Martens, D. A.; Wershaw, R. L.; Thompson, M. *Geoderma* **2008,** *143,* 115-122.
6. Malo, D. D.; Worcester, B. K.; Cassel, D. K.; Matzdorf, K. D. *Soil Sci Soc Am J* **1974,** *38,* 813-818.
7. Schaetzl, R.; Anderson, S., *Soils: Genesis and geomorphology* Cambridge Univ. Press: Cambridge, 2005.
8. Walker, P. H.; Ruhe, R. V. *Trans. Inter. Congr. Soil Sci.* **1968,** *58,* 561-568.
9. Parton, W. J.; McKeown, B.; Kirchner, V.; Ojima, D. S. Century Users Manual. . Colorado State University, Fort Collins, Colorado, USA., **1992**.
10. Kogel-Knabner, I. *Soil Biology and Biochemistry* **2002,** *34,* 139-162.
11. Gleixner, G.; Czimczik, C. I.; Kramer, C.; Luhker, B.; Schmidt, M. W. I., Plant compounds and their turnover and stabilization as soil organic matter. In *Global Biogeochemical Cycles in the Climate System*, Schulze, E.-D.; Heimann, M.; Harrison, S.; Holland, E.; J., L., Eds. Academic Press: San Diego, 2001; pp 201-215.
12. Mahieu, N.; Powlson, D. S.; Randall, E. W. *Soil Sci. Soc. Am. J.* **1999,** *63,* 307-319.

www.manaraa.com

13. Schmidt, M. W. I.; Knicker, H.; Kögel-Knabner, I. *Org. Geochem.* **2000,** *31,* 727-734.
14. Kleber, M.; Sollins, P.; Sutton, R. *Biogeochemistry* **2007,** *85,* 9-24.
15. Nelson, D. W.; Sommers, L. E., Total carbon, organic carbon and organic matter. In *Methods of soil analysis. Part 3. Chemical methods. Book Ser. 5*, Sparks, D. L., Ed. Soil Sci. Soc. Am.: Madison, WI., 1996; pp 539-577.
16. Grossman, R. B.; Reincsh, T. G., Bulk density and linear extensibility. In *Methods of soil analysis. Part 4. Physical methods*, Duane, J. H.; Topp, C. G., Eds. Soil Sci. Sco. Am., : Madison, WI, 2002; pp 201 - 228.
17. Fouts, W. L.; Highland, J. D., Soil survey of Black Hawk County, Iowa. U.S. . In Dep. Agric., W., DC., Ed. 1978.
18. Sherwood, M. A., Soil survey of Greene County Iowa U.S. In Dep. Agric., W., DC., Ed. 1985.
19. Leifeld, J.; Kögel-Knabner, I. *Geoderma* **2005,** *124,* 143-155.
20. Dixon, W. T. *J. Chem. Phys.* **1982,** *77,* 1800-1809.
21. Mao, J.-D.; Hu, W.-G.; Schmidt-Rohr, K.; Davies, G.; Ghabbour, E. A.; Xing, B. *Soil Sci. Soc. Am. J.* **2000,** *64,* 873-884.
22. Mao, J.-D., Schmidt-Rohr, K. *Solid State Nucl. Magn. Reson.* **2004,** *26,* 36-45.
23. Mao, J.-D.; Holtman, K. M.; Scott, J. T.; Kadla, J. F.; Schmidt-Rorh, K. *J. Agric. Food Chem.* **2006,** *54,* 9677-9686.
24. Mao, J.-D.; Hundal, L.S.; Thompson, M.L.; Schmidt-Rorh, K. *Environ. Sci. Technol.* **2002,** *36,* 929-936.

www.manaraa.com

CHAPTER 8. Nonaromatic core-shell structure of nanodiamond from solid–state NMR

Submitted to The Journal of the American Chemical Society

X.-W. Fang[1], J.-D. Mao[2], E. M. Levin[3,4], K. Schmidt-Rohr[1,3*]

Abstract

The structure of synthetic nanodiamond has been characterized by ^{13}C nuclear magnetic resonance (NMR) spectral editing combined with measurements of long-range ^{1}H-^{13}C dipolar couplings and ^{13}C relaxation times. The surface layer of these ~4.8-nm diameter carbon particles is mostly protonated or bonded to OH or NH_n groups, while sp^2-hybridized carbons make up less than 1% of the material. The surface protons surprisingly resonate at 3.8 ppm, but their bonding to carbons is proved by dipolar sidebands in ^{1}H-^{13}C heteronuclear correlation NMR. ^{1}H-^{13}C distance measurements, based on $^{13}C\{^{1}H\}$ dipolar dephasing by surface protons, show that seven carbon layers, in a shell of 0.63 nm thickness that contains ~60% of all carbons, predominantly resonate more than 8 ppm downfield from the 37-ppm peak of bulk diamond (i.e., within the 45 - 80 ppm range). The location of unpaired electrons (~40 unpaired electrons per particle) was studied in detail, based on their strongly distance-dependent effects on $T_{1,C}$ relaxation. The slower relaxation of the surface carbons, selected by spectral editing, showed that the unpaired electrons are not dangling bonds at the surface. This was confirmed by detailed simulations, which indicated that the unpaired electrons are mostly located in the disordered shell, at distances between 0.4 and 1 nm from the surface. On the basis of these results, a nonaromatic core-shell structural model of nanodiamond particles has been proposed.

KEYWORDS: Nanodiamond; nanocrystals; solid-state NMR; unpaired electrons; dangling bonds;

Introduction

Nanodiamond, consisting of crystalline balls of a few thousand carbon atoms often with ~ 2% nitrogen, is a fascinating material that is present in carbonaceous meteorites[1-3] and has

www.manaraa.com

been synthesized by detonation or shock from carbon-containing precursors,[4, 5] with applications in drug delivery,[6] fluorescent marker for cell imaging,[7] protein purification,[8] catalysis,[9] coatings and lubricants[4] as well as nucleation centers for the growth of diamond films.[10] While the diameter of the crystalline core in synthetic nanodiamond is found consistently between 4 and 5 nm,[11-13] their surface and interior structure is still a matter of debate: Do they have a buckyball[14] or onion-shell surface[15], or are they fully protonated? Are there dangling bonds at the surface?[16] Is the interior hollow?[17] Why is the diameter of the crystalline core between 4 and 5 nm quite independent of synthesis conditions?[4, 11, 18-20] Is the diamond lattice distorted, and if so, why?[20] How common are defects?[21] Where is the nitrogen?[22] Does slow growth in the interstellar medium result in the same structure as shock synthesis? What is the origin of the broad downfield "foot" in the ^{13}C spectrum? [5, 16]

Many of these questions can be addressed by nuclear magnetic resonance (NMR) spectroscopy, relaxation-time, and internuclear-distance measurements. Previous studies have touched on some of these issues,[5, 16, 23, 24] but we will show that important spectral features have not been attributed correctly and several proposed conclusions have to be revised. Crucial new insights are provided by ^{1}H-^{13}C distance measurements and quantitative analyses of the nuclear relaxation produced by unpaired electron spins, which had not been performed before.

The quantitative ^{13}C NMR spectrum in Figure 1(a) shows that about half of the carbon resonates in broad bands downfield from the main diamond resonance at 37 ppm, but signals of sp^2-hybridized carbons are negligible. Our studies further reveal that nanodiamond exhibits other unusual NMR properties such as an unexpected ^{1}H chemical shift. We have applied spectral-editing techniques in addition to quantitative ^{13}C NMR to characterize the surface and subsurface composition of nanodiamond, including a sample annealed at 600 ^{o}C in a nitrogen atmosphere. Based on ^{1}H-^{13}C long-range dipolar dephasing, it is shown that the carbons resonating downfield form a disordered shell. Its thickness was estimated based on spectrally resolved $^{13}C\{^{1}H\}$ HARDSHIP NMR dephasing. Strong effects of unpaired electrons on longitudinal ($T_{1,C}$)[16] relaxation times of ^{13}C nuclei have now been observed with spectral resolution, revealing slower relaxation of surface carbons. Specifically, the distance of the unpaired electrons from the surface and core of the particles is estimated by

www.manaraa.com

quantitative analysis of $T_{1,C}$ relaxation. On this basis, a relatively detailed model of the nonaromatic core-shell structure of nanodiamond is proposed.

Experimental Section

Materials. Nanodiamond (97% purity) and microdiamond (natural monocrystalline powder, ca. 1 μm size, 99.9% purity) was purchased from Sigma-Aldrich (USA) and used without any additional chemical treatments. In order to study structural changes after annealing, the nanodiamond was heated at 600 ^{o}C for three hours under an argon atmosphere. Another nanodiamond sample of somewhat lower purity (95%) was also studied, and gave similar results (not shown here).

Elemental analysis. After freeze-drying the sample overnight, a triplicate measurement of C, H, N concentrations was performed using a Perkin Elmer Series II Analyzer 2400. The instrumental precision is within 0.3%.

Wide-angle X-ray diffraction. Wide-angle X-ray diffraction experiments were conducted to estimate the diameter of the crystalline core of the nanodiamond particles. The samples were placed in plastic or quartz sample holders, which allows us to clarify the origins of a band around $2\theta = 13^{o}$ reported in ref.[15] A microdiamond sample was also measured for reference.

NMR spectroscopy. The NMR experiments were performed using a Bruker DSX400 spectrometer at 400 MHz for ^{1}H and 100 MHz for ^{13}C. A Bruker 4-mm double-resonance magic-angle spinning (MAS) probe head was used for the 13 and 14-kHz MAS experiments, while the 6.5-kHz MAS experiments were performed with larger 7-mm sample rotors in a 7-mm Bruker double-resonance probe head.

High-speed quantitative ^{13}C DP/MAS NMR. Quantitative ^{13}C DP/MAS (Direct Polarization / Magic Angle Spinning) experiments were run at a spinning speed of 14 kHz, with an exorcycled[25] Hahn echo for dead-time free detection that ensures perfect baselines without linear phase correction. The 90^{o} ^{13}C pulse length was 4 μs. Recycle delays were tested by the CP/T_1/TOSS technique to make sure that all carbon sites are fully relaxed. The details of

www.manaraa.com

this technique have been described elsewhere [26]. In order to obtain quantitative information on nonprotonated carbons, DP/MAS ^{13}C NMR spectra were acquired under the same conditions with a dipolar dephasing time of 68 μs. Chemical shifts were referenced to C1 of glycine at 176.49 ppm. In order to see the presence of sidebands of the sample, ^{13}C DP/MAS spectra MAS were measured on 600 MHz Bruker NMR spectrometer, with 2-s recycle delay at 0-, 12-, and 14-kHz MAS. In order to look for signals of sp^2 hybridized carbons, direct polarization experiments with four-pulse total suppression of sidebands (TOSS)[27] were also performed at spinning speeds of 13 kHz and 6.5 kHz, using 4- and 7- mm diameter rotors, respectively, with recycle delays of 4 s in order to maximize the signal-to-noise ratio, and of 400 s in order to ensure detection of potential long-T_1 sp^2-hybridized carbons.

^1H NMR probehead background suppression. One-dimensional solid-state ^1H NMR spectra were recorded at 0, 6.5 kHz and 30 kHz. Probe-head background signal was suppressed by the simple and reliable scheme of reference.[28] In short, two one-pulse spectra, with pulse flip angles of β and 2β (e.g. 90° and 180°), are acquired. The essentially background-free spectrum is obtained by subtracting the second spectrum, scaled by 0.5, from the first. Chemical shifts were referenced to water at 4.9 ppm.

Spectral editing of protonated carbons (CH_2 + CH). The spectrum of carbons bonded to H can be obtained with good sensitivity based on cross-polarization and dipolar dephasing [29]. Two spectra are recorded. The first one is a CP/TOSS spectrum with a short CP contact time of 0.2 ms; the second one is a CP/TOSS spectrum with the same CP contact time but 40-μs dipolar dephasing. The first spectrum is predominantly that of protonated carbons, but residual peaks of quaternary carbons result from two-bond magnetization transfer. The second one contains only the residual signals of quaternary carbons or mobile segments. The difference of these spectra is the spectrum of the CH_2 and CH carbons.

CH spectral editing. For CH selection, a robust method based on C-H multiple-quantum coherence was used [30]. CH-group multiple-quantum coherence is not dephased by the spin-pair CH dipolar coupling, while CH_2 group coherence is dephased by the dipolar coupling of

www.manaraa.com

the carbon to the second proton. The first of a pair of spectra recorded contains signals of CH, as well as residual quaternary-carbon peaks. The latter are removed by taking the difference with a second spectrum acquired with the same pulse sequence, except for additional 40-μs dipolar dephasing before detection. The spinning speed was 5.787 kHz.

Two-dimensional ^{1}H-^{13}C NMR. Two-dimensional (2D) ^{1}H-^{13}C wideline separation (WISE) and heteronuclear correlation (HETCOR) NMR experiments with frequency-switched Lee-Goldburg homonuclear decoupling during the evolution time was performed at a spinning speed of 6.5 kHz. Lee-Goldburg cross polarization of 0.1 ms was used to suppress ^{1}H-^{1}H spin diffusion during polarization transfer and show mostly one-bond ^{1}H-^{13}C connectivity.

Long-range C-H REDOR. The signals of nonprotonated carbons near the surface, detected via CP/TOSS from surface protons followed by gated decoupling, can be distinguished efficiently from interior carbons, detected via DP/TOSS/gated decoupling, using recoupled dipolar dephasing (REDOR), with two 8-μs ^{1}H 180^{o} pulses per rotation period that prevent MAS from averaging out weak CH dipolar couplings.[31] The spinning speed was 14 kHz. The "γ-averaging" was employed to suppress sidebands up to the fourth order.[32]

$^{13}C\{^{1}H\}$ HARDSHIP NMR. $^{13}C\{^{1}H\}$ HARDSHIP (HeteronucleAr Recoupling with Dephasing by Strong Homonuclear Interactions of Protons) experiments [33] were performed at 6.5 kHz MAS in order to quantify the diameter of nanodiamond particles and the thickness of the disordered shell more accurately. This approach is based on the strongly distant-dependent dipolar couplings between the protons in the surface layer and ^{13}C-nuclei in the inner layers. The CH_n multispin dynamics of HARDSHIP are more tractable than those in the corresponding REDOR experiments, since ^{1}H-^{1}H dipolar couplings do not significantly affect the ^{1}H-^{13}C dephasing during HARDSHIP.[33]

^{13}C T_1 relaxation measurements and simulations. The ^{13}C T_1 relaxation behavior was measured by CP/ or DP/T_1-TOSS[34] at 6.25 kHz MAS combined with spectral editing techniques, such as selection of protonated carbons or long-range C-H dipolar dephasing

www.manaraa.com

after direct polarization, to obtain the T_1 values of different types of carbons. The recovery times varied from 1 ms to 2,000 ms. The recycle delay was 10 s. For reference, the T_1 relaxation times of synthetic and of natural microdiamonds were also measured, using saturation recovery with TOSS detection with recycle delays of 1 s to 2,000 s.

T_1 relaxation curves were simulated in full detail in a model 4.8-nm diameter sphere made up of 24 carbon layers spaced by 0.1 nm, with a lateral C-C spacing of 0.2 nm. Relaxation was generated by 35 to 40 unpaired electrons distributed randomly within a specified range of depths from the particle surface, with rates of $1/T_{1,C} = \frac{1}{3.5\ s/nm^6} \sum_{n_{electron}} 1/r_n^{\,6}$, where r_n is the distance between a given carbon and the n^{th} unpaired electron. Carbons within a certain range (typically 0.3 nm) from the unpaired electrons were treated as unobservable (see details below). Each sphere was surrounded by six neighboring spheres with the same distribution of unpaired electrons.

Results and Discussion

After a brief generic characterization of the nanodiamond sample by ^{13}C NMR and wide-angle X-ray diffraction, we will first prove that the nanodiamond surface is protonated, then describe measurements of depth from this protonated surface, and finally characterize the interior in more detail, focusing on the location of unpaired electrons in the nanodiamond, based on their effects on nuclear relaxation.

I. Generic Characterization

Quantitative, unselective ^{13}C NMR. Figure 1 shows quantitative ^{13}C NMR spectra of nanodiamond and microdiamond, obtained with 90^o-pulse excitation and a Hahn echo after 5-s and 1,000-s recycle delays, respectively, at 13-kHz and 6.5 kHz MAS. We observe a sharp, narrow peak at 37 ppm in the microdiamond spectrum, which is assigned to the diamond core. In contrast, the chemical shift range of nanodiamond is very broad, from 20 to 85 ppm, with an asymmetric broad downfield wing from 40 to 85 ppm. The main band around 37 ppm arises mostly from the nanodiamond core, while the asymmetric broad wing must be assigned to disordered layers close to the surface, as will be shown by ^1H-^{13}C

www.manaraa.com

dephasing below.

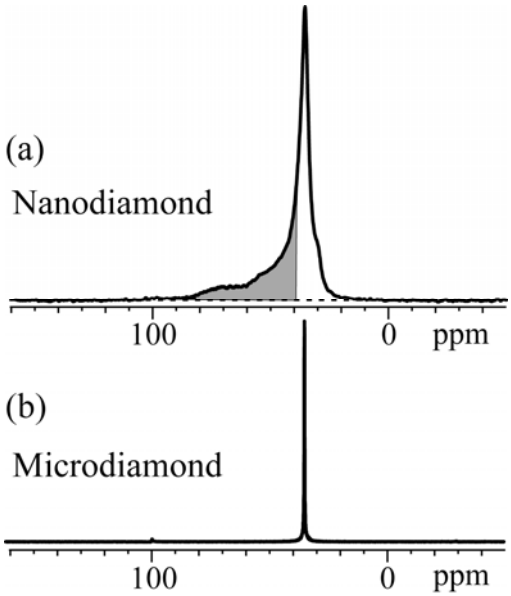

Figure 1. Quantitative direct-polarization ^{13}C NMR spectra of (a) nanodiamond and (b) microdiamond, measured at 14 kHz and 6.5 kHz MAS, respectively. A Hahn echo was used before detection for obtaining perfect baselines. The highest peaks at 37 ppm in both spectra represent the carbon signals from crystalline diamond. Signal in the shaded range in (a), between ~40 and 85 ppm, must be assigned to disordered carbon in nanodiamond.

Wide-angle X-ray diffraction. The wide-angle X-ray diffraction pattern of nanodiamond powder is shown in Figure 2. Data obtained in a quartz and a plastic sample holder are compared. The latter shows a broad reflection near 13°, similar to those reported previously for nanodiamond and interpreted in terms of a surface structure containing many sp^2-hybridized carbons.[15] However, the absence of this band in the data obtained with the quartz sample holder reveals it to be an artifact.

In spherical nanocrystals, a finite crystal diameter L results in a broadening $\Delta\theta$ of a given Bragg reflection at scattering angle θ, according to the Scherrer equation

$$L = \frac{0.9\lambda}{\beta_{1/2}\cos\theta} \qquad (1)$$

where $\beta_{1/2}$ is the full width at the maximum peak, and 2θ is the diffraction angle. Analysis of the peaks in Figure 2 gives a diameter of the crystalline core of 4.1 ± 0.2 nm in our sample.

www.manaraa.com

Elemental analysis. Elemental analysis yields C : H : N atomic ratios of 100 : 14 : 2. The uncertainty of the C and H abundances is ± 1, mostly due to the likely presence of residual adsorbed water.

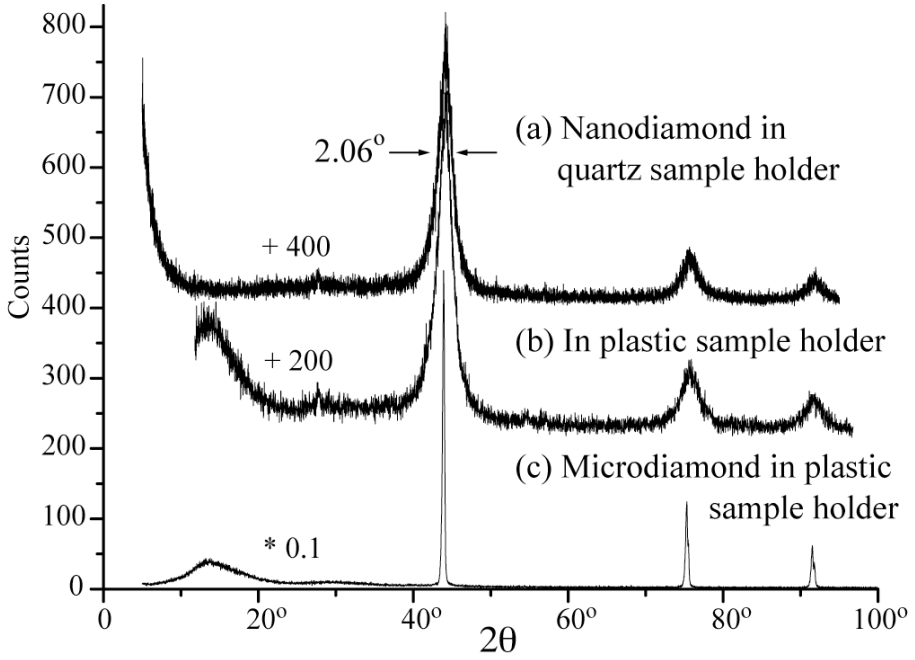

Figure 2. Wide-angle X-ray diffraction (WAXD) pattern of (a, b) nanodiamond and (c) microdiamond powder, conducted with the sample in (a) a quartz or (b, c) plastic sample holder. For clarity, intensity patterns of (a) and (b) were vertically shifted by 400 counts and 200 counts, respectively, while the intensity in (c) was scaled down 10 times.

II. The Protonated Nanodiamond Surface

We have characterized the surface layers of nanodiamond by 1D NMR with spectral editing, and by 2D ^{1}H-^{13}C HETCOR experiments.

Search for sp^2-hybridized C. The quantitative ^{13}C spectrum in Figure 1 shows no apparent peaks in the > 100 ppm region, where sp^2-hybridized carbons resonate. In order to ensure that we do not overlook long-$T_{1,C}$ sp^2-hybridized carbons, we acquired a spectrum with 400-s recycle delay and total suppression of sidebands at 6.5-kHz MAS in a 7-mm rotor, see Figure 3(a). No signals from sp^2 carbons are observed. We can also look for such sites with a 4-s recycle delay and many more scans in a 4-mm rotor at 13 kHz MAS, and in a larger 7-mm rotor at 6.5 kHz MAS with TOSS. In the resulting spectra shown in Figure 3(b,c), we

www.manaraa.com

observe only residual spinning sidebands at ~160 ppm. The intensity, which could be from one of MAS sidebonds of alkyl carbons at 37 ppm due to the large paramagnetic shift anisotropies (see details below), accounts for less than 1% of all carbons.

By contrast, Panich et al.[16] reported a peak at ~ 111 ppm, which they attributed to aromatic surface sites. The position of this signal would match a sideband of the main alkyl peak at 35 ppm if the experiment was performed at 11.4 kHz MAS in their magnetic field of 14 T; this interpretation is supported by the lack of any other spinning sideband, which should be observed due to the combined chemical and paramagnetic shift anisotropies. Figure 3(d-f) demonstrates that sidebands of the band centered at 37 ppm can be clearly seen in the 100 – 150 ppm region under equivalent conditions. Unfortunately, ref.[16] does not seem to report the spinning frequency used in their experiment, and an inquiry with the corresponding author was inconclusive. An alternative assignment would be to Teflon, $(CF_2)_n$, commonly used as a pliable spacer material in solid-state NMR, which is invisible in CP, but produces a peak at ~111 ppm in DP experiments.

Evidence of protons directly bonded to carbon. Figure 4(a) presents the ^{1}H spectra of nanodiamond at slow MAS (6.5 kHz). The width of the observed bands indicates a significant proton density on the surface. The narrow (2.6-kHz wide) signal reported by Panich et al.[16] and its interpretation as resulting from relatively isolated protons bonded to nanodiamond surface carbon in C-H and/or C-OH groups is not corroborated in our experiments, which employed probehead background suppression. Care must be taken to avoid absorption of water by the hygroscopic sample.[35, 36] We also found that heating to remove water may lead to an alteration of the surface structure. The interference from mobile water can be circumvented by indirect detection of the ^{1}H spectrum using ^{1}H-^{13}C WISE with ^{13}C decoupling during ^{1}H evolution and short Lee-Goldburg cross-polarization, which provides a spectrum of the ^{1}H bonded to ^{13}C. The broad sideband pattern observed, Figure 4(b), confirms that the sharp line reported by Panich et al.[16] is mostly not from surface-bonded protons.

www.manaraa.com

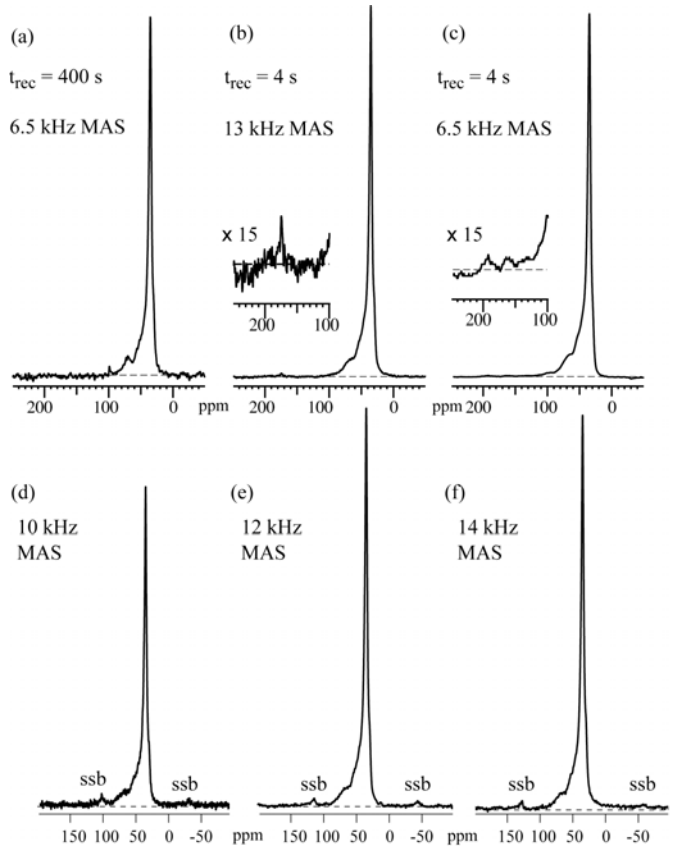

Figure 3. (a-c) Search for graphitic or other sp^2-hybridized carbon signals in quantitative DP/TOSS ^{13}C NMR spectra, with 400 s (at 6.5 kHz MAS) and 4 s (at 13 and 6.5 kHz MAS) recycle delays, for full relaxation and maximum sensitivity, respectively. The insets in (b) and (c) show the region from 100 to 250 ppm enlarged 15 times; less than 1 % of carbon could be sp^2 carbon or could be a spinning-side band signal. (d-f) DP/MAS ^{13}C NMR spectra taken at 150 MHz (in a field of 14.1 T) at 10, 12 and 14 kHz MAS. They clearly show side bands from the highest alkyl carbon peak.

The 30-kHz MAS spectrum, shown in Figure 4(c), reveals that the ^1H chemical shift is at 3.8 ppm, which is unusual for alkyl groups. The assignment to C-H, rather than H_2O, protons is confirmed by the cross peak between the 3.8-ppm ^1H and 37-ppm ^{13}C resonances in the ^1H-^{13}C HETCOR spectrum of Figures 4(d); this spectrum was acquired with short LGCP and is therefore dominated by signals of directly bonded ^{13}C-^1H pairs. In addition, obvious spinning sidebands are observed in the ω_1 dimension of the 2D HETCOR spectrum (see Figure 5(a)), proving strong ^1H-^{13}C dipolar couplings and thus close carbon-hydrogen proximity. In order to confirm quantitatively that the protons and carbons are directly bonded, we have extracted the ω_1 (^1H) slice at ω_2 (^{13}C) = 37 ppm from the 2D HETCOR

www.manaraa.com

spectrum, see Figure 5(b), and analyzed the ratio of first-order sidebands to the centerband. In order to determine the contribution of ≥2-bond couplings to the centerband, we recorded two 1D ^{13}C NMR spectra with a LG-CP time of 0.1 ms and dipolar dephasing times of 0 and 40 μs, respectively, shown in Figure 5(c). The thicker line in Figure 5(c) represents nonprotonated carbons, which is at least two bonds away from protons. The intensity ratio of the highest peaks between thicker and thinner lines at 37 ppm, the same position as the slice shown in Figure 5(b), is ~ 0.27. In other words, nonprotonated carbons contribute 27% of the centerband in Figure 5(b). The dipolar coupling strength ω_d between ^{13}C and ^{1}H of a C-H group is ~$0.577\times2\pi\times21$ kHz and that of two-bond coupling of C-C-H is ~ $0.577\times2\pi\times1.5$ kHz, with the FSLG scaling factor of 0.577. At the MAS spinning frequency of $\omega_r = 2\pi\times6.5$ kHz, the ratio of one of two first-order sidebands to the centerband intensity is ca. 0.30 for the one-bond C-H coupling, according to the Herzfeld-Berger graphical tables,[37] which matches the experimental first-sideband to centerband ratio (thin bars in Figure 5(b)). The ratio is much smaller, ca. 0.003, for the C-C-H two-bond coupling (thick bars). The strong dipolar sidebands prove that the protons and carbons are directly bonded, and that the 3.8 ppm ^{1}H peak is due to CH rather than OH protons.

Protonated surface carbons. The DP/MAS ^{13}C NMR spectrum of Figure 6(a) provides quantitative information on all carbons, and Figure 6(b) displays the corresponding spectrum of nonprotonated carbons obtained under the same conditions but after a recoupled gated decoupling time of 68 μs. The difference of these spectra results in a spectrum dominated by signals of protonated carbons, shown as Figure 6(c); it accounts for 6% of total carbons. Note that the chemical shifts of these 6% protonated carbons overlap with the chemical shift ranges of both the diamond core and the nonprotonated carbons in the disordered shell.

The elemental analysis indicates that ~12% of all C are part of CH or COH groups, and the first carbon layer of nanoparticles with a diameter of ~ 4.8 nm and a 0.1-nm layer spacing accounts for ~ 12% of all carbons [22]. From data shown in Figure 6(c) we have found that 6% CH carbons are protonated. This means that about half of the carbons at the nanodiamond surface are protonated. The rest may be bonded to OH and NH_n groups.

In order to obtain more detailed information on the protonated carbons, a series of

www.manaraa.com

spectral editing techniques were applied. Carbons near protons can be observed selectively in ^{1}H-^{13}C CP NMR. Figure 7(a) shows the CP/TOSS spectrum with a contact time of 0.2 ms, selecting primarily signal from protonated carbons, and some from nonprotonated carbons close to protons. Figure 7(b) shows the CP/TOSS spectrum with 0.2-ms CP and 40-μs dipolar dephasing, showing the nonprotonated carbons sufficiently close to protons. The difference of the two spectra is the spectrum of the protonated carbons (CH_2 + CH) shown in Figure 7(c). All three spectra are plotted on an absolute intensity scale; the large band centered at 40 ppm is assigned to alkyl carbons, and the weak band at 70 ppm may come from OCH carbons. The CH-only spectrum shown in Figure 7(d) demonstrates a similar, relatively symmetrical band around 40 ppm. No significant CH_2 signals were observed in CH_2-only spectra (not shown).

III. Comparison with Annealed Nanodiamond

We also applied spectral editing to nanodiamond annealed by heating at 600 ^{o}C for three hours under argon protection. For annealing at this temperature, Raman scattering shows an unexplained decrease in the intensity of the diamond bands, while significant graphitic signals are not yet observed.[38] While the direct polarization ^{13}C NMR spectrum shows relatively little change with annealing (not shown), the NMR results shown in Figure 7(e-h) reveal clear modifications in the surface structure after the annealing. The disappearance of the signals observed at 70 ppm for the unannealed sample shows that the COH groups have been removed from the nanodiamond surface. In addition, the chemical shift of the main protonated-carbon peak moved downfield, see Figure 7(e, g, h). The CH_n spectrum, Figure 7(g), shows that some CH signals appear at the sp^2 carbon position, marked by an arrow. These protonated aromatic carbons account for 3% of all C.

IV. Depth Measurements

Given that only the surfaces of the nanodiamond particles are protonated, we can use ^{1}H-^{13}C dipolar couplings to measure the depth of any spectrally resolved carbon site from the surface protons.

www.manaraa.com

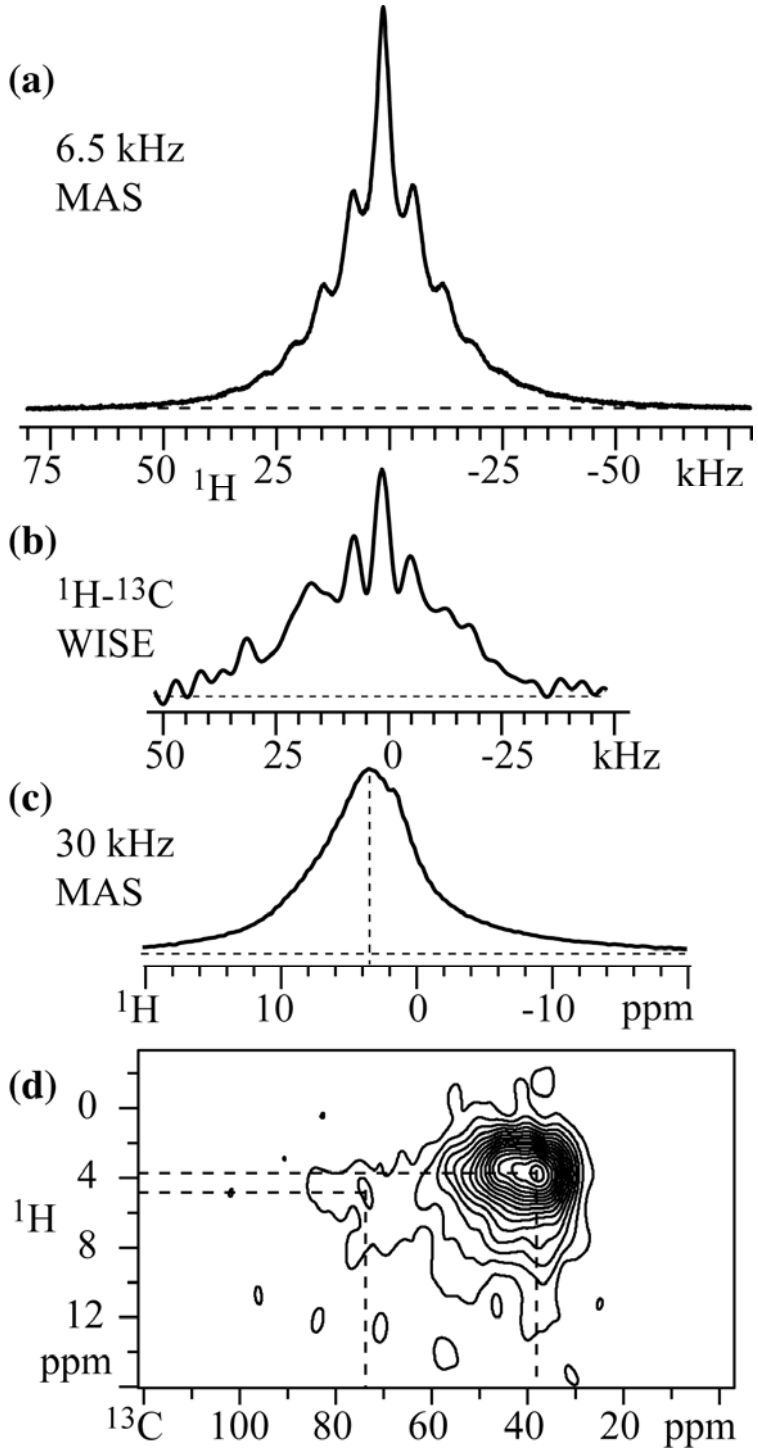

Figure 4. ^{1}H spectra of nanodiamond: (a) One-dimensional spectrum at slow (6.5-kHz) MAS, with background suppression. (b) ^{1}H projection from a 2D ^{13}C-^{1}H wide line separation spectrum taken at 6.5 kHz MAS. (c) 30-kHz MAS spectrum, with background suppression. (d) 2D ^{13}C-^{1}H HETCOR spectrum taken at 6.5 kHz MAS.

www.manaraa.com

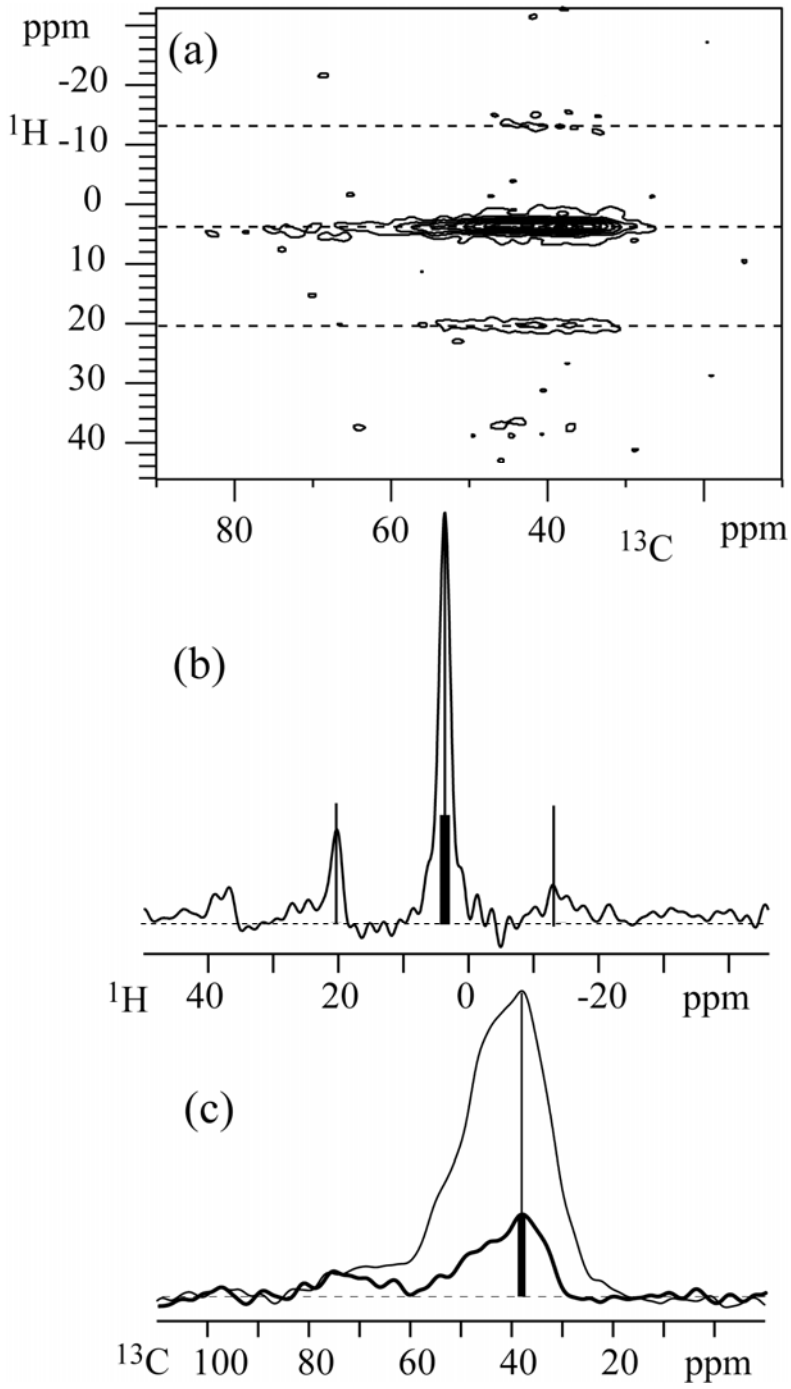

Figure 5. 2D ^{13}C-^{1}H HETCOR NMR at 6.5 kHz MAS. (a) Full view of the 2D spectrum; spinning sidebands in the ω_1 dimension are marked by dashed lines. (b) Projection onto the ω_1 axis, showing the C-H dipolar sidebands. Simulated stick spectra are also shown. The thin sticks represent the intensity of directly bonded C-H groups, while the thick stick represents the intensity of quaternary carbons, as determined from (c) the corresponding 1D ^{13}C spectra after LG-CP of 0.1 ms duration, without (thin line) or with (thick line) 40 μs gated decoupling.

www.manaraa.com

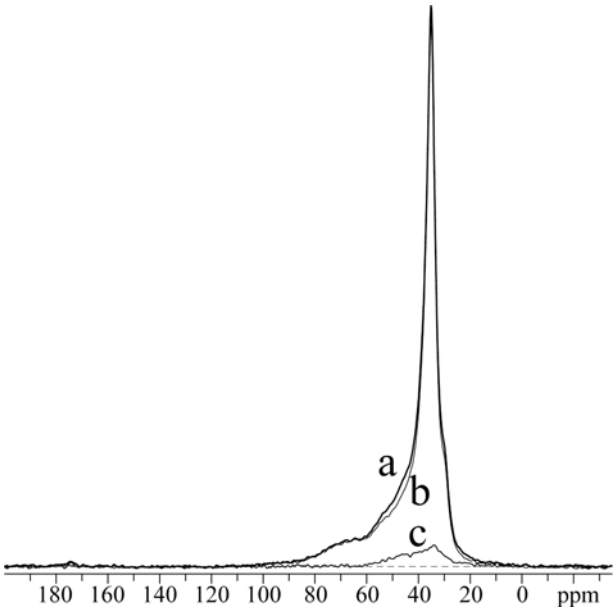

Figure 6. Quantitative ^{13}C NMR spectra of nanodiamond, acquired after a Hahn echo at an MAS frequency of 14 kHz. (a) Spectrum of all carbon. (b) Corresponding spectrum of quaternary carbons, obtained after 68 μs dipolar dephasing centered on the ^{13}C 180° pulse. (c) Difference spectrum obtained by subtracting (b) from (a), dominated by signals of protonated carbons.

REDOR recoupled C-H dephasing. The most commonly used pulse sequence for recoupling heteronuclear interactions is REDOR. We have demonstrated that its use for recoupled long-range C-H dephasing enables distinction of nonprotonated carbons at various distances from the nearest protons.[31] Figure 8(a) shows the recoupled C-H dipolar dephasing of nonprotonated carbons, with the intensity of the signal after 68 μs of dipolar dephasing normalized to unity. In the experiment with direct polarization, the carbons in the region of 30-40 ppm dephase more slowly than those between 40 and 75 ppm. This shows that the signals from 30-40 ppm represent predominantly the diamond core while those in the range of 40-75 ppm must be assigned to the outer shell of a given particle. By using the recoupled C-H dipolar dephasing experiment after CP and gated decoupling at 6.25 kHz MAS, we can monitor the dephasing of nonprotonated carbons in the subsurface layers since CP selects carbons near protons and thus close to the surface. As expected, the carbons in the subsurface layers decay the fastest since they are closest to protons.

$^{13}C\{^1H\}$ HARDSHIP NMR. The REDOR data are difficult to analyze quantitatively, due to

www.manaraa.com

the effect of the strong homonuclear couplings during the long heteronuclear dephasing.[33] We have shown that the HARDSHIP dephasing method avoids these difficulties, by terminating a given period of heteronuclear dephasing before homonuclear effects become significant; this relatively short heteronuclear recoupling period is repeated many times to generate significant dephasing.[33] Figure 8(b) presents the dephasing of carbons using $^{13}C\{^{1}H\}$ HARDSHIP NMR. Three sets of data points are shown: from signals within 25-40 ppm, within 40-82 ppm, and within 25-82 ppm (total with differential-T_2 correction; same data as shown in ref. [33]). The curves were simulated assuming 4.8-nm diameter particles with 60% C-H and 40% O-H groups at the surface. The simulation results indicate that there are 7 outer carbon layers with a thickness of 0.63 nm contributing to the signal between 40-82 ppm, and that 35% of the 7 outer layers resonate in the 25-40 ppm range, overlapping with the core-carbon peak. The thickness of the partially disordered layer is quite consistent with a recent simulation of small nanodiamond grains, where the thickness of the structurally disturbed surface layer was approximately 0.5 nm.[22]

V. Unpaired Electrons in Nanodiamond

In magnetic measurements, it has been found that a ~4.6-nm diameter nanodiamond grain contains ~ 30 unpaired electrons (or 35 electrons in a 4.8-nm particle) on average.[39] In the EPR spectrum of detonation nanodiamond, the triplet characteristic of the 2I+1 = 3 orientations of the ^{14}N nuclear spin is not observed. This shows that the unpaired electrons are mostly not due to N, but bonding defects in the carbon lattice.[20, 40, 41] We have observed the effects of the electron spins on the NMR relaxation times and analyzed the longitudinal relaxation quantitatively as described in the following.

Invisible carbon near unpaired electrons. Due to thermal averaging, the effective "Curie" spin S_c of an unpaired electron in nanodiamond is given by

$$S_C = \frac{-\gamma_e \hbar S(S+1)B_0}{3kT} \qquad (2)$$

where γ_e is the gyromagnetic ratio of the electron (-1.76×10^{11} s^{-1} T^{-1} = 658.5 γ_{1H}), $\hbar$ is Planck's constant/2π, S is the electron spin quantum number (0.5), B_0 is the magnetic field, k

www.manaraa.com

is the Boltzmann factor ($1.38 \cdot 10^{-23}$ J/K), and T is the absolute temperature.[42] Under our experimental conditions, with B_0 = 9.4 T and T = 293 K, we obtain S_C = -0.011. Comparing with the full S = 1/2, this means that the electrons are 2.2% polarized.

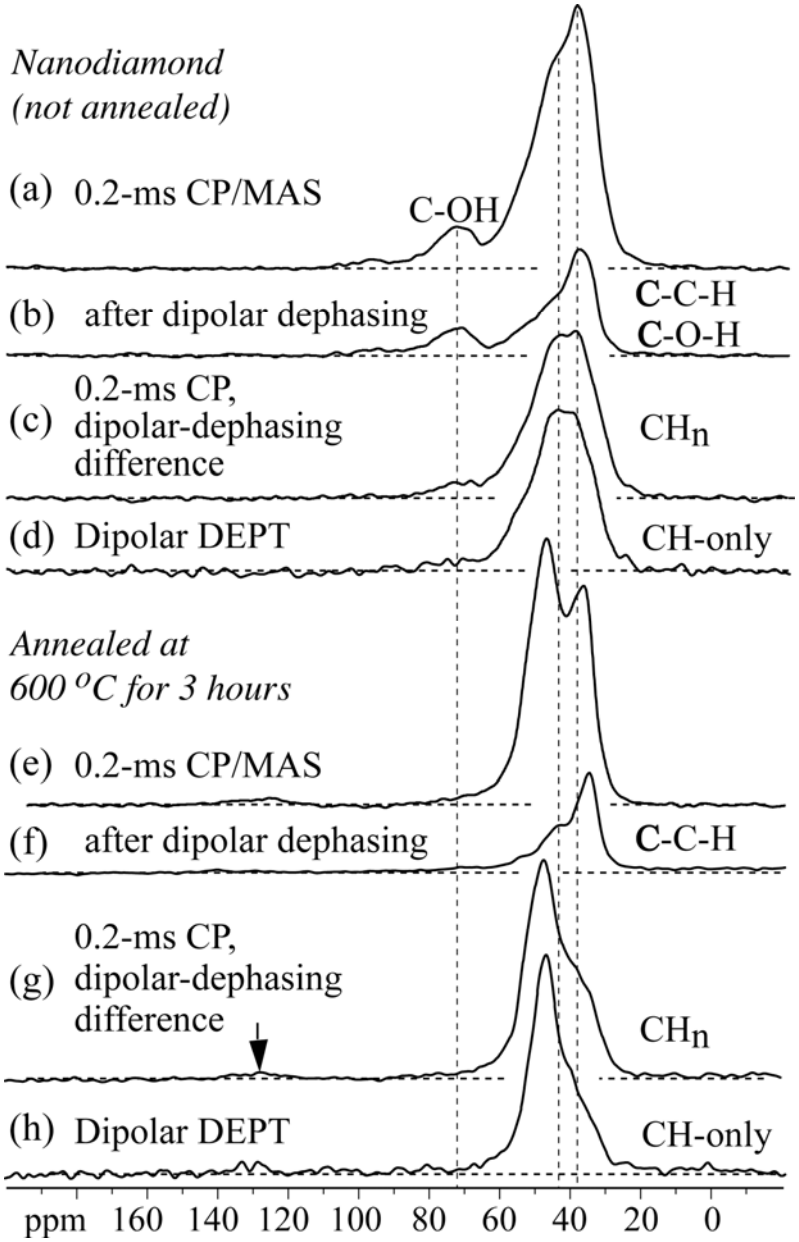

Figure 7. Selective ^{13}C NMR spectra of surface and subsurface carbons, for (a-e) unannealed nanodiamond and (e-h) nanodiamond powder annealed at 600 °C under argon for three hours. (a), (e): Spectra of all carbon close to protons, obtained after 0.2-ms CP. (b), (f) Spectra of the subsurface layer, obtained after 0.2-ms CP and 40-μs dipolar dephasing. (c), (g) Spectra of protonated surface carbons (CH_n), obtained as the difference between the two preceding spectra. (d), (h) Spectra of the CH (methine) groups, obtained by dipolar DEPT at 5787 Hz MAS.

www.manaraa.com

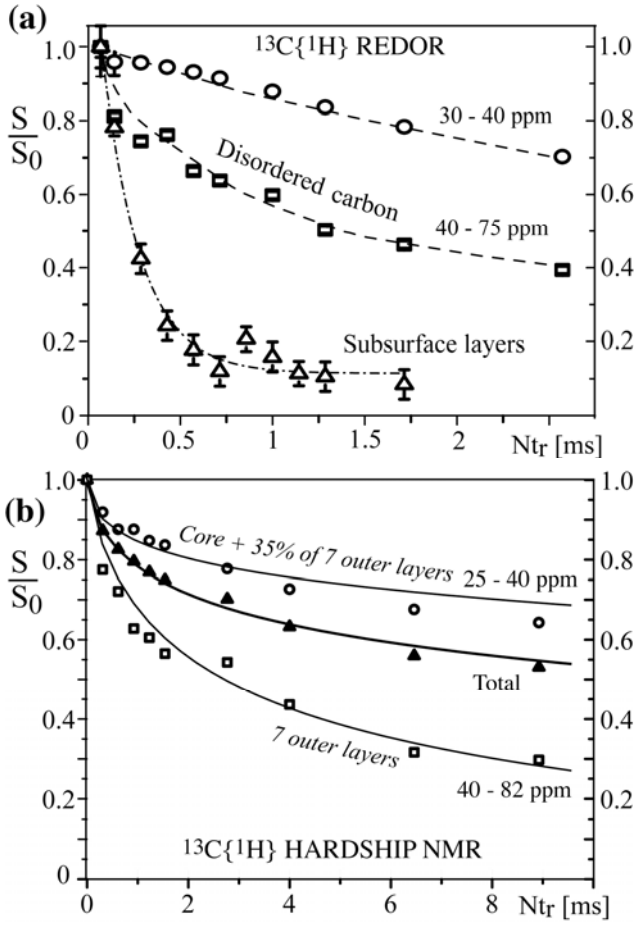

Figure 8. $^{13}C\{^{1}H\}$ dephasing in nanodiamond. (a) $^{13}C\{^{1}H\}$ REDOR dephasing of nonprotonated carbons at 14 kHz MAS. Circles: core (30 to 40 ppm); Squares: disordered carbon (40 to 75 ppm); Triangles: subsurface carbon obtained after CP and dipolar dephasing. Dashed lines are guides to the eye. (b) $^{13}C\{^{1}H\}$ HARDSHIP dephasing of all carbons at 6.5 kHz MAS, with fit curves. Circles: Signal from 25 to 40 ppm; squares: Disordered-carbon signal from 40 to 82 ppm; triangles: total signal from 25 to 82 ppm. Fit curves for 4.8-nm diameter nanodiamond particles, with 7 outer layers of disordered carbon, 65% of which resonate within 40-82 ppm and 35% within 25-40 ppm, are also shown.

Due to the thermal averaging of the electron spin S_Z to the Curie spin S_C, the effect of the electron-nuclear Hamiltonian is reduced to that of a B-field with the strength of the dipolar coupling constant and can be expressed as follows:[42]

$$\delta_{PSA} = \frac{-\mu_0 \hbar \gamma_e \gamma_{^{13}C}}{4\pi r^3} 2S_C = -S_C \; 2\pi \; 39.5 \; MHz \frac{\overset{o}{A}^3}{r^3} \qquad (3)$$

The field-proportional and orientation-dependent coupling in Eq.3 behaves essentially like a

www.manaraa.com

chemical-shift anisotropy (CSA), and is referred to as the paramagnetic-shift anisotropy (PSA).[43, 44] At T = 293 K, for distances > 0.3 nm we find δ_{PSA} < 15 kHz, which is sufficiently small for the signal to be mostly observable. At shorter electron-carbon distances, the intensity of the carbon centerband is strongly reduced. This effect makes < 8% of carbon unobservable.

Fast $T_{1,C}$ relaxation. Combining ^{13}C DP- or CP- REDOR with T_1 relaxation measurements, T_1 relaxation of core and shell carbons can be obtained quite selectively. The nanodiamond ^{13}C T_1 ($T_{1,C}$) relaxation curves of carbons directly bonded to hydrogen, in the subsurface layers, in the whole disordered shell, and in the core are shown in Figure 9(a). Long-range ^1H-^{13}C dipolar dephasing did not change the $T_{1,C}$ curve of the core carbon signal significantly (not shown). For reference, the $T_{1,C}$ relaxation curves of natural and synthetic microdiamonds are also plotted in Figure 9(a). The $T_{1,C}$ values of all parts of nanodiamond are within one second, compared to hundreds of seconds for micrometer-size diamonds. In addition, the relaxation curves in nanodiamond are nonexponential. Both observations indicate the presence of unpaired electrons.

Electron T_1 relaxation produces a fluctuating field at the ^{13}C nucleus that drives its longitudinal ($T_{1,C}$) relaxation. $T_{1,C}$ is strongly dependent on the distance r_n between a given carbon and the n^{th} unpaired electron:

$$1/T_{1,C} = A^{-1} \sum_{n_{electron}} 1/r_n^{\,6} \qquad (4)$$

where the prefactor A^{-1} depends on the longitudinal relaxation time $T_{1,e}$ of the unpaired electrons, as detailed in ref.[42]. In Figure 9(a) the $T_{1,C}$ of the disordered shell is shorter than that of the surface or of the core, indicating that disordered carbons are closer to unpaired electrons. It is particularly interesting to note the $T_{1,C}$ of carbons in the surface and subsurface layers is longest, which was seen consistently in both CP and DP dipolar-dephasing difference experiments (latter not shown). This combination of spectral editing with $T_{1,C}$ measurements indicates that the ad-hoc assignment of the short $T_{1,C}$ component to surface carbons proposed in ref. [16] is incorrect. This observation also shows that the unpaired electrons are not due to dangling bonds on the surface. For quantitative confirmation, Figure 9(b) shows a simulation of the relaxation curves for a model nanodiamond grain with 35

www.manaraa.com

unpaired electrons present as dangling bonds in the outer 0.2 nm of the spherical particle of 4.8-nm diameter. As expected, the relaxation for the core (plus 35% of the shell carbon, which overlaps) in this dangling-bond model is significantly slower than that of the shell or the surface layer, contrary to the experimental observation. In order to preempt potential concerns, carbons within 0.6 nm from the unpaired electron were considered as unobservable; with a smaller unobservable radius, the contrast between core and shell relaxation would be even larger.

The data in Figure 9(a) can be fitted with a model where unpaired electrons are found at depths between 0.4 and 1 nm from the particle surface. The value of A in Eq.(4) was set to 3.5 s/nm^6, and carbons within 0.3 nm from the unpaired electrons were treated as unobservable. The spherical particle contained 40 unpaired electrons, consistent with recent magnetic analyses of the same material.[39] At a lower number of electrons per particle, the depth dependence of the relaxation curves is less pronounced than observed experimentally, because there are large sections of the unpaired-electron containing layers that are actually free of unpaired electrons. The distribution of depths (0.4 to 1 nm) of the unpaired electrons from the particle surface is directly reflected in the multimodal relaxation of the carbons in the surface layer. The fraction of unpaired electrons near (~0.4 nm from) the particle surface is also crucial for making the relaxation of the carbons in the core slower than that of the shell carbons, since they affect the core less than the shell. For a model with a distribution of electrons throughout the whole particle, the difference between the relaxation curves is too small, as should be expected, see Figure 9(c). While for a fully homogeneous distribution of electrons, all relaxation curves would coincide, the surface carbons in this model still relax slightly slower than those in the core since even with unpaired electrons in six neighboring particles included in the simulation, the concentration of unpaired electrons outside the particle is still lower than inside.

Chemical shift dispersion. The 5 – 30 ppm "chemical" shift differences between carbons in the core and the multi-layer shell of nanodiamond are considerable and call for further analysis. About 30% of all carbons are within 3 bonds from the particle surface. Chemical shifts may occur due to proximity to hydrogen and oxygen. It is interesting to note that an

www.manaraa.com

ab-initio calculation showed a 75-ppm chemical shift for amorphous sp^3-hybridized carbon.[45] In this context, it should also be noted that the 37-ppm chemical shift of neat diamond cannot be understood in terms of standard substitution rules for alkyl carbons,[46] which predict a value >50 ppm. Nevertheless, the 37-ppm chemical shift has been reproduced in ab-initio calculations.[45] In addition, Knight shift cannot be excluded since hydrogenated diamond surfaces are 4 to 5 orders more conductive than undoped diamond.[47, 48] More than 10% of all carbon atoms are within 3 bonds from an unpaired electron, and some paramagnetic shift due to the unpaired electrons, as well as chemical shift due to lattice distortions near their associated defects, is to be expected. The shell could also contain a significant number of defects that are not paramagnetic.[41]

VI. Synopsis

Comparison with previous models. Several nanodiamond structural models have been proposed in the literature, such as a buckyball-surface model,[14] an model featuring an aromatic onion shell,[15, 20] and a hollow-center model.[17] For a nanodiamond grain with a diameter around 4.8 nm, the first carbon layer accounts for 10% of all carbons. Since less than 1% is from sp^2 carbon (Figure 3), and no "onion shell" diffraction peak at 13^o is seen in the X-ray diffraction pattern (Figure 2), we can clearly rule out the buckyball- and onion shell surface models. [14-17 20] Note that all previous NMR studies of purified nanodiamond [5, 16, 23, 24] have also failed to show a convincing signal of sp^2-hybridized carbons; the peak at 111 ppm in ref. [16] is not at the expected ~130-ppm resonance position and is most likely an artifact, as discussed above. The strong dipolar sidebands in the 2D HETCOR spectra show that more than half of the (sp^3-hybridized) surface protons are directly bonded to carbon. In turn, the $^{13}C\{^1H\}$ REDOR and HARDSHIP results confirm that the ordered diamond carbons are far from the protons, i.e. in the core, while the disordered sp^3-hybridized carbons are closer to the surface. The $T_{1,C}$ experiments indicate that unpaired electron are located at an intermediate depth, not in the center, and also not as dangling bonds on the surface. The hollow center structural model is also not suitable for our detonation nanodiamond sample because no sp^2 carbons are observed and T_1 of core carbon is longer than the T_1 of other carbon species.

www.manaraa.com

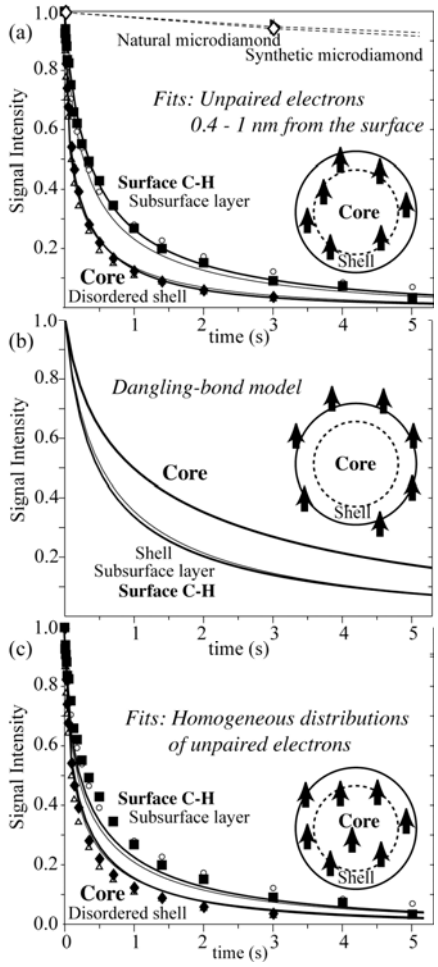

Figure 9. $T_{1,C}$ relaxation data for nanodiamond measured at 6.25 kHz MAS, with simulation curves. (a) Filled squares: Carbon directly bonded to H; open circles: subsurface layer (from dipolar-dephasing difference after cross polarization); filled diamonds: core (25-47 ppm); open triangles: disordered carbon (47 –85 ppm). The T_1 relaxation curves of two microdiamond samples are shown for reference at the top. Simulated fit curves are for a model with 40 unpaired electrons per particle, at depths between 0.4 and 1 nm from the surface. (b) Simulated relaxation curves for a model with dangling bonds, unpaired electrons at the particle surface. The relaxation is slowest for the core, contrary to the experimental data in (a). (c) Simulated relaxation curves for a homogeneous distribution of unpaired electrons, with the data points from (a) superimposed.

NMR-based model of nanodiamond. Figure 10 displays the nonaromatic core-shell model of detonation nanodiamond developed based on our experimental NMR results. The nanodiamond particle has a diameter of 4.8 nm and contains close to 10,000 carbon atoms.[49] The nanodiamond surface carbons are bonded to protons, OH, and NH_n groups. Only 39% of carbons are in the 3.6-nm diameter ordered diamond core; 40% of carbons are in a 5-layers thick, partially disordered shell containing unpaired electrons; and additional 21% carbons are located in the two outermost carbon layers. The thickness of the partially disordered shell

www.manaraa.com

is around 0.63 nm. The crystalline core diameter of 4 nm deduced from WAXD includes the ordered core and ordered regions in the partially disordered shell. Unpaired electrons are located mostly in the disordered shell, at distances of 0.4 to 1-nm from the surface, with a density of ~ 40 unpaired electrons per 4.8-nm diameter particle. The fraction of carbon that is unobservable due to close proximity (< 0.3 nm) to an unpaired electron is < 8%.

A partially disordered shell of 0.5 – 0.7 nm thickness containing sp^3-hybridized carbon has been generated or postulated in some simulations of hydrogen-terminated nanodiamond,[22, 50, 51] while simulations for extended hydrogenated diamond crystals find only a reconstruction of the 0.2-nm thick surface layer.[52] Barnard and Sternberg found a 0.5-nm thick disordered layer in DFT simulations aimed at identifying the energetics of nitrogen in nanodiamond.[22] Palosz et al. have postulated a 0.7-nm thick strained shell for SiC and nanodiamond particles, based on considerations of surface tension and surface curvature preventing a simple reconstruction of the surface layer.[50, 51]

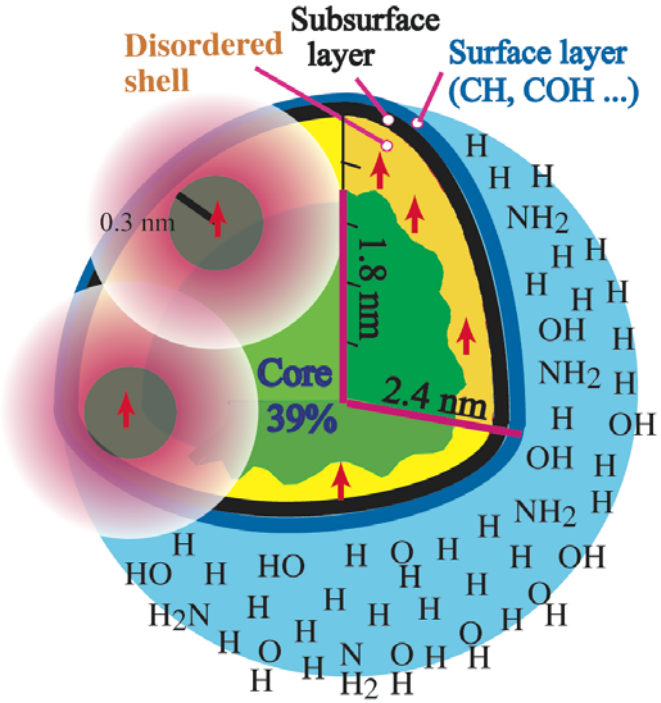

Figure 10. Schematic model of the structure of nanodiamond. The hydrogenated surface is part of a 0.6-nm thick shell of seven partially disordered carbon layers that contain 61% of all C and produce downfield-shifted ^{13}C NMR signals. Unpaired electrons (red arrows) occur with a density of ~ 40 per particle and are located 0.4 - 1 nm from the surface. About 8% of all carbon is within 0.3 nm from the unpaired electron and thus unobservable by NMR.

www.manaraa.com

Conclusions

We have studied synthetic nanodiamond with a crystalline core of ~4-nm diameter. Short ^{1}H-^{13}C dipolar dephasing shows that about 6 % of all carbons, about half of surface sites, are protonated, while the other half are bonded to OH groups. No aromatic carbons were found, ruling out buckyball or graphitic surface layers in the two samples studied. A scattering feature previously attributed to graphitic onion shells was not observed here and shown to be most likely an artifact of a plastic sample holder. ^{1}H NMR and $^{13}C\{^{1}H\}$ HETCOR consistently showed an unexpected 3.8-ppm chemical shift position of the surface protons; the protons were proved to be bonded to carbons (rather than O in –OH or H_2O) by strong ^{13}C-^{1}H dipolar sidebands in HETCOR spectra. Given the protonated surface, ^{1}H-^{13}C HARDSHIP NMR can probe the depth of various sites from the surface. The upfield signals dephased faster than the ideal-diamond carbon signal, corroborating the assignment of the broad upfield bands to a disordered shell of ~0.63 nm thickness, in a particle of 4.8-nm diameter. Fast $T_{1,C}$ relaxation (<1 s) observed for all carbons in nanodiamond is due to interactions with ~40 unpaired electrons per grain. The longer $T_{1,C}$ of the protonated surface carbons and the layer underneath proves that most unpaired electrons are not from dangling bonds at the surface, but from unpaired electrons at depths of 0.4 – 1 nm.

Acknowledgments

This work was supported by the National Science Foundation (Grant CHE-0138117).

References

1. Gilmour, I.; Russell, S. S.; Arden, J. W.; Lee, M. R.; Franchi, I. A.; Pillinger, C. T. *Science* **1992,** *258,* 1624-1626.
2. Lewis, R. S.; Anders, E.; Draine, B. T. *Nature* **1989,** *339,* 117-121.
3. Dai, Z. R.; Bradley, J. P.; Joswiak, D. J.; Brownlee, D. E.; Hill, H. G. M.; Genge, M. J. *Nature* **2002,** *418,* 157.
4. Dolmatov, V. Y. *Russ. Chem. Rev.* **2001,** *70,* 607- 626.
5. Donnet, J. B.; Fousson, E.; Delmotte, L.; Samirant, M.; Baras, C.; T.-K., W.; Eckhardt, A. *Phys. Theor. Chem.* **2000,** *3,* 831-838.

www.manaraa.com

6. Krueger, A. *J. Mater. Chem* **2008,** *18,* 1485-1492.
7. Yu, S.-J.; Kang, M.-W.; Chang, H.-C.; Chen, K.-M.; Yu, Y.-C. *J. Am. Chem. Soc.* **2005,** *127,* 17604–17605.
8. Bondar, V. S.; Pozdnyakova, I. O.; Puzyr, A. P. *Phys. Sol. State* **2004,** *46,* 758–760.
9. Bogatyreva, G. P.; Marinich, M. A.; Ishchenko, E. V.; Gvyazdovskaya, V. L.; Bazalii, G. A.; Oleinik, N. A. *Phys. Sol. State* **2004,** *46,* 738-741.
10. Vul', A. Y.; Golubev, V. G.; Grudinkin, S. A.; Krüger, A.; Naramoto, H. *Phys. Astron.* **2002,** *28,* 787-789.
11. Badziag, P.; Verwoerd, W. S.; Ellis, W. P.; Greiner, N. R. *Nature* **1990,** *343,* 244-245.
12. Raty, J. Y.; Galli, G. *Nat. Mater.* **2003,** *2,* 792-795.
13. Wang, C.; Chen, J.; Yang, G.; Xu, N. *Angew. Chem. Int. Ed.* **2005,** *44,* 7414-7418.
14. Raty, J. Y., Galli, G. *J. Electroanal. Chem.* **2005,** *584,* 9-12.
15. Aleksenskii, A. E.; Baidakova, M. V.; Vul, A. Y.; Siklitskii, V. I. *Phys.Solid State* **1999,** *41,* 668-671.
16. Panich, A. M.; Shames, A.I.; Vieth, H. M.; Osawa, E.; Takahashi, M.; Vul, Y. A. *Eur. Phys. J. B.* **2006,** *52,* 397-402.
17. Vereshchagin, A. L.; Yur'ev, G. S. *Inorg. Mater.* **2003,** *39,* 247-253.
18. Baidakova, M. V.; Vul, A. Y.; Siklitski, V. I.; Faleev, N. N. *Phys. Solid State* **1998,** *40,* 715-718.
19. Kruger, A.; Kataoka, F.; Ozawa, M.; Fujino, T.; Suzuki, Y.; Aleksenskii, A. E.; Vul, A. Y.; Osawa, E. *Carbon* **2005,** *43,* 1722-1730.
20. Shames, A. I.; Panich, A. M.; Kempinski, W.; Alexenskii, A. E.; Baidakova, M. V.; Dideikin, A. T.; Osipov, V. Y.; Siklitski, V. I.; Osawa, E.; Ozawa, M.; Vul, A. Y. *J. Phys. Chem. Solids* **2002,** *63,* 1993-2001.
21. Duijvestijn, M. J.; Van, D. L. C.; Smidt, J.; Wind, R. A.; Zilm, K. W.; Staplin, D. C. *Chem. Phys. Lett.* **1983,** *102,* 25-28.
22. Barnard, A. S.; Sternberg, M. *J. Phys. Chem. B* **2005** 17107-17112.
23. Alam, T. M. *Mater. Chem. Phys.* **2004,** *85,* 310-315.

www.manaraa.com

24. Cody, G. D.; Alexander, C. M. O. D.; Tera, F. *Geochim. Cosmochim. Acta* **2002,** *66,* 1851-1865.
25. Bodenhausen, G.; Freeman, R.; Turner, D. L. *J. Magn. Reson.* **1977,** *27,* 511-514.
26. Mao, J.-D.; Hu, W.-G.; Schmidt-Rohr, K.; Davies, G.; Ghabbour, E. A.; Xing, B. *Soil Sci. Soc. Am. J.* **2000,** *64,* 873-884.
27. Dixon, W. T. *J. Chem. Phys.* **1982,** *77,* 1800-1809.
28. Chen, Q.; Hou, S.-S.; Schmidt-Rohr, K. *Solid State Nucl. Magn. Reson.* **2004,** *26,* 11-15.
29. Wu, X.; Burns, S. T.; Zilm, K. W. *J. Magn. Reson., A* **1994,** *111,* 29-36.
30. Liu, S. F.; Mao, J. D.; Schmidt-Rohr, K. *J. Magn. Reson.* **2002,** *155,* 15-28.
31. Mao, J.-D., Schmidt-Rohr, K. *J. Magn. Reson.* **2003,** *162,* 217-227.
32. deAzevedo, E. R.; Hu, W.-G.; Bonagamba, T. J.; Schmidt-Rohr, K. *J. Chem. Phys.* **2000,** *112,* 8988-9001.
33. Schmidt-Rohr, K.; Rawal, A.; Fang, X. W. *J. Chem. Phys.* **2007,** *126,* 054701 1-6.
34. Torchia, D. A. *J. Magn. Reson.* **1978,** *30,* 613-616.
35. Ji, S.-F.; Jiang, T.-L.; Xu, K.; Li, S.-B. *Appl. Surf. Sci.* **1998,** *133,* 231-238.
36. Iakoubovskii, K.; Mitsuishi, K.; Furuya, K. *Nanotech.* **2008,** *19,* 155705 1-5.
37. Herzfeld, J.; Berger, A. E. *J. Chem. Phys.* **1980,** *73,* 6021-6030.
38. Chen, J.; Deng, S.-Z.; Chen, J.; Yu, Z.-X.; Xu, N.-S. *Appl. Phys. Lett.* **1999,** *74,* 3651-3653.
39. Levin, E. M.; Fang, X.-W.; Bud'ko, S. L.; Straszheim, W. E.; McCallum, R. W.; Schmidt-Rohr, K. *Phys. Rev. B* **2008,** *77,* 054418 1-10.
40. Newton, M. E.; Baker, J. M. *J. Phys.: Conden. Matt.* **1989,** *1,* 9801-9803.
41. Banaszak, A.; Fabisiak, K.; Kaczmarski, M.; Kozanecki, M. *Cryst. Res. Technol.* **2006,** *41,* 535.
42. Gueron, M. *J. Magn. Reson.* **1975,** *19,* 58-66.
43. Bertini, I.; Luchinat, C. *Coord. Chem. Rev.* **1996,** *150,* 29-75.
44. Antonijevic, S.; Persson, E. *J. Chem. Phys.* **2007,** *126,* 014504 1-7.
45. Mauri, F.; Pfrommer, B. G.; Louie, S. G. *Phys. Rev. Lett.* **1996,** *77,* 5300 - 5303.

www.manaraa.com

46. Bovey, F. A.; Jelinski, L.; Mirau, P. A. *Nuclear magnetic resonance spectroscopy*. 2nd ed.; Academic Press: San Diego, 1988.

47. Andriotis, A. N.; Mpourmpakis, G.; Richter, E.; Menonx, M. *Phys. Rev. Lett. 100,* 106801 1-14.

48. Hirama, K.; Takayanagi, H.; Yamauchi, S.; Yang, J.-H.; Kawarada, H.; Umezawa, H. *Appl. Phys. Lett.* **2008,** *92,* 112107 1-3.

49. Jones, A. P.; d'Hendecourt, L. *Astron. Astrophys.* **2000,** *355,* 1191-1200.

50. Palosz, B.; Grzanka, E.; Gierlotka, S.; Stelmakh, S.; Pielaszek, R.; Bismayer, U.; Neuefeind, J.; Weber, H.-P.; Proffen, T.; Von Dreele, R.; Palosz, W. *Z. Kristallogr.* **2002,** *217,* 497-509.

51. Palosz, B.; Grzanka, E.; Gierlotka, S.; Stel'makh, S.; Pielaszek, R.; Bismayer, U.; Neuefeind, J.; Weber, H.-P.; Palosz, W. *Acta Phys. Polonica A* **2002,** *1,* 57-82.

52. Kern, G.; Hafner, J. *Phys. Rev. B ,* **1997,** *56,* 4203 - 4210.

www.manaraa.com

CHAPTER 9. Solid-state ^{13}C NMR characterization of carbon-modified TiO_2 photocatalysts

Submitted to the journal of "Chemistry of Materials"

Erin M. Rockafellow, Xiaowen Fang, Klaus Schmidt-Rohr, William S. Jenks**

Abstract

^{13}C-modified TiO_2 was prepared in order to facilitate study of the dopant atoms and trace their chemical fate throughout the process. In the pre-annealed material, NMR showed strong evidence of many Ti-O-C bonds. After annealing, surface-bound coke is a major component. NMR also showed that a washing step before annealing led to the generation of orthocarbonate (CO_4) centers, observed at 126 ppm, which are located deep inside the TiO_2 particles. Both NMR and XPS confirmed the presence of small amounts of carbonate species in all briefly annealed samples, while annealing for longer times led to the complete removal of CO_n species. Quantitative NMR also shows the degree of carbon loss that accompanies annealing. Some variation in the chemical degradation of quinoline is noted among the catalysts, but coke-containing TiO_2 catalysts are not qualitatively better catalysts for use with visible light with this substrate.

KEYWORDS. Carbon-modified TiO_2, photocatalytic degradation, quinoline.

Introduction

It is well known that titanium dioxide is one of the most effective photocatalysts for the complete mineralization of pollutants in water and air.[1-8] However, although TiO_2 is cheap, robust, and thermally stable, it is not yet ideal.[9,10] The recombination rate of photoseparated charges responsible for the oxidative chemistry effected upon the organic pollutants is quite rapid — this significantly lowers the efficiency of TiO_2-mediated degradation of organic pollutants. Furthermore, because the onset of absorption by TiO_2 is at wavelengths near 400 nm, it is capable of using less than 5% of terrestrial solar light. This inefficient use of a small fraction of the ambient photon supply limits its potential for large-scale commercial remediation.

www.manaraa.com

Surface modification of TiO_2 has been successful in lowering the excitation energy threshold, for example, by doping with metals and nonmetals.[8,10,11] Coupling TiO_2 to dyes is also a popular method used most commonly in solar cells.[12,13] The dye generally acts as a sensitizer by absorbing a visible photon and transferring an excited electron to the conduction band of the TiO_2 platform. However, the dye itself can be susceptible to thermal degradation or oxidation mediated by TiO_2, thus prompting some recent studies to focus on finding more stable, yet efficient dyes for catalysis.[14,15]

While transition metal dopants have been shown to increase visible absorbance, the experimental observations often include a decrease in the overall efficiency of the photocatalyst, and sometimes thermal instability.[16-20] The loss in efficiency has been interpreted as meaning that the dopant sites act as efficient charge recombination centers. Noble metals have also been used to achieve increased visible absorption, and can serve as electron traps, in turn reducing recombination.[10,21-23] Generally, the noble metal is present as a deposit on the surface and is not actually incorporated into the TiO_2 lattice.

Doping TiO_2 with main group elements, rather than metals, is also a promising approach. These materials are usually thermally stable and the dopant usually does not act as a site that facilitates charge recombination. However, some workers have reported that nitrogen and sulfur might act as recombination centers at higher concentrations.[24-27] Main group doping increases visible absorption by creating narrow, localized bands of orbitals within the band gap, as well as by promoting other defects of the TiO_2 lattice.[28-35] For example, nitrogen doping of TiO_2 has been correlated to an increase in oxygen vacancies, which are believed to be involved with the observed increased visible light activity.[29,31,34,35]

Nitrogen-,[36-40] sulfur-,[41-44] and carbon-doped[43,45-52] titanium dioxides have displayed efficient photocatalytic degradation of some small organic molecules and dyes under visible irradiation. Sakthivel and Kisch have shown carbon modification of TiO_2 led to a greater enhancement of photocatalytic efficiency under visible irradiation than N-TiO_2, which is in agreement with theoretical predictions.[32,46,53] Thus, carbon-modified TiO_2 is of great interest as a potential visible-light photocatalyst for pollutant remediation.

Several methods have been used to prepare carbon-doped catalysts.[43,46-48,52,54-59] Among them is treatment of titanium carbide by sputtering or heating in an oxidative atmosphere.

www.manaraa.com

Khan *et al.* reported that flame pyrolysis of Ti metal with natural gas produced a dark gray material.[57] The color was attributed to carbon impurities remaining in the material, which was capable of splitting water with visible light. Simple sol-gel techniques have also been used to produce C-doped titania. Lettman *et al.* reported a coke-containing catalyst prepared through acid-catalyzed condensation of various titanium alkoxides precursors at low temperature.[45] Ohno generated carbonate species within the TiO_2 using urea as a carbon source.[60] It was demonstrated by Sakthivel and Kisch that even tetrabutyl ammonium hydroxide could end up leaving carbon in the titania prepared by sol-gel methods.[61] Xu *et al*. prepared carbon-doped titania powder and films using glucose as a source of carbon.[62-65]

With all these differing doping methods, characterization of the resulting carbon dopant obviously becomes very important. Most groups report the results of surface-sensitive techniques, such as X-ray photoelectron spectroscopy (XPS), energy-dispersive X-ray spectroscopy (EDX), or IR spectroscopy to attempt to characterize and/or quantify the carbon dopant. XPS can be particularly useful, in that oxidation states can be immediately determined, but it is not without shortcomings. While XPS gives a good indication of the higher oxidation states of the carbon dopant, adsorbed ambient carbonaceous materials interfere with more reduced oxidation states. In particular, XPS is able to indicate the presence of coke in principle, but the XPS chemical shift of the coke species overlaps with that of the adventitious carbon, making the identification and quantification challenging. Argon etching can be used to remove adventitious carbon, but often results in destroying or completely removing the very surface species that may be crucial to the visible photoactivity of the material.[39] The concentration of carbon can instead be determined by EDX, but adventitious carbon from exposure to air is also included in this concentration value, making the accuracy questionable. Therefore, it would be beneficial to use alternative methods of characterization in combination with XPS and/or EDX to alleviate these analytical shortcomings.

Regardless of these shortcomings, some very promising structural information has been reported. It was found that oxidation of TiC to carbon-doped TiO_2 yield materials in which reduced carbon species remain from some of the Ti-C bonds being preserved through incomplete oxidation.[48,51,66] In contrast, Xu *et al.* used IR and powder diffraction to

www.manaraa.com

demonstrate the absence of Ti-C bonds in their materials.[63-65,67] Others report carbonate; however, many reports are ambiguous on the presence of coke.

We report here a study of carbon-doped TiO_2, prepared from ^{13}C-labeled glucose, following the precedent of Xu, et al.[63] We considered this among the most "chemically sensible" schemes for including carbon within the TiO_2 condensation process and found the idea of carbohydrates, with their built-in alcoholic linkages very appealing as precursors. Furthermore, because of demand in the biological community, ^{13}C-labelled glucose is commercially available at an approachable cost.

Labeling with ^{13}C allows the structural tool of solid state NMR to be added to the array of characterization tools to characterize the chemical nature of the dopant. An analogous study has been carried out with several ^{15}N-labeled nitrogen precursors.[40] Reyes-Garcia et al. were able to observe probable amino, ammonium, nitrate, and imido species present in various samples but were unable to quantify the amount of nitrogen in each sample. We expand on the techniques used by these authors, allowing us to remark upon the functionality, quantity, and location of carbon within the samples. The photocatalytic ability of the carbon-modified TiO_2 samples is also reported, using quinoline as an organic probe molecule.

Experimental Section

Chemicals. Chemicals, ordered at the highest commercially available purity, were used as received. ^{13}C-Labeled glucose was obtained in two forms: (1) uniformly and completely labeled and (2) labeled only at the anomeric (C1) carbon. Water was purified to a resistivity above 18 MΩ/cm.

Preparation of photocatalysts. The preparation is based on the procedure reported by Xu et al.[63] Glucose (0.02 M) was dissolved in ethanol, and the resulting solution was chilled to near 0 ºC. Neat $TiCl_4$ was added dropwise, and the temperature was maintained, until a final Ti concentration of 0.1 M was achieved. Aqueous NaOH (1 M) was added, also while maintaining the low temperature, until the pH reached 5.5, and a precipitate formed. The solution was allowed to warm and then stand for ~150 hours at room temperature. The yellow-hued sol-gel was centrifuged and the solvent removed. It was placed in a 70 ˚C oven to dry for 12 hours. The dried material was hand-milled with an agate mortar and pestle

www.manaraa.com

resulting in a brown-orange solid, which was then annealed under air as indicated. After cooling, all annealed materials were thoroughly washed with purified water, filtered, and dried.

The notation used hereafter for the materials follows the format (C)-TiO_2-(prewashed or not)(calcination), as shown in Table 1. "C" represents the presence of carbon and the type of glucose precursor: C is used for unlabeled, $^{13}C_6$ for uniformly labeled, and $^{13}C1$ for the ^{13}C label only at carbon 1. The number after TiO_2 indicates the duration of the time spent at 500 ºC, in minutes.

In some cases, the modified titania was washed after oven drying and before annealing, which is noted by a "W" before the calcination number. For example, a material prepared in the presence of $^{13}C1$-labeled glucose that was washed after oven drying and then annealed for 5 minutes at 500 ºC is given the notation: $^{13}C1$-TiO_2-W5. As a control, undoped TiO_2 was prepared by the same process, save that no glucose was used. This was viewed as a better control than the use of a commercial TiO_2 sample such as Degussa P25.

Routine physical characterization. Powder x-ray diffraction (XRD) spectra were taken with a diffractometer employing Cu K radiation. X-ray photoelectron spectroscopy (XPS) was done using a multitechnique spectrometer utilizing nonmonochromatized Al K radiation with a 1 mm^2 sampling area. The take-off angle was fixed at 45˚. In no case were either nitrogen or sulfur detected. Diffuse reflectance spectra were obtained with a UV/Vis spectrophotometer equipped with a diffuse reflectance attachment with MgO as a reference. For transmission electron microscopy (TEM) measurements, an aliquot of the powder was sonicated in purified water for 15 min. A single drop of this suspension was placed on a lacey-carbon-coated copper TEM grid and dried in air. The TEM examination was completed on an instrument operated at 200 kV with electron optical magnification of 64,000 to 550,000. Surface area analysis of the materials was performed by nitrogen sorption isotherms in a sorptometer. The surface areas were calculated by the Brunauer-Emmett-Teller (BET) method.

NMR parameters. The NMR experiments were performed on a Bruker DSX400 spectrometer at 400 MHz for ^1H, 100 MHz for ^{13}C. A Bruker 4-mm triple-resonance magic-angle spinning (MAS) probe head was used for measurements at various MAS speeds. ^{13}C

www.manaraa.com

and ^{1}H chemical shifts were referenced to TMS, using the COO resonance of glycine at 176.49 ppm as a secondary ^{13}C reference and the hydroxyapatite proton resonance at 0.18 ppm as a secondary ^{1}H reference. The 90° pulse lengths were 4 s for both ^{13}C and ^{1}H.

High-speed quantitative ^{13}C DP/echo/MAS NMR. In order to quantitatively account for the glucose carbon in TiO_2 particles, quantitative direct polarization (DP) /MAS ^{13}C NMR spectra were acquired at 14 kHz MAS. A Hahn echo was used to avoid baseline distortions and two-pulse phase modulation (TPPM) decoupling was applied during detection. The recycle delays were estimated by measuring cross-polarization (CP)/T_1/TOSS[68] (total suppression of sidebands) spectra with two or three different $T_{1,C}$ filter times. The $T_{1,C}$ filter time where the remaining carbon signals were less than 5% of the full intensity, was chosen as the recycle delay of the quantitative DP/MAS experiment to ensure that all carbons are essentially fully relaxed. More details are given in ref 69.

^{13}C chemical-shift-anisotropy filter. The ^{13}C chemical-shift-anisotropy (CSA) filter technique[70,71] with five pulses was used to select signals of sp^3-hybridized (alkyl) carbons, which have small CSA due to their nearly tetrahedral bonding symmetry. A filter time of 38 μs and a spinning frequency of 5 kHz were used. During detection, TPPM decoupling was applied.

CH spectral editing. The signals of methine (CH) carbons can be selectively observed based on CH-group multiple-quantum coherence not being dephased by the spin-pair CH dipolar coupling, while CH_2 group coherence is dephased by the dipolar coupling of the carbon to the second proton.[72] The residual quaternary carbon and partial CH_3 carbon signals were subtracted out by acquiring a second spectrum under the same conditions with an additional 40 μs gated decoupling before detection. The spinning frequency was 5.787 kHz.

CH_2 spectral editing. Spectral editing of CH_2 signals was achieved by selection of the three-spin coherence of CH_2 groups, using a ^{13}C 90° pulse and ^{1}H 0°/180° pulses applied after the first quarter of one rotation period with MREV-8 decoupling.[73] The spinning frequency was 5.787 kHz.

Two-dimensional ^{13}C-^{13}C spin exchange. In order to see the C-C connectivities in the *$^{13}C_6$*-glucose-modified, unannealed TiO_2 sample, a mixing time of 50 ms was used to produce the dipolar ^{13}C-^{13}C spin exchange. For sideband suppression, TOSS was applied before and

www.manaraa.com

time-reversed TOSS after the evolution time,[74,75] and normal TOSS was used before detection. The MAS frequency was 7 kHz.

Table 1. Description of preparation and nomenclature for synthesized photocatalysts.

Photocatalyst	Synthesis Description
Undoped TiO_2	Prepared without carbon source; annealing time of 5 minutes
C-TiO_2-5	Prepared with glucose as carbon source; annealing time of 5 minutes
$^{13}C_6$-TiO_2-5	Prepared with uniformly ^{13}C labeled glucose; annealing time of 5 minutes
$^{13}C1$-TiO_2-5	Prepared with glucose containing ^{13}C label at carbon 1; annealing time of 5 minutes
C-TiO_2-5W	Prepared with glucose as carbon source; washed between oven drying and annealing; annealing time of 5 minutes
$^{13}C_6$-TiO_2-5W	Prepared with uniformly ^{13}C labeled glucose; washed between oven drying and annealing; annealing time of 5 minutes
$^{13}C1$-TiO_2-5W	Prepared with glucose containing ^{13}C label at carbon 1; washed between oven drying and annealing; annealing time of 5 minutes
C-TiO_2-120	Prepared with glucose as carbon source; annealing time of 120 minutes

Selection of signals of isolated ^{13}C spins. In order to determine if the ^{13}C giving rise to a specific resonance is bonded to another ^{13}C, dephasing by the homonuclear J-coupling was measured. The dephased signal S after 10 ms of evolution under the J-coupling shows only the signals from isolated ^{13}C spins. A reference signal S_0 of all spin pairs and isolated ^{13}C spins was generated by a Hahn-solid-Hahn echo[76] that refocuses the J-coupling.[77] Direct polarization (DP) at an MAS frequency of 14 kHz was used to obtain clear spectra of all carbons.

www.manaraa.com

$^{13}C\{^1H\}$ HARDSHIP NMR. HeteronucleAr Recoupling with Dephasing by Strong Homonuclear Interactions of Protons (HARDSHIP)[78] NMR experiments were performed in order to estimate the distance of the CO_4 carbons from the nearest ^1H spins, presumably at the surface of the TiO_2 particles. The CH_n multispin dynamics of $^{13}C\{^1H\}$ HARDSHIP are more tractable than those in the corresponding $^{13}C\{^1H\}$ REDOR experiments, since ^1H-^1H dipolar couplings do not significantly affect the ^1H-^{13}C dephasing during HARDSHIP.[78] The spinning frequency was 6.5 kHz.

^{13}C T_1 relaxation measurements. The ^{13}C T_1 relaxation behavior was measured by CP/T_1/TOSS.[79] The T_1-filter times varied from 0 to 20 s.

Degradations. Titania (70 mg) and water (35 mL) were placed in a cylindrical Pyrex reaction vessel and sonicated for 5 minutes, followed by at least 10 minutes of stirring. Next, 35 mL of a 3 mM aqueous stock solution of quinoline was added to reach the desired final concentration of quinoline (0.15 mM). The pH was adjusted to 6 and maintained throughout the photolysis with careful addition of aqueous NaOH. The solution was purged with O_2 and stirred in the dark for at least 30 minutes. Reactions were irradiated with 350 nm broad range 4 W fluorescent tubes in a Rayonet minireactor or light from a 75 W Xe arc lamp passed through a water filter and a 495 nm long pass filter. Potassium ferrioxalate was used as a chemical actinometer to normalize lamp intensities.[80-82] All reactions were carried out at ambient temperature with continuous stirring and O_2 bubbling.

For kinetics, 1 mL aliquots were removed from the sample and acidified with H_2SO_4, centrifuged, filtered through a syringe tip filter containing a PES membrane with a 0.2 μm pore size, and analyzed by HPLC. HPLC analysis was done using a C18 reverse phase column on a system equipped a diode array detector. Retention times and UV/vis spectra were compared to authentic samples to identify components. All rates were obtained as the mean of at least two reactions.

www.manaraa.com

Results and Discussion

Catalyst preparation. In most respects, the method of Xu, *et al.*, was used in preparing these carbon-doped catalysts from glucose and $TiCl_4$.[63] An aging time of 150 h was used, following Xu's report of greatest visible light activity. The material obtained after centrifuging the sol-gel was oven dried at 70 ˚C for about 12 hours. The dried powder was then either annealed directly at 500 ˚C under air or exposed to an additional washing step beforehand. The purpose of the extra wash was originally to try to remove residual sodium chloride that was present in the final product as observed by XPS (*vide infra*). Annealing times were either 5 minutes, like the dwell time reported by Xu,[63] or 120 minutes, as noted. As reported below, some samples were also characterized without being annealed. All carbon-modified materials annealed for 5 minutes without the additional washing step (C-TiO_2-5, $^{13}C_6$-TiO_2-5, and $^{13}C1$-TiO_2-5) were dark gray in color. The other annealed samples (C-TiO_2-W5, $^{13}C_6$-TiO_2-W5, and $^{13}C1$-TiO_2-W5) and C-TiO_2-120 were an obviously lighter shade of gray. Both colors vary from Xu's report of brown material.[63]

Characterization. *C-TiO_2-5.* The morphology of the sample is anatase (Figure 1a), and the average particle diameter found by Scherrer's formula ($d = 0.9\lambda/\beta_{1/2}\cos\theta$) was 9 nm. TEM images (Figure 2) of C-TiO_2-5 agglomerates show some visible crystallinity and a particle size range of 5-15 nm, in good agreement with the value obtained from Scherrer's equation. Nitrogen sorption data showed the BET surface area to be 110 m^2/g. Figure 1b shows the material has a strong absorbance far into the visible spectral range.

Both Na and Cl were present in the XP spectrum, most likely from residual sodium chloride produced in the synthesis. This artifact is addressed below. In the range of greater interest, XPS analysis shows three major components in the C1s region with binding energies of 288.9 eV, 286.5 eV, and 284.7 eV (Figure 1c). The first two are assigned to CO_3 and C=O respectively, based on known chemical shifts.[83] The 284.7 eV peak is attributable to other reduced carbonaceous material (C-C/C-H), which can be coke and/or ambient atmospheric species deposited on the surface.

Upon fitting the data to Gauss-Lorentz curves (70 – 95% Gauss), a small shoulder at 282.4 eV becomes clear, possibly arising from a Ti-C bond. This phenomenon is illustrated using

www.manaraa.com

the spectrum of C-TiO_2-W5 in Figure 1d. Since the materials are annealed under oxidative conditions, it is more likely that this Ti-C species is present as an interstitial carbon also bound to oxygen as opposed to a highly reduced carbon substituting for oxygen.[32] (The ordinary chemical shift for TiC is 281.7 eV.)

Argon etching and remeasurement generally resulted in significant reduction of the peaks attributed to oxidized carbon species, leaving mostly C-C/C-H species and the shoulder at 282.4 eV. The signal at 282.4 eV often became more prevalent after argon etching.

C-TiO_2-120. This sample was also found to be anatase with an average particle size of 10 nm (Figure 1a) and a BET surface area of 114 m^2/g. Figure 1b shows the diffuse reflectance absorption spectrum of the material has a tail absorbing far into the red, but more weakly than the absorbance observed for C-TiO_2-5, correlating with its lighter appearance. The XP spectrum (Figure 1c) displayed features similar to those of C-TiO_2-5.

C-TiO_2-W5. The XRD data (Figure 1a) and TEM images (Figure 2) obtained for samples of this class provided information nearly identical to that of C-TiO_2-5. The diffuse reflectance spectrum shows features similar to those of C-TiO_2-120 (Figure 1b). Again, XPS results suggest the possible presence of several types of carbon components from carbonate to carbide-like species. The additional washing step lowered the sodium and chloride in this material to undetectable levels.

Undoped TiO_2. Like the other samples annealed for 5 minutes, Figure 1a shows the undoped material is anatase with a calculated average particle size of 9 nm. The BET surface area is 100 m^2/g. Diffuse reflectance measurements indicated the material has an absorbance cut-off near 400 nm (Figure 1b). Less carbon is seen in the XP spectrum of the undoped TiO_2 spectrum compared to the carbon-modified material, but the undoped sample does show weaker signals at 288.9 eV, 286.5 eV, and 284.7 eV. Importantly, however, no carbon remains detectable after argon etching of thoroughly washed undoped titania.

It should be noted that the fits were done using standard Gauss-Lorentz, symmetric peaks (70-95% Gauss) for the C1s region since there was no apparent reason to deviate for normal parameters (Figure 1d). It is possible that certain peaks could be made less significant or absent by changing certain parameter limits.

www.manaraa.com

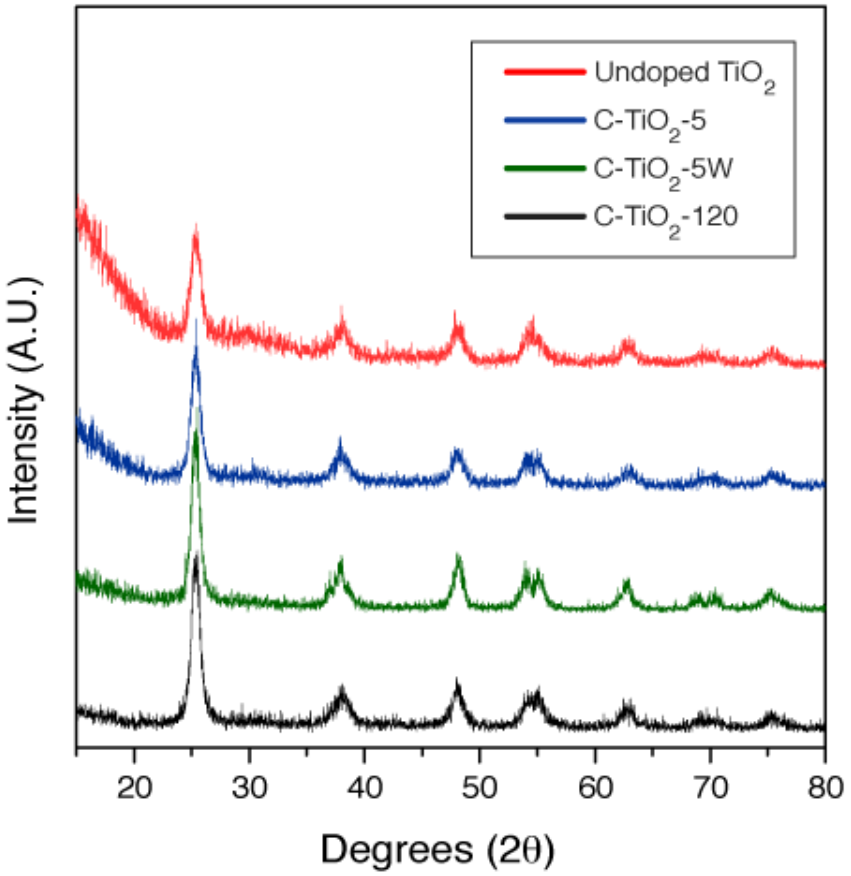

Figure 1. (a) X-Ray powder diffraction patterns, (b) diffuse reflectance spectra and (c) XP spectra of undoped and doped titania. (d) Show a fitted spectrum of ^{13}C1-TiO_2-5W.

NMR of samples before annealing. ^{13}C NMR spectra of the samples after glucose is exposed to the titanium-containing precursor but before annealing are shown in Figures 2 and 3. The reaction causes significant changes to its structure, as seen by the comparison to a reference spectrum of glucose in Figure 2a. The quantitative spectrum of Figure 2b exhibits many new bands, spanning much of the spectral range of ^{13}C. They can be assigned based on their chemical shifts and CH_n spectral editing, as shown in Figures 2b-2e. The strongest signal, at ~83 ppm, with a shoulder at ~73 ppm, is due to OCH groups (Figure 2d). Several unresolved bands of O-CH-O groups are detected between 100 and 115 ppm, but there are no signals of CH groups not bonded to O, which would resonate at ~ 50 ppm. In the CH_2-only spectrum of Figure 3e, we observe not only a C-CH_2-C resonance at 38 ppm and a CH_2-OH

www.manaraa.com

peak at 63 ppm, but also a strong OCH_2 band with a maximum at an unusually downfield chemical shift of ~78 ppm. A strong COO signal at 183 ppm, as well as weaker signals of ketones at ~210 ppm, of CH_3 groups at ~22 ppm, and of aromatic C (mostly furan at ~150 ppm) are identified after C-H dipolar dephasing (Figure 2b, thin line).

The resonance frequencies of the strongest OCH, O-CH-O, OCH_2, and COO signals are all unusually downfield, by about 10 ppm, from their usual positions in organic compounds.[84] This is an indication of bonding to Ti via the O, since the literature shows a comparable downfield chemical shift for ^{13}C in Ti-O-CH_2 groups.[85] After a chemical shift anisotropy filter that selects sp^3 hybridized carbons (Figure 2c), the alkyl signals are seen to extend to 130 ppm, again unusually downfield. The CH-only spectrum (Figure 2d and Figure 3c) also reveals a small signal of an unusual C-H resonating at 170 ppm, which is found to be an isolated ^{13}C (not bonded to other C) in J-dephasing experiments. On that basis, the peak at 170 ppm is assigned to a formate ester R-O-CHO, where the downfield chemical shift from 160-165 ppm for R = C[84] indicates that R = Ti. We cannot rule out a small amount of direct C-Ti bonding, which might be obscured by other oxygenated functionality.[86]

Further information about the connectivity of the observed carbon species was obtained by selective labeling from glucose-$^{13}C1$ and by ^{13}C-^{13}C correlations on the fully ^{13}C-labeled sample. The spectrum of $^{13}C1$-TiO_2-0 (i.e., dried, but unannealed material) is dominated by the COO-Ti signal; comparison with the peak intensity for the fully labeled sample shows that glucose C1 accounts for about half this species. This proves that significant rearrangement involving C1 has occurred: the glucose C1 site contributes to about half of the C-CH_3 species, but does not form C-CH_2-C and relatively little OCH or OCH_2. A large fraction of the O-CHR-O species comes from C1, as in the original structure glucopyranose. The ^{13}C-^{13}C correlation spectrum of $^{13}C_6$-TiO_2-0 is shown in Figure 4a. It shows pronounced cross peaks between COO and OCH, COO and CH_2 (meaning C-CH_2-C), OCH and OCH, OCH and OCH_2, OCH and CH_2, as well as OCH and O-CH-O signals. Based on these and the $^{13}C1$ labeling pattern, we propose two likely six-carbon fragments (Figure 4b). The cross-peak pattern of furan (150–110 ppm) is also detected. Other structures accounting for the remaining carbon species must also be present and might be identified in a more detailed study.

www.manaraa.com

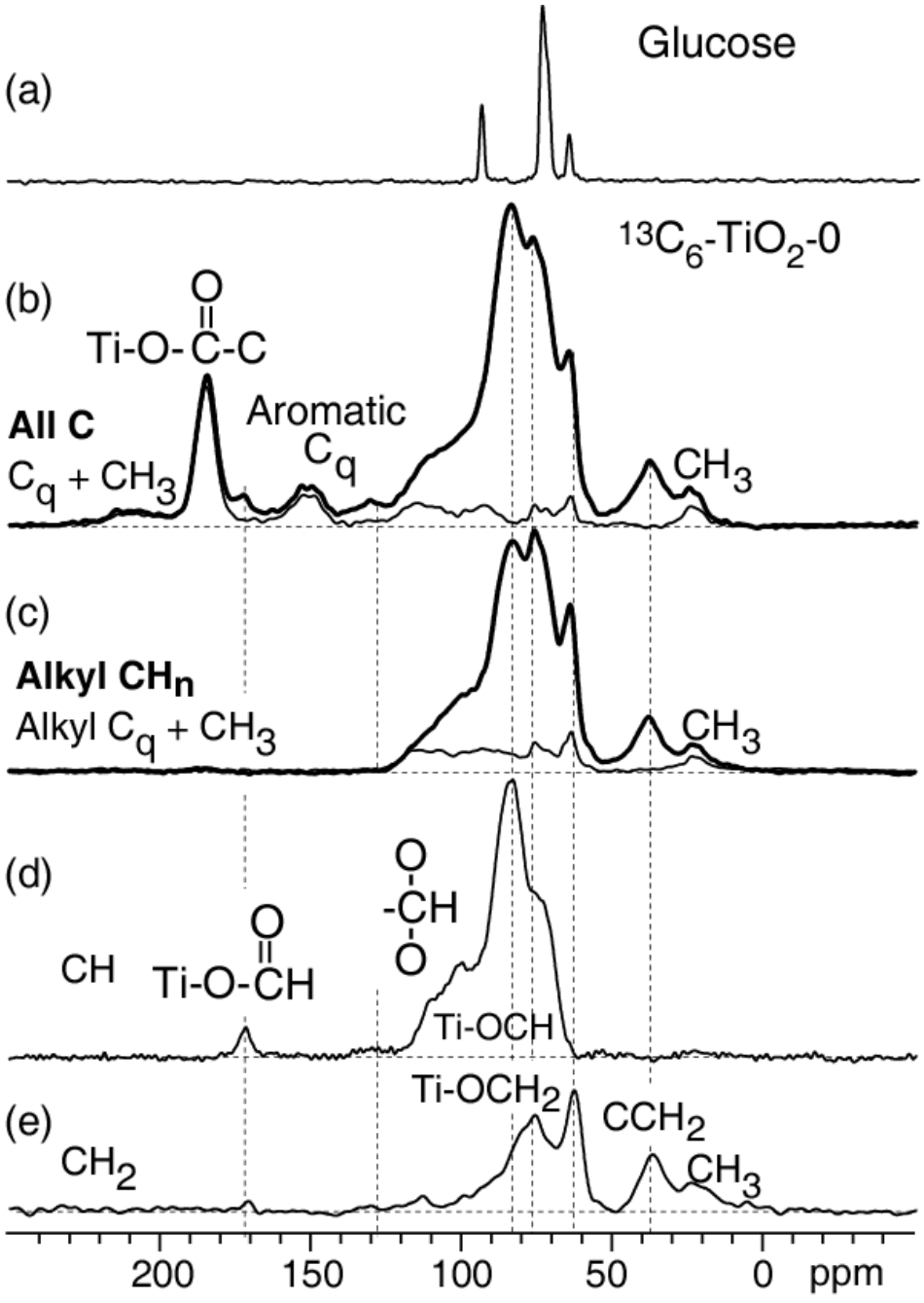

Figure 2. ^{13}C NMR spectra of materials before annealing. (a) Spectrum of glucose for reference. (b) – (e) Spectra of $^{13}C_6$-TiO_2-0 with spectral editing. (b) Quantitative spectrum of all C (thick line), and corresponding spectrum of nonprotonated C plus CH_3 (thin line) at 14 kHz MAS. (c) Spectrum after a chemical shift anisotropy (CSA) filter, which selects signals of sp^3-hybridized carbons (thick line), with signals extending to 120 ppm. The corresponding spectrum of quaternary carbon and CH_3 signals (thin line) was selected by 40 s of gated decoupling before detection. (d) CH-only and (e) CH_2-only spectra. All CH are polar alkyl and substituted by oxygen, according to their downfield chemical shift.

www.manaraa.com

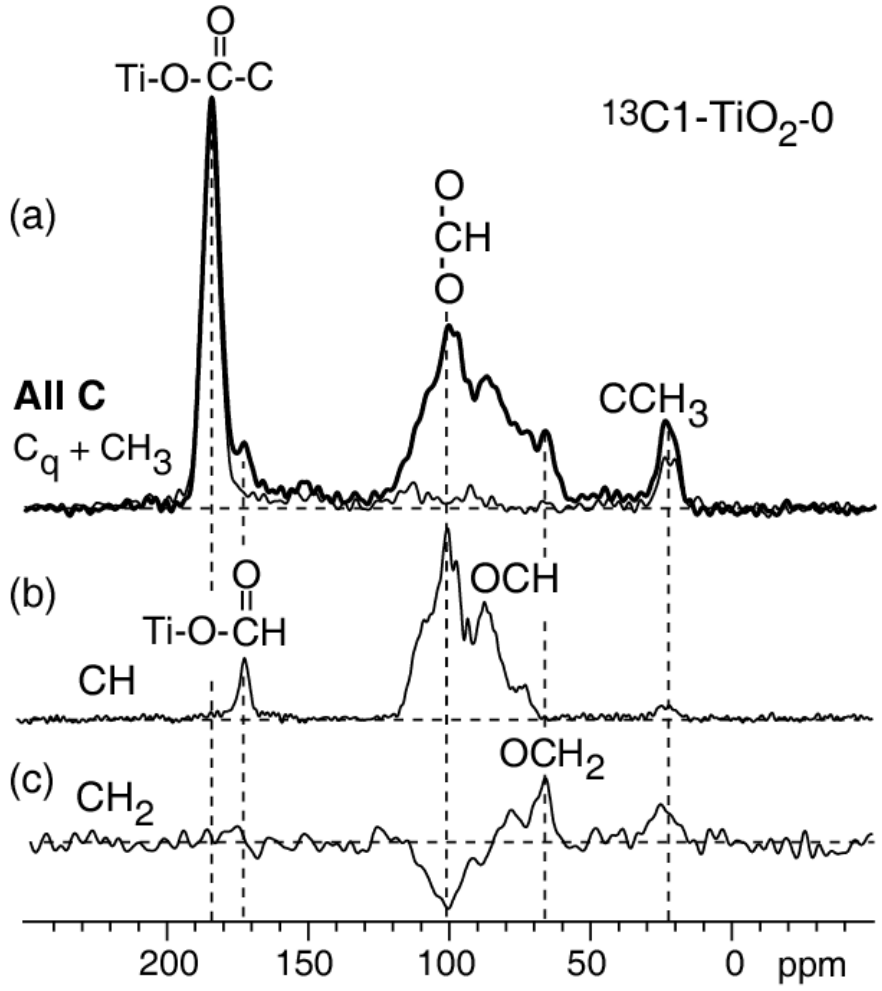

Figure 3. ^{13}C NMR of ^{13}C1-TiO$_2$-0 with spectral editing. (a) Quantitative spectrum of all C (thick line) and nonprotonated C (thin line) at 14 kHz MAS. (b) CH-only and (c) CH$_2$-only spectra.

The conditions used to prepare the doped TiO_2 expose the glucose to a strongly acidic environment followed by the addition of base. To determine whether the harshly acidic reaction conditions were responsible for the changes observed in the NMR spectra, a control experiment was performed. The reaction was set up as described in the experimental section except that HCl was added at the appropriate concentration instead of $TiCl_4$. The solution was concentrated by evaporation and a sticky solid residue was obtained after oven drying, and completely dried by lyophilization. The sample was analyzed in DMSO by solution ^{13}C NMR. No change in chemical shifts relative to those in the spectrum of unreacted glucose

www.manaraa.com

was observed. This indicates that simple acidic conditions are not sufficient to explain the significant transformations of glucose. Presumably, specific Lewis acid catalysis by $TiCl_4$ or other intermediate Ti-containing products catalyze these reactions and/or drive dehydration.

NMR after annealing. High-temperature annealing dramatically alters the forms of carbon in the samples, mostly leading to dehydration and condensation. The spectra in Figure 5a,b for samples annealed at 500°C for 5 and 120 minutes, respectively, are dominated by a broad aromatic-carbon band at 130 ppm. Of these aromatics, 72±2% are not protonated; given that no alkyl substitutents are present, this shows that systems of typically >8 fused aromatic rings are present. In addition, a clear shoulder between 170 and 200 ppm, assigned to C=O species, is observed in the sample annealed for 5 minutes. XPS confirmed the presence of small amounts of carbonate (CO_3) carbons in all samples that were annealed for 5 minutes. After heating otherwise identical samples for 120 minutes, all the carbon present is converted to aromatic species, likely highly condensed coke (Figure 5b). Comparison of the total ^{13}C NMR intensities shows that only a small fraction of the original carbon remains in the sample; see below.

An interesting, additional spectral feature, a sharp peak at 126 ppm (see Figure 6), is observed in a sample that was washed between the drying and annealing steps, an act originally intended to remove residual NaCl. This signal was reproduced in a second sample. While the chemical shift of 126 ppm might initially suggest an aromatic carbon, spectral editing proves that it must be assigned to a tetracoordinate alkyl orthocarbonate (CO_4) functionality. Gated decoupling proves that this is a nonprotonated carbon (Figure 6a). It experiences no J-coupling to another ^{13}C, as proved by the absence of J-dephasing, see Figure 6b; thus, it cannot be bonded to ^{13}C, which rules out an aromatic structure. This is confirmed by the minimal dephasing by a CSA-filter, which is characteristic of an sp^3-hybridized carbon with nearly tetrahedral bonding symmetry.[70] Given that the four bonds cannot be to carbon or hydrogen, orthocarbonate, CO_4, is the only reasonable structure. Such a structure is in good agreement with the observed downfield chemical shift: ketals and acetals resonate around 100 ppm, orthoesters at approximately 115 ppm, and orthocarbonate bands generally arise around 120 ppm.[84] To the best of our knowledge, no previous reports

www.manaraa.com

of a CO_4 species in TiO_2 have been made. The narrow lineshape, see Figure 6c, is indicative of a well-defined crystalline environment, strongly suggesting that the CO_4 centers are incorporated into the TiO_2 lattice.

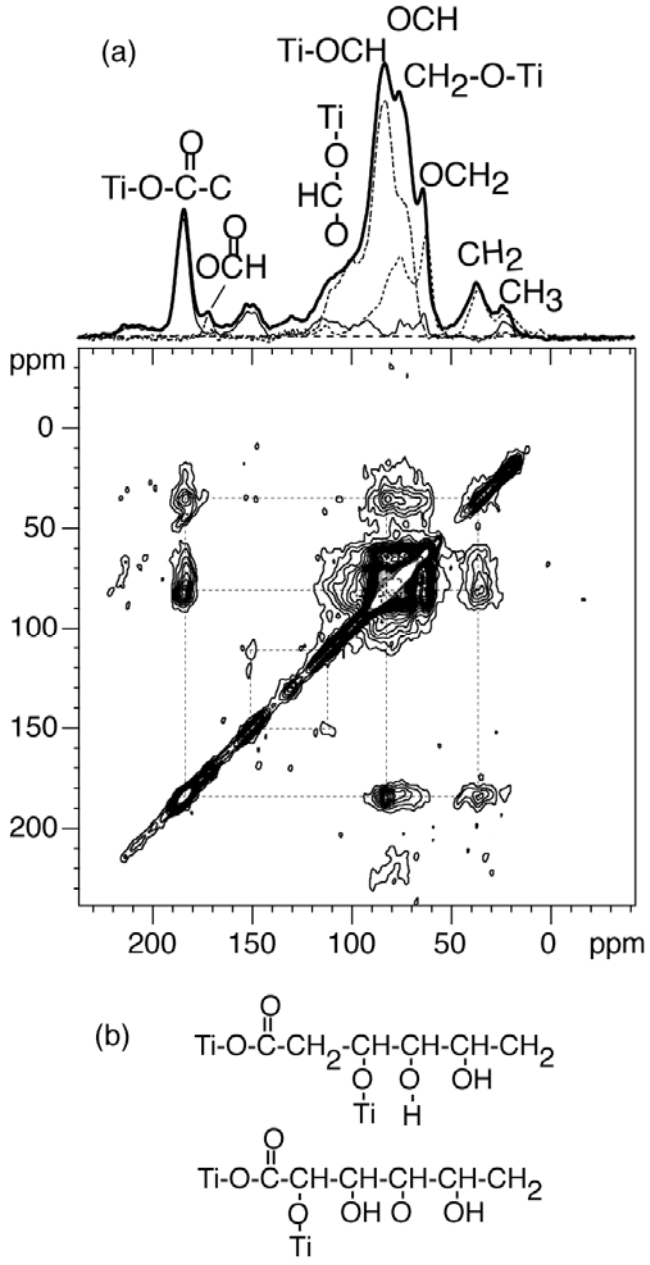

Figure 4. (a) Two-dimensional ^{13}C-^{13}C correlation spectrum of $^{13}C_6$-TiO_2-0 with a mixing time of 50 ms at 14 kHz MAS. At the top, one-dimensional spectra of all C (thick line), CH (dash-dotted line), and CH_2 (dashed line) are shown superimposed to facilitate peak assignment. (b) Two structural fragments consistent with the observed cross peaks in (a).

www.manaraa.com

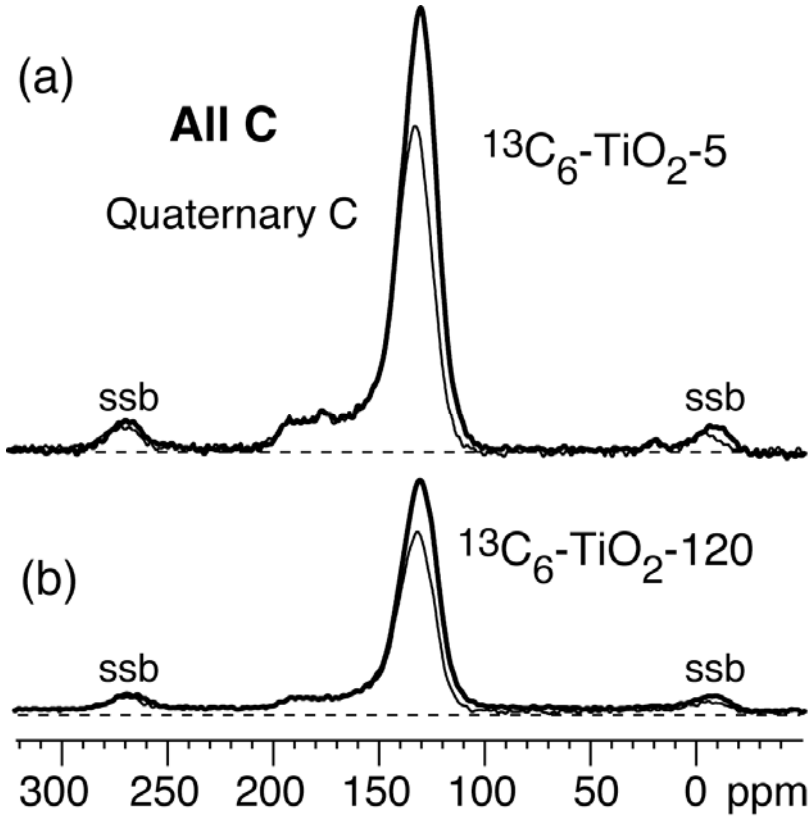

Figure 5. Comparison between the quantitative ^{13}C NMR spectra of (a) $^{13}C_6$-TiO$_2$-5 and (b) $^{13}C_6$-TiO$_2$-120, plotted on a correct relative vertical scale. Thick lines: spectra of all C; thin lines: spectra of quaternary C. Spinning frequency: 14 kHz. Spinning side bands are marked ssb.

In order to look for the relation between the washing step and the formation of the orthocarbonate centers, Figure 7 compares ^{13}C NMR spectra of samples with and without washing with water before annealing. Only subtle changes are observed (Figures 7a and 7b). Washing removes the minor furan-like components and increases the signal for some C=O species, which in effect fill the volume vacated by the components that were washed out. However, after collection and lyophilization of the aqueous washes, little organic material was observed by either ^{1}H or ^{13}C solution-phase NMR, confirming that most of the material removed by the washing step was NaCl.

After calcination, the washed and unwashed samples generally had very similar C1s XP spectra, but NMR showed a significant difference, with the former having the striking CO_4 peak at 126 ppm (37% by integration) and a more pronounced CO_3 peak (7%, Figures 6a and

www.manaraa.com

7c). The removal of small amounts of furan-like materials by washing does not seem like an adequate rationalization to explain the changes. It is possible that this change is instead a result of the presence of water at the beginning of the annealing period.

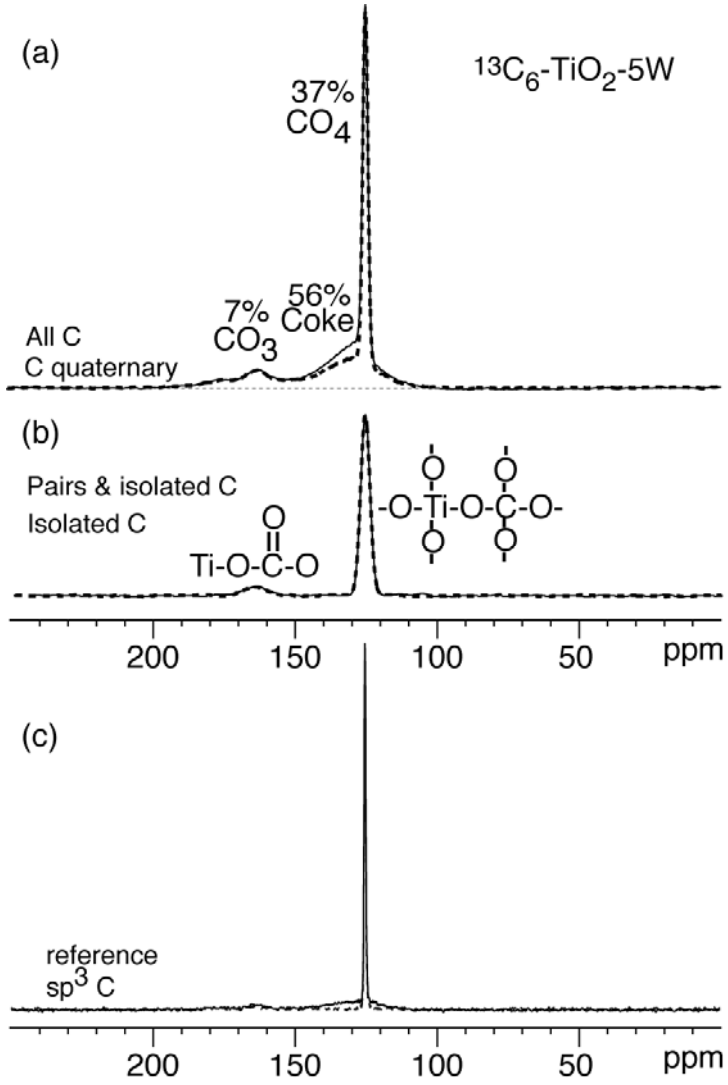

Figure 6. ^{13}C NMR spectra of $^{13}C_6$-TiO_2-W5. (a) Quantitative (DP) spectrum of all C (thick line) and corresponding spectrum of nonprotonated C (thin line). Strong line broadening was applied to make the coke and CO_3 bands better visible. (b) J-modulated dephasing spectra. Solid line: Reference spectrum S_0 of ^{13}C-^{13}C spin pairs and isolated ^{13}C spins. Dashed line: Spectrum S after dephasing by ^{13}C-^{13}C J-coupling. The two spectra are very similar and prove that the two sharp peaks are from isolated carbons. Strong line broadening was applied to make the CO_3 band better visible. (c) Selection of sp^3-hybridized C by a five-pulse CSA filter. Thick line: reference spectrum with minimum CSA dephasing time (1 s). Thin line: spectrum after a CSA dephasing time of 38 s at 6.5 kHz MAS. In this spectrum with minimal line broadening applied, the small natural width of the peak at 126 ppm is apparent.

www.manaraa.com

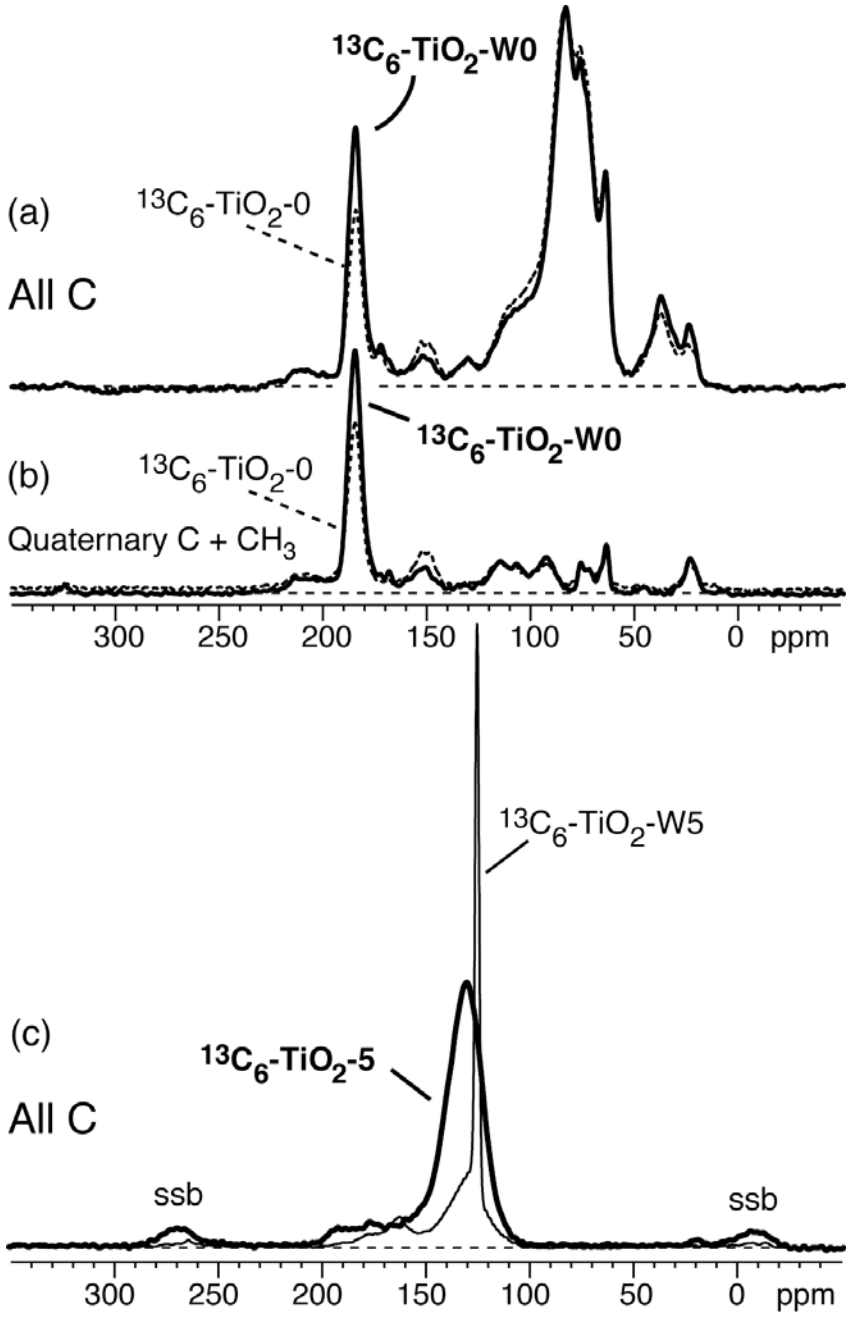

Figure 7. Effects of washing oven-dried material before annealing on ^{13}C spectra before and after annealing. (a) Quantitative ^{13}C NMR spectra of $^{13}C6$-TiO_2-W0 (solid line) and of $^{13}C6$-TiO_2-0 (dashed line) (b) Corresponding quantitative spectra of quaternary and methyl C. (c) Quantitative ^{13}C NMR spectra of $^{13}C6$-TiO_2-W5 (thin line) and of $^{13}C6$-TiO_2-5 (thick line).

The slow dephasing of the CO_4 signal in $^{13}C\{^1H\}$HARDSHIP[78] distance measurements, see Figure 8, indicates that the CO_4 species is far (> 1 nm) from any ^1H: it is thus not a

www.manaraa.com

surface species, which may be why it is not observed in the XP spectrum (Figure 8). By contrast, the fast dephasing of the coke signal in Figure 8 demonstrates that the coke component is close to protons, suggesting this species is on the surface containing aromatic C-H and possibly nearby Ti-OH bonds.

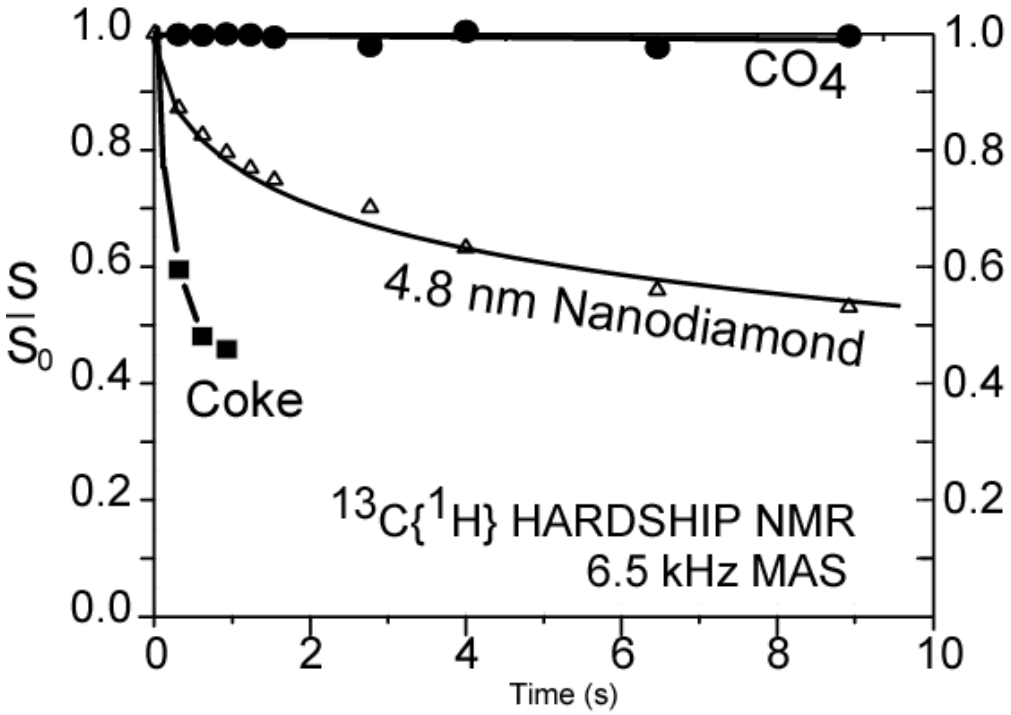

Figure 8. $^{13}C\{^{1}H\}$ HARDSHIP NMR decay curves of the CO_4 and coke signals in $^{13}C_6$-TiO_2-W5. The decay curve for 4.8-nm diameter nanodiamond is used as a reference. The slow decay of the CO_4 signals shows that orthocarbonate is located deep inside the TiO_2 nanoparticles.

Figure 9 shows that the two major components of $^{13}C_6$-TiO_2-W5 have similarly short ^{13}C spin lattice relaxation times of around 4 seconds. This implies the presence of unpaired electrons inside the TiO_2 particles, given that there are no other couplings of carbon in CO_4 that could drive relaxation.

Figure 10 compares the ^{13}C NMR signal intensity for samples before and after annealing, indicating a major loss of carbon. The carbon mass fractions in the six samples studied were determined from the total integrated intensity of the direct-polarization ^{13}C NMR spectra.

www.manaraa.com

Spectra were normalized per scan and mass of sample in the rotor (Figure 10), based on a calibration line determined by NMR and elemental analysis of several model compounds (circles) and validated on many samples of plant and soil organic matter (open triangles).[87] This enables us to convert the measured ^{13}C NMR intensity of each sample studied here to an approximate carbon weight % (taking into account the ^{13}C labeling level). The three samples before annealing have 6-7 wt% C, which corresponds to an organic volume fraction around 15%, given the ~2.5 times higher density of TiO_2 relative to glucose. Without washing, 5-minute annealing reduces the carbon to 1.3 wt%, and 120-minute annealing further to 0.6 wt%. After washing and 5-min annealing, the carbon weight fraction is also 0.6 wt%.

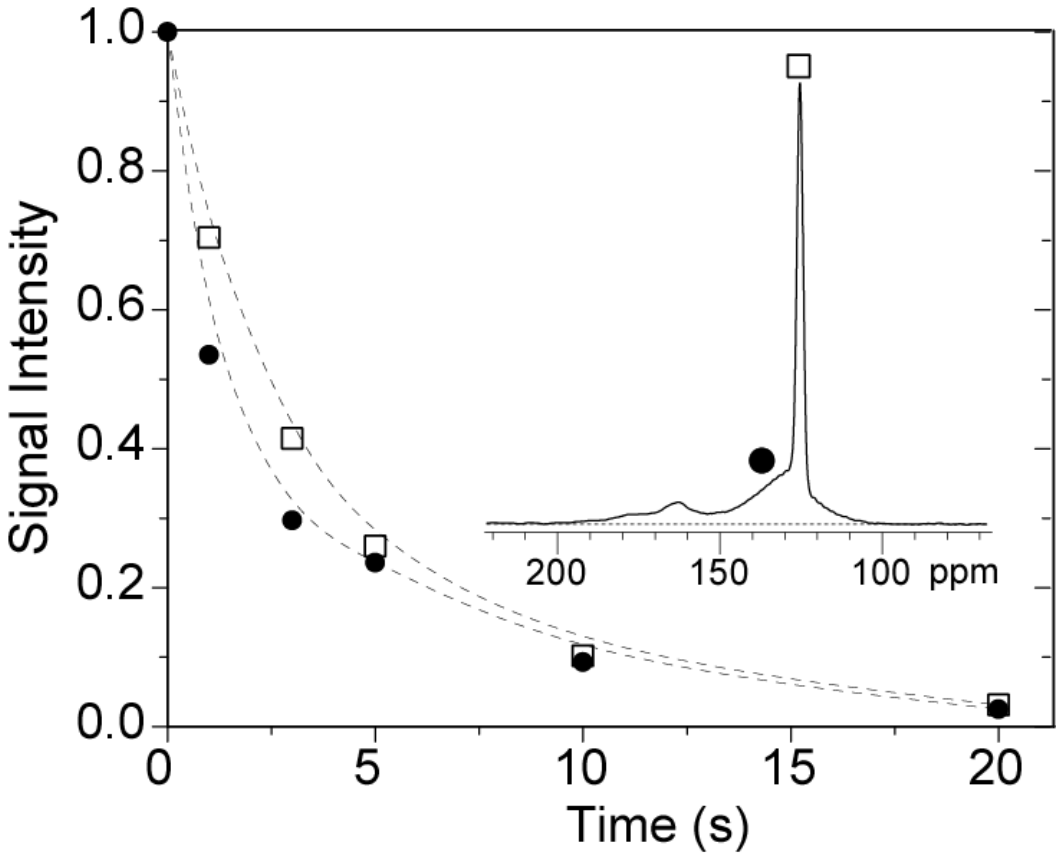

Figure 9. ^{13}C spin-lattice relaxation time measurements of orthocarbonate (CO_4) centers (squares) and coke (circles) in $^{13}C_6$-TiO_2-W5. The dashed lines are guides to the eye.

www.manaraa.com

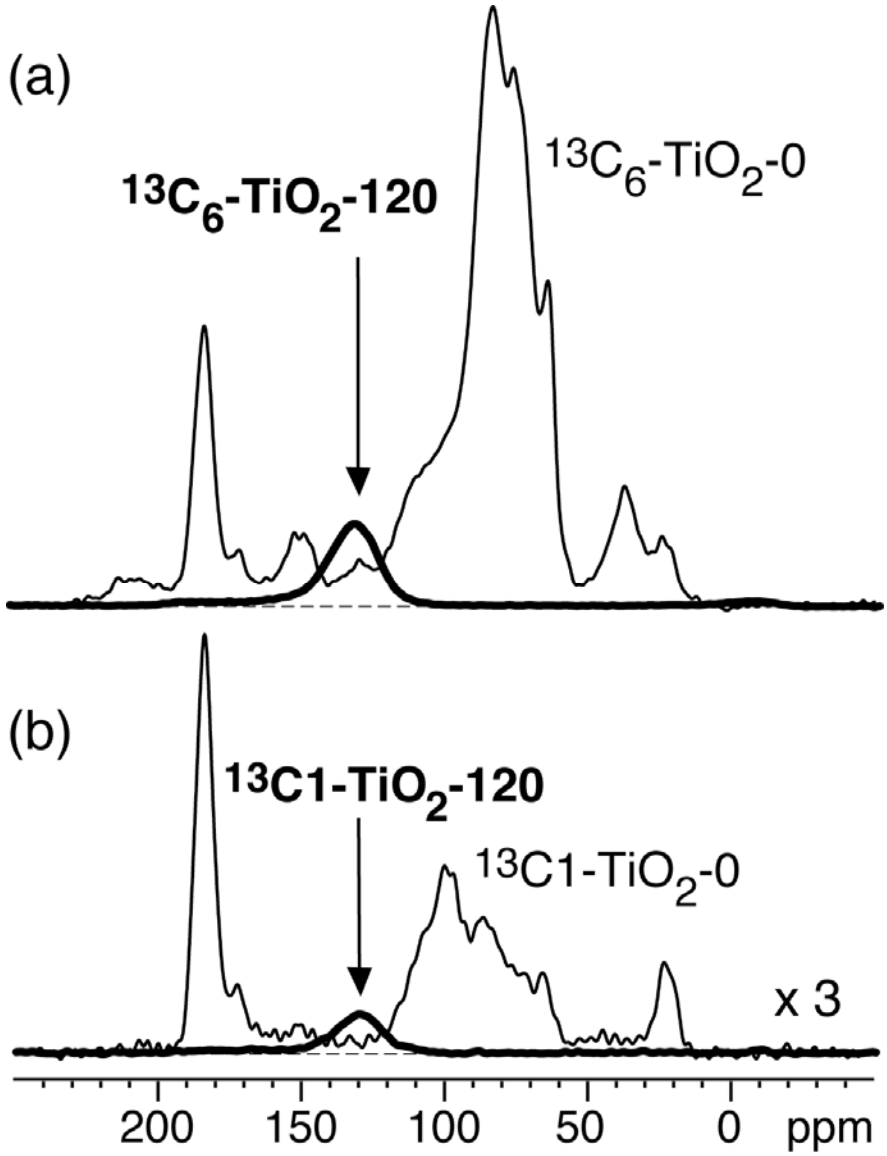

Figure 10. Comparison between the quantitative spectra of Ti-containing materials before and after annealing. (a) Comparison of $^{13}C_6$-TiO$_2$-0 (dashed line) and ^{13}C1-TiO$_2$-0 (solid line), plotted on a correct relative vertical scale. (b) Comparison of ^{13}C1-TiO$_2$-0 (thin line) and ^{13}C1-TiO$_2$-120 (thick line). (b) is scaled up by 300% relative to (a).

The NMR data strongly suggest there is more than a physical interaction between the glucose and the titanium-containing precursor, and chemical reaction does occur during the aging and/or drying stages. Upon annealing of washed samples, carbon trapped inside the

www.manaraa.com

TiO_2 particles ultimately ends up substituting for a Ti atom and carbon nearer to the surface seems to be condensed into coke.

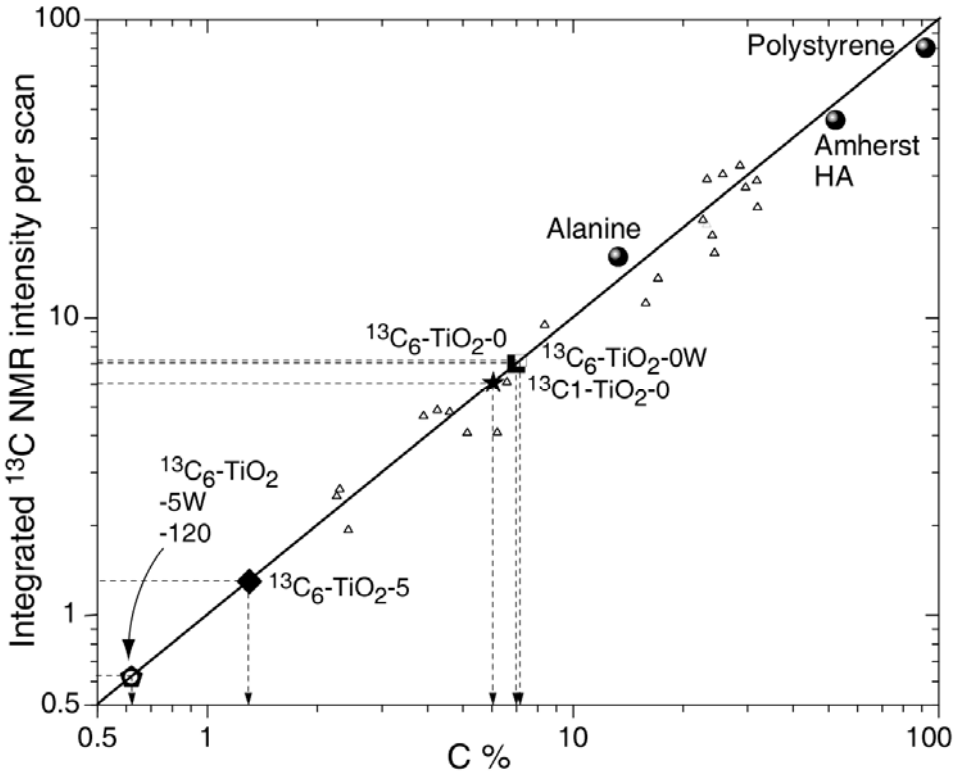

Figure 11. Carbon mass percentages in glucose-^{13}C modified TiO_2 from correlations of integrated DP ^{13}C NMR intensities per scan and mg of sample (ordinate) with the carbon mass fractions from elemental analysis (abscissa), calibrated using alanine, polystyrene, humic acid from Amherst, and numerous soil samples (open triangles). $^{13}C_6$-TiO_2-0: filled square, $^{13}C_1$-TiO_2-0: star; $^{13}C_6$-TiO_2-W0: open small square; $^{13}C_6$-TiO_2-W5: filled diamond; $^{13}C_6$-TiO_2-120 filled pentagon; $^{13}C_6$-TiO_2-W5: open pentagon. The degree of ^{13}C labeling has been taken into account in determining the overall carbon percentage. Carbon content declines substantially on extended annealing.

Conclusions

NMR is shown to be a useful tool for probing the structure of magnetically accessible nuclei in carbon-doped TiO_2. It shows that a strategy of using glucose (as a representative poly-ol) as a dopant does provide true covalent interactions (Ti-O-C bonds) in the sol-gel stage of the catalyst preparation, and furthermore, that significant chemical change of the carbon structure occurs during this time. It confirms the previously somewhat ambiguous conclusion that coke is the major carbon-containing component of most of these hybrid

www.manaraa.com

materials, but also shows that orthocarbonate structures — with C-for-Ti substitutions deep inside the titania particles — do occur in certain annealed samples.

Carbon doping does not qualitatively affect the rate of photocatalytic degradation of quinoline, or the predominance of SET-induced products in the early stages of degradation, except for the C-TiO_2-W5 catalyst. Here, hydroxyl chemistry was more competitive, just as the orthocarbonate structure was only observed in this material. However, the causality of this association is not established. Inasmuch as visible light irradiation (≥495 nm) does not photocatalyze decomposition of quinoline but that a reasonable rationalization for this exists through the intervention of the coke, we suggest that preparing coke-free C-TiO_2 may be critical for proving the utility of such materials for visible-light applications.

Acknowledgement. The authors thank the National Science Foundation (CHE 0518586) for financial support of this work. We are grateful to Clemens Burda for allowing us to obtain diffuse reflection spectra on his instrumentation. We also gratefully acknowledge the assistance of Jim Anderegg with the XPS data.

References

(1) *Photocatalysis: Fundamentals and Applications*; Serpone, N.; Pelizzetti, E., Eds.; John Wiley & Sons: New York, 1989.

(2) Pichat, P.; Guillard, C.; Maillard, C.; Amalric, L.; D'Oliveira, J. C. *Trace Met. Environ.* **1993**, *3 (Photocatalytic Purification and Treatment of Water and Air)*, 207-223.

(3) Mills, A.; Davies, R. H.; Worsley, D. *Chem. Rev.* **1993**, *22*, 417-25.

(4) Malati, M. A. *Environ. Technol.* **1995**, *16*, 1093-1099.

(5) Bahnemann, D.; Cunningham, J.; Fox, M. A.; Pelizzetti, E.; Pichat, P.; Serpone, N. In *Aquatic and Surface Photochemistry*; Helz, G. R., Zepp, R. G., Crosby, D. G., Eds.; Lewis Publishers: Boca Raton, 1994, p 261-316.

(6) Serpone, N.; Khairutdinov, R. F. *Stud. Surf. Sci. Catal.* **1997**, *103*, 417-444.

(7) Konstantinou, I. K.; Albanis, T. A. *Appl. Catal. B* **2003**, *42*, 319-335.

(8) Fox, M. A.; Dulay, M. T. *Chem. Rev.* **1993**, *93*, 341-357.

(9) Legrini, O.; Oliveros, E.; Braun, A. M. *Chem. Rev.* **1993**, *93*, 671-698.

www.manaraa.com

(10) Linsebigler, A. L.; Lu, G.; Yates, J. T., Jr. *Chem. Rev.* **1995**, *95*, 735-758.

(11) Thompson, T. L.; Yates, J. T., Jr. *Chem. Rev.* **2006**, *106*, 4428-4453.

(12) Deb, S. K. *Solar Energy Materials & Solar Cells* **2005**, *88*, 1-10.

(13) Hagfeldt, A.; Graetzel, M. *Acc. Chem. Res.* **2000**, *33*, 269-277.

(14) Choi, H.; Baik, C.; Kang Sang, O.; Ko, J.; Kang, M.-S.; Nazeeruddin Md, K.; Gratzel, M. *Angew. Chem., Int. Ed.* **2008**, *47*, 327-30.

(15) Zhang, X.-T.; Taguchi, T.; Wang, H.-B.; Meng, Q.-B.; Sato, O.; Fujishima, A. *Res. Chem. Int.* **2007**, *33*, 5-11.

(16) Choi, W.; Termin, A.; Hoffmann, M. R. *J. Phys. Chem.* **1994**, *98*, 13669-13679.

(17) Anpo, M. *Catal. Surv. Jpn.* **1997**, *1*, 169-179.

(18) Wang, C.-Y.; Bahnemann, D. W.; Dohrmann, J. K. *Chem. Commun.* **2000**, 1539-1540.

(19) Coloma, F.; Marquez, F.; Rochester, C. H.; Anderson, J. A. *Phys. Chem. Chem. Phys.* **2000**, *2*, 5320-5327.

(20) Burda, C.; Lou, Y.; Chen, X.; Samia, A. C. S.; Stout, J.; Gole, J. L. *Nano Letters* **2003**, *3*, 1049-1051.

(21) Fujishima, A.; Honda, K. *Nature* **1972**, *238*, 37-8.

(22) Kraeutler, B.; Bard, A. J. *J. Am. Chem. Soc.* **1978**, *100*, 4317-4318.

(23) Kraeutler, B.; Bard, A. J. *J. Am. Chem. Soc.* **1978**, *100*, 5985-5992.

(24) Irie, H.; Watanabe, Y.; Hashimoto, K. *J. Phys. Chem. B* **2003**, *107*, 5483-5486.

(25) Okato, T.; Sakano, T.; Obara, M. *Phys. Rev. B* **2005**, *72*, 115124/1-115124/6.

(26) Yang, K.; Dai, Y.; Huang, B. *J. Phys. Chem. C* **2007**, *111*, 12086-12090.

(27) Liu, S.; Chen, X. *J. Haz. Mat.* **2008**, *152*, 48-55.

(28) Asahi, R.; Morikawa, T.; Ohwaki, T.; Aoki, K.; Taga, Y. *Science* **2001**, *293*, 269-271.

(29) Asahi, R.; Morikawa, T. *Chem. Phys.* **2007**, *339*, 57-63.

(30) Batzill, M.; Morales, E. H.; Diebold, U. *Phys. Rev. Lett.* **2006**, *96*, 026103/1-026103/4.

(31) Batzill, M.; Morales, E. H.; Diebold, U. *Chem. Phys.* **2007**, *339*, 36-43.

(32) Di Valentin, C.; Pacchioni, G.; Selloni, A. *Chem. Mater.* **2005**, *17*, 6656-6665.

www.manaraa.com

(33) Di Valentin, C.; Finazzi, E.; Pacchioni, G.; Selloni, A.; Livraghi, S.; Paganini, M. C.; Giamello, E. *Chem. Phys.* **2007**, *339*, 44-56.

(34) Kuznetsov, V. N.; Serpone, N. *J. Phys. Chem. B* **2006**, *110*, 25203-25209.

(35) Serpone, N. *J. Phys. Chem. B* **2006**, *110*, 24287-24293.

(36) Sakthivel, S.; Kisch, H. *ChemPhysChem* **2003**, *4*, 487-490.

(37) Sakthivel, S.; Janczarek, M.; Kisch, H. *J. Phys. Chem. B* **2004**, *108*, 19384-19387.

(38) Chen, X.; Lou, Y.; Samia, A. C. S.; Burda, C.; Gole, J. L. *Adv. Funct. Mater.* **2005**, *15*, 41-49.

(39) Balcerski, W.; Ryu, S. Y.; Hoffmann, M. R. *J. Phys. Chem. C* **2007**, *111*, 15357-15362.

(40) Reyes-Garcia, E. A.; Sun, Y.; Reyes-Gil, K.; Raftery, D. *J. Phys. Chem. C* **2007**, *111*, 2738-2748.

(41) Ohno, T.; Mitsui, T.; Matsumura, M. *Chem. Lett.* **2003**, *32*, 364-365.

(42) Umebayashi, T.; Yamaki, T.; Itoh, H.; Asai, K. *Appl. Phys. Lett.* **2002**, *81*, 454-456.

(43) Ohno, T.; Tsubota, T.; Toyofuku, M.; Inaba, R. *Catal. Lett.* **2004**, *98*, 255-258.

(44) Ho, W.; Yu, J. C.; Lee, S. *J. Solid State Chem.* **2006**, *179*, 1171-1176.

(45) Lettmann, C.; Hildenbrand, K.; Kisch, H.; Macyk, W.; Maier, W. F. *Appl. Catal. B* **2001**, *32*, 215-227.

(46) Sakthivel, S.; Kisch, H. *Angew. Chem. Int. Ed.* **2003**, *42*, 4908-4911.

(47) Irie, H.; Watanabe, Y.; Hashimoto, K. *Chem. Lett.* **2003**, *32*, 772-773.

(48) Choi, Y.; Umebayashi, T.; Yoshikawa, M. *J. Mater. Sci.* **2004**, *39*, 1837-1839.

(49) Ohno, T.; Tsubota, T.; Nishijima, K.; Miyamoto, Z. *Chem. Lett.* **2004**, *33*, 750-751.

(50) Rincon, M. E.; Trujillo-Camacho, M. E.; Cuentas-Gallegos, A. K. *Catal. Today* **2005**, *107-108*, 606-611.

(51) Liu, H.; Imanishi, A.; Nakato, Y. *J. Phys. Chem. C* **2007**, *111*, 8603-8610.

(52) Dong, C. X.; Xian, A. P.; Han, E. H.; Shang, J. K. *Diffus. Defect Data, Pt. B* **2007**, *121-123*, 939-942.

(53) Wang, H.; Lewis, J. P. *J. Phys.: Condens. Matter* **2005**, *17*, L209-L213.

(54) Ren, W.; Ai, Z.; Jia, F.; Zhang, L.; Fan, X.; Zou, Z. *Appl. Catal. B* **2007**, *69*, 138-144.

www.manaraa.com

(55) Wang, X.; Meng, S.; Zhang, X.; Wang, H.; Zhong, W.; Du, Q. *Chem. Phys. Lett.* **2007**, *444*, 292-296.

(56) Li, Y.; Hwang, D.-S.; Lee, N. H.; Kim, S.-J. *Chem. Phys. Lett.* **2005**, *404*, 25-29.

(57) Khan, S. U. M.; Al-Shahry, M.; Ingler, W. B., Jr. *Science* **2002**, *297*, 2243-2245.

(58) Wong, M.-S.; Hsu, S.-W.; Rao, K. K.; Kumar, C. P. *J. Molec. Catal. A* **2008**, *279*, 20-26.

(59) Cui, X.; Gu, H.; Lu, J.; Shen, J.; Zhang, Z. *J. Nanosci. Nanotechnol.* **2007**, *7*, 3140-3145.

(60) Ohno, T.; Tsubota, T.; Nishijima, K.; Miyamoto, Z. *Chem. Lett.* **2004**, *33*, 750-751.

(61) Sakthivel, S.; Neppolian, B.; Shankar, M. V.; Arabindoo, B.; Palanichamy, M.; Murugesan, V. *Sol. Energy Mater. Sol Cells* **2003**, *77*, 65-82.

(62) Xu, C.; Killmeyer, R.; Gray, M. L.; Khan, S. U. M. *Electrochem. Commun.* **2006**, *8*, 1650-1654.

(63) Xu, C.; Killmeyer, R.; Gray, M. L.; Khan, S. U. M. *Appl. Catal. B* **2006**, *64*, 312-317.

(64) Xu, T.-h.; Song, C.-l.; Liu, Y.; Han, G.-r. *J. Zhejiang Univ., Sci., B* **2006**, *7*, 299-303.

(65) Xu, C.; Shaban, Y. A.; Ingler, W. B.; Khan, S. U. M. *Solar Energy Materials & Solar Cells* **2007**, *91*, 938-943.

(66) Irie, H.; Watanabe, Y.; Hashimoto, K. *Chem. Lett.* **2003**, *32*, 772-773.

(67) Xu, C.; Khan, S. U. M. *Electrochem. Solid-State Lett.* **2007**, *10*, B56-B59.

(68) TOtal Suppression of Sidebands

(69) Mao, J. D.; Hu, W. G.; Schmidt-Rohr, K.; Davies, G.; Ghabbour, E. A.; Xing, B. *Soil Sci. Soc. Am. J.* **2000**, *64*, 873-884.

(70) Mao, J. D.; Schmidt-Rohr, K. *Solid State Nucl. Magn. Reson.* **2004**, *26*, 36-45.

(71) Chan, J. C. C.; Tycko, R. *J. Chem. Phys.* **2003**, *118*, 8378-8389.

(72) Mao, J. D.; Schmidt-Rohr, K. *J. Mag. Res.* **2003**, *162*, 217-227.

(73) Mao, J. D.; Schmidt-Rohr, K. *J. Mag. Res.* **2005**, *176*, 1-6.

(74) Kolbert, A. C.; Griffin, R. G. *J. Magn. Reson.* **1990**, *66*, 87-91.

(75) Geen, H.; Bodenhausen, G. *J. Chem. Phys.* **1992**, *97*, 2928-2937.

(76) Schmidt-Rohr, K.; Spiess, H. W. *Macromolecules* **1991**, *24*, 5288-5293.

(77) Fang, X.-W.; Schmidt-Rohr, K. *manuscript in preparation* **2008**.

www.manaraa.com

(78) Schmidt-Rohr, K.; Rawal, A.; Fang, X. W. *J. Chem. Phys.* **2007**, *126*, 054701/1-054701/16.

(79) Torchia, D. A. *Journal of Magnetic Resonance (1969-1992)* **1978**, *30*, 613-16.

(80) Hatchard, C. G.; Parker, C. A. *Proc. Royal. Soc. A* **1956**, *235*, 518-536.

(81) Calvert, J. C.; Pitts, J. N. *Photochemistry*; Wiley: New York, 1966.

(82) Bowman, W. D.; Demas, J. N. *J. Phys. Chem.* **1976**, *80*, 2434-2435.

(83) Moulder, J. F.; Stickle, W. F.; Sobol, P. E.; Bomben, K. D. *Handbook of X-Ray Photoelectron Spectroscopy*; Perkin-Elmer Corporation (Physical Electronics): Eden Prairie, MN, 1992.

(84) Pretsch, E.; Bühlmann, P.; Affolter, C. *Structure Determination of Organic Compounds: Tables of Spectral Data*; Third Completely Revised and Enlarged English ed.; Springer: New York, 2000.

(85) Foris, A. *Magn. Reson. Chem.* **2000**, *38*, 1044-1046.

(86) Berger, S.; Bock, W.; Frenking, G.; Jonas, V.; Müller, F. *J. Am. Chem. Soc.* **1995**, *117*, 3820-3829.

(87) Fang, X.-W.; Chua, T.; Schmidt-Rohr, K.; Thompson, M. L. *manuscript in preparation* **2008**.

(88) Cermenati, L.; Pichat, P.; Guillard, C.; Albini, A. *J. Phys. Chem. B* **1997**, *101*, 2650-2658.

(89) Nicolaescu, A. R.; Wiest, O.; Kamat, P. V. *J. Phys. Chem. A* **2005**, *109*, 2829-2835.

(90) Yan, X.; Ohno, T.; Nishijima, K.; Abe, R.; Ohtani, B. *Chem. Phys. Lett.* **2006**, *429*, 606-610.

(91) Agrios, A. G.; Gray, K. A.; Weitz, E. *Langmuir* **2003**, *19*, 1402-1409.

(92) Agrios, A. G.; Gray, K. A.; Weitz, E. *Langmuir* **2004**, *20*, 5911-5917.

(93) Kim, S.; Choi, W. *J. Phys. Chem. B* **2005**, *109*, 5143-5149.

(94) Orlov, A.; Watson, D. J.; Williams, F. J.; Tikhov, M.; Lambert, R. M. *Langmuir* **2007**, *23*, 9551-9554.

(95) Chen, D.; Jiang, Z.; Geng, J.; Wang, Q.; Yang, D. *Ind. Eng. Chem. Res.* **2007**, *46*, 2741-2746.

www.manaraa.com

CHAPTER 10. General conclusions

Several carbon-containing materials, including the Maillard reaction products, soil, detonation nanodiamond, and glucose-modified TiO_2, have been studied using advanced solid state NMR techniques.

The structure of the Maillard reaction products is complicated due to their great heterogeneity. Our studies focused on the model reaction products from glucose reacting with glycine in a 1:1 ratio. The fate of glycine, the fate of glucose, alkyl fragements, and several complex nitrogen-containing structures have been elucidated.

(1) To determine the fate of glycine, the resulting structural units and their percentages have been characterized by various ^{13}C, ^{15}N, and ^{13}C-^{15}N NMR experiments applied to melanoidins made from various isotopically labeled glycines reacted with isotopically unlabeled glucose, in dry and solution reactions. About half of glycine stays intact. The C1 carbon remains mostly in carboxyl groups, while the nitrogen is incorporated into a wide range of amine, amide, and pyrrolic species. Nonprotonated N predominates (>80%) and may be a characteristic marker of Maillard reaction products, distinguishing them from proteinaceous materials and aminosugars, where most nitrogen is in NH groups.

(2) To determine the fate of glucose, various solid-state NMR techniques, including spectral editing of CH, CH_2, and alkyl carbon signals, ^{15}N-^{13}C MELODI selection, 2D ^{15}N-^{13}C correlation, and 2D ^{13}C-^{13}C spin exchange, have been applied to melanoidins made from glucose with various ^{13}C-labeled sites reacted with ^{15}N labeled glycine in a 1:1 ratio in dry condition. Quantitative ^{13}C spectra show that alkyl units contain ~ 48 % of carbon in melanoidins. The spectra show striking differences between the structures formed by different carbons (C1 through C6) of glucose, proving that specific structural units are formed during the Maillard reaction. The reactivity of the glucose-C1 carbon stands out: more than half of C1 carbons form additional C-C bonds, a much larger fraction than for the other sites. C2 carbons are all bonded to heteroatoms and mostly not protonated, while C3 is predominantly protonated and has a significant fraction of sites not bonded to heteroatoms. Only C4 and C5 remain significantly (~ 40%) in alkyl OCH sites. C6 undergoes the least

www.manaraa.com

transformation, mostly remaining in the OCH_2 form; in addition, it forms some C-CH_2-C units and ~1/5 is lost from the sample. C1 and C6 form CH_3 end groups in similar quantities (together, 2% of all C). C2-C5 are involved in formation of furan, which accounts for less than 15% of total sugar carbons, while nitrogen-containing five-membered aromatic rings are formed from all carbons. Based on the experimental data, specific structural fragments have been identified. Besides new bond formation, we also find specific evidence of sugar fragmentation, specifically C_5+C_1, C_1+C_5, and C_2+C_4, generally consistent with Tressl's proposal.

(3) In the Maillard reaction of sugar with amine compounds, nitrogen plays a crucial role for structural transformations of glucose, especially under dry reaction conditions. Two-dimensional ^{15}N-^{13}C and ^{13}C-^{13}C spin exchange as well as three-dimensional ^{15}N-^{13}C-^{13}C solid state NMR techniques have been applied to ^{15}N- and ^{13}C-labeled melanoidins made in a dry reaction of glucose with glycine in a 1:1 molar ratio. The carbons associated with a downfield nitrogen band at 203 ppm indicated the presence of oxazolium mesoions. Based on the cross peak patterns in 3D cross sections of nitrogen resonating at 203 and 60 ppm, specific oxazolium structures have been proposed. Nitrogen resonating at 180 ppm is bonded to one nonprotonated C2 and two protonated C1 carbons of glucose, with C1 and C2 bonded to each other. Furthermore, one-dimensional CN_2 spectra proved that the downfield protonated C1H is bonded to two aromatic nitrogen atoms. On that basis, an imidazolium structure was proposed. For nitrogen resonating near 153 ppm, a clear cross peak pattern of a downfield protonated carbon bonded to a high-field quaternary carbon was observed and 4-oxopyridinyl was proposed as a tentative structure to match those constraints. Our multidimensional NMR experiments also showed that CH_3 (mostly from C6) and HC=O (from C1) is bonded to specific pyrrole structures instead of furan. A specific amide structure with nitrogen chemical shift at ~120 ppm, proposed in our previous work, has also been confirmed. Although pyridines and pyrazines are often reported as Maillard reaction products in low molecular weight or volatile products, our multinuclear solid state NMR results suggested that their amounts are insignificant compared to imidazolium and oxazolium.

www.manaraa.com

The capability of NMR to characterize the composition of the soil organic matter (SOM) after miniral sample treatment has been demonstrated in a study of three different aggregation size of four soil samples from two fields in Iowa. The quantitative ^{13}C DP/MAS NMR analyses allowed us to conclude (1) that the HF treatment had little impact on the organic carbon functional groups in the samples, the acidification of HCl/HF with or without heating only converts COO^- to COOH; (2) that organic carbon was detectable even in untreated soil materials, which contain paramagnetic ions; (3) that esters are only a minor fraction of SOM in these Mollisols; (4) that the aromatic components of SOM were enriched in the clay fractions (compared with the whole soils) and in the poorly drained soils (compared with the well-drained soils); (5) that nonpolar, non-protonated aromatic C, interpreted as a proxy for charcoal C, composed 28 – 36 % of total organic C in the unfractionated soil and clay-fraction samples and dominated the aromatic C in all soil samples. ^{13}C CP/TOSS spectra display the transformation from plant to particulate organic matter (POM) and then to humic substances in whole and clay-fraction soils with loss of the crystalline cellulose in plants to form noncrystalline saccharides in POM and soil, while selectively preserving oxidized char-coal components.

The structure of detonation nanodiamond with a crystalline core of ~4-nm diameter was studied by ^{13}C NMR and ^{1}H-^{13}C distance measurements. Short ^{1}H-^{13}C dipolar dephasing shows that about 6 % of all carbons, about half of surface sites, are protonated, while the other half are bonded to OH groups. No aromatic carbons were found, ruling out buckyball or graphitic surface layers in the two samples studied. A scattering feature previously attributed to graphitic onion shells was not observed here and shown to be most likely an artifact of a plastic sample holder. ^{1}H NMR and $^{13}C\{^{1}H\}$ HETCOR consistently showed an unexpected 3.8-ppm chemical shift position of the surface protons; the protons were proved to be bonded to carbons (rather than O in –OH or H_2O) by strong ^{13}C-^{1}H dipolar sidebands in HETCOR spectra. Given the protonated surface, ^{1}H-^{13}C HARDSHIP NMR can probe the depth of various sites from the surface. The upfield signals dephased faster than the ideal-diamond carbon signal, corroborating the assignment of the broad upfield bands to a disordered shell of ~0.63 nm thickness, in a particle of 4.8-nm diameter. Fast $T_{1,C}$ relaxation (<1 s) observed for all carbons in nanodiamond is due to interactions with ~40 unpaired

www.manaraa.com

electrons per grain. The longer $T_{1,C}$ of the protonated surface carbons and the layer underneath proves that most unpaired electrons are not from dangling bonds at the surface, but from unpaired electrons at depths of 0.4 – 1 nm.

The forms of carbon in glucose-modified TiO_2 photocatalyst were characterized using various solid-state ^{13}C NMR techniques. In the preannealed material, NMR showed strong 10 ppm downfield chemical shift of many Ti-O-C bonds, indicating that an actual chemical reaction between glucose and the titanium-containing precursor has occurred. After annealing, NMR results verified the presence of coke, which is not easy to identify by XPS due to the likely overlap with atmospheric carbon adsorbed on the surface. An additional washing step before annealing at 500 ^{o}C led to the generation of a CO_4 species proved by its small chemical shift anisotropy, no bonding with hydrogen or other carbons, and its downfield chemical shift. According to the comparison of HARDSHIP simulation curves among CO_4, coke and nanodiamond core, the carbon in CO_4 form is doped deeply inside of TiO_2 crystallites, while the coke covers the surface. The short ~4 s spin-lattice relaxation time of both coke and CO_4 suggests the presence of unpaired electrons. NMR also detected small amounts of CO_3 in all carbon-modified material annealed for 5 minutes. Annealing for longer times led to the removal of CO_n species. Quantitative ^{13}C NMR intensity measurements showed how the carbon mass percentage varies with the synthesis conditions.

www.manaraa.com

Acknowledgements

I would like to acknowledge and extend my heartfelt gratitude to:

Professor Klaus Schmidt-Rohr for his knowledgeable direction and encouragements. All the work in this dissertation would not be completed without his contributions;

Professor Mei Hong for her teaching on NMR theory;

Professor Jingdong Mao for bringing me the interesting nanodiamond project originating from the Murchison meteorite study;

I also deeply appreciate the help from **Charles, Dr. Levin, Adu, Wenbin, Ming, Rajee, Sara, Tim, Yanyan, Xueqian, Yongchao, and Yuan**.

I would like also thank our collaborators:

Professor Michael Thompson and **Dr. Chua** for providing soil samples and enlightening discussions;

Professor William Jenks and **Erin** for sample preparations and sharing experimental results.

www.manaraa.com